Rifting in the northern Tyrrhenian Sea Basin:
A multichannel and wide-angle seismic study

Dissertation
zur Erlangung des Doktorgrades
der Mathematisch-Naturwissenschaftlichen Fakultät
der Christian-Albrechts-Universität zu Kiel

vorgelegt von
Stefan Möller

Kiel, Mai 2013

1. Gutachter: Prof. Dr. Ingo Grevemeyer
2. Gutachter: Prof. Dr. Christian Berndt
Tag der mündlichen Prüfung: 20. Juni 2013
Zum Druck genehmigt: 20. Juni 2013

gez. Prof. Dr. Wolfgang J. Duschl, Dekan

Abstract

Rifted continental margins or basins are the results of continental lithospheric extension and a fundamental process in geodynamics. Extension is expressed by normal faulting and block rotation in the brittle upper crust and ductile deformation in the lower crust. Conjugate rifted margins are often asymmetric and reveal different amounts of crustal stretching and thinning. Shallow dipping crustal-scale detachment faults are thought to be the controlling mechanism of this asymmetry, although the development of such features is debated. This PhD thesis presents the results of a seismic campaign from the northern Tyrrhenian Sea Basin. It is a continental back-arc basin exhibiting rift features preserved at the early stages of rifting. Two W-E orientated multichannel seismic profiles (MCS) cross the region between Corsica, Sardinia and mainland Italy. The data are processed up to prestack-depth and time migrated images in order to investigate the style of faulting and sedimentary structures. Coincident refraction- and wide-angle seismic data were acquired using OBH-stations. Joint refraction and reflection tomography reveal the crustal architecture and thickness.
The MCS image of the northern profile shows that the geometry of upper Tortonian to Early-Pliocene sediments (8-4 Ma) reflects the active rift phase. Fault displacements are localized on major normal faults dipping mainly to the east (30°-40°) forming a succession of asymmetric half-grabens. Major blocks generate the majority of the entire horizontal extension which is estimated to be ∼30%. Faults seem not to be linked at the brittle-ductile transition zone (∼3-4 km). The tomographic model shows, that the crust has thinned from ∼24 km to a thickness of ∼17 km (β=1.3). The thinning matches the estimated amount of horizontal extension (30%).
Towards the southern transect, the width of the basin increases. Seismic data display an asymmetric margin configuration. This is expressed by crustal thinning from ∼24 km in the west (Sardinia) to ∼11 km in the east (β-factor=2.2). Moreover, the Sardinia Margin comprises large fault-bounded blocks where the crust is relatively thick. Blocks of smaller size are observed further east, where the crust has thinned more. This zone (∼ 100 km wide) is characterized by reduced p-wave velocities which correlates with intensive faulting as imaged on the MCS section. A reliable estimation of the amount of brittle extension is not possible due to the presence of complex small-scale faults. However, the thinning-factor of the lower crust matches the thinning-factor of the entire crust. This implies that the amount of brittle extension should be similar. In this zone, reflections within sedimentary sub-basins are related to basalt flows. A narrow zone with similar characteristics is also observed on the northern line.
In the vicinity of the Sardinia Margin, post-rift sediments indicate that tectonism has ceased before Early-Pliocene time, whereas young faults cut the seafloor in the center and in the eastern region (near mainland Italy). The different ages of syn-tectonic sequences indicate an apparent W-E rift propagation. The comparison of both transects shows a NW-SE orientated crustal thinning resulting in mantle exhumation in the Vavilov Basin. Diminishing block sizes and concomitant crustal thinning reflect increasing

strain rates in NW-SE direction.
The data provide no evidence for potential long-lived detachment faults controlling the development of the asymmetric rift configuration. However, it can be explained by the regional plate-tectonic setting and subduction roll-back. Rifting propagated toward the east, following the retreatment of the subduction zone. The pole of rotation is located north of the basin. Thus, with increasing distance from the pole toward the south, stretching rates increase. This led to the differences of syn-sedimentary ages, block sizes and NW-SE crustal thinning.

Kurzfassung

Passive Kontinentalränder und Riftbecken sind das Ergebnis gedehnter kontinentaler Lithosphäre und ein fundamentaler geodynamischer Prozess. Extension der spröden Oberkruste ist gekennzeichnet durch Abschiebungen und der Verkippung kontinentaler Blöcke. Die Deformation der Unterkruste findet duktil statt. Häufig wird beobachtet, dass ehemals zusammenhängenden Kontinentalränder durch Asymmetrie gekennzeichnet sind, z.B. durch stark variierende Dehnungsfaktoren. Ein möglicher Mechanismus der zur Erklärung der Variabilität herangezogen wird, ist die Trennung der gesamten Kruste entlang flach einfallenden Störungen. Allerdings ist dies mechanisch umstritten.
Diese Arbeit präsentiert die Ergebnisse seismischer Messungen im nördlichen Tyrrhenischen Becken. Es handelt sich hierbei um ein kontinentales Randbecken in einem frühen Extensionsstadium, dass durch verkippte Krustenblöcke gekennzeichnet ist. Zwei in W-E Richtung angelegte, reflexionsseismische Profile verlaufen zwischen Corsica, Sardinien und dem italienischem Festland. Ein Teil dieser Arbeit beschäftigt sich mit der Bearbeitung dieser Daten um tiefen- und zeitmigrierte Sektionen zu erstellen auf denen die Abschiebungscharakteristik und sedimentäre Strukturen abgebildet sind. Weiterhin wurden auf denselben Profilen refraktions- und weitwinkelseismische Messungen durchgeführt, die von Ozean-Boden-Hydrophonen registriert wurden. Durch gemeinsame Inversion refraktierter und reflektierter Phasen wurden Geschwindigkeitsmodelle erstellt, die den Aufbau und die Mächtigkeit der Kruste zeigen.
Die reflexionsseismischen Sektionen zeigen anhand der sedimentären Ablagerungscharakteristik, dass die aktive Dehnungsphase zwischen dem spätem Tortonium und frühem Pliozän stattgefunden haben muss (8-4 Ma). Der Großteil der gesamten Dehnung im Becken ($\sim$30%) wird durch Versätze entlang von Hauptstörungszonen hervorgerufen, die unter einem Winkel von 30°-40° nach Osten einfallen und eine Abfolge asymmetrischer Halbgräben ergeben. Das Krustenmodell zeigt, dass sich die Gesamtkruste von 24 auf 17 km ausgedünnt hat (β-Faktor=1.3). Dies ist betragsgleich zur horizontalen Extension.
Weiter südlicher wird das Becken breiter und die Daten zeigen asymmetrische Beckenränder. Dies zeigt sich durch eine Abnahme der Krustenmächtigkeit von ursprünglich 24 km unterhalb Sardiniens auf ein Minimum von 11 km im Osten (β-Faktor=2.2). Weiterhin ist zu beobachten, dass nahe Sardiniens, dort wo die Kruste relativ dick ist, große Krustenblöcke zu finden sind. Zunehmend kleinere Blöcke sind in der Zone von geringerer Krustenmächtigkeit zu finden. Diese $\sim$100 km breite Zone ist außerdem durch eine reduzierte P-Wellen Geschwindigkeit gekennzeichnet. Die reflexionsseismischen Sektionen zeigen, dass dies im Zusammenhang mit stärkerer Bruchbildung steht. Eine Abschätzung von der durch Sprödbruch generierten Extension ist aufgrund der strukturellen Komplexität nicht möglich. Allerdings ist der Ausdünnungsfaktor der gesamten Kruste ähnlich dem der unteren Kruste. Dies lässt darauf schließen, dass die spröde Oberkruste ähnlich stark gedehnt wurde. Starke Reflexionen innerhalb dieser Zone können auf basaltische Schichten zurückgeführt werden. Eine ähnliche Zone, allerdings

von geringerer Ausdehnung, existiert ebenso auf dem nördlichen Profil. Seewärts von Sardinien zeigen ungestörte Sedimentablagerungen, dass die Rift-Phase vor dem frühen Pliozän inaktiv wurde. Im Zentralteil und im Osten sind allerdings junge Abschiebungen zu finden, die durch einen Versatz des Meeresbodens gekennzeichnet sind. Die unterschiedlich alten syn-tektonischen Sedimente zeigen das Fortschreiten das Rifts in Richtung Osten an. Der Vergleich beider Profile zeigt eine NW-SE orientierte krustale Ausdünnung. Dies spiegelt einen zunehmenden Spannungszustand wider, der schließlich zur Freilegung des oberen Mantels im südlich gelegeneren Vavilov-Becken führt.

Die seismischen Daten geben keinen Hinweis für anfänglich existierende und großräumige Störungszonen, die die Ursache für die asymmetrische Entwicklung des Beckens sind. Die strukturellen Unterschiede können jedoch anhand der platten-tektonischen Situation erklärt werden. Das Becken entwickelte sich ostwärts aufgrund der Verlagerung der Subduktionszone. Da sich der Rotationspol nördlich des Beckens befindet, nehmen mit zunehmender Entfernung in Richtung Süden die Streckungsraten zu. Dies führt zu den unterschiedlichen syn-sedimentären Ablagerungen, die Abnahme der Blockgrößen und die NW-SE ausgerichtete Krustenausdünnung.

Contents

1. Preface

"The Mediterranean has the distinction of simultaneously being one of the smallest, most accessible, most closely studied and least understood of all the major salt-water basins in the world" (Duschenes et al., 1986)

1.1. Introduction

Rifting of the continental lithosphere is one major process of the plate-tectonic cycle that shapes the topography of the earth. The idea of continental plates that move through time, goes back to Alfred Wegener who postulated the concept of continental-drift in 1912 and later in his book "Die Entstehung der Kontinente und Ozeane (1915)". He took into account the corresponding coast lines of South America and Africa to argue, that these plates were once joined together. His concept was also supported by formerly continuous mountain ranges or fossils that were found on both continents. The driving forces that lead to continental break-up and the mechanisms that separate the plates were still unknown at Wegener´s time. Today, it is generally accepted that the driving mechanism for plate tectonics are convection currents within the mantle (Condie, 2005).

Extensional forces in the lithosphere lead either to the formation of intra-continental rift basins that become failed rifts (aulacogens) if extension ceased, or if extension continues, full continental break-up may occur and a pair of passive conjugated margins is generated. Conjugated rifted margins can be found worldwide and seam for instance most of the Atlantic Ocean (Fig.1.1). While tectonic activity at intra-continental rift basins can abandon at an early rift phase due to changes in stress field, rifting in the Atlantic continued and an active spreading center developed, the Mid-Atlantic-Ridge (MAR). Decompression in the upwelling asthenosphere leads to the generation of melts that continuously form new oceanic crust by cooling and fill the gap between the newly formed oceanic lithospheric plates. The sea-floor-spreading process at divergent plate margins increases the distance between the former connected continental lithosphere. This makes a reconstruction of the initial conditions during the early-stage of rifting difficult. Moreover, thermal subsidence and additional load of thick postrift sedimentary deposits cause that subsequently pre-rift crustal structures are buried at deeper levels.

At many rifted margins, continental break-up is also accompanied by incipient volumi-

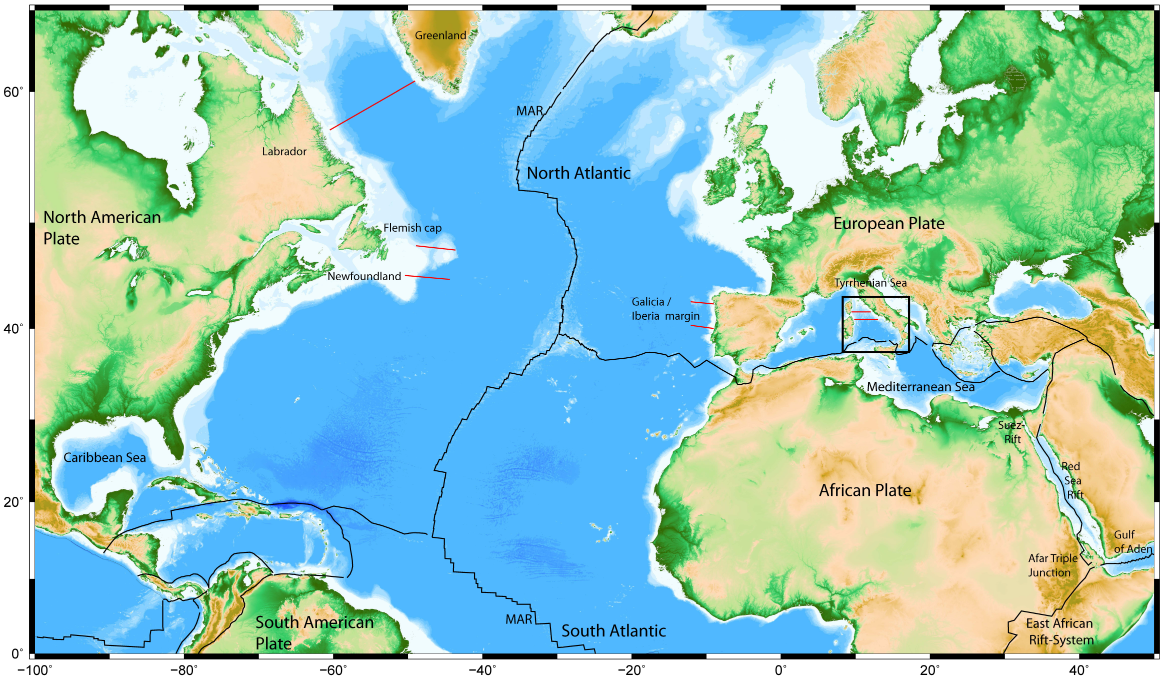

Figure 1.1.: Continental break-up in the Late Triassic to Early Jurassic led to conjugated rifted margins in the North-Atlantic (Shillington et al., 2006). The conjugated and magma-poor margins of Galicia/Iberia and Newfoundland/Flemish Cap are well investigated margin configurations. In this study, the young Tyrrhenian Sea in the Western Mediterranean (black box) serves as a natural laboratory to study the incipient and early phases of continental rifting. Thin red lines show the seismic transects presented in this thesis.

nous volcanic activity caused by mantle melting processes (e.g. White and McKenzie (1989)). Pairs of conjugated rifted margins on the northern hemisphere, which exhibit best the pre- and syn-tectonic structures are the so-called magma-poor margins (see section 1.2), for instance the configuration of the Galicia/Iberia Margin (Fig.1.1) which is located opposite to the Flemish Cap/Newfoundland Margin (Shillington et al., 2006; Ranero and Perez-Gussinye, 2010) as well as the margins of Greenland and Labrador (Chian et al., 1995). The rifted margins comprise the shallow water areas as well as the deeper regions of the shelf and are bounded seawards by a transition zone that leads over to oceanic crust (Fig.1.1). They are sites of major hydrocarbon reservoirs, since faulting processes may form traps where oil and gas can accumulate. Therefore, those margins are interesting regions for the oil and gas industry. An improved understanding of their formation processes is very important, especially for exploration in deep water areas.

Classical conceptual rift models like the proposed pure-shear model (McKenzie, 1978) or the simple-shear model (Wernicke, 1985) attempt to explain the formation of rift basins and margins (Fig. 1.2). However, they do not fully satisfy the observations made on seismic sections. The geological processes of stretching by normal faulting and contemporaneous crustal thinning are still a matter of debate (e.g. Ranero and Perez-Gussinye (2010); Reston (2005)). The debates center around two enigmas: 1) Seismic studies show, that the architecture of conjugate margins or rift basins reveal asymmetric tectonic features (Bosworth, 1985; Perez-Gussinye et al., 2003). This is contradictory to symmetric margin configuration as predicted by the pure-shear model in which opposing major listric faults sole out at the brittle-ductile transition zone and crustal thinning is accompanied by passive upwelling of the asthenosphere. Hence, this model has limited applicability (Lister et al., 1991).

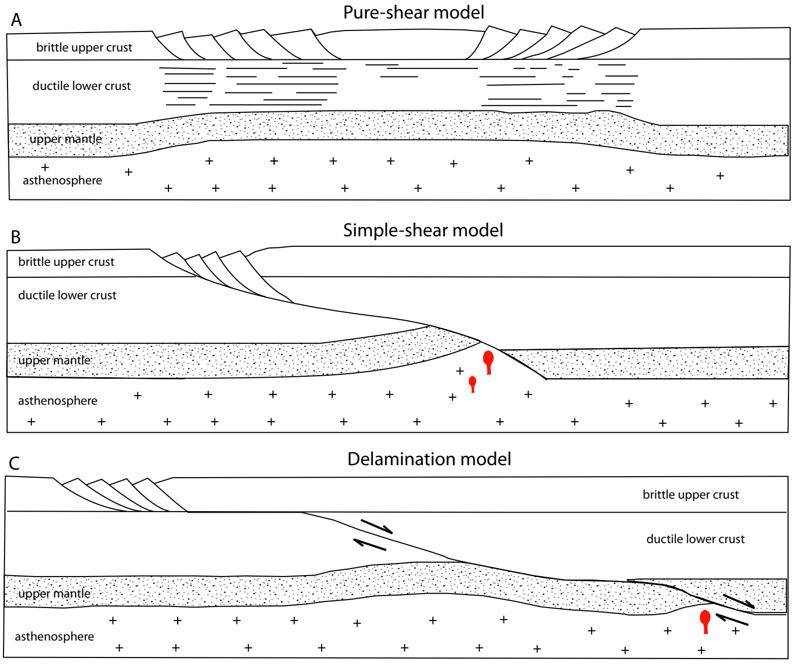

Figure 1.2.: Conceptual models for continental extension. The pure-shear model predicts a symmetric margin configuration, while the simple-shear and the delamination model predict asymmetric margins controlled by a crustal-scale or even lithospheric-scale detachment fault (redrawn from Lister et al. (1991)).

2) Observations from rift basins and rifted margins show, that the amount of horizontal extension, that is generated by normal faults due to the displacement of footwall and hangingwall, is less than the amount of vertical crustal thinning (β-factor) observed at crustal-scale models. Such models are for example derived from seismic refraction data or gravity modelling. This observation implies, that the amount of ductile extension in the lower crust might be higher than brittle deformation in the upper crust. This differential stretching has been reported as depth-dependent stretching (Davis, 2004). The role of crustal-scale detachment faults dipping at shallow angles is also debated

(Bosworth, 1985). Detachment faults might play an important role during the rift evolution. Such a feature would separate the crust into a lower plate and an upper plate as represented by the simple-shear model of Wernicke (1985) (Fig.1.2). From the surface expression of the upper plate, it would not be recognisable that the crustal thinning is considerably higher. This phenomena is called the "upper plate paradox" (Driscoll and Karner, 1998). However, clear evidences for crustal-scale detachments from seismic data at the initial stages of rifting are missing. Furthermore, the generation of low-angle normal faults at angles <30° remain controversial, because they are not conform with the fault-mechanical theory (Axen, 2007). However, such features exist and have been mapped e.g., in the Basin and Range Province (western USA), but it is debated if those faults initiated at higher angles (∼60°) and rotated to shallow angles (∼30°) (Buck, 1993).

Another conceptual model, the delamination model (Fig.1.2), predicts the delamination of the weak lower crust or the entire lithosphere. It is known that the viscosity in the lower crust and within a certain depth of the upper mantle is lower than in the brittle upper crust (Meissner and Mooney, 1998). Hence the lower crust can flow in both extensional and compressional regimes. Such a detachment fault would run horizontally along the brittle-ductile transition zone, steepen and run along the crust-mantle boundary into the upper mantle (Lister et al., 1991). A "ramp-flat-ramp" detachment geometry has been suggested to explain extension and subsidence rates in the Northern Carnarvon Basin, northwest Australia (Driscoll and Karner, 1998). Delamination is also evident on seismic sections from the collisional setting of the Alps (Meissner and Mooney, 1998).

To explain the extension discrepancy other authors suggest, that the amount of horizontal extension may not fully be recognisable because of the limited resolution on seismic sections. Hence, the contribution of small-scale faults could be underestimated (e.g. Walsh et al. (1991); Marrett and Allmendinger (1992); Reston (2007)).

If brittle crust fails (Mohr-Coulomb-criterion), faults initiate typically at dip-angles of ∼60°-70° (Abers, 2009) because most rocks have coefficents of friction of μ=0.6-0.85 according to experimental Byerlee´s law (Byerlee, 1978). Moreover, it is observed that fault-bounded blocks can rotate and lock at 30°-35° during ongoing extension. This leads to another concept that takes into account several phases of faulting, so-called polyphase faulting (Reston, 2005). If faults get locked during ongoing extension, a new generation of faults is forced to generate and mask previous fault patterns leading to significant underestimation of brittle extension. Another concept, that uses the same initial constraints, can predict the structures of the Iberia Margin but takes into account sequential fault propagation instead of cross-cutting faults. This explains both, extension discrepancy and margin asymmetry (Ranero and Perez-Gussinye, 2010). Such a sequential fault propagation has also been reported from an onshore field study of the young Suez-Rift (Fig.1.1, Gawthorpe et al. (2003)).

A key, to contribute to these issues of faulting and stretching mechanisms at rifted margins, is the investigation of a rift setting that resembles passive continental margins at an early-stage of extension, like the young northern Tyrrhenian Rift Basin (9-5 Ma; Rosenbaum et al. (2002). The basin is located in the Western Mediterranean Sea (Fig.1.1) in the convergent plate setting between Africa and Europe. The Tyrrhenian Rift has formed as a W-E extending continental back-arc basin due to tensile stress behind the retreating Apennine subduction system (Rosenbaum et al., 2002). The northern portion represents an ideal natural laboratory to investigate the evolution of rifted continental crust by normal faulting and stretching, because the basin widens from north to south. Hence, the basin comprises crust that has been stretched by increasing extension factors (β) up to continental break-up and mantle exhumation in the south-eastern part of the basin (Fig.1.4) where serpentinized peridotites and basalts have been drilled at Site 651 in the Vavilov Basin (Sartori et al., 2004). Although in the peri-tyrrhenian regions volcanic activity is present, it is not such extensive that rifted continental features have been buried by thick volcanic layers. Although it represents a kind of failed rift, the basin can be seen as a pre-stage for a magma-poor margin configuration. The rift-related and fault-bounded horst and graben structures are well preserved and exhibited in the bathymetric data. These block structures are just covered by a thin sedimentary layer that makes the basin an ideal place to study the early-stage rift processes of faulting and crustal thinning by evaluation of new multichannel seismic images and crustal-scale velocity models derived from refraction- and wide-angle seismic data.

1.1.1. Continental rifts

Rifts can be divided into two distinct categories depending on the causes that lead to the mechanisms of extensional forces (Ruppel, 1995). They are either active or passive. Active rifting involves the interaction of a nearby sub-lithospheric mantle plumes (e.g., the Iceland plume) or hot material within the lithopshere. Instead of subsidence, a thermal anomaly of just 150° above normal leads to doming of the lithosphere above sea level (White and McKenzie, 1989). This is accompanied by the formation of elongated graben systems, for instance the recent East African Rift system (Fig. 1.1) or large igneous provinces. Passive rifting involves the formation of rifts due to lithospheric extension, where tensile stress is transferred through the plate and generated by a far-field. The Tyrrhenian Basin belongs to the latter category, because the tensile stress is generated by the rollback of the subduction zone behind the Apennines that leads to back-arc extension of continental crust in the hinterland.

Anyway, extension leads either to (failed) rifted basins or to passive conjugate margins. The term "passive" in passive margins does not refer to the causal effect for extension; it just states the opposite to an active continental margin where the lithosphere, either oceanic or continental, is subducted. Depending on the latter categories, rifted continental margins and basins can be further classified into two-end members (Franke, 2013; Reston, 2009): 1) volcanic margins and 2) magma-poor margins. The classifica-

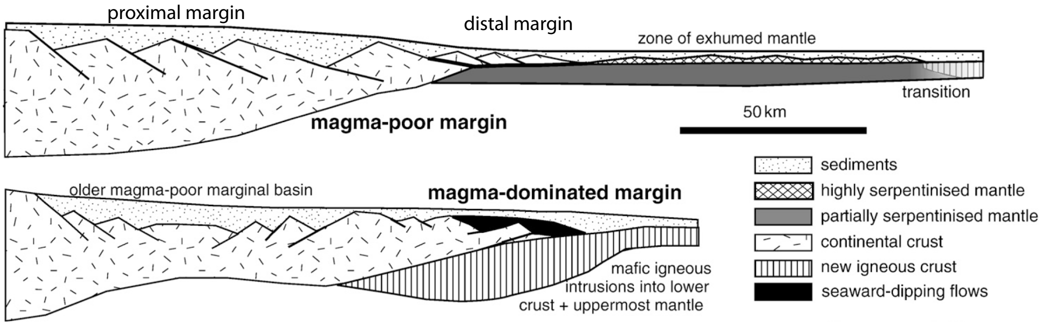

Figure 1.3.: Structural differences of a magma-poor and a magma-dominated (volcanic) rifted margin. Modified from Reston (2009).

tion depends on the volumes of extrusive magmatism that is generated as a response to extension and decompression which depends on the thermal state of the mantle prior to rifting. However, the same rift setting can exhibit both, volcanic and magma-poor margins e.g., the passive margins of the North Atlantic.

Volcanic margins

Rifted margins and basins where extension was accompanied by voluminous volcanic activity, are called volcanic margins (Fig.1.3). They represent the majority of passive continental margins worldwide and have been drilled for example off Norway, the British Isles or off Greenland (Franke, 2013). It has been suggested, that their formation is related to the presence of nearby mantle plumes (White and McKenzie, 1989). Rifting above such a thermal anomaly can generate huge amounts of melt in the asthenosphere. This is related to the effect of decompression during ongoing thinning of the lithosphere. The melt rapidly moves upwards and is a fundamental process for the growth of continental crust (White and McKenzie, 1989). Common features that characterize this type of passive rifted margin are syn-rift igneous rocks that reveal a wedge-like shape. Seismic reflection images show that this wedge consists of several seaward-dipping reflectors (SDR´s). Results of drilling show, that they are related to sub-aerial lava flows. The transition to oceanic crust is also relatively narrow and is suggested to be located at the tip of the SDRs (Franke, 2013). At these locations, the lower crust reveals velocities with values above 7.2 km/s. The high p-wave velocities are presumably related to mafic underplating or caused by sills that intruded into the lower continental crust (White et al., 2008).

Magma-poor margins

Magma-poor margins, also named non-volcanic margins are sites where syn-rift volcanic activity and thermal mantle anomalies have not played a major role during the active rift process. Examples for magma-poor margins are the Galicia Margin where the crust prior rifting was relatively cold and not thickened (Perez-Gussinye et al., 2003) or the distal Thetys margin that outcrop in the Alps (Whitmarsh et al., 2001). Pre-rift sub-continental mantle temperature has been estimated to be ∼550°, which is relatively cold (Whitmarsh et al., 2001). At those margins extension generates crustal stretching by normal faulting and block rotation (Fig.1.3). There is seismic evidence that the crust thins from an initially ∼30 km over a distance of 100-200 km to a few kilometers by rotated fault blocks (Reston, 2009). This zone of crustal thinning is sub-divided into the proximal margin, showing high-angle normal faults that bound continental blocks and the distal margin where the crust has extremely thinned to a few kilometers. The transition of the proximal and distal margin occurs rapidly in a narrow necking zone of ∼10-20 km. Another observation at some magma-poor rifted margins is the occurrence of a high-amplitude reflector e.g., the S-reflector off Iberia or the P-reflector in the Porcupine Basin (Reston et al., 2004). This reflector is assumed to be a detachment fault, but likewise may represent the boundary between continental crust and serpentinized peridotites. The impedance contrast might be generated due to water, that might reach the mantle during the rift process as the lower crust might enter shallower levels, subsequently cools and changes its rheological behavior from ductile to brittle (Perez-Gussinye et al., 2003). Hence, faults can act as pathways for water into the mantle. If such detachment faults or shear zones are already present at the early phases of rifting and control the rift is not clear. Investigations in the Porcupine Basin reveal that detachment faults develop at larger stretching factors controlling the future rift development, but are no feature of the early rift phase (Reston et al., 2004).

The continent-ocean-transition zone (COT), between the last unambiguous continental block and the oceanic crust reveals anomalous basement. Sampling and drilling of this zone show partially serpentinized mantle peridotites e.g., at the Iberian Margin (Fig.1.1) or at the COT offshore Newfoundland (Whitmarsh et al., 2001; Shillington et al., 2006). It is suggested that the basement is exhumed mantle. A roll-over of the fault migth be responsible for mantle exhumation and can also explain large offsets of isolated continental blocks that might be allochthonous features lying directly on mantle rocks (Whitmarsh et al., 2001).

1.2. Goals of the study

This thesis is based on multichannel seismic data (MCS), that allows imaging the sedimentary and upper crustal structures on two transects in the northern Tyrrhenian Sea (Fig. 1.4). The MCS data are processed up to prestack-depth and prestack-time migrated sections. A true geometrical image of sub-surface structures, like faults or tilted blocks, are only provided on the prestack-depth migrated section, which takes into account the effect of ray-bending and is not distorted by lateral velocity variations like on time sections. Coincident wide-angle seismic data (WAS) are recorded by ocean-bottom-hydrophones (OBH) and by additional landstations installed onshore Corsica and Sardinia. It is the first seismic wide-angle survey in this region that comprises such a dense receiver interval to reveal the entire crustal domain and the uppermost mantle. The seismic lines presented within this thesis, cross the northern Tyrrhenian Basin between the southern part of Corsica and the Latium Margin of the mainland of Italy (line AB). Further south, the line is orientated between Sardinia and the Campania Margin. The main objectives of this study are:

- What is the relationship between horizontal stretching by normal faulting and crustal thinning along the seismic transects? To achieve this goal, estimations of the amount of extension on prestack-depth migrated sections (PSDM) are carried out. The crustal thickness is determined by the refraction- and wide-angle seismic data after tomographic inversion. The velocity model states the current crustal thickness. Thus, the thinning-factor β can be calculated using the initial crustal thickness revealed by former studies (e.g. Mele and Sandvol (2003)). If an extension discrepancy would exist, controlling factors can be investigated. Furthermore, the control of shallow dipping detachment faults can be evaluated, because such features should be imaged on the PSDM.

- What is the typical incipient style of extension in a young continental rift like the northern Tyrrhenian? The line AB reveals, that faults bound half graben structures and that horizontal displacement is localized on large faults which are the main contributors to the entire amount of stretching. These observations are compared with findings from other rift settings.

- What is controlling the evolution of asymmetric conjugated margins in the Tyrrhenian Sea. From the PSDM/PSTM it is recognized, that the size of the blocks as well as the fault spacing decrease from west to east. This is coincident with the variation of the crustal thickness, as revealed by the WAS data and the age of tectonic activity. At the eastern margin, the seismic section reveals that the seafloor is cut by normal faults, indicating tectonic activity. A W-E rift propagation is confirmed from the age of volcanic rock samples (Cherchi and Montadert, 1982; Savelli, 2002) and drilling results of ODP Leg 107 (Kastens et al., 1988).

1.3. Additional geophysical data and previous work

The Tyrrhenian Basin has been the subject of several studies, mainly based on multichannel seismic data and the drilling results of the Ocean Drilling Program (ODP), Leg 107. For the northern and central part of the basin, gravity and magnetic data with a grid resolution of 0.02° and 0.01° are available. The data are a courtesy of Getech (UK). These additional data sets support the interpretation of the crustal-scale velocity

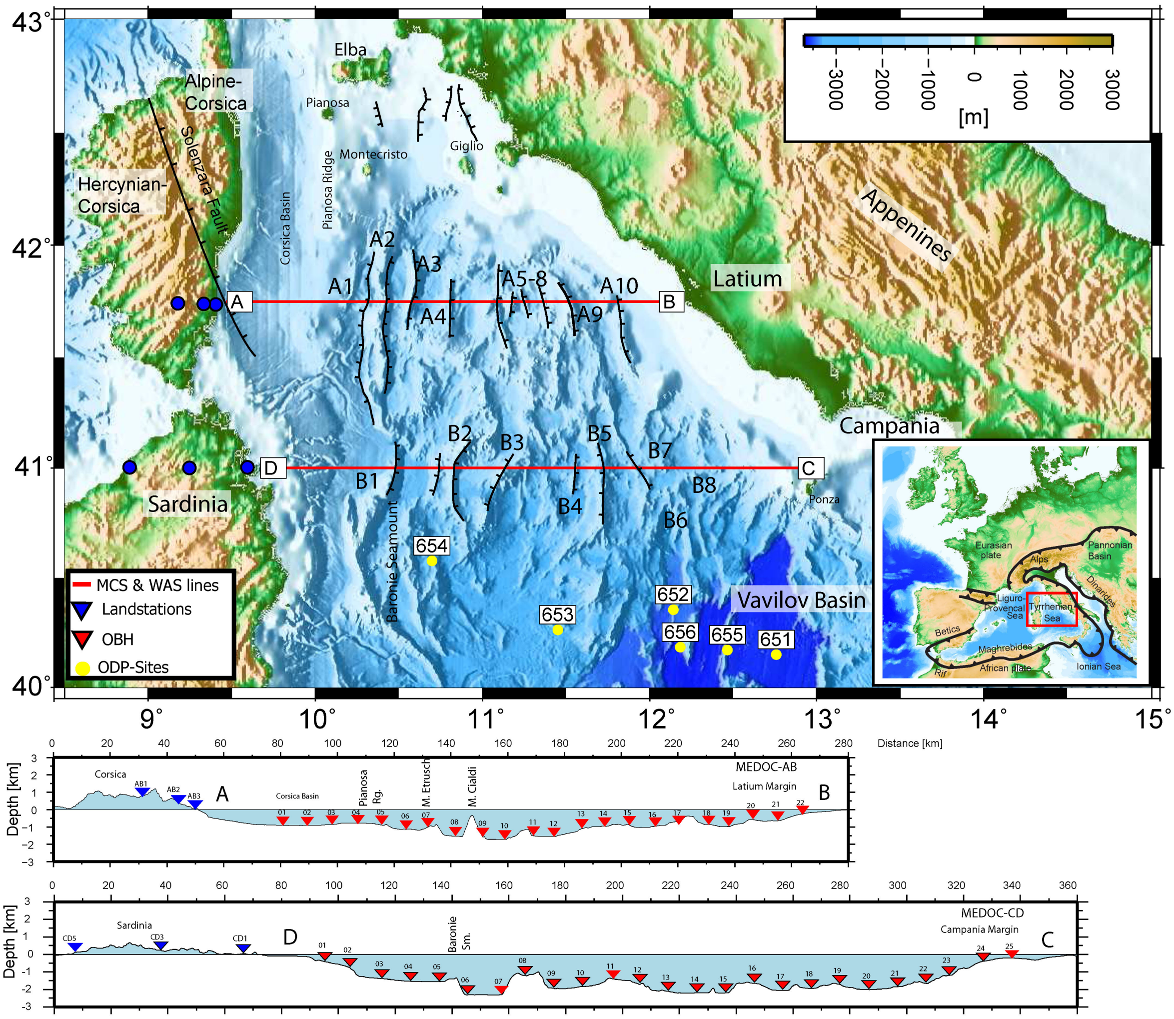

Figure 1.4.: The study area in the northern Tyrrhenian Basin located in the tectonic setting of the Western Mediterranean Sea (see inset). The results of two W-E orientated seismic lines crossing rifted structures perpendicular. Both MCS and WAS data are available and presented within this thesis (line AB and line CD). The orientation of faults come either from this study or are taken from Mauffret et al. (1999). Shots for the WAS experiment are recorded at 22 and 25 OBHs (red triangles) and on land stations (blue triangles). Yellow dots mark locations of ODP Leg 107 (Kastens et al., 1988).

models. The bathymetry data is a compilation of multibeam echo-sounder data with a resolution of 500 m (e.g., Fig.1.4). Gaps in the data have been filled by data of a global topography grid (Smith and Sandwell, 1997).

Seismic refraction and wide-angle experiments using ocean-bottom instruments have been conducted in the 80‘s to investigate the major elements of the crustal architecture. However, these studies are mainly concentrated on the central and southern part of the Basin. A 550 km long explosive seismic experiment on a NW-SE orientated transect between the southern tip of Corsica and the Calabrian arc used 5 OBS and 43 shots (Steinmetz et al., 1983). This experiment revealed roughly the depth of the crust-mantle boundary from head-wave Pn-arrivals. The crust has been found to be ∼20 km thick beneath the Baronie Seamount and thins towards the Vavilov Seamount (Fig. 1.4) to a thickness of 5 km. However, the data did not reveal information of the crustal architecture itself. Some years later two N-S orientated and 100 km long refraction experiments in the center of the Basin (Duschenes et al., 1986) extended the preceding data. Two areas in the centre (Vavilov Basin) and in the south-eastern corner of the Tyrrhenian Sea (Marsili Basin) located at a water depth of more than 3000 m, comprise crust with oceanic-like velocity character and large volcanic edifices, the Vavilov and Marsili volcanoes. These highly stretched areas with a flat Moho in ∼10 km depth are probably separated by a thicker continental saddle (Malinverno and Ryan, 1986) which is also indicated by the refraction experiment of Steinmetz et al. (1983). North of the Vavilov Basin the study shows that the velocity distribution is rather related to thinned continental crust.

The findings of the refraction experiments are consistent with the Bouger-gravity anomalies in the northern and central part of the basin (Fig.1.5 A). Along the northernmost line AB, the values are low in the western part offshore Corsica (-10 to +20 mGal) and higher in the eastern part of the basin (50-70 mGal). The low values are related to the thick sedimentary infill of the Corsica Basin. This study and also former studies (Mauffret et al., 1999) show, that the Corsica Basin hosts 6-7 km of sediments. East of the Corsica Basin, the gravity data indicate, that the crust presumably is not changing significantly in thickness. The direction of a noticeable change is orientated towards the south-east. The values in the Vavilov Basin increase to +180 mGal, indicating a progressive thinning of the crust caused by increasing stretching factors.

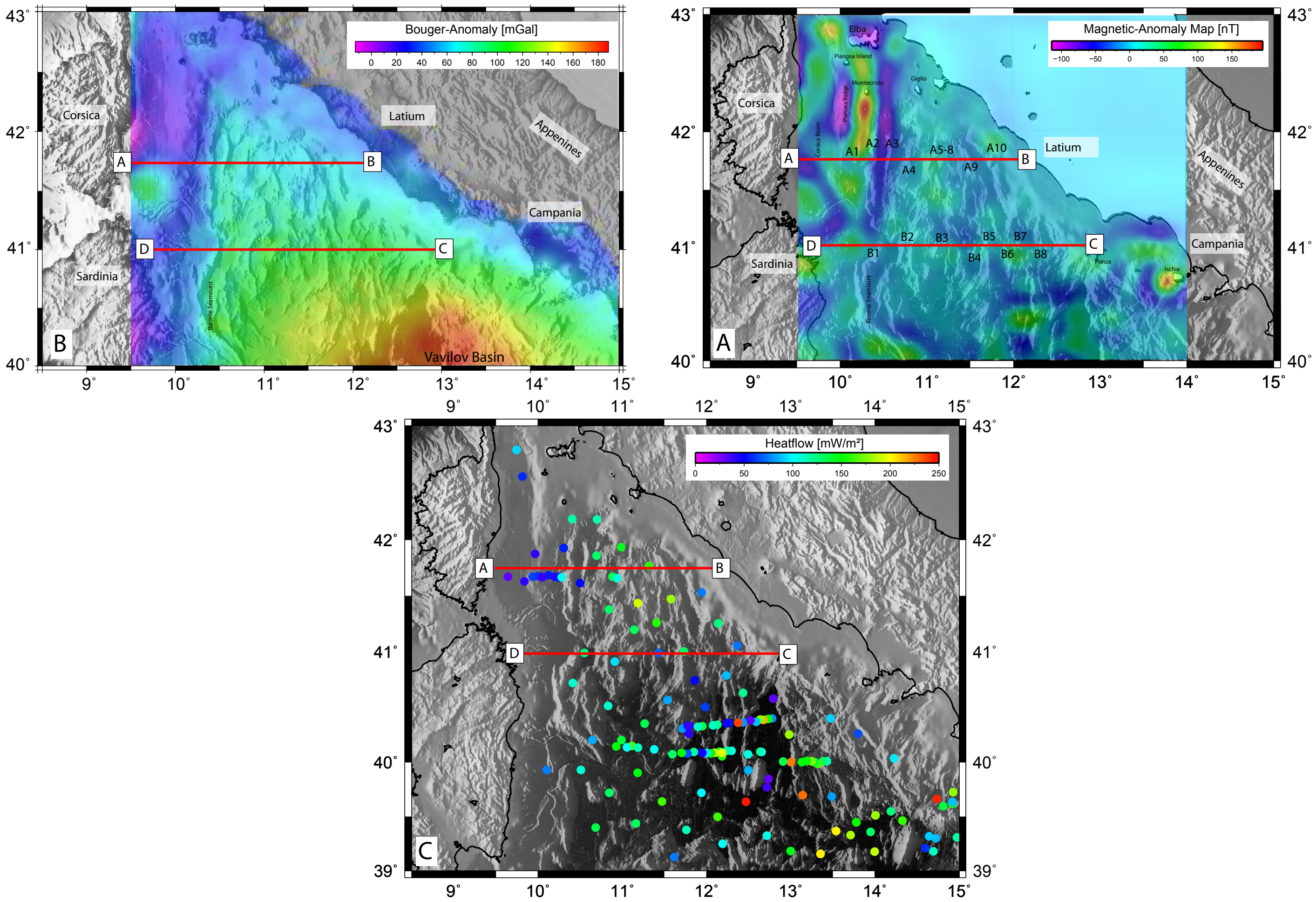

Figure 1.5.: (A)-(B) show the Bouger-gravity and magnetic anomaly map of the northern and central part of the Tyrrhenian Basin. Magnetic data are reduced to pole (RTP) so that anomalies better coincide with the location of their origin. (C) shows the distribution of heat flow measurements (Della Vedova et al., 1984)

A compilation of heat flow measurements is provided by Della Vedova et al. (1984) for the entire Tyrrhenian sector. The distribution shows, that the heat flow in the western part of the Basin, especially in the Corsica Basin, are relatively low ($\sim 50\frac{mW}{m^2}$) and typical for an old and thermally stable continental (Della Vedova et al., 1984). Further east, the heat flow is much higher and values exceed locally 140-150 $\frac{mW}{m^2}$ between the seismic transects. High heat flow values in the bathyal plain coincide with the higher stretched lithosphere as derived from the positive gravity-anomaly and the presence of large volcanoes. The presence of higher heat-flow values of larger than $150\frac{mW}{m^2}$ can be related to hydrothermal circulations.
Prominent magnetic anomalies are observed within the ridges (Pianosa- and Montecristo Ridge) that bound the Corsica Basin to the north and east as well as west of Elba Island. The origin for these anomalies are probably related to granitic plutons, but an ophiolitic body has also been discussed (Contrucci et al. (2005); Mauffret et al. (1999) and references therein).

Stratigraphy and results of ODP Leg 107

The main goals of the ODP Leg 107 was to investigate the basalt-floored sub-basins to find out the timing of the entire basin formation and to test the hypothesis if the Tyrrhenian has developed by slab-rollback (Kastens et al., 1988). If so, syn-tectonic deposits should decrease in age along the NW-SE orientation of the drill sites (Fig.1.4). This rift propagation has been confirmed by the drilling results in the central Tyrrhenian Basin. Drilling results of Site 654 at the upper Sardinia Margin show, that the fault bounded continental block tilted during Tortonian to Messinian age. At the lower Sardinia Margin, which is located more to the east, drilling at Site 652 documented, that the active tectonic phase occurred during Messinian to Pliocene age (Kastens et al., 1988). Thus, it has been demonstrated that rifting propagated in the central and southern basin through time towards the Calabrian arc, where the subduction process is still recently active and marked by deep earthquakes. Moreover, for the two basalt-floored sub-basins it has been shown, that the Vavilov Basin created between 5-2 Ma ago and that the Marsili Basin further south is not older than 2 Ma (Mascle and Rehault, 1990). Unfortunately, no scientific drilling has been carried out in the northern Tyrrhenian Basin. However, the drill Site 654 is located on a tilted continental block just 50 km south of the line CD and is part of the passive rifted margin of Sardinia (Fig.1.6 A). The results, for instance reported in Sartori (1990) or Kastens et al. (1988), can be extrapolated onto the block B2 which is approximately the prolongation of the drill site (Fig.1.6 B). Seismic images from this drill site indicated that sedimentary geometries might be related to pre-, syn and post-tectonic deposits. The uppermost sedimentary units are of Plio-Pleistocene age, appear relatively transparent and consist mainly of nannofossil ooze. This unit represents the post-rift succession. At the transition to Pleistocene age, a 2 m thick extrusive basaltic layer has been drilled. The basalt is probably related to

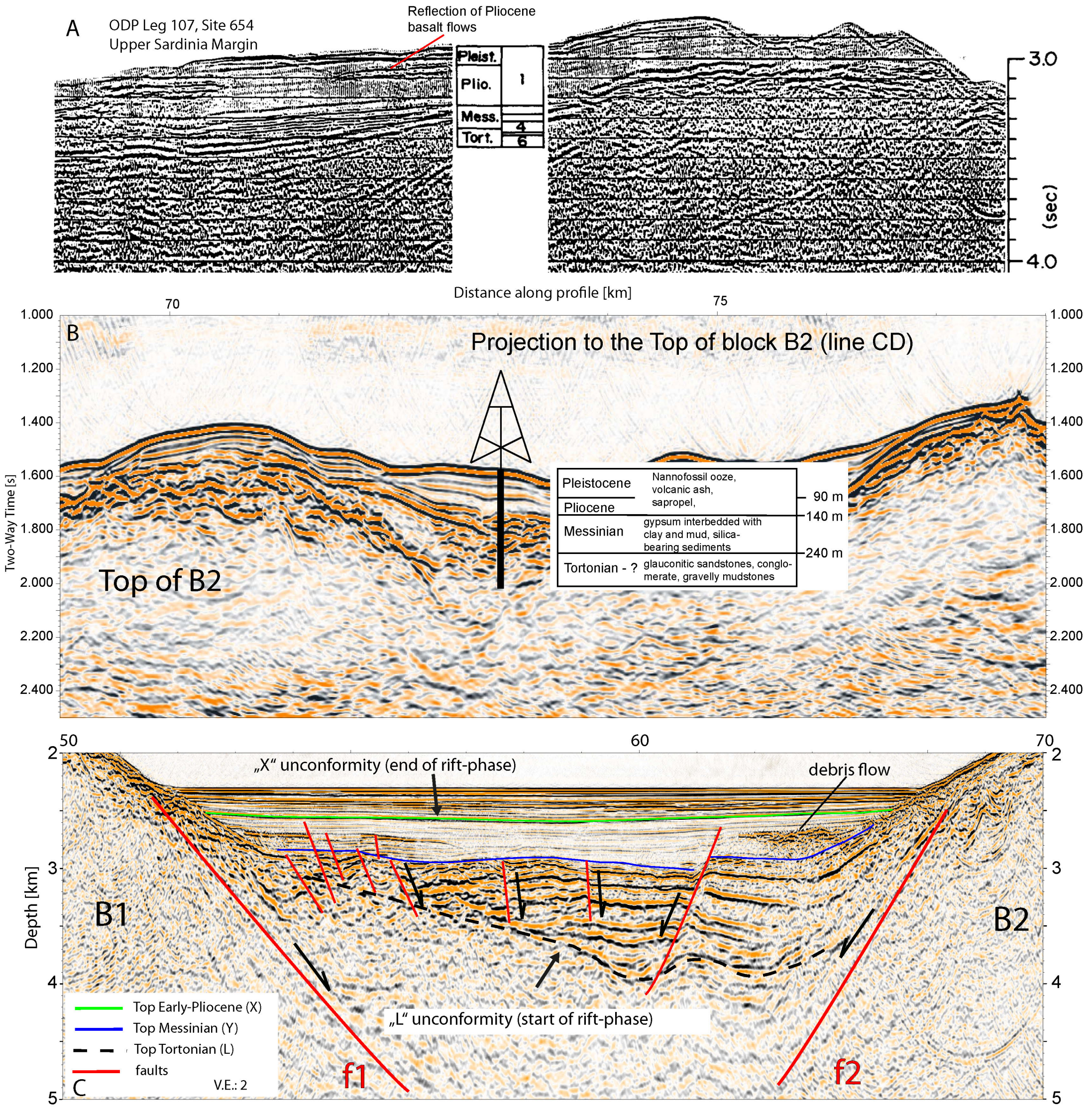

Figure 1.6.: (A) shows the seismic image of the continental block at drill Site 654 (modified from Kastens et al. (1988)). The drill hole is located ~50 km south of the line CD (Fig. 1.4). (B) Projection of the stratigraphic units and ages on the top of the continental block B2 (line CD). (C) Interpretation of seismic unconformities that mark the start and end of active rifting in the Tyrrhenian Sea. In the sub-basin close to the Sardinia Margin "X" confine also parts of the post-rift sediments.

post-tectonic volcanic activity (Fig.1.6). Such features are also observed in several sub-basins on the seismic images of line CD (see Chapter 6). Beneath the post-tectonic unit a strong reflector is related to Messinian evaporites. Evaporites have been deposited when the water exchange was restricted and the Mediterranean region desiccated (Hsu et al., 1977). Their presence is wide-spread in the Tyrrhenian Basin, especially at the Sardinia Margin where salt-layers even develop diapiric structures (Curzi et al., 1980). Drilling at Site 654 revealed a 70 m thick evaporitic unit of 5 discrete finely laminated layers of gypsum interbedded with clay and mudstones. Below the evaporitic unit, silica-bearing sediments of Messinian age and Tortonian glauconitic sandstones, gravel conglomerates and gravelly mudstones were drilled. The Messinian and upper Tortonian sequences represent the syn-rift units and build altogether a classical transgressive sequence (Kastens et al., 1988). However, the base of the syn-tectonic unit has not been fully drilled and the exact age and rock composition of the pre-tectonic sequence is still unknown.

Previously interpretations of multichannel seismic data in the Tyrrhenian Sea document, that the start and end of the active rift phase is linked with the occurrence of two unconformities. The "X" unconformity mark the end of the rift phase at Early-Pliocene age and the "L" unconformity mark the start of the rifting which is upper Tortonian (Trincardi and Zitellini, 1987; Zitellini et al., 1986). These unconformities are well identifiable, especially in deep sub-basins like the one west of the block B2 (Fig.1.6 C). Here, the two unconformities confine a wedge-like shaped syn-tectonic sequence of thick Messinian evaporites and sediment deposits which are partly cut by normal faults. In this region, however, "X" confine also parts of post-tectonic deposits.

1.4. Seismic data acquisition

The seismic data sets presented in this project were collected during the MEDOC-Cruise in April and May 2010 in a joint project of scientists from Spain (CSIC), Italy (ISMAR-CNR/IDPA-CNR) and Germany (GEOMAR). The aim of the first leg was to collect refraction- and wide-angle seismic data (WAS) in a two-ship experiment that allows investigating the large-scale structure and nature of the crust and upper mantle. In the northern Tyrrhenian sector, 22 and 25 GEOMAR ocean-bottom-hydrophones (OBH) were deployed on line CD and line AB, aboard the Italian vessel *RV Urania* (Fig. 1.4). Both lines are extended by three landstations onshore Corsica and Sardinia. The data collected on these two transects are presented in this thesis, but even more data in the central and southern Tyrrhenian have been acquired. The profile orientations have been chosen in a way, that they cross the large-scale topographic structures perpendicular to the main strike-direction. This reduces the effect of sideswipes from the 3-D recorded wave-field on 2-D seismic sections. Thus, the dip of structures on ground-truth sections can be assumed to be the true dip.

The shooting for the refraction experiment was carried out by the Spanish vessel

Sarmiento de Gamboa using an airgun-array that consisted of two sub-arrays of 12 G-II airguns. The total volume of this configuration was 4600 in^3 and the shooting interval was 90 s. This interval assures that energy of the previous shot has decreased in the water column before the next shot was triggered. The main frequency of the airgun-signal in this configuration ranged between 8 and 15 Hz. The hydrophone unit mounted on the OBS was either an E-2PD hydrophone from OAS Inc., or a HTI-01-PCA hydrophone from HIGH TECH INC.. Recording units were MLS (Marine Longterm Seismocorder) and MBS (Marine Broadband Seismocorder) built by the company SEND. These recording units sampled with a sufficient sampling rate of 200 Hz and 250 Hz, respectively. The storage media were PCMCIA flash disks. Before and after deployment of the OBH, the recording unit was synchronized with the GPS-time to correct for drifts of the internal clock after recovery. The land station of type Lennartz Le3D/5s were installed by IDPA/CNR (Italy). They recorded the data at a sampling rate of 125 Hz. During the shooting, carried out by the *Sarmiento de Gamboa*, the *RV Urania* used the time for oceanographic investigations, for instance CTD measurements. Velocity information of the water-column were integrated in the processing of the MCS data. After recovery of the OBH-stations the data were stored and transferred to a back-up storage system.

The MCS data acquisition on coincident lines was carried out by the *Sarmiento de Gamboa* alone. As an adequate source, generating higher frequencies, the airguns were rearranged to an array consisting of 7 guns and a total volume of 3040 in^3. A digital solid state streamer with a total length of 3450 m recorded the shots. This streamer was composed of 23 segments each 150 m long with 276 channels in total. The minimum offset was 150 m and the maximum offset 3600 m. The group spacing of the channels was 12.5 m and the airgun was triggered every 50 m. The raw data were stored in the SEG-D format at a sampling rate of 2 ms with an entire record length of 18 s. Seismic navigation were stored in the P2/94 exchange format for raw marine positioning data (UKOOA).

1.5. Thesis outline

In the following chapter 2 an overview of the processing steps that are applied to the MCS data as well as some theoretical aspects are given. The approach of iterative focusing-analysis (residual-moveout analysis) and prestack-depth migration to achieve an appropriate velocity field is described in Chapter 3. The processing of the WAS data, the forward-modelling and tomographic inversion is described in Chapter 4.

The Chapter 5 contains a stand-alone manuscript that has been accepted for publication in *Geochemistry, Geophysics, Geosystems (G-Cubed)*. Both, the results of tomographic inversion of WAS data and the interpretation of the prestack depth migrated section of the northernmost line AB are presented in this chapter (Fig.1.4). This manuscript is aimed to investigate the fault characteristics and the style of rifting during the early

phases of basin opening. The results are compared with observations from other young rift settings.
Chapter 6 contains a second manuscript that is submitted to *Journal of Geophysical Research: Solid Earth (JGR)*. It investigates the formation of the basin from the less extended region, as transected by the line AB, to the higher extended area in the vicinity of line CD. The results of tomographic inversion of both lines as well as the prestack-time migrated sections are presented. The development of asymmetric rift structures and the occurrence of magmatic features (lava flows) are discussed. Based on observations on the seismic sections and wide-angle velocity models, a general evolutionary model is suggested.
An overview of the tectonic setting and the evolution of the Tyrrhenian Basin in the context of slab-rollback can be found within these two manuscripts.
Chapter 7 summarizes the main results and concludes them in a broader context.

2. Analysis and processing of MCS data

This chapter describes the processing steps and some basic theoretical aspects that are applied to the seismic raw data. The overall goal is to generate prestack depth and prestack time migrated sections for interpretation. For the basic processing steps, including multiple attenuation, the software package "Omega2" (WesternGeco) is used. A second software package "Sirius Earth-Wave" (GX-Technology) provide tools for focusing-analysis and velocity model building. Subsequently prestack depth and time migration, based on the Kirchoff integral solution is carried out. This procedure is presented in chapter 3. A simplified overview of the main processing steps is illustrated in the flowchart in Figure 2.1

2.1. Seismic navigation and geometry

An essential requirement for the processing of multichannel seismic data are accurate information of the acquisition geometry, for instance the distances from GPS-antenna to the source, source-receiver distances as well as coordinates for each receiver and trigger time of every shot. During acquisition these information were stored in the P2/94 exchange format for raw marine positioning data (UKOOA). It contains all necessary coordinates and geometry information.

For calculating the detector and midpoint positions along a short streamer, a regular geometry is sufficient, because the streamer can be projected straight behind the ship with equidistant detector spacing. This assumption is not true for a long streamer like the one used in this project with a total length of 3450 m. Water currents can force the streamer to drift away from the actual profile line, especially at the rear of the streamer (Levin, 1983). Furthermore, due to wind conditions, the sail-line is not always equal to the ships heading and hence the streamer is crooked behind the ship. This effect is called "streamer feathering". To reconstruct the deflection and shape of the streamer, five compasses were attached along the streamer measuring the azimuthal direction. A GPS-based antenna mounted on the tail buoy logged the end coordinates of the streamer. Unfortunately, shot and tail-buoy coordinates written to the navigation files are not consistent. Hence, a full reconstruction after acquisition was not possible. The best approximation for determine the detector positions is to assume that the streamer followed the crooked ship track. The coordinates of the ship

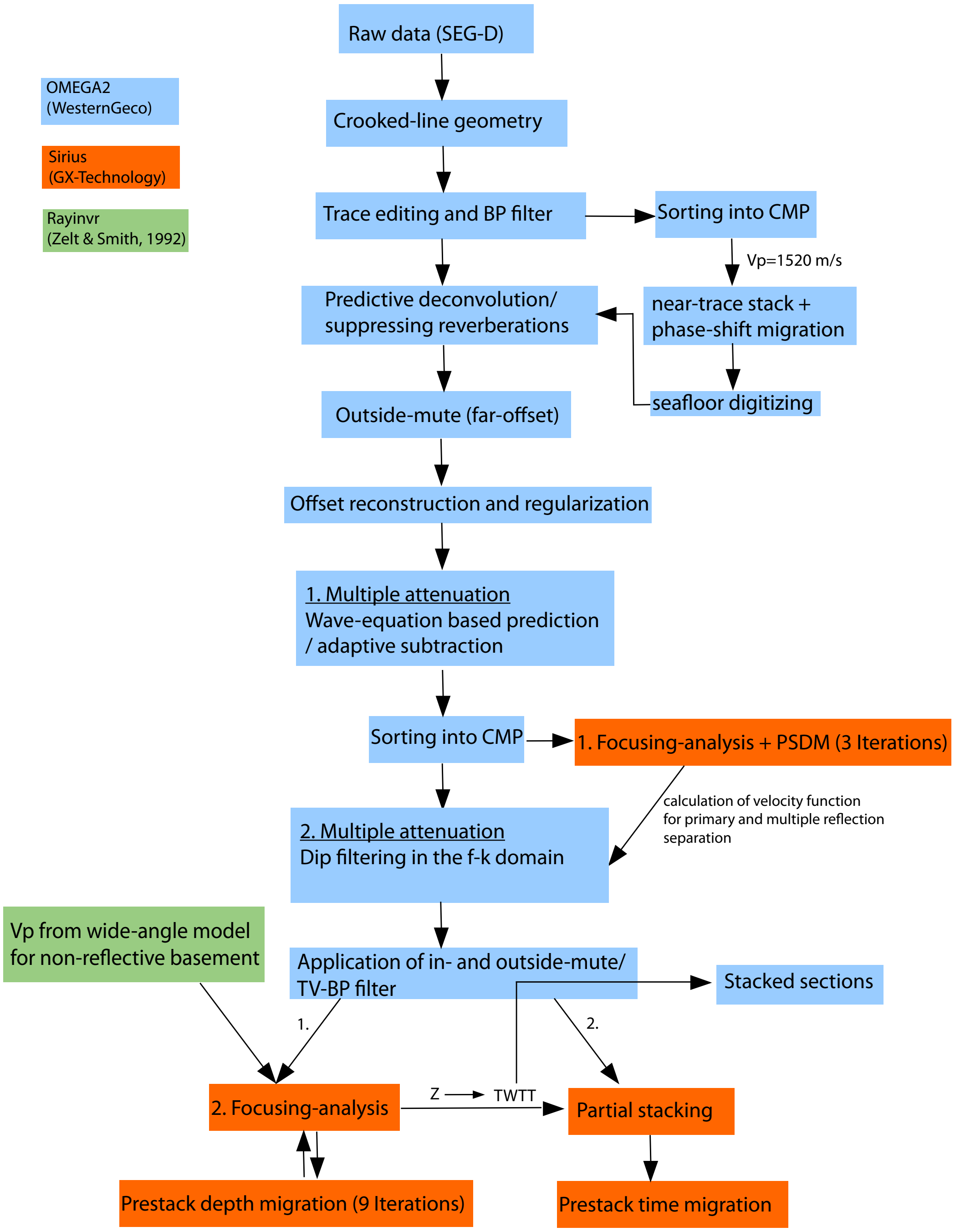

Figure 2.1.: Flowchart for the processing of MCS data using the software packages OMEGA2 (Western Geco) and Sirius (GX-Technology). Abbreviations: CMP = common-midpoint gather, PSDM = Prestack-depth migration, TV-BP = Time-variant bandpass filter.

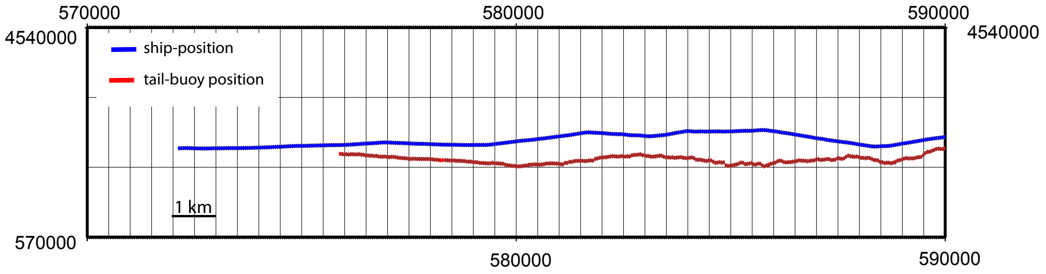

Figure 2.2.: Track of the ship position (blue line) and position of the tail buoy (red line) at the western end of seismic line CD. The influence of water currents toward the south, force the rear of the streamer to deviate from the actual ship position. This effect is called streamer feathering.

were logged every second. Therefore, it is possible to reconstruct the detector positions by backtracking the streamer along the ship track. Knowing the exact nominal offset from the ship GPS antenna and streamer-drum to every receiver along the hose of the streamer, it is possible to reconstruct the ship position at a certain distance and time. This position is assumed to be the position of the respective receiver when the source has been triggered behind the current ship position. However, larger deviation at the rear of the streamer related to the influence of strong water currents cannot be fully corrected with this method.

Figure 2.2 shows the western end of profile CD offshore Sardinia. Here, the rear of the streamer is deviated ∼250 m from the actual profile line, whereas in other places the deviation was even ∼500 m. This corresponds to an feathering-angle of 8°. However, Levin (1983) showed that the effect of feathering for the computed depth of a reflector is small and when the profile is orientated perpendicular to the strike direction of the subsurface structures, the difference in traveltime for a particular source-receiver combination is minimal, even at large offsets. This is the case for the MEDOC profiles, because the striking direction of horst and graben structures are aligned mainly N-S while the profiles are orientated perpendicular in W-E direction. If the dip of the subsurface structures would be aligned parallel to the profile feathering effects are not negligible, particularly if the reflector dip is steep. The calculated coordinates for source and receiver position are subsequently set to the shot-gather sorted seismic trace headers and a geometry database is created.

2.1.1. Crooked line geometry

For a straight seismic profile the midpoint location of a reflected seismic trace is by definition half the distance ($x/2$) between source and detector. This point is lying directly on the profile. The principal of the CMP technique in seismic reflection data is to group traces that have the same midpoint coordinates. Sorting traces build a CMP-gather (common-midpoint gather). A CMP-gather should theoretically image reflection points within the subsurface beneath its location. However, this assumption is only valid for horizontal layering. If the seismic line is crooked, the midpoint locations are scattered and the CMP position represents rather a reflection area than a reflection point. This can lead to the effect of CMP smearing. For this reason a crooked geometry processing is applied to calculate CMP locations. The result is a crooked survey profile on which midpoint locations are averaged and create a centroid CMP location.

2.2. Raw data inspection and near-stack

Two shot-gather records of the line AB are shown in Figure 2.3. The data are already band-pass filtered with a low-cut-frequency of 5 Hz. Shot 302 has been recorded in the area of the flat and sedimentary filled Corsica Basin and shot 3002 in the rough area of horst and graben topography. First, an inspection of the time-series recorded at the first channel (smallest offset) has been carried out to check the timing of seismic arrivals to avoid potential time-shifts in the data. A discrepancy between the primary and multiple seafloor reflection of 48 ms has been found. All traces are shifted so that the multiple reflection on the first channel (nearly zero-offset) is twice the time of the primary reflection. A conceivable explanation for this time difference could be related to the possibility that during the acquisition the source was triggered on the wrong flank of the trigger-signal.

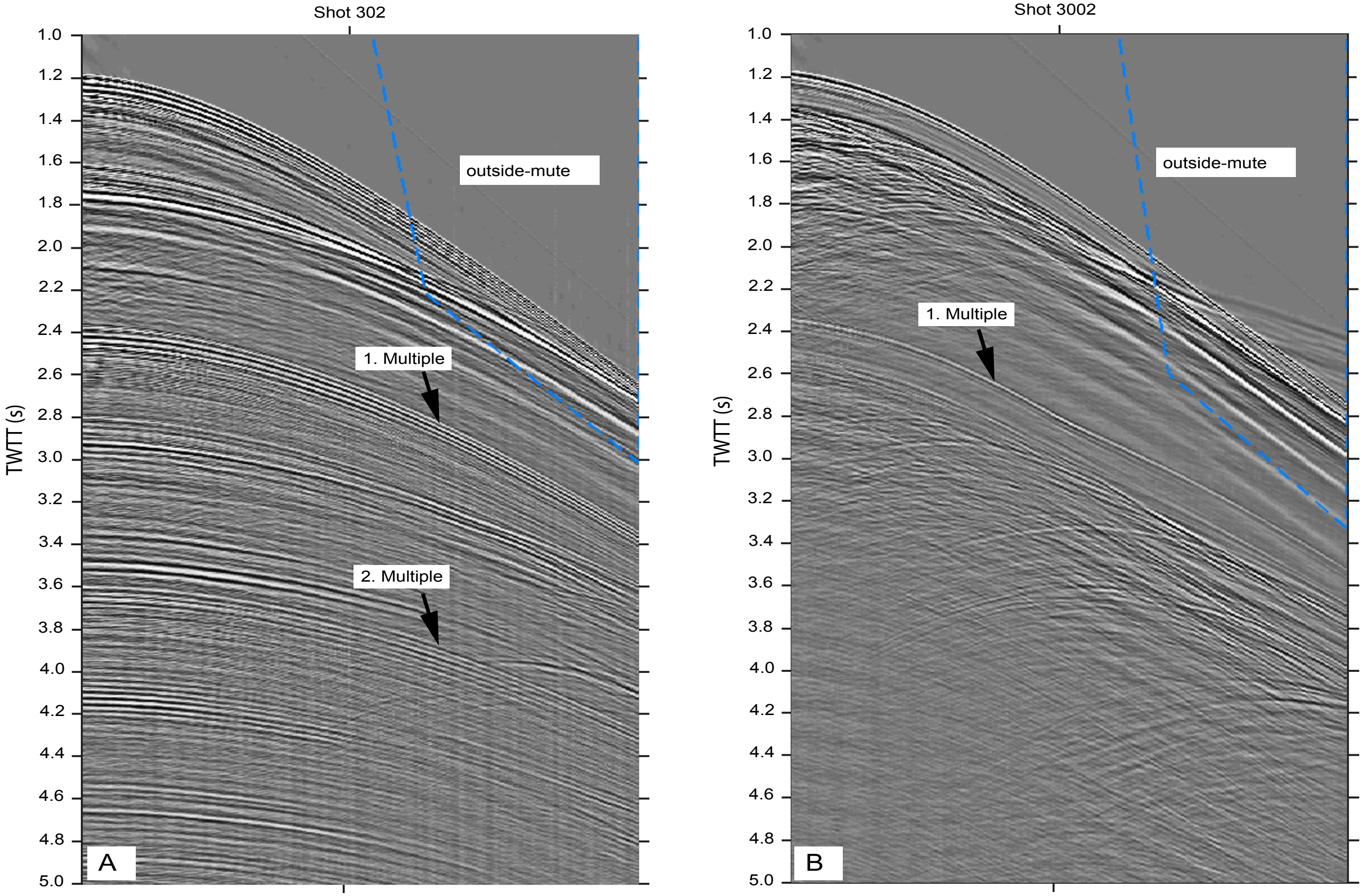

Figure 2.3.: Examples of two shot-gathers. A) Shot-gather recorded at the sedimentary Corsica Basin. B) Shot-gather recorded over a continental block structure

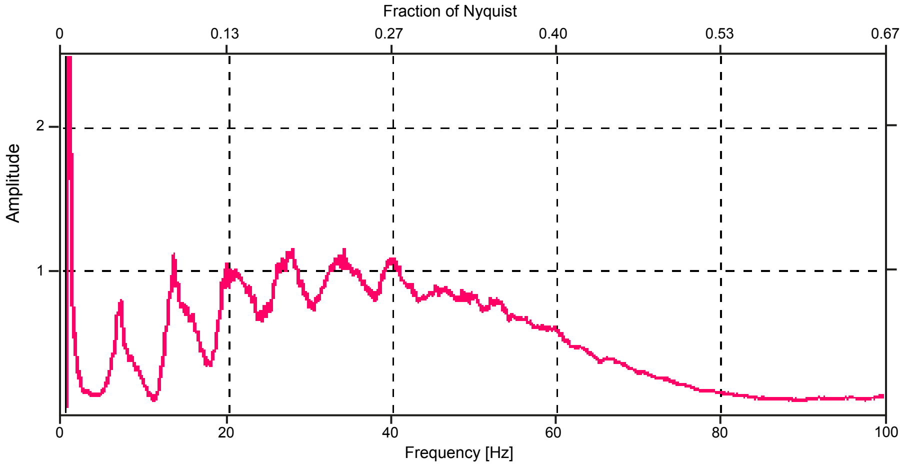

Figure 2.4.: Amplitude-frequency spectrum of a near-offset trace of a raw shot-gather. The main frequencies range between 15-45 Hz. Low frequency noise (< 5 Hz) are removed by a band-pass-filter, while higher frequencies contain still useful energy (> 80 Hz).

The amplitude-frequency spectra of the raw shot-gathers reveal that the data contain frequencies of up to 80 Hz (Fig. 2.4). However, the dominant and useful signals for the seismic image range between frequencies of 15 Hz to 45 Hz. The high amplitude signals and long-wave-length noise below 5 Hz appear along all traces as stripes and are presumably related to swell. To remove the long wave-length and to improve the signal-to-noise ratio, a low-cut filter with a cutoff frequency of 5 Hz is applied to the data (Fig. 2.3). Frequencies higher than 45-80 Hz drop linear in amplitude, but contain still useful energy.
In the last third of the shot-gather, refracted arrivals occur travelling faster than the seafloor reflection. This type of waves are unwanted in reflection seismic data and are removed by applying an outside-mute (Fig.2.3). Another unwanted signal, typical for marine seismic data, is the oscillating characteristic of the wave-field due to the bubble-effect. To remove these reverberations a predictive deconvolution is applied to the data within a move-out window below the hyperbolic seafloor reflection. Thus, the processing step requires time information of the seafloor. Seafloor-digitizing has been carried out on a poststack time migrated section using just the near-offset traces (1500 m offset). The migration algorithm was a phase-shift migration using a 1D velocity function of 1520 m/s. This correspondes to the average water velocity and results in a smoothed seafloor without diffractions for subsequent digitizing. The stacks of both lines are shown in Figure 2.5. The multiples after stacking are still very strong and the effect of signal reverberations disturb the stacked sections.

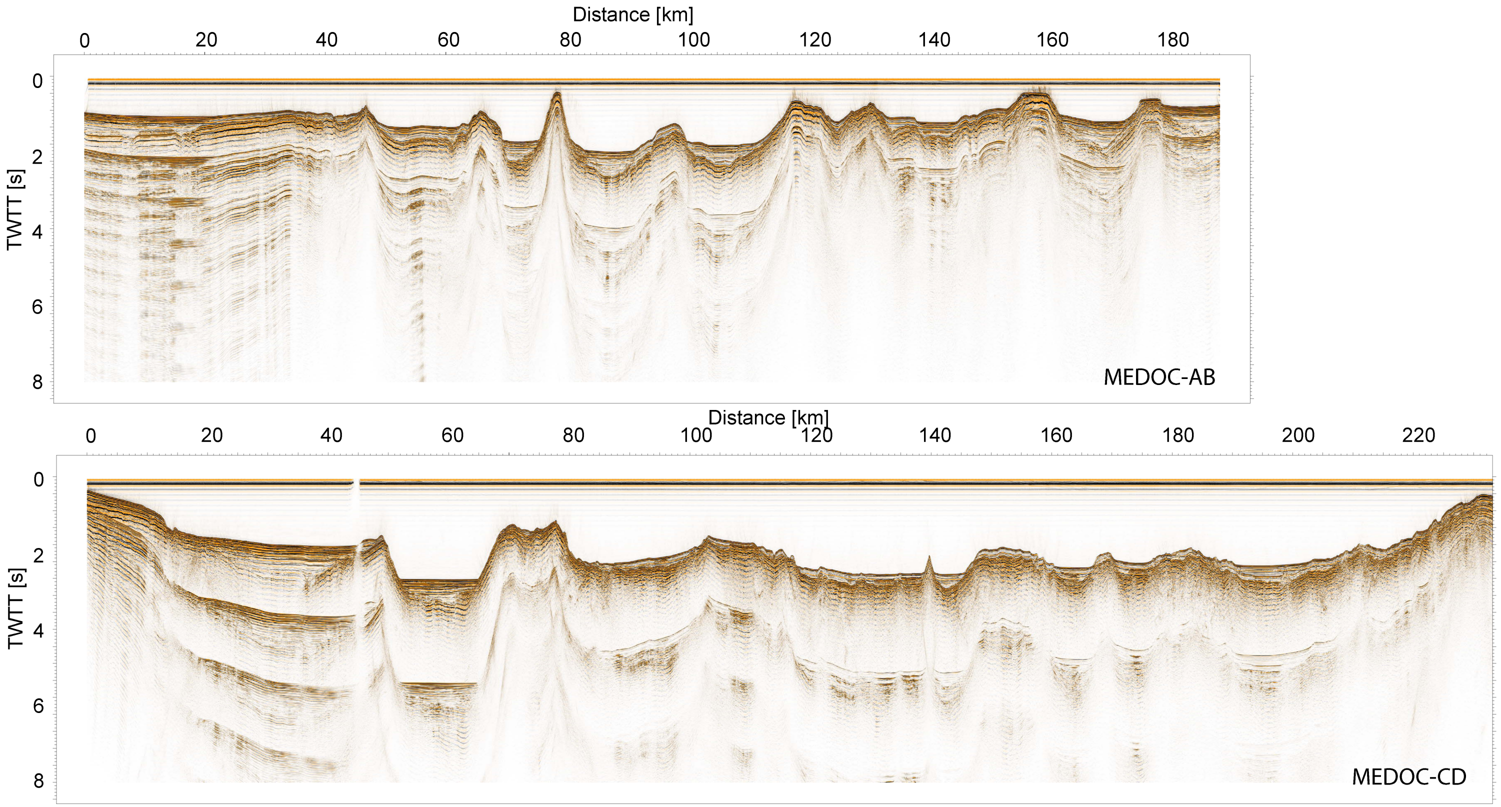

Figure 2.5.: A phase-shift migration is applied to the near-trace stacks of line AB and CD with the aim to generate a diffraction free seafloor for digitizing. Further processing steps will be targeted to attenuate reverberations and multiple reflections.

2.3. Deconvolution

The general aim of deconvolution applied to seismic data is to improve the temporal resolution of seismic traces. Furthermore, deconvolution can be used to predict a time advanced version of signals. This attribute is useful to remove and attenuate multiples or reverberations. Just the periodic signals are predictable but not the uncorrelated reflection series $e(t)$ of the earth response. In the convolution model (Yilmaz, 2001) the recorded seismic time-series $x(t)$ is in general the result of the convolved source wavelet $w(t)$ with the earth impulse response (reflectivity) $e(t)$ and additional ambient noise $n(t)$ (Eq. 2.1).

$$x(t) = w(t) * e(t) + n(t) \tag{2.1}$$

Assuming that the noise is negligible, a deconvolution operator is in principal an inverse filter $f(t)$ that can enhance the temporal resolution of the seismogram $x(t)$. Reflection events are ideally compressed back into a spike form. The filter for this operation $f(t)$ is described by the inverse of the source wavelet $w(t)$ where δ is the Kronecker symbol. However, deconvolution is limited, because it is assumed that the wavelet is minimum phase to get a stable inverse wavelet.

$$f(t) = \delta(t) * \frac{1}{w(t)} \tag{2.2}$$

This shows that applying deconvolution requires estimation of the basic wavelet.

Wavelet estimation

As the source wavelet signature is not known (the contrary to deterministic deconvolution), the wavelet used for the deconvolution process is estimated from the autocorrelation function $r(\tau)$ of $x(t)$. This can be done, because the amplitude spectra $X(\omega)$ of $x(t)$ and the spectra $W(\omega)$ of the basic wavelet $w(t)$ are of similar shape (Yilmaz, 2001). That the autocorrelation r_τ of $x(t)$ is also a scaled version of r_w has been shown by Peacock and Treitel (1969). The z-transform $R_{xx}(z)$ of the autocorrelated seismogram $x(t)$ is given after rearrangement by:

$$R_{xx}(z) = [E(z)E(1/z)][W(z)W(1/z)] \tag{2.3}$$

This expression is equivalent to the z-transform of equation 2.1 and shows that the same is valid for the autocorrelation.

$$r_{xx}(\tau) = r_{ee}(\tau) * r_{ww}(\tau) \tag{2.4}$$

As $e(t)$ is the unpredictable part of $x(t)$, the energy E_e in the autocorrelation is

$$r_{ee}(\tau) = E_e \qquad for \;\; \tau = 0 \tag{2.5}$$

and

$$r_{ee}(\tau) = 0 \qquad for \;\; \tau \neq 0 \tag{2.6}$$

Therefore, Equation 2.4 can be rewritten to:

$$r_{xx}(\tau) = \sum_t r_{ee}(t) r_{ww}(\tau - t) = E_e r_{ww}(\tau) \tag{2.7}$$

This shows that the autocorrelation of $x(t)$ is the scaled signal of the autocorrelation of $w(t)$ and thus a wavelet for deconvolution can be estimated (Peacock and Treitel, 1969).

Wiener filter

To achieve predictive deconvolution, Wiener filters $f(t)$ are designed from the estimated wavelet $w(t)$(Fig.2.6E) for every trace within the gather. The start of the process has been set below the time of the primary sea floor reflection (digitized in the migrated near-stack). Basically, the filter $f(t)$ is designed, so that the error L (Eq. 2.8) in a least-square sense becomes a minimum between the actual output $y(t)$ and the desired output $d(t)$ (Yilmaz, 2001).

$$L = \sum_t (d_t - y_t)^2 \tag{2.8}$$

The convolution of $f(t)$ with the input series $x(t)$ yields the output $y(t)$. Substituting this relation into Equation 2.8 is expressed by

$$L = \sum_t (d_t - \sum_\tau f_\tau x_{t-\tau})^2 \tag{2.9}$$

Equation 2.9 represents an extreme problem and the filter $f(t)$ that yields the minimum error L can be found when

$$\frac{\partial L}{\partial f_i} = 0 \qquad i = 0, 1, 2, ..., (n-1) \tag{2.10}$$

Taking the partial derivatives of Equation 2.9 and setting to zero yields the following expression after rearrangement :

$$\sum_\tau f_\tau \sum_t (x_{\tau - t} x_{t-i}) = \sum_t (d_t x_{t-i}) \tag{2.11}$$

The second term on the left side is the autocorrelation $r_{i-\tau}$ of the input series $x(t)$. The right side represents the crosscorrelation g_i of the desired output $d(t)$ with the input series $x(t)$. Equation 2.11 can be rewritten to

$$\sum_{\tau} f_\tau r_{i-\tau} = g_i \qquad i = 0, 1, 2, ..., (n-1) \tag{2.12}$$

and Wiener filter coefficients can be computed.

Predictive deconvolution

Solving the convolution model requires that the basic wavelet is minimum-phase, respectively an ideal spike to recover the earth reflectivity series. The predictive deconvolution process predicts a time series $x(t)$ at a certain distance $x(t+\alpha)$, where α is the prediction lag or prediction distance. The operator that remain the unpredictable part is the so-called prediction error filter. In the case of predictive deconvolution a time advanced version of $x(t)$ is the desired output $d(t)$. Hence, the Wiener filter $f(t)$ has to be predict (Yilmaz, 2001):

$$d(t) = x(t+\alpha) \tag{2.13}$$

Substituting 2.13 into 2.11 leads to:

$$g_\tau = \sum_t d_t x_{t-\tau} = \sum_t x_{t+\alpha} x_{t-\tau} = \sum_t x_t x_{t-(\alpha+\tau)} \tag{2.14}$$

In general the autocorrelation is defined as:

$$r_\tau = \sum_t x_t x_{t-\tau} \tag{2.15}$$

For an $\tau + \alpha$ lag Equation 2.15 is also valid. Rearrangement shows that the autocorrelation is the time-advanced version of the crosscorrelation $g(\tau)$ (Eq. 2.16).

$$r_{\alpha+\tau} = g_\tau \tag{2.16}$$

Substitution into 2.12 and rearrangement gives normal equations that can be expressed in the matrix form to find the prediction filter coefficents.

$$\begin{pmatrix} r_0 & r_1 & r_2 & \cdots & r_{n-1} \\ r_1 & r_0 & r_1 & \cdots & r_{n-2} \\ \vdots & \vdots & \vdots & \ddots & \vdots \\ r_{n-1} & r_{n-2} & r_{n-3} & \cdots & r_0 \end{pmatrix} = \begin{pmatrix} f_0 \\ f_1 \\ f_2 \\ \vdots \\ f_{n-1} \end{pmatrix} = \begin{pmatrix} r_\alpha \\ r_{\alpha+1} \\ \vdots \\ r_{\alpha+n-1} \end{pmatrix} \tag{2.17}$$

The desired output is in principal the predictable part of the data, such as periodic reverberations or multiples. The unpredictable part is related to the random earth impuls response $e(t)$. This series is called the error-series that can be extracted from the original data by an predictive-error-filter (Yilmaz, 2001).

Result of deconvolution

The approach of predictive deconvolution (statistical deconvolution) is applied to attenuate the strong reverberations from the source signal in the seismic data. Traces of the autocorrelogram in the shot-gather domain are averaged (trace mixing) and a deconvolution operator determined. Before computing this operator, instantaneous gain (AGC) with a window-length of 500 ms is applied. The operator length is 300 ms. This is approximately twice the length of the signal repetition. The prediction distance α is 120 ms.

In Figure 2.6A shot-gather 3002 is shown without the predicive deconvolution after band-pass filtering. Signal reverberations affect the entire gather and have high amplitudes at far offsets. After applying a predictive deconvolution to the gathers (B) the reverberated energy is considerably reduced. The difference of these gathers before and after deconvolution is shown in Figure 2.6C. The autocorrelogramm of the gather in (A) is shown in (D) and (E) shows the estimated wavelet.

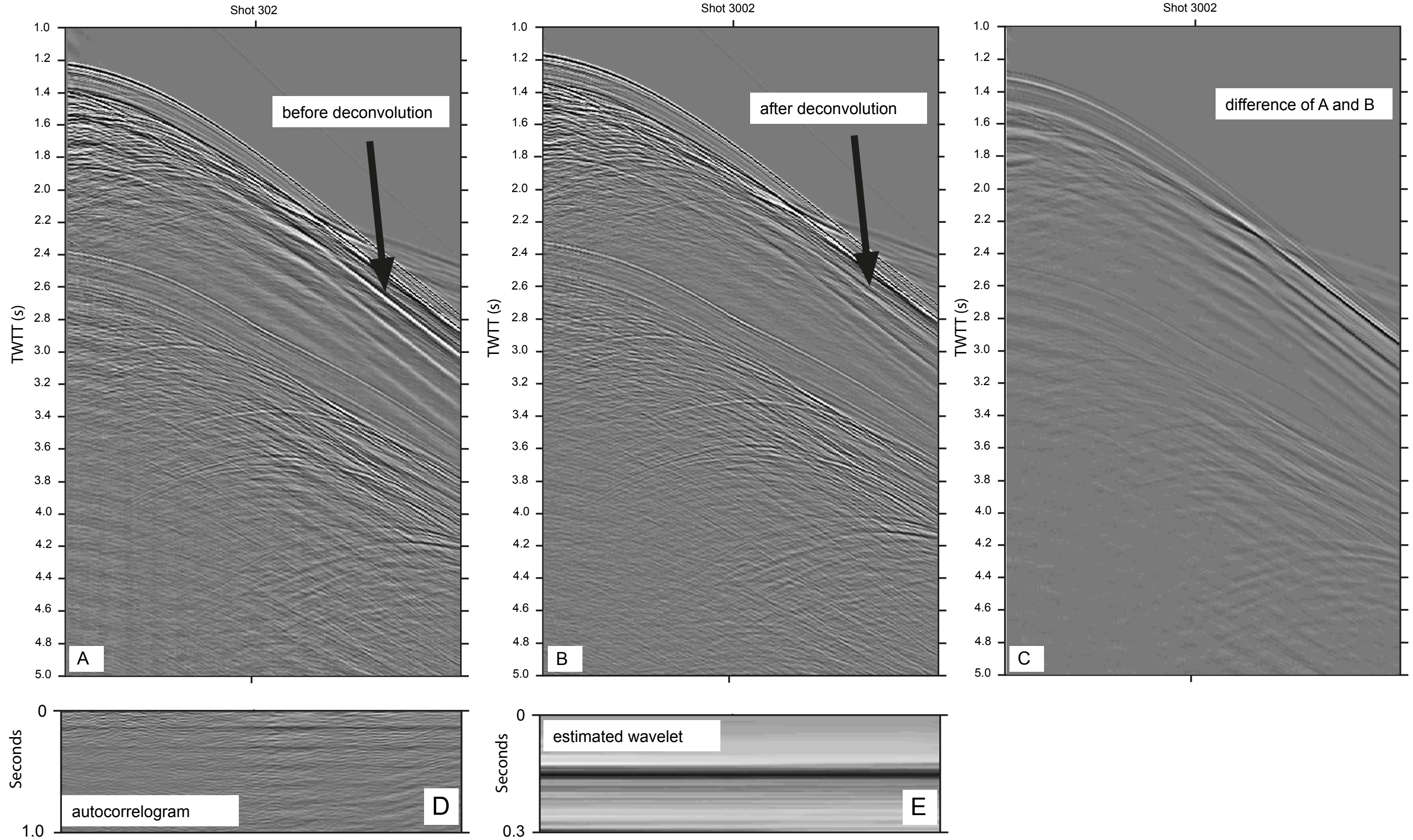

Figure 2.6.: Predictive deconvolution is applied to the shot-gathers to remove signal-reverberations.

2.4. Multiple attenuation

Multiples are a general problem in marine seismic data. Surface-related multiples are the results of the propagating wave-field that reflects at the seafloor and subsurface structures. At the sea surface it is almost completely reflected. Especially when the seafloor is shallow and multiple energy cover the structures of interest; they have to be removed carefully. For this data two methods are applied to attenuate multiples. Firstly, a wave-equation based prediction is used, followed by adaptive subtraction. Secondly, dip-filtering in the frequency-wavenumber domain (f-k domain) is applied. Multiple and primary energy are separated in terms of their dip.

2.4.1. Wave-equation multiple attenuation

A wave-equation based prediction method is the first approach to remove multiple energy from the shot gathers. Such methods applied to data with complex subsurface structures, like the rough seafloor in the northern Tyrrhenian Sea, are often successful (Verschuur et al., 1988). The general idea is to predict multiples and subsequently subtract them adaptively from the original records (Wiggins, 1988). Some methods require a subsurface model to generate synthetic multiples, e.g. by extrapolating the propagating wave-field to another datum (Berryhill and Kim, 1986). The method used here generates an operator by the data itself without knowledge of the arrival times of the primary seafloor reflections. This method of Verschuur et al. (1988) is carried out in the space-frequency domain (x-w) by matrix multiplications and requires equidistant station spacing starting at zero-offset. This was achieved by offset reconstruction using a Radon-transformation and intra-gather interpolation.

After Verschuur et al. (1988) the upgoing seismic wave-field P_0^- recorded at the free surface ($z = z_0$) can be described as,

$$P_0^-(z_0) = Q(z_0)S^+(z_0) \tag{2.18}$$

where $S^+(z_0)$ is the source wave field travelling downwards and $Q(z_0)$ is the sum of primary reflections of M reflectors and internal multiples (Eq. 2.19).

$$Q(z_0) = \sum_{m=1}^{M} W^-(z_0, z_m)R^+(z_m)W^+(z_m, z_0) + M_{int}^-(z_0) \tag{2.19}$$

In equation 2.19 $W^+(z_m, z_0)$ is the downward propagating wave from $z = z_0$ to $z = z_m$ and $W^-(z_0, z_m)$, respectively. $R^+(z_m)$ is the reflectivity at $z = z_m$. In principal the expression $Q(z_0)$ contains the impulse response of the earth including internal multiples but not the reflection from the sea-surface. However, when the wave-field is travelling upwards and reflects at the free surface it can be seen as a new source wave-field. This is exploited for prediction. Further rearrangements and expansion of the total upgoing wave-field into Taylor series, including surface related multiples, (Equation 2.18 allows to predict multiple energy.

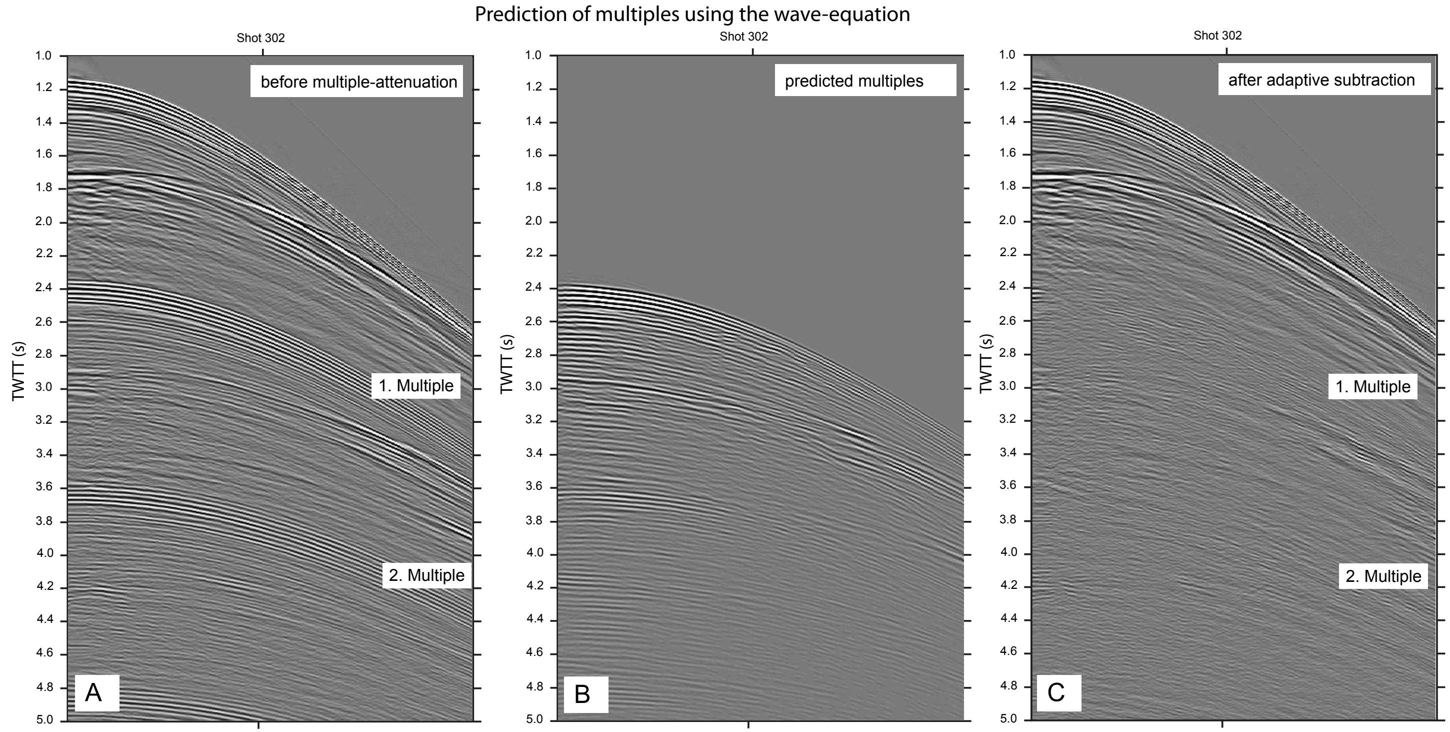

Figure 2.7.: Prediction of multiples by using a wave-equation based approach. A) The multiples in the raw shot-gather are predicted and the result shown in (B). Subsequently (B) is adaptively subtracted from (A) and results in (C).

After prediction of the multiple wave-field, the data are subtracted from the original record. This is carried out by adaptive subtraction, which helps (e.g. by a least-square adaptive filtering approach) to preserve primary events during the attenuation stage (Julien and Raoult, 1989).

Results

In Figure 2.7 the wave-equation based prediction method is applied to the shot-gather 302 in the flat Corsica Basin (A). The surface-related multiples occur at 2.4 s and 3.6 s and are predicted successfully in (B). In (C) the predicted multiples are removed by adaptive subtraction. This excellent result is related to the fact that the topography is not changing significantly. Hence, the shape of the multiple can be predicted accurately. In a region with rough topography, the multiple may reflect at a point at the seafloor that may differ in water-depth and slope angle from the primary reflection. It might not follow a hyperbolic trajectory. The prediction method is just moderately successful in 2D and parts of the multiple remain in the data where the topography was complex.

2.4.2. Frequency-wavenumber filtering

After applying the predictive deconvolution and multiple attenuation to shot-gathers, filtering in the frequency-wavenumber domain (f-k) is applied. This is carried out on common-midpoint-gathers (CMP), thus traces have been sorted. The nominal receiver-group spacing was 12.5 m and the shot spacing during acquisition was 50 m. This yields a CMP-gather size of 35 traces with a trace spacing of 100 m offset. Gathers are transformed into the f-k domain by the 2-D Fourier transformation (Yilmaz, 2001) which is defined as:

$$P(k_x, w) = \int \int P(x,t) exp(ik_x x - i\omega t) dx dt \tag{2.20}$$

Filtering in the f-k plane can be applied to remove different types of noise in seismic data. It also helps to attenuate multiples. The simple relationship between the time-space domain (t-x) and the f-k domain is the following (Yilmaz, 2001):

$$\frac{\Delta x}{\Delta t} = \frac{f}{k} \tag{2.21}$$

A reflection event in the t-x domain has a certain (apparent) velocity and thus a certain dip. If a reflection event within a gather would be a mono-frequent signal and horizontally orientated (no dip) it would appear with equation 2.21 on a single point in the f-k domain at k=0. A dipping event with a certain frequency content would map as a straight line between the minimum and maximum frequency in the f-k plane. The origin would be k=0. Transforming seismic traces into the f-k domain is in principal a decomposition of the wave field into mono-frequent plane-waves (Yilmaz, 2001). It is convention that a positive dipping event has a positive wavenumber and events that dip opposite have negative wavenumber. This is exploited to separate primary and multiple reflections in the f-k plane. They map on different quadrants if an appropriate velocity-function for normal-move-out-correction (NMO) is applied.

Primary and multiple separation

A normal-moveout-correction (NMO) with a velocity function that leads to overcorrected primaries (upward-dipping) and undercorrected multiples (downward-dipping) can separate these reflections in terms of different dips. An initial velocity field for this purpose is achieved by focusing-analysis and iterative prestack depth migration (Fig. 2.1). Afterwards, the velocity is calculated in a way that primary reflections at multiple reflection times dip upward and multiples downward. The calculation estimated an apparent velocity so that the moveout of the multiple is only a half correction of the original multiple moveout.

Results

Figure 2.8 shows a CMP-gather where partial energy of the first order multiple is still present (A). In (B) a NMO-correction with a velocity-function between primaries and multiplies is applied in order to separate them. Late primary reflections dip upwards (very weak reflections) while the dip of early primary reflections just decrease. Attenuation where set to start below the first multiple. It is tapered within a 200 ms long window before multiple times. Before transforming the CMP-gathers into the f-k plane, trace-interpolation is applied to avoid spatial aliasing. Spatial aliasing occurs for higher frequencies and for steep dipping events in the f-k plane, or when the trace-spacing is insufficient. An event with a certain dip and frequency content can apparently dip in the wrong direction. This is expressed by a wraparound of frequencies in the f-k plane to the wrong quadrant. The original trace spacing in the CMP-gather was 100 m. This spacing was decreased to 25 m by 1:4 trace interpolation. Figure 2.8C shows the f-k spectrum of the interpolated CDP 6377. Most of the energy is located within half the fraction of Nyquist. The spectrum is not affected by spatial aliasing. Most of the energy is aligned along the frequency-axis, because events dip less after NMO-correction. Thus, the wavenumber decreases. The positive quadrant of the f-k domain contains the multiples. It is fully rejected and the data transformed back into the t-x domain. After that inverse NMO-correction is applied (Fig.2.8D).

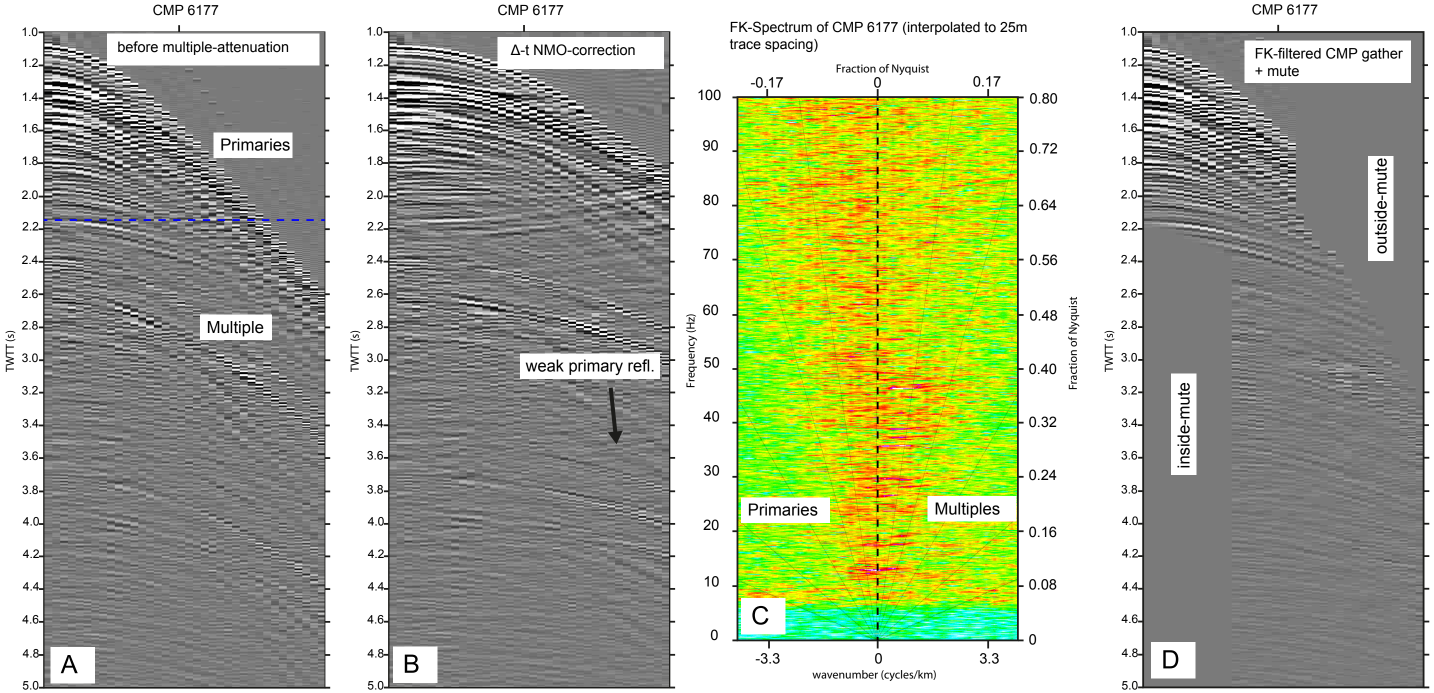

Figure 2.8.: Frequency-wavenumber filtering in the CMP-domain. (A) shows a CMP-gather where remains of the multiple are still present. In (B) primaries and multiples are separated by their dip. (C) shows the respective f-k spectra of (B) (trace-interpolated). (D) shows the CMP-gather after deleting the positive quadrant of the f-k spectra. Additionally, an inside- and outside-mute have been applied.

2.4.3. Mute, BP-Filter and Stack

As reflections at near-offset traces have just small moveout differences they cannot be separated by their velocity. The effect of multiple attenuation in the f-k plane is minor. At those offsets, multiple energy remains present. It is rejected by applying an inside-mute window after dip-filtering. Furthermore, refracted arrivals at the far-offset traces are removed by applying an outside-mute window that has been determined within the shot-gather domain (Fig. 2.3). As frequencies decrease with increasing travel-time, a time-variant bandpass-filter (Tab. 2.1) is applied within two overlapping windows (500 ms overlap).

Window	Start-Time	End-Time	low-cut [Hz]	high-cut [Hz]
1	-200	3000	7	65
2	2500	8000	4	35

Table 2.1.: Bandpass-filtering within two overlapping windows.

Afterwards, the effect of geometrical spreading is compensated. A NMO-correction is applied using the final velocity field that has been obtained by focusing-analysis and iterative prestack depth migration. This velocity field is transformed into two-way-traveltime (TWT). Traces are stacked and the results of both transect after multiple attenuation and predictive deconvolution are shown in Figure 2.9. The predictive deconvolution achieved that the "ringy" character is removed. Multiples are clearly attenuated.

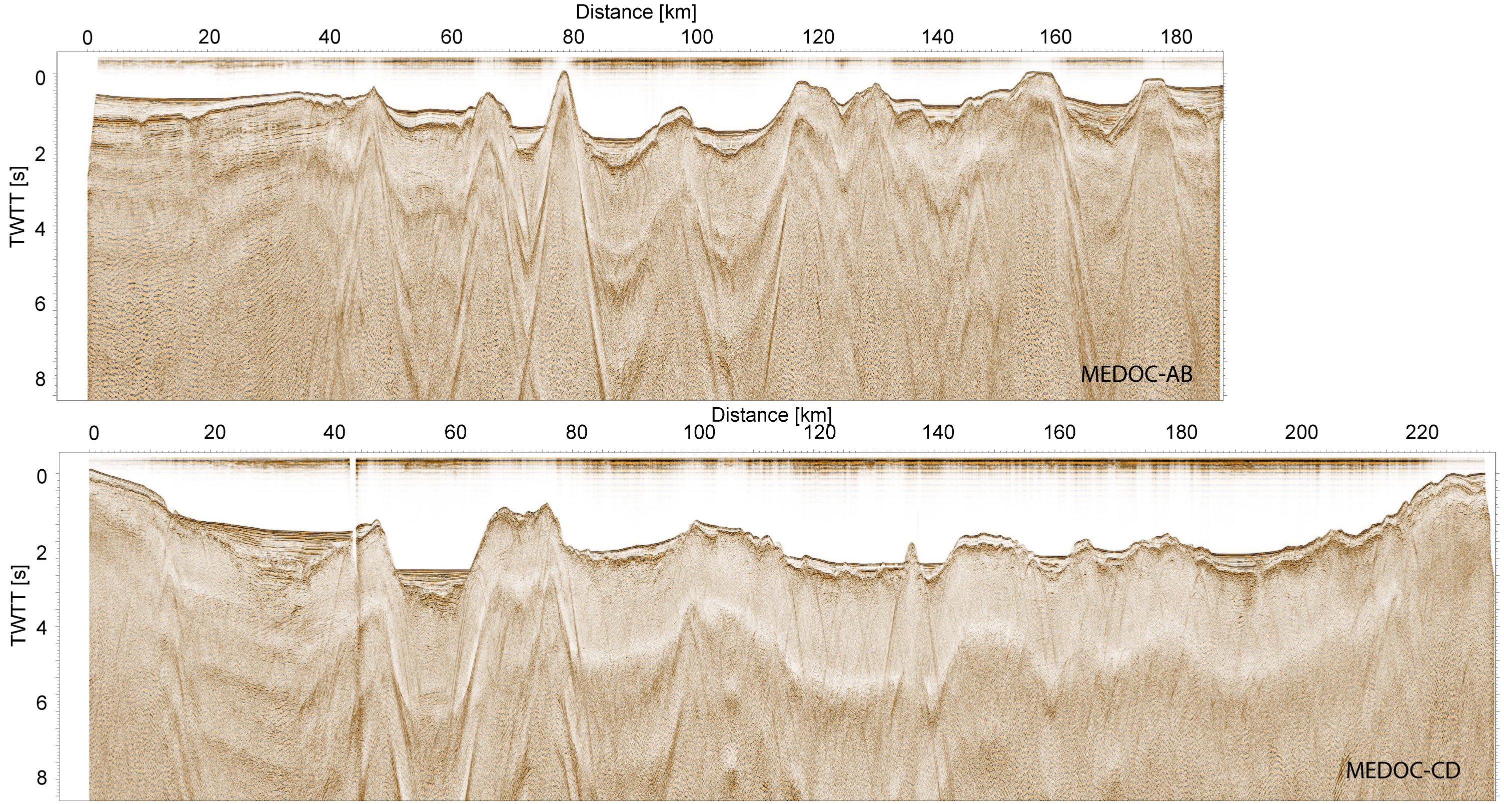

Figure 2.9.: Stack after predictive deconvolution, wave-equation based multiple attenuation, dip-filtering in the f-k domain and muting.

3. Velocity model building and prestack migration

The migration of seismic data is the process that shifts subsurface structures to their true position. For example, diffraction energy collapses into its apex point or the dip of reflectors is corrected. Migration can applied to both, poststack and prestack seismic data (Jones et al., 2008).
In regions of complex topography, subsurface structures and strong lateral velocity contrasts, (poststack) time migrated sections are often distorted and thus will not represent the true geometries of subsurface geological features. Furthermore, strong ray-bending occurs with regard to Snell´s Law and reflection events may not follow hyperbolic traveltimes trajectories when gathered (Yilmaz, 2001). For instance, the distortion effect has been shown for a shallow dipping detachment at the Galicia Margin (S-reflector). The detachment appears to be discontinuous and offset on poststack time migrated sections. However, after prestack depth migration it seems to be a continuous feature (Hoffmann and Reston, 1992). This example demonstrates the need of a true ground model for interpretation in complex geological settings. Prestack migration handles both, reflector dips and lateral velocity variation (Liu, 1995).
As the first part of the study (Chapter 5) focuses on the geometry of faults and rotated blocks, it is necessary to carry out the interpretation on a depth-migrated section. The effect of ray-bending is compensated and migration is carried out before stack (prestack). This supports that the image of the subsurface would be in principle a true ground model (Jones et al., 2008). However, this provides that the "true" depth velocity model is used for migration.

3.1. Velocity analysis

Two basic methods exist to achieve an appropriate velocity field for depth imaging (Liu, 1995): Depth-Focusing-Analysis (DFA) and Residual-Moveout-Analysis (RMO). The latter approach for velocity model building is used here.

Depth-Focusing-Analysis

In DFA, the wave-field recorded at the surface is propagated downward using the scalar wave-equation. This is equivalent to a progressive downward continuation of shots and receivers (MacKay and Abma, 1992). Propagating the data to another datum is like recording them at another depth. If a reflector exists at this certain depth and assuming that the migration velocity was the real velocity, the energy of this reflection event would focus at zero-time ($t = 0$) and zero-offset ($h = 0$). These are the imaging conditions and provide the migrated depth section (MacKay and Abma, 1992). If a wrong migration velocity is used, the focused energy of the reflection event is erroneous. It will not appear at the zero-time condition. Migration velocities are iteratively updated until the depth-error converges to zero or is negligible.

Residual-Moveout-Analysis

Residual-Moveout-Analysis (RMO) is based on measuring the curvature of reflection events on migrated common-reflection gathers (CRPs) in order to estimate migration velocities. This approach was basically implemented in the Sirius Software and used for this project. It is based on the principal that a reflection event in a common-reflection gather (CRP) should be imaged at the same location and depth. This should be true for all traces of the gather, although recorded at different offsets (Liu, 1995). This is valid under the assumption, that the velocity model is the real model. Then, reflection events in the CRP-gather should be aligned horizontally (Al-Yahya, 1989). An approach for estimating the residual moveout and the generation of semblance panels is presented in the following (after Al-Yahya (1989)).
For horizontal layering the two-way-traveltime t can be described by the following hyperbolic expression assuming straight raypaths:

$$t = 2\sqrt{x^2 + z^2}\omega \tag{3.1}$$

Here, x is the half distance between shot and receiver, z is the depth to the reflection point and ω is the slowness (reciprocal velocity). If the slowness above the reflector would be wrong (ω_m), the reflector appears to be located at the wrong depth z_m. Because the travel-time is constant, an ambiguity between slowness and imaged reflector depth exists (Al-Yahya, 1989). The expression becomes:

$$t = 2\sqrt{x^2 + z_m^2}\omega_m \tag{3.2}$$

When the travel-time t is eliminated from 3.1 and 3.2, the depth of the reflector is described as:

$$z_m = \sqrt{\gamma^2 z^2 + (\gamma^2 - 1)x^2} \tag{3.3}$$

In Equation 3.3 the new expression γ is the ratio of the true migration slowness and the inaccurate slowness.

$$\gamma = \frac{\omega}{\omega_m} \tag{3.4}$$

From 3.3 it can be seen, that the difference of the real reflector depth z and the apparent reflector depth z_m converges to 0 if $\gamma = 1$. In the case that $\gamma \neq 1$, meaning that the velocity is too slow or too fast, the reflector in a CRP-gather is not aligned horizontally. It is shifted along the zero offset axis and a residual movout remains at offsets > 0. Rearrangement of the equation 3.3 into time τ (Eq. 3.5) shows that no residual moveout exists when ω_m has values that fulfill the requirement of $\gamma = 1$. For $\gamma < 1$ or $\gamma > 1$ the reflector image will be curved upward or downward.

$$\tau_m = \sqrt{\tau^2 + (\gamma^2 - 1)x^2\omega_m^{-2}} \tag{3.5}$$

Although in the equations above horizontal layering is assumed, Al-Yahya (1989) showed that the effect of subsurface structures diminishes, the closer γ converges to 1. This points out the importance of an accurate velocity model for depth imaging.

Semblance analysis

To estimate and update velocities from CRP-gathers for iterative depth imaging, velocity scans are carried out. This results in semblance panels for velocity picking and estimation of the depth error. At each travel-time, curves are defined for a range of different values for γ (Al-Yahya, 1989). Subsequently, the amplitudes along the trajectories of all curves are summed and normalized. The semblance is maximal where energy focuses for reflection events that fit the trajectorie of the curve for a certain γ. The semblance panel $g(\tau, \gamma)$ can be created of the data $p(\tau_m, x)$ of the migrated CRP-gathers. It is defined by the following expression (Al-Yahya, 1989):

$$g(\tau, \gamma) = \frac{\left[\sum_x p(\tau_m = \sqrt{\tau^2 + (\gamma^2 - 1)x^2\omega_m^{-2}}, x)\right]^2}{\sum_x \left[p(\tau_m = \sqrt{\tau^2 + (\gamma^2 - 1)x^2\omega_m^{-2}}, x)\right]^2} \tag{3.6}$$

3.1.1. Depth migration: Practical procedure

The input data for velocity analysis and iterative prestack depth migration are the common-midpoint sorted gathers (CMP). For the first 4 iterations (Iteration 0-3) CMP gathers still contain multiple energy. Multiples will be removed after an appropriate velocity field is determined. In the 3rd to 8th iteration the de-multiple and muted CMP-gathers (Fig. 2.8) are used to achieve a final depth migrated section. In the initial iteration (0) the data is migrated using a constant 1-D velocity field of 1520 m/s. This velocity corresponds to the average velocity of the water column. It has been derived by CTD measurements carried out aboard the RV Urania.

For the Kirchoff migration operator, traveltimes are computed by a ray-tracing algorithm which is based on finite differences. Rays are generated at locations of 25 m spacing along the profile and the travel-times are stored in so called travel-time maps having an extent of ± the largest offset in the data (3600 m). The output after the migration process is the depth-migrated section and a set of common-reflection-point gathers (CRP´s). Subsequently, a velocity scan generates depth focusing-panels from the CRP´s in terms of depth-error along the x-axis. On these panels focused energy can be picked in order to determine a new and improved migration velocity for the next iteration step.

Modelling strategy

The strategy for building an accurate velocity field, is to develop a macro-model consisting of distinct domains which are bounded by velocity interfaces. Interfaces are coincident with reflections and velocity changes at prominent geological boundaries. Anisotropy is not assumed during modelling. The model is iteratively improved in a so called layer-stripping approach. This means, that the model and the depth of geological interfaces are iteratively updated and improved from top to bottom.

After the initial iteration, using just a 1-D function of the water velocity for migration, the seafloor appears as a smooth reflector and is digitized to define the uppermost interface. Deeper interfaces are defined at those depths, where reflections can be continuously traced along the entire section and from which energy focuses on the depth-focusing panels.

As an example, Figure 3.1A shows the depth image of the sedimentary basin which is bounded between the two large continental blocks B1 and B2 at the western portion of line CD. The interpretation of this sub-basin is also shown in chapter 1, Fig.1.6C. In the focusing panel (Fig.3.1B) the semblance from the sea-floor reflection in Fig. 3.1D has a maximum at an interval velocity of 1520 m/s. The reflection is horizontally aligned in the CRP-gather. The depth error for this event is close to 0. At greater depth, the data is imaged using an interval-velocity that is too slow. The apparent depth of the interfaces at 2500 m and 2800 m depth are in error of +100 m respectively +300 m. Thus, these reflectors appear too shallow and the reflections are curved upwards on the CRP gather. Focused energy on the panel reveal new interval velocities of 1800 m/s for the upper part of the sedimentary infill (red-green) and 2600 m/s for the lower part (green-blue) (Fig. 3.1C). Velocities have been estimated on every 200th CRP which is fairly sufficient for building a macro velocity model.

At places where the sedimentary cover is thin and the crystalline basement located close to the seafloor, no energy is focused to estimate migration velocities. This is because no (strong) impedance contrast exists within the crystalline crust and thus less reflected energy is recorded. Therefore, velocities for the non-reflective domains are adopted from the preliminary wide-angle model that has been modelled in a forward-modelling approach (chapter 4) using the software 'Rayinvr' (Zelt and Smith, 1992).

After picking the centre of the focusing points, a new velocity field is built. It progressively evolves closer to the real velocities for every domain along the section. Velocity changes occur abruptly in the lateral dimension at the changeover from sedimentary to crystalline rocks (for instance in the grabens), or in the vertical direction between the sedimentary infill, the underlying Messinian evaporites and the crystalline basement. However, the migration velocity field has to be smooth and strong velocity contrasts should be avoided.

Figure 3.2A shows the final depth-section after 8 iterations. Deeper sedimentary structures (syn-rift sediments) are now clearly imaged. The interval velocity in the entire horizontally deposited sedimentary section has evolved to 2000 m/s constantly. The layer below the green dashed interface is formed by alternating sequences of Messinian evaporites and clay. It is characterized by a velocity jump to 3300 m/s. In order to avoid that the contrast between the above lying soft sediments is too high ($>$ 600 m/s), a thin and artificial layer has been inserted (green-blue). Within this layer the velocity gradient is set to be high, so that velocities at the base match the actual interval velocity of the domain. The smoothness of the velocity field is important to avoid the generation of artifacts. The focusing panel in Figure 3.2B shows that the depth error evolved close to zero in the upper part ($<$ 10-20m). At a depth of 3600 m the error is smaller than 50 m. Reflections on the CRP-gather appear horizontally.

Additional smoothing has been applied to the entire velocity field prior to migration. The smoothed velocity field for this specific sub-basin is shown in Figure 3.3. Interval velocities for the different domains are summarized in Table 5.1. The velocities within the crystalline blocks and the basement (higher than 3600 m/s) are obtained from the result of forward-modelling seismic wide-angle data (WAS) and not by focusing-analysis.

The depth-migrated section of the line AB is presented within chapter 5. The depth migrated section of line CD as well as the migration velocity-fields of both lines are attached to the Appendix A.1 and A.2 of this thesis.

Depth-image after 0. Iteration (velocity=const=1520 m/s)

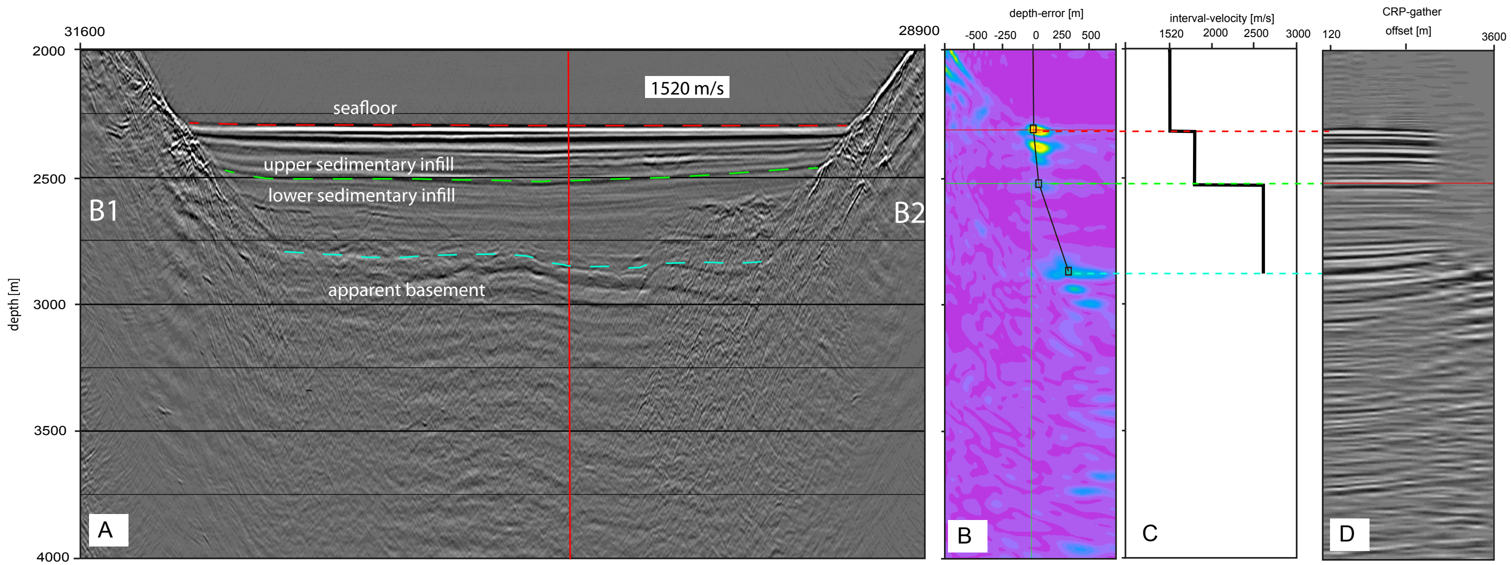

Figure 3.1.: Image after initial depth-migration using a constant migration velocity of 1520 m/s. Red solid line shows the CRP location.

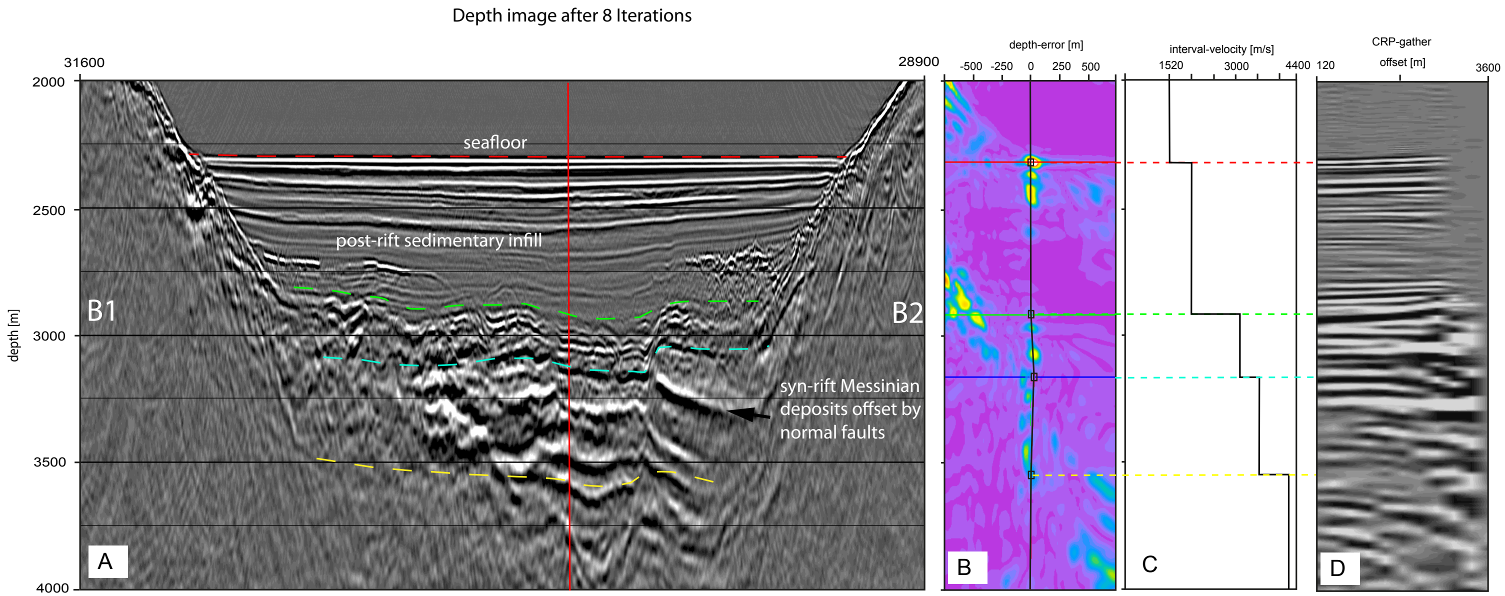

Figure 3.2.: Depth-image after 8 iteration using the final velocity model obtained from focusing-analysis (RMO).

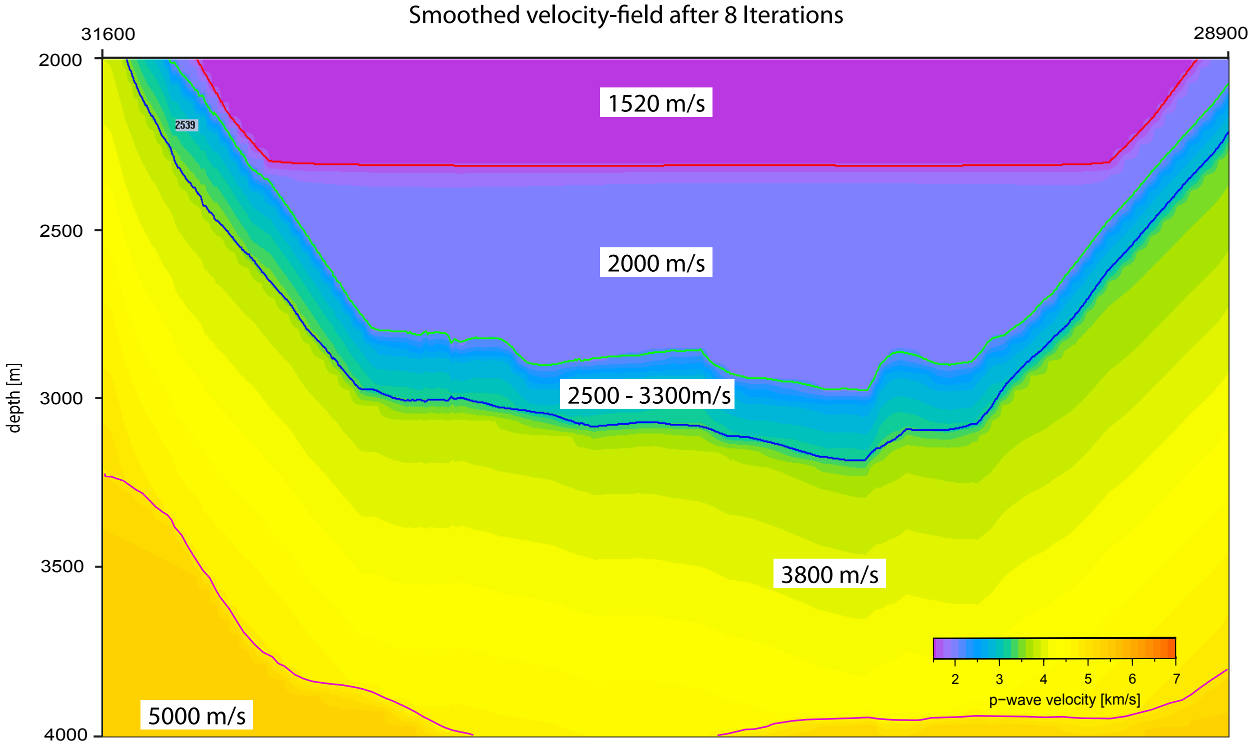

Figure 3.3.: Smoothed velocity field used for the last iterative migration step.

Domain	V_p [m/s] Top	V_p [m/s] Base
post-rift	1800-2000	const.
syn-rift	2600	3300-3600
upper basement (WAS)	3800	5000
middle-lower crust (WAS)	5500	6600

Table 3.1.: Smoothed interval velocities.

3.1.2. Partial stacking and time migration

For prestack time migration of the data, the final velocity field obtained from focusing-analysis is transformed into two-way-traveltime (RMS). Time migration is also carried out using the Sirius-Software. Due to size limitations of the input data, partial stacking has been applied to the CMP-gathers before migration. The partial stack width is 200 m. This reduces the data set to one-third of the file size, because the trace-spacing in the original CMP-gathers was 100 m. The use of a well estimated velocity field for NMO-correction before partial stacking, deliver accurate results for the entire time-series/offset. It improves the signal-to-noise ratio. The half-aperture width used for Kirchhoff migration was 3600 m. The time-migrated sections are presented in Chapter 6.

4. Refraction and wide-angle seismic data

Seismic energy for the refraction experiment was generated by the 4600 in^3 airgun-cluster that transmitted a center frequency of 8 Hz. As the wavefield propagates through the crustal and uppermost mantle domains, seismic energy is refracted (turning-waves) and reflected. The traveltimes are recorded at the hydrophones attached to the OBH stations. The propagation-velocity of seismic energy through a homogenous medium is basically related to its elastic parameters and the density. A velocity model, that explains the arrival-times observed at different offsets, can be interpreted for instance in terms of crustal composition or degree of fracturing.

This chapter describes the processing sequence and tests (Fig. 4.1) that lead to the final crustal-scale velocity models used for interpretation. The procedure is demonstrated for the southern seismic line (line CD), located between Sardinia and the mainland of Italy (Fig.1.4). The parameters used for the northern line AB are similar. For the basic seismic data processing, the software package 'Seismic Unix' and existing codes developed at GEOMAR are used. Traveltime picking and forward modelling has been carried out with *Zplot* and *Rayinvr* (Zelt and Smith, 1992) to obtain a preliminary velocity model. This model is used as a starting model for iterative refinement by tomographic inversion using the code *TOMO2D* (Korenaga et al., 2000).

4.1. Pre-processing

4.1.1. OBH data

The data recorded by the OBH stations were stored in an internal recorder format and finally converted into the SEG-Y format following a GEOMAR standard processing sequence. Receiver and shot positions, the trigger time of the airgun, the waterdepth as well as the time skew of the recorders were merged into a seismic navigation file, following the formatting of the UKOOA exchange format. The skew is the deviation between the synchronized GPS-time before deployment and after recovery. It is distributed on the entire record length, assuming the drift occurred linearly. To achieve common-receiver-sections for each OBH station, the continuously recorded time series were cut into 20 s long traces and sorted by offsets using an existing code (*dat2segy*). The time scale was reduced by a velocity of 8 km/s, so that refracted waves travelling

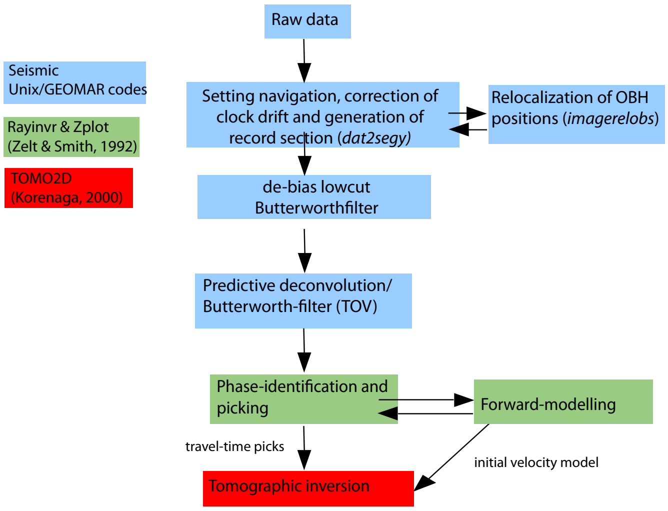

Figure 4.1.: The flowchart shows the processing steps that were applied to the refraction and wide-angle seismic data to achieve a crustal-scale velocity model.

through the upper mantle would be horizontally aligned. As an example record section OBH06 is shown in Figure 4.2. Trace-balancing is applied to the record section by subtracting the mean. A low-cut Butterworthfilter removed low-frequency noise (< 2 Hz) related to a DC-shift (de-bias).

Relocalization of OBH positions

The position during the deployment of the instrument was taken from the ship´s standard GPS-antenna. However, during the descend of the OBH, water currents may force the instrument to deviate from the deployment position. Thus, the final position at the seafloor is unknown. In deep water areas the deviation can be several hundred meters. A wrong position of the station along the profile is expressed in an asymmetry of the direct water-wave due to wrong offsets. The code *imagerelobs* allows the recalculation of the instrument position at the seafloor. However, minimizing the deviation is restricted to the component that is orientated parallel to the profile direction (2D).
To achieve relocalization, the direct water-wave has been flattened to gain coherence for digitizing the arrival times of the direct wave. A 1D velocity-function of 1520 m/s is used. Afterwards, a new receiver position is calculated, the seismic navigation files updated and the record sections built new. In this iterative approach, the horizontal alignment of the direct wave is viewed again and the procedure eventually repeated, until the direct wave reveal a symmetric shape. A correct position at the seafloor can be assumed.

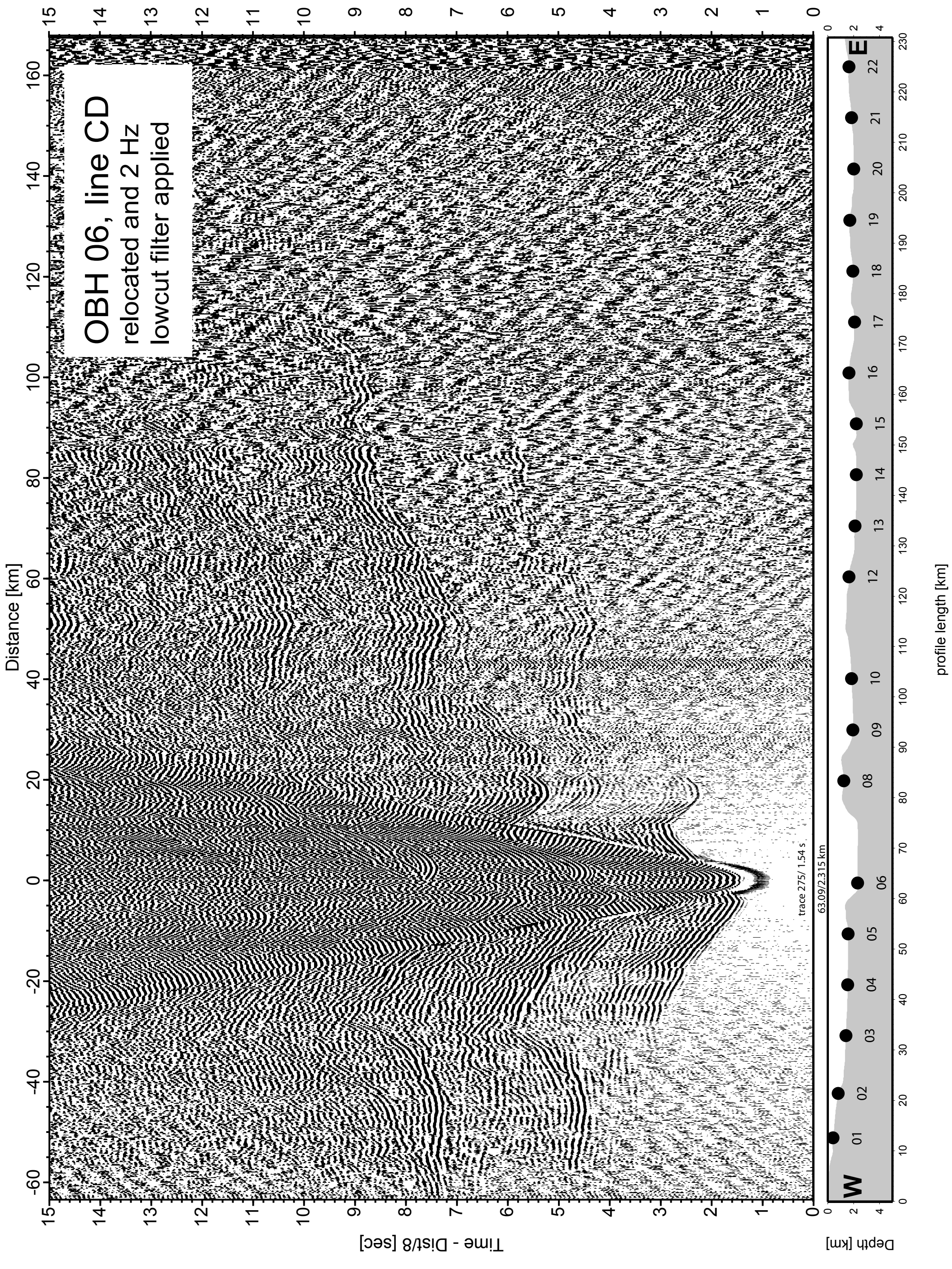

Figure 4.2.: Example of an OBH record section (OBH06). Trace balancing and a bandpass filter to remove a low-frequency content of <2 Hz is applied. Subsequently, the position of the station at the seafloor is relocated.

Predictive deconvolution

After trace balancing and the removal of low frequencies (< 2 Hz), a predictive deconvolution is applied to the common-receiver-sections. A theoretical background of predictive deconvolution is given in section 2.3.
The goal of predictive deconvolution is to attenuate signal reverberations which are related to the bubble-effect of a marine seismic source. Hence, the signal-to-noise ratio can be improved. Parameter tests reveal, that a prediction distance of 23 ms and an operator length of 1 s represents a good choice for the near offset traces (Fig.4.3). Smaller prediction distances than 23 ms suppress the reverberation successful, but partly destroy the coherence of first arrival branches, for instance a prediction length of 8 and 10 ms. Deconvolution with larger prediction distances do not attenuate the "ringy" character of the wavefield sufficiently. The deconvolution operator is averaged over 11 traces from the autocorrelation function (trace-mixing). These values are also sufficient for the far-offset domain. Examples of filtered and deconvolved record section are presented in Fig. 4.6, within chapter 5, chapter 6 and shown in Appendix A.3.

Time- and offset-variant filtering

As the wavefield propagates through the crust and traveltime and offset increase, the high frequency content is damped faster than waves of lower frequencies. Octave-filter panels are used to analyze the frequency content at near (Fig. 4.4) and far offsets (Fig. 4.5). The lower part of the panels shows the amplitude spectra of the displayed and filtered traces. The near-trace panel containing the unfiltered data show, that energy of up to 90 Hz is present. However, a filter panel with a passband between 64-80 Hz reveals that those frequencies are restricted to the direct wave. Refracted arrivals do not contain frequencies higher than 30 Hz at near offsets. The dominant frequencies generated by the airgun-cluster range between 5 to 18 Hz. At far-offset (80-100 km), first arrivals contain just low frequencies within a narrow band ranging between 4-10 Hz. Because of the frequency decay with increasing travel time and offset, Butterworth-filters within four windows and decreasing passbands (4.5-20 Hz and from 3.5-10 Hz) are applied to the data. Fig.4.6 shows the deconvolved and bandpass filtered record section of OBH06. The low frequency content, especially at near offsets and time is removed and the "ringy" character of the data decreased.

4.1.2. Land stations

The data recorded by the landstations onshore Corsica and Sardinia are provided by IDPA/CNR (Milan) and available in ASCII-format. A shell-script was developed that used standard SU commands to read in the data sequentially in order to transform them into traces of standard SEGY-format. Moreover, all necessary header information are set to prepare the data for further seismic processing and phase identification. The

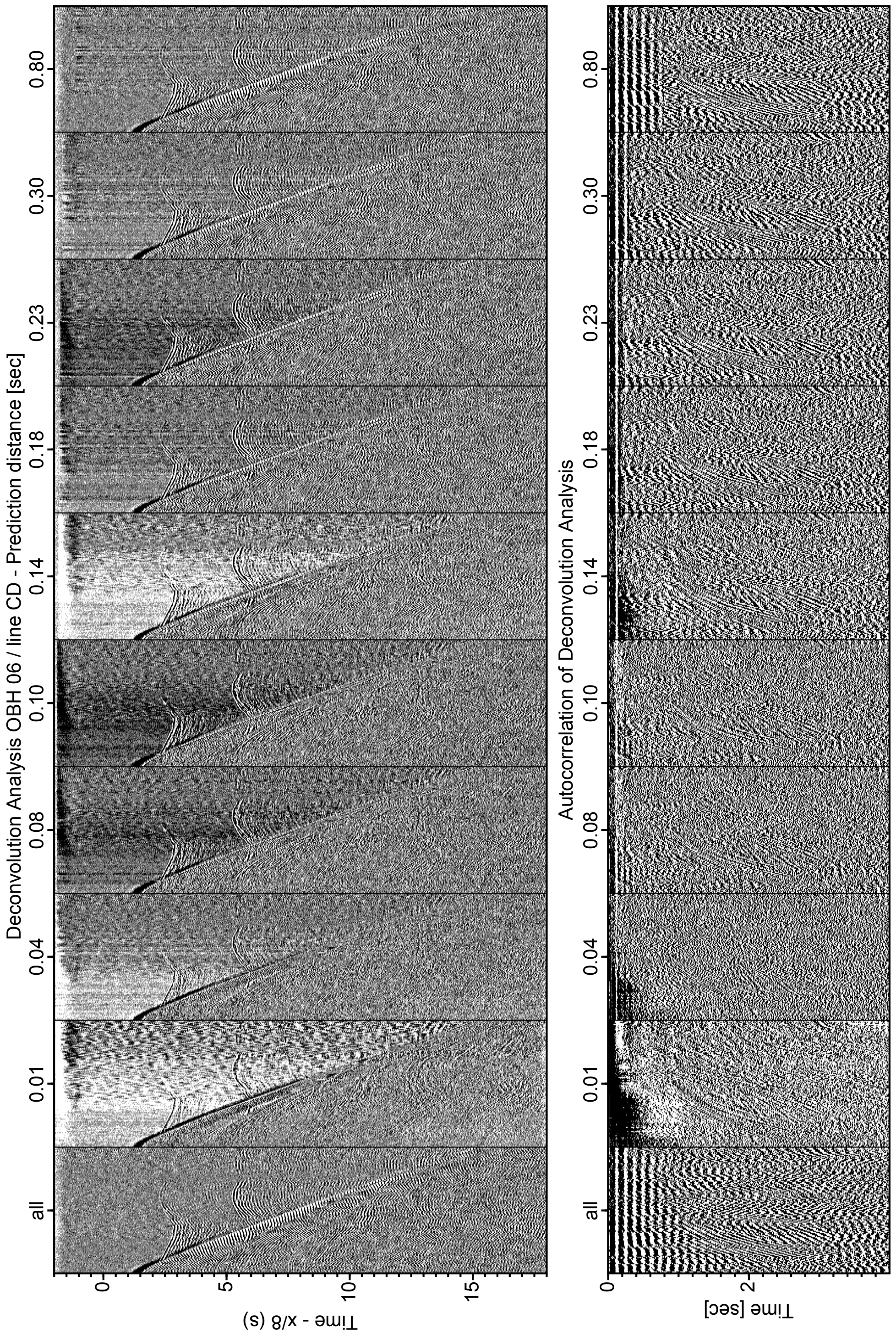

Figure 4.3.: Test panels for a range of different prediction distances for statistical deconvolution (OBH 06). An appropriate prediction distance is 0.23 s. The operator length is 1 s.

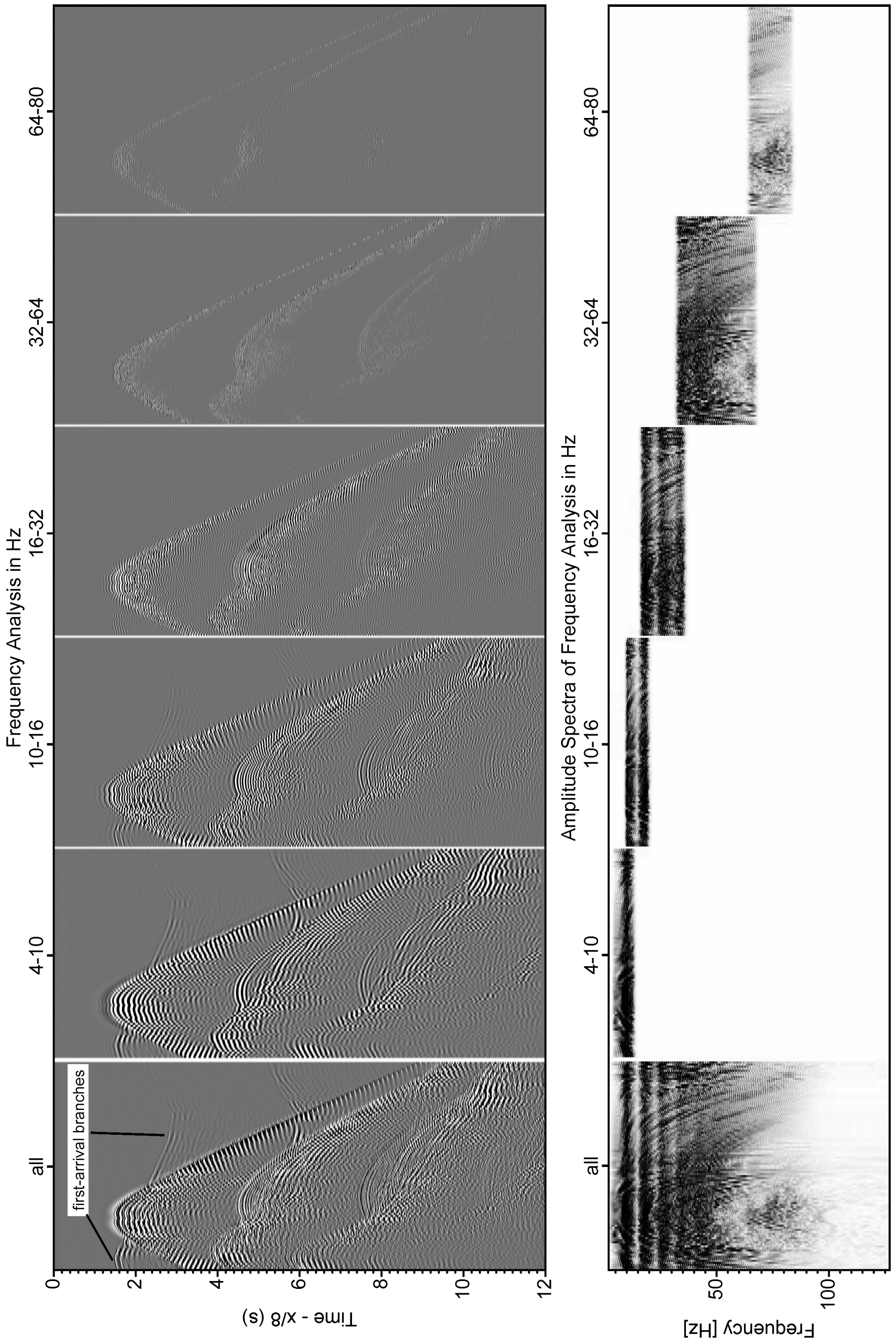

Figure 4.4.: OBH06: Frequency analysis for a range of different pass-bands at near-offset traces. The lower part shows the amplitude-spectra of the filtered sections.

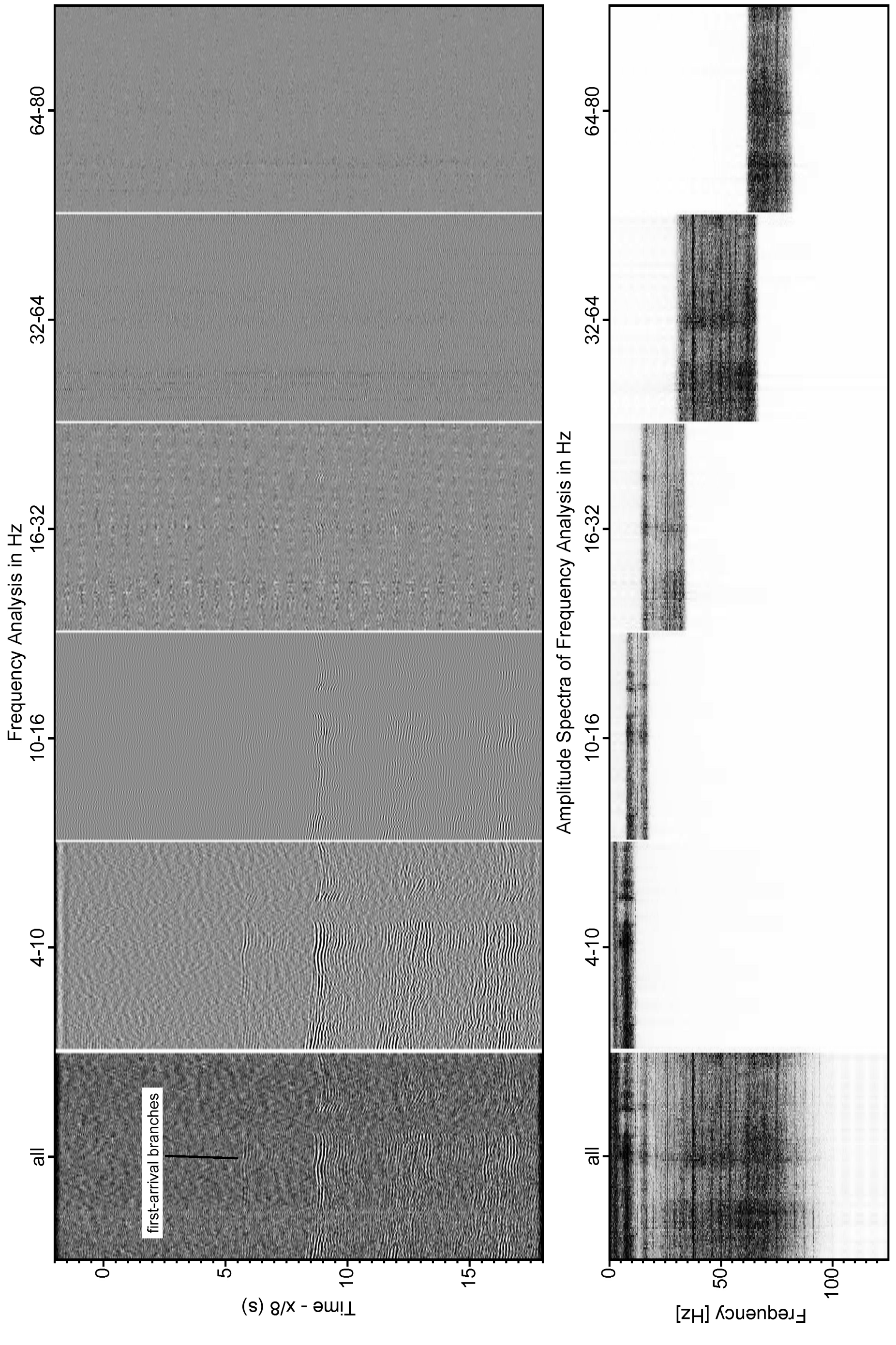

Figure 4.5.: Frequency analysis (OBH06) for a range of different pass-bands at far-offset traces (80-100km). The lower part shows the amplitude-spectra of the filtered sections.

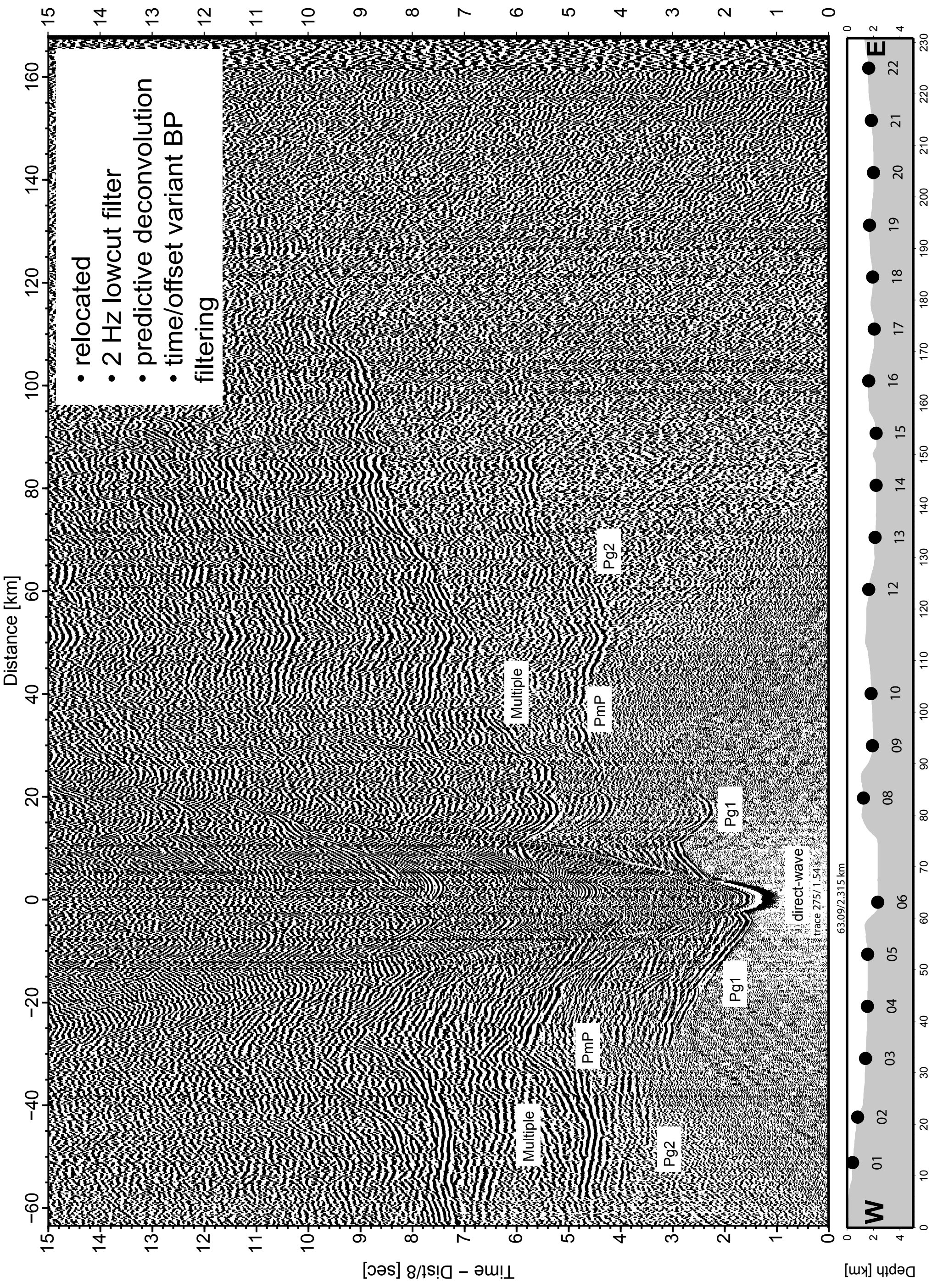

Figure 4.6.: Deconvolved and filtered record section of OBH06. Identified seismic phases are labeled as listed in Table 4.1.

minimum offset from the shots to the station is 20 km on the line AB and 40 km on the line CD. The maximum recorded offset exceeded 320 km. Due to the large distances, the recorded frequency content on the entire record sections is relatively low. A simple zero-phase filter with corner frequencies of 3-4-10-15 Hz is appropriate to filter the data and to identify first arrivals. A predictive deconvolution has been tested but not applied because the result had rather shown a set back than an improvement to some parts of the first arrival branches. An example of a record section is shown in Figure A.15.

4.2. Forward modelling

The goal of the forward modelling approach is to build a velocity model that approximately explains the traveltimes of the observed seismic phases. It also provides a rough estimation for the depth of the Moho and the classification of upper and lower crust with respect to a high and low velocity gradient. It is also a useful method to clarify by a trial and error method to which domain seismic phases belong to. This is especially important for the classification of secondary arrivals. The result of forward modelling will be subsequently used as an input model for tomographic inversion. Forward modelling and traveltime picking has been carried out using the codes *Zplot* and *Rayinvr* (Zelt and Smith, 1992).

4.2.1. Phase identification

Table 4.1 gives an overview of the identified seismic phases recorded by the OBH and land stations. P_g phases are crustal-refracted phases travelling through the (granitic) crust. They are divided into near offset arrivals from the upper crust and far offset arrivals from the middle and lower crust.

P_{g1} phases are picked up to ∼30 km offset. This is approximately the offset where the apparent velocity gradient changes over from high to low. It is expressed by a flattening of first arrival branches. P_{g2} phases travel through deeper crustal levels with a lower velocity gradient between 30-80 km offset. P_mP phases, which are wide-angle reflections from the crust-mantle-boundary (Moho), are recorded on almost every station and help to constrain the depth and shape of the discontinuity. Clear P_n arrivals travelling through the upper part of the mantle, are just observed by the landstations located on Sardinia where the signal-to-noise ratio is high. Another secondary reflected phase is recorded on several stations near the Corsican Margin (line AB) at offsets between 60 - 80 km. Their origin might be related to an intra-mantle feature and is labeled $P_{im}P$. Pick uncertainties increase with increasing offset and include also the effects of phase-shifts due to filtering and deconvolution. Uncertainties are estimated to be 50 ms at the near offsets and 100 ms for far-offset arrivals and wide-angle reflections. A detailed description of the seismic refraction- and wide-angle data is given within chapter 5 and chapter 6.

Seismic Phase	Zone	min. offset [km]	max. offset [km]	pick-uncertainty [ms]
P_{g1}	upper crust	0	30	50
P_{g2}	middle+lower crust	30	50	50
P_mP	Moho	30	80	100
P_n	uppermost mantle	120	300	100
$P_{im}P$	intra-mantle	60	80	100

Table 4.1.: Identified seismic phases observed on record sections of OBH and land stations.

4.2.2. Ray-tracing algorithm

The code *Rayinvr* computes synthetic traveltimes and ray paths by solving the eikonal-equation for an isotropic medium (Eq. 4.1). This expression is the high-frequency approximation of the acoustic wave-equation where T is the traveltime function and v the p-wave velocity (Cerveny, 2001).

$$(\nabla T)^2 = \frac{1}{v^2} \tag{4.1}$$

The eikonal-equation can be solved in 2-D by two ordinary differential equations (Zelt and Smith, 1992)

$$\frac{dz}{dx} = cotan(\theta) \quad ; \quad \frac{d\theta}{dx} = \frac{v_z - v_x cotan\theta}{v} \tag{4.2}$$

$$\frac{dx}{dz} = tan(\theta) \quad ; \quad \frac{d\theta}{dz} = \frac{v_z tan\theta - v_x}{v} \tag{4.3}$$

and the boundary constraints for the source position.

$$x = x_0 \quad ; \quad z = z_0 \quad ; \quad \theta = \theta_0 \tag{4.4}$$

In the differential equations 4.2 and 4.3, θ is the angle between the ray and the z-axis. Further, v_x and v_z are the partial derivatives of the p-wave velocity in horizontal and vertical direction, given at a certain point in the model. The entire raypath is computed along small ray-steps (ray-step length). Reflection at an interface is implemented by taking into account Snell´s Law (Zelt and Smith, 1992) which is defined as:

$$\frac{sin\theta_1}{sin\theta_2} = \frac{v_1}{v_2} \tag{4.5}$$

Here, θ_2 is the angle of refraction and v_2 the velocity beneath the interface. The traveltimes are calculated by integration along the entire ray path.

4.2.3. Model parameterization and results

The model consists of different layers and interfaces which are defined by depth and velocity nodes at the top and bottom of each layer (see rectangles in Fig. 4.7 C). Hence, the layer thicknesses and velocity gradients can be varied laterally. Interfaces must be consistent along the entire profile length. Crossing interfaces are not allowed, but for layers that terminate between the start and end of the profile a 'pinch-out' can be realized, either on the interface to the top or to the bottom.

The uppermost layer (#1) is the water column bounded to the top by the sea-surface and the topography of Sardinia in the western part of the profile. The base of the layer is constrained by the seafloor topography. This interface is forced to pinch out, so that the layer has zero thickness at the onshore region to the west. Topography and bathymetry data are extracted from a global grid (Smith and Sandwell, 1997) and the multibeam echo sounder data collected during the seismic survey. The node spacing is 750 m sampling the rough topography sufficiently. The layer below the water column is the sedimentary post-rift cover (#2). The fine-scale distribution and geometries of these deposits, as well as the interval velocities are well constrained by the prestack-depth migrated sections and integrated directly into this starting model. The p-wave velocities (Vp) are set to 1.7-1.8 km/s at the top of the layer and to 2.0 km/s at its base. This layer is not varied during modelling. Coordinates of OBH and land stations are converted into "distance along profile" and represent the source points of rays travelling through the model. Subsequently, synthetic traveltimes are recorded at the sea-surface. The parameter defining the accuracy of the ray trajectory was set to 10 m (ray-step-length).

The strategy for developing a smooth velocity-field begins by adjusting carefully the traveltimes of the direct wave to avoid error propagation. Afterwards arrivals of P_{g1} phases are modeled in order to match synthetic with observed arrival times. Successively, all deeper refracted arrivals are modeled. The preliminary depth of the crust-mantle boundary (Moho) is found by fitting P_mP wide-angle reflections.

The fit of the synthetic traveltimes (thin black lines in Fig. 4.7) and the observed seismic phases are presented in B. The widths of the traveltime picks on the time-scale represent the pick-uncertainty as listed in Table 4.1. Fig. 4.7 A shows the ray coverage within the forward model. The crust and the Moho is well covered between km 120 and km 320. However, at places where the topography is complex, for instance where a large block forms a topographic high adjacent to a deep sediment filled graben, first arrivals of P_{g1} phases are partly difficult to model. Here, synthetic traveltimes deviate significantly from the observed traveltimes. This is probably related to the strong lateral velocity contrast between sediment and basement rocks. Late arrivals of P_mP reflections and P_n mantle-phases are less sensitive to the upper structures and fit well the observed traveltime picks.

The final result of the forward modelling is shown in Fig.4.7 C. Beneath the post-rift sedimentary deposits, Vp increases from 3.5-4.0 km/s to 5.9-6.1 km/s at a depth of 5-6 km below the sea-surface (layer #3). This accords to an upper crustal gradient of ~0.8 s^{-1} to 1 s^{-1}. In the middle and lower part of the crust (layer #4+5), Vp increases from 6.1-6.5 km/s at a depth of 8 km to 12 km. The gradient is ~ 0.1 s^{-1}. Vp values at the base of the crust increase to ~6.7 km/s and are mainly constrained by P_mP reflections. Furthermore, P_mP wide-angle reflections help to constrain the depth of the Moho. In the forward model the Moho is located at a depth of ~14-16 km below the sea-surface. Beneath the coastal area of Sardinia, it is located at a depth of ~24 km. Vp in the uppermost mantle is determined by P_n arrivals recorded by the three land stations. First arrivals of the P_n can be identified up to an offset of ~300 km. To model these arrivals, Vp was set to a constant value of 7.9 km/s beneath the Moho interface. As a gradient is needed to generate turning rays, Vp was set to 8.6 km/s at a depth of 50 km.

The Vp-distribution obtained in the upper and middle part of the crust (layer #2+3) is integrated in the velocity-field that has been used for migration of MCS data (Chapter 3).

4.3. Tomographic inversion

TOMO2D includes a hybrid forward ray-tracing algorithm and allows to invert jointly for seismic refraction and reflection arrival-times to obtain a refined 2-D velocity structure (Korenaga et al., 2000). Input for this code are the traveltime picks of refracted and reflected arrivals and the result of velocity modelling from the forward approach using *Rayinvr* (Fig.4.7 C).

4.3.1. Hybrid forward approach

The hybrid forward ray-tracing approach in *TOMO2D* (Korenaga et al., 2000) is based firstly on the graph-method and secondly on the refinement of the ray-trajectory by the ray-bending method. This combination is efficient in memory and computation time. It allows the accurate calculations of traveltimes and ray paths from source to receiver. The graph method is also known as the shortest path method. It computes the shortest connection from a starting node to the surrounding nodes by a given forward-star. Translated to a propagating seismic wavefront or ray, the shortest path is the path with the minimum traveltime as related to Fermat´s principle. The disadvantage of this method is, that traveltimes can be overestimated. This occurs, because the number of nodes, respectively the accuracy of the mesh, is limited and the length of the ray path could be too long. Therefore, the ray-bending method (Moser et al., 1992) is applied to refine the graph solution by minimizing the traveltime along the ray path.

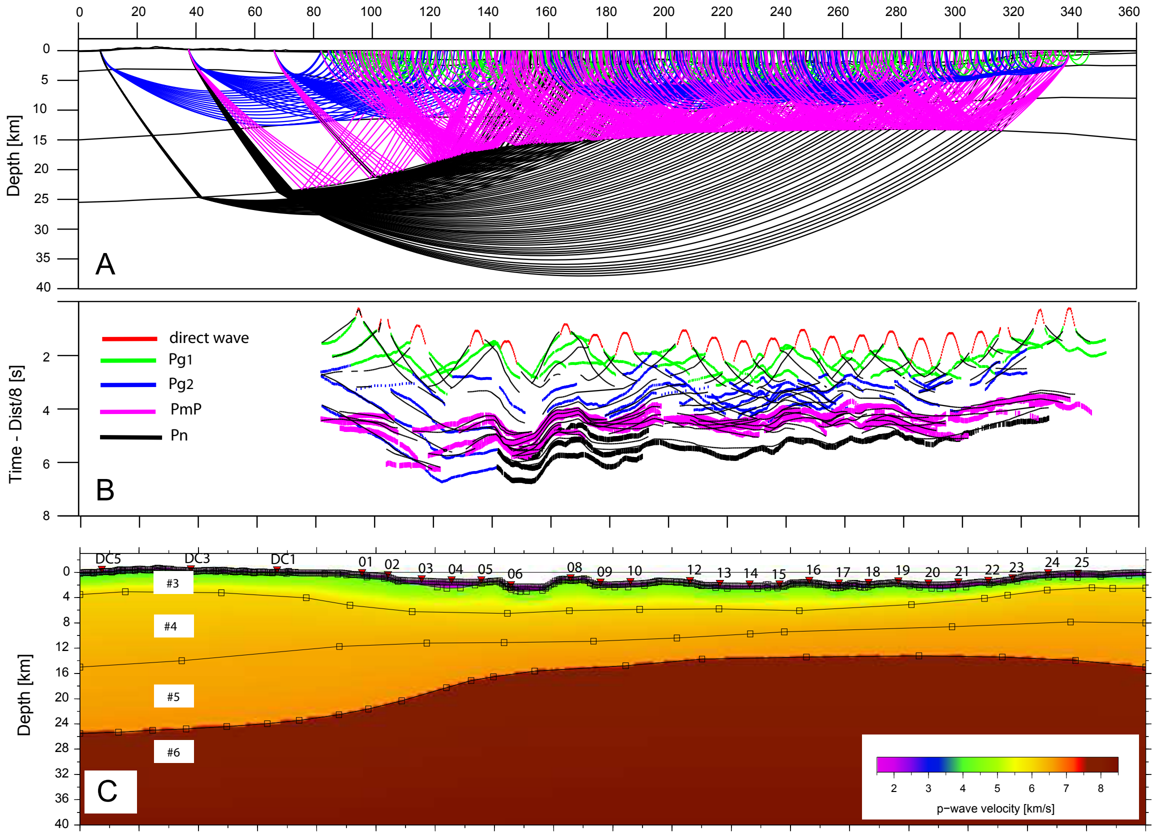

Figure 4.7.: Raypaths through the final model after forward modelling (A). In B the fit of the observed traveltimes of different seismic phases (colored) and the calculated arrival times (thin black lines) are presented. C shows the final velocity model built up by different layers.

4.3.2. Inverse method

The inversion process which is implemented into *TOMO2D* can be mathematically described as follows (Korenaga et al., 2000):
An initial velocity model is assumed, which is disturbed and does not fully satisfy the traveltime picks observed in the real data. The resulting traveltime residuals δT_j for synthetic refracted rays travelling through the model is expressed by the slowness perturbation δu along the ray path Γ_j by the following path integral:

$$\delta T_j = \int_{\Gamma_j} \delta u d\Gamma \tag{4.6}$$

Furthermore, the traveltime residual of a reflected ray can be expressed by equation 4.7.

$$\delta T_j = \int_{\Gamma_j} \delta u d\Gamma + \left.\frac{\partial T}{\partial z}\right|_{x=x_j} \delta x(x_j) \tag{4.7}$$

Here, x_j is the reflection point of the jth ray. The equations 4.6 and 4.7 are combined and expressed by the following matrix equation:

$$d = G\delta m \tag{4.8}$$

In 4.8, d is the traveltime residual vector and G the Fréchet derivative matrix. δm represents the vector containing the unknown model perturbations. This matrix equation is the base of the travel time tomography as implemented in *TOMO2D* (Korenaga et al., 2000). It represents a linearized system that is iteratively applied, until convergence of the model is reached. This is expressed in RMS traveltime misfit or the χ^2 value. Within the Frechét matrix G, the velocity sensitivity part are the path lengths of the rays, distributed between the bilinear interpolated velocity field. Furthermore, for the depth part, the matrix includes the incident angle of rays, the reflector dip and the velocity at a certain reflector point. The uncertainties of the observed traveltime picks are included in the covariance matrix which is part of the normalized expression for G and δ_m of equation 4.8. The normalized and regularized linear system of 4.8 is:

$$\begin{pmatrix} d \\ 0 \\ 0 \\ 0 \end{pmatrix} = \begin{pmatrix} G_v & wG_d \\ \lambda L_{Hv} & 0 \\ \lambda L_{Vv} & 0 \\ 0 & w\lambda_d L_d \end{pmatrix} \begin{pmatrix} \delta_m v \\ \frac{1}{w}\delta m_d \end{pmatrix} \tag{4.9}$$

Within this matrix equation, v and d represent the velocity and depth matrix components. L_{Hv} and L_{Vv} are matrices, that contain correlation lengths to apply horizontal and vertical smoothing for slowness perturbation. λ_v and λ_d are factors that control the weighting of the smoothing parameters. L_d is the smoothing matrix for depth perturbations. Smoothing is generally important for stabilizing the inversion process and to avoid singularities. The factor w is called 'depth kernel weighting' parameter. It adjusts the relative weighting of depth sensitivity in the Fréchet derivative matrix G. If $w = 1$, depth and velocity nodes are equally weighted. Increasing the value for w leads to larger depth perturbations and smaller velocity perturbations. After finding the final model, this can be exploited to evaluate the degree of velocity-depth ambiguity (Bickel, 1990; Korenaga, 2011). The matrix equation is efficiently solved by using the sparse matrix solver LSQR. This algorithm has been developed by Paige and Saunders (1982) and is implemented in *TOMO2D*. Data with too large residuals, that represent outliers, are removed and damping constraints for velocity D_v and depth nodes D_d are implemented in the code. This avoids further instabilities for subsequent iterations during the inversion process. Large residuals may occur, if the velocity model is too far away from the true model (Korenaga et al., 2000). With the additional damping matrices, the regularized system 4.9 becomes:

$$\begin{pmatrix} d \\ 0 \\ 0 \\ 0 \\ 0 \\ 0 \end{pmatrix} = \begin{pmatrix} G_v & wG_d \\ \lambda L_{Hv} & 0 \\ \lambda L_{Vv} & 0 \\ 0 & w\lambda_d L_d \\ \alpha_v D_v & 0 \\ 0 & w\alpha_v D_v \end{pmatrix} \begin{pmatrix} \delta_m v \\ \frac{1}{w}\delta m_d \end{pmatrix} \tag{4.10}$$

α_v and α_d are weighting factors controlling the damping. The effect of different weighting parameters for smoothing and damping (α and λ) and the correlation length are tested during several runs of tomographic inversion.

4.3.3. Modelling strategy and parameterization tests

The input velocity model for *TOMO2D* is constrained by the land- and seafloor topography to the top. It is realized as a sheared mesh grid below the topography. Nodal spacings are variable in both dimensions and bilinear interpolation is applied to cells, resulting in an continuous velocity-field. It is suggested by Korenaga et al. (2000), that the spacing is finer than the expected velocity variations because a coarse grid may result in an inaccurate solution by the graph method. After several tests, the final horizontal grid-cell size is fixed to 200 m. This cell-size is fine enough to include small-scale variations of a rough basement topography beneath the sedimentary cover sufficiently. In the vertical dimension, the cell-size is set to 100 m below the seafloor and increases to ~750 m at a depth of 45 km within the preliminary upper mantle. The increase is controlled by the following equation:

$$d_z = 0.1 + \sqrt{0.01 * z} \qquad for \quad z = 1, 2, 3, ..., 45 \tag{4.11}$$

The choice of the cell-size is also appropriate regarding the expected structural vertical and horizontal resolution. Assuming Vp of ~4.0-5.0 km/s for the upper part of the basement and the dominant frequencies f of 8-15 Hz, the vertical resolution is ~70-150 m using the approximation $\frac{Vp}{4f}$. Horizontal resolution is restricted by the aperture D of the first-order Fresnel-Zone which can be approximated by (Sheriff, 1980)

$$D \approx \sqrt{2z\frac{Vp}{f}} \tag{4.12}$$

Here, z is the depth to the target. Assuming again Vp of ~4.0-5.0 km/s within the upper basement, the horizontal resolution would be limited. For instance, the resolution beneath a thin sedimentary basin of 200 m thickness, would be ~300-500 m.
The preliminiary Moho is implemented as a floating reflector as it has been previously modeled in the forward approach using *Rayinvr*. The horizontal resolution at frequencies of 4-8 Hz can be expected to be ~5000-7000 m, assuming the Moho is located at a depth of 15 km and the velocity within the lower crust is 6.8 km/s. Nodes of the floating reflector are re-sampled by a spacing increment of 0.5 km.
The strategy is to invert first for seismic phases that travel through the upper crustal structures (P_{g1}). Progressively, all deeper phases are included and jointly inverted. The number of iterations are set in a way, that convergence is reached when the difference to the iteration prior is less then $\sim$ 1 ms. For inverting secondary seismic phases, like the P_n phases on line CD and the $P_{im}P$ phases on line AB, the crustal domain is additionally damped. Thus, the update of the velocity model is mainly limited to these specific areas.

Parameter tests

Parameters for inversion have to be suitable, so that the final velocity model explains the observed traveltimes sufficiently. Moreover, the velocity distribution has to be reliable in a geological sense. Therefore, tests for the different parameters that control the inversion process are carried out. Especially the interaction between the values for the correlation lengths and the four parameters for smoothing and damping are tested and evaluated. The depth kernel weighting factor is set to $w = 1$ during these tests. Hence, inversion for velocity and depth nodes are balanced. The following labeling of parameters is consistent with the nomenclature used in the manual for *TOMO2D* (Korenaga, 2003):

- L_{h_t}, L_{h_b} - horizontal correlation length of velocity nodes at the top and bottom of the model

- L_{v_t}, L_{v_b} - vertical correlation length of velocity nodes at the top and bottom of the model

- L_{h_R} - horizontal correlation length of reflector nodes

- SV, SD - weighting factors for velocity and depth smoothing
- DV, DD - weighting factors for velocity and depth damping
- w - depth kernel weighting factor

These parameters are tested in combination with finer and coarser cell sizes. The initial test-model for tomographic inversion has a cell size of 500 m in horizontal direction and 50 m in vertical direction. Horizontal correlation lengths are set to L_{h_t}= 3 km and L_{h_b}= 10 km. Vertical correlation lengths are set to L_{v_t}= 1 km and L_{v_b}= 5 km. The correlation length of the floating reflector is set to L_{h_R}=10 km. Weighting factors for smoothing (SV, SD) and damping (DV, DD) are set to 50/30 and 30/30, respectively. After inversion of P_g and P_mP phases the model reveals a velocity structure containing artifacts which are not reliable to explain the nature of the crust. Therefore, the correlation lengths are increased to 4 and 10 km horizontally and 2 and 5 km vertically in order to increase the smoothness of the model. Other parameters are kept fixed to evaluate the effects of the correlation lengths. However, the tomographic inversion results in a model evolving not far from the initial model. RMS-residuals for Pg- and PmP-phases exceed 150 ms. These initial tests show the influence of the correlation length regarding the smoothness of the model.
More than 40 different models were tested to find appropriate parameters. The best results for the velocity models of both lines are obtained by using a fine velocity grid, small correlation length and a high value for horizontal smoothing (weighting factor SV). The parameters used for the final tomographic model are listed in Table 4.2

Seismic Phase	L_{h_t,h_b} [km]	L_{v_t,v_b} [km]	L_{h_R} [km]	SV	SD	DV	DD
P_{g1}	1/5	0.75/2	-	160	40	30	20
P_{g1}+P_{g2}	1/5	0.75/2	-	170	40	30	20
P_{g1}+P_{g2}+P_mP	1/5	0.75/2	5	170	40	30	20
P_{g1}+P_{g2}+P_mP+P_n	1/5	0.75/2	5	170	40	30	20

Table 4.2.: Parameters used in tomographic inversion leading to the final velocity models of both seismic lines. The cell size of the model is constantly 0.2 km in horizontal direction and 0.1 km at the top of the model in vertical direction. Vertical cell size increases as given by equation 4.11.

4.4. Results

Figure 4.8 shows the evolution towards the final model by including the different phases step by step. In (A) the initial velocity model obtained from forward-modelling is shown. The forwards model contains a priori information of the upper sedimentary

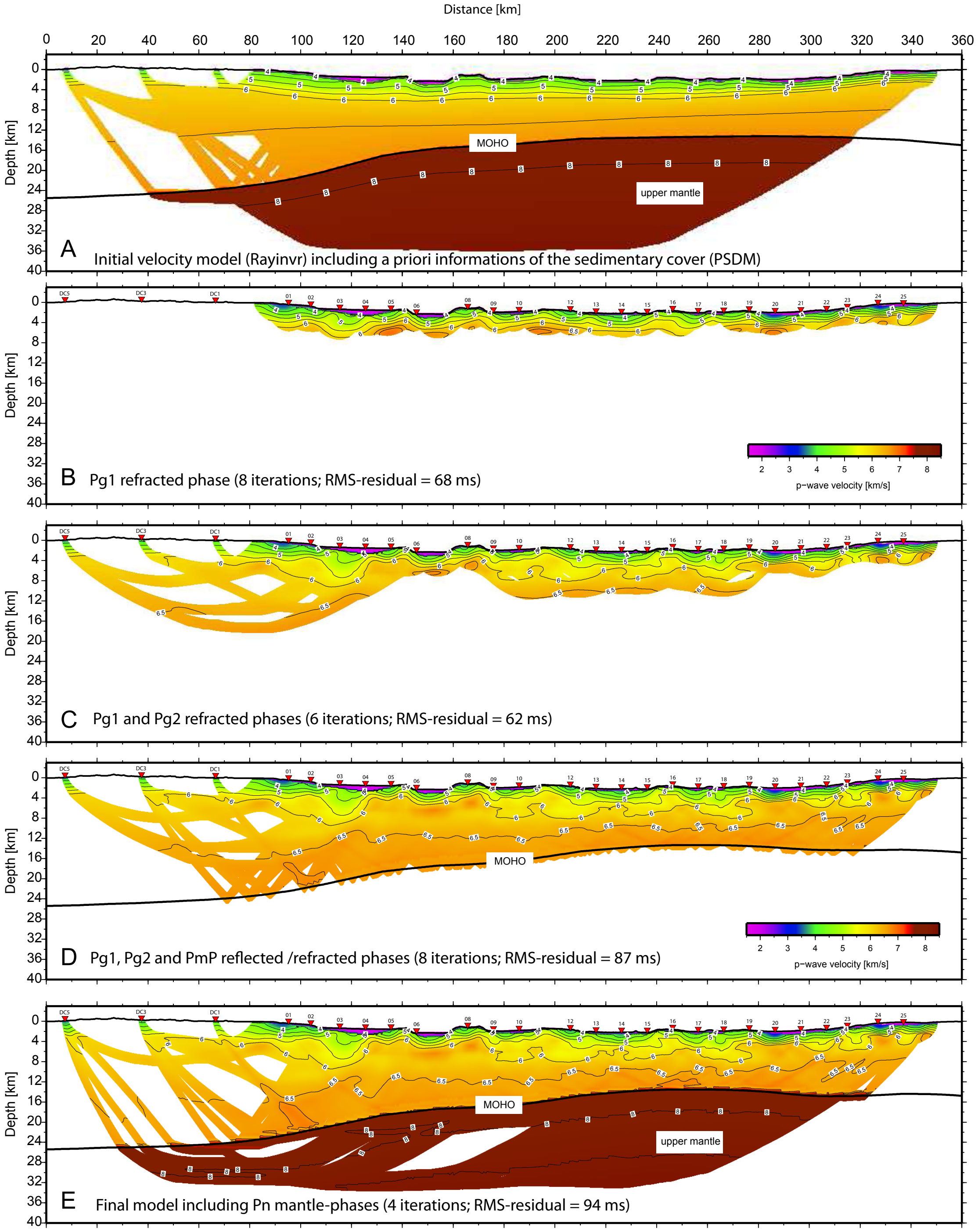

A Initial velocity model (Rayinvr) including a priori informations of the sedimentary cover (PSDM)

B Pg1 refracted phase (8 iterations; RMS-residual = 68 ms)

C Pg1 and Pg2 refracted phases (6 iterations; RMS-residual = 62 ms)

D Pg1, Pg2 and PmP reflected /refracted phases (8 iterations; RMS-residual = 87 ms)

E Final model including Pn mantle-phases (4 iterations; RMS-residual = 94 ms)

Figure 4.8.: Seismic phases are progressively included into tomographic inversion. (A) is the initial model that is achieved by forward-modelling. B-D shows the evolution of the model from top to bottom. Spacing of iso-velocity contour lines is 0.5 km/s in the crustal domain and 0.2 km/s in the upper mantle.

structures as imaged in the PSDM section. Iterative inversion of P_{g1} phases updates the initial velocity model and improves the resolution of fine structures within the upper crust. The RMS-residual after 8 iterations is 68 ms. After that, P_{g2} traveltimes (B) are included and unravel deeper crustal regions. Below Sardinia, the crust is revealed up to a depth of 16 km (RMS-residual of 62 ms). A significant update of the upper structure, that is determined before by P_{g1} rays, is not observed. This can be seen as an indicator for well resolved upper structures and accurate picking. After inversion of all crustal phases both, refracted and reflected arrivals, the structure of the entire crust is determined. The lower part of the crust is sampled by inverted rays of P_mP wide-angle reflections and not by refracted (turning) waves, because the velocity gradient is too low for deeper penetration. Vp in the uppermost mantle is determined by P_n phases recorded by the landstations.

A detailed description of the velocity structures for both lines can be found in chapter 6 and 7 (paper 1 and paper 2).

4.4.1. Resolution and uncertainties

The resolution of seismic data is an interaction between survey geometry, frequency content and the signal-to-noise ratio of the seismic signals. However, in a velocity model after tomographic inversion, the resolution is not only limited by the latter factors. The cell-size of the model and the ray-coverage play an important role. In areas where the coverage is poor, the model might be affected by velocity-depth ambiguity.

To evaluate the resolution and the uncertainties of the velocity models, the standard deviation is calculated and a checkerboard test carried out. Moreover, the influence of velocity-depth ambiguity is investigated.

Velocity standard deviation

For estimating uncertainties in the velocity model, a range of perturbed starting models is generated from the initial forward-model that lead to the final inverted model. Uncertainty tests have been carried out without inverting for P_n arrivals, because the control of the mantle velocities is difficult due to the absence of crossing rays.

In a first group of velocity models, the depth of the Moho is varied by ± 1,2 and 3 km to check if the depth of the discontinuity converges towards the reflector-depth as determined in the final model. In a second set of perturbed models, Vp is increased and decreased by 5%. Perturbation to the sedimentary cover has not been applied, because Vp is well constrained by the PSDM section. A third set of models is a combination of ± 5% velocity and ± 3 km Moho perturbation. This allows to check for convergence of the (floating) Moho discontinuity and the remaining Vp uncertainties.

Two of these four perturbed starting models are shown in Figure 4.9. (A) is the starting model in which Vp is decreased and the Moho is shifted constantly down by 3 km. The result after 8 iterations (B) including all phases, depicts that Vp in the upper and middle part of the crust tend towards the final model. However, the RMS-residual of 105 ms is worse, compared to the traveltime residual of 87 ms remaining in the final model (Fig. 4.8 E). To some extent, the higher residuals might be related to the lower part of the crust which has not been significantly updated. The reason is, that the lower crust is just constrained by the P_mP reflections as indicated by the derivative weight sum (DWS). The DWS is a measurement of rays travelling through each cell (Korenaga et al., 2000) and is shown in Fig. 4.10. The depth of the Moho in this model is shifted towards the previous position. Thus, it can be assumed that the depth error is less than +3 km.

The model with fast (5%) crustal velocities and a Moho shifted 3 km upwards is shown in (C). The inverted model (D) shows significantly decreasing values for Vp, with a tendency towards the velocities that are revealed in the final model. The RMS-residual is even similar. Again, the only exception is the Vp distribution determined within the lower crust which is not significantly updated. The depth of the Moho is shifted back to the original position due to the traveltime of the P_mP reflections.

By including all perturbed and additional models that are close to the final model during parameter testing, an average model is calculated. It allows computing the standard deviation for velocity and Moho depth of the models. For the line CD the standard deviation is shown in Fig. 4.9 and discussed in chapter 6. Uncertainties of the line AB are discussed in chapter 5.

Checkerboard test and DWS

The aim of the checkerboard test is to evaluate the size of structures that can be effectively resolved in the velocity model after tomographic inversion. The test has been carried out as follows: First, a checkerboard pattern with velocity variation of ±10% is added to the final velocity model. For the first test, the dimensions of a single rectangular are set to 5 km x 2.5 km in horizontal and vertical direction, for a second test to 10 km x 5 km, respectively. Subsequently, rays are traced trough the perturbed model. The new synthetic traveltimes are now disturbed by the added checkerboard pattern and used for another inversion with the initial velocity model applying the same parameterization. In an ideal case, assuming a theoretical full resolution, the checkerboard pattern should be recovered after inversion. However, this is not expected due to limitations of the resolution power as well as the influence of smoothing and damping.

The results for both patterns are shown in Figure 4.10. In (A) the pattern is clearly recovered in the upper 3-5 km of the crust, although smearing effects occur at the transitions to neighboring patterns. In this part of the crust, it can be assumed that the model is able to resolve a structure with dimension of at least the size of a rectangular. At the onshore part of Sardinia, where the crust is not constrained by crossing rays, the checkerboard pattern cannot be recovered. The derivative weight sum (DWS), representing the ray coverage, shows in (C) that the upper 3-5 km of the crust is the

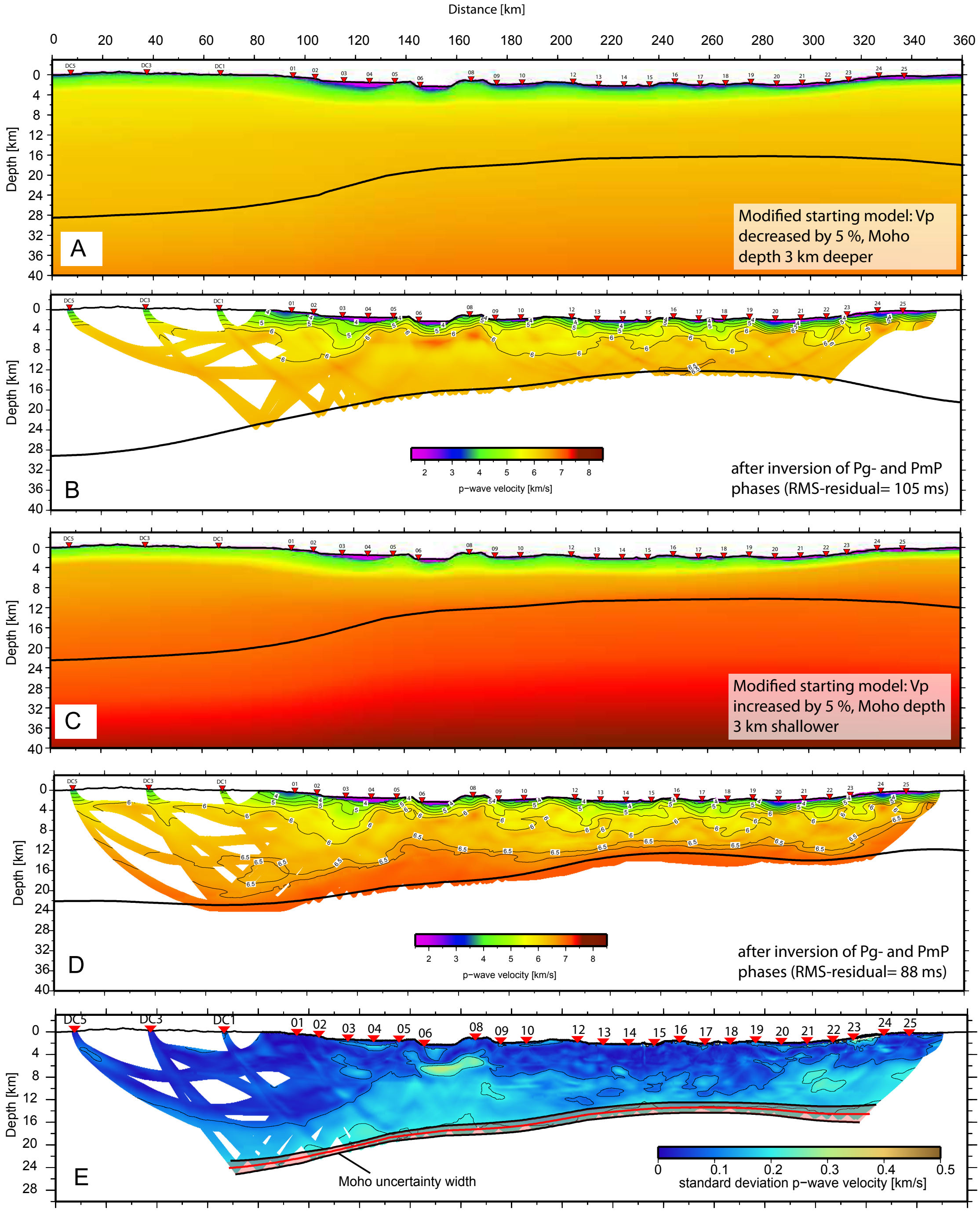

Figure 4.9.: Two examples of a set of perturbed starting models. (A) shows a model with too low velocities and a deeper Moho. A model too high and a shallower Moho is shown in (C). (B) and (D) are the resulting models after tomographic inversion. (E) shows the standard deviation of velocities and Moho depth for the line CD.

best covered region along the profile. Beneath this depth, structures smaller than the used checkerboard pattern cannot be accurately resolved and smearing effects occur. The only exception is the area in the centre of the profile (km 200-280), where the crust is thin and the ray density is higher than at adjacent regions to the west and to the east (see DWS in C).

The recovery of larger checkerboard patterns (Fig. 4.10 B) indicates, that structures within the lower crust are, to some extent, just recovered in the center of the profile (km 200-280). This is related to P_{g2} phases, travelling through the lower part of the crust, because the velocity gradient is higher than in the surrounding lower crust. Structural resolution within the upper mantle is not possible.

The evaluation of the checkerboard test and the DWS indicates a direct relation between the resolution power and the number of crossing rays passing each cell. At the margins of the profile and in the deeper regions, ray density is less. Here, smearing effects occur and do not allow to resolve particular structures.

Depth kernel weighting

Velocity-depth ambiguity states that the true depth of a reflection point cannot be determined exactly, if the velocity is erroneous. Either, its origin is located at shallower levels if the velocity in the layer above is estimated too slow, or it is located at deeper levels if the velocity above is estimated too high. Korenaga (2011) investigated this relationship by varying the depth kernel weighting factor and found that the degree of velocity-depth ambiguity depends on how good an area is constrained.

Here, two end members for a high ($w = 100$) and a low value for w ($w = 0.01$) are investigated. A high value for w leads to an inversion being more sensitive to depth nodes. For low values, model updates are mainly restricted to velocity nodes and not to depth. In an ideal case, these two end-members model would not show significant differences if the velocity model corresponds to the true model.

The result after inversion using $w = 100$ (Fig. 4.11 B) shows small differences compared to the final model (A). The depth of the Moho and iso-velocity contours has not changed noticeable. The model represents rather a smoothed version of the final model, because small-scale velocity variations are attenuated.

The model in (C) shows the results using $w = 0.01$. In the uppermost crust the model does not reveal large-scale differences compared to the result of the final model. In the lower crust larger variations between 6.5 km/s and 6.7 km/s are observed. This result shows again, that velocities in the lower crust are not as good determined as in the upper crust. It is directly related to the fact, that velocities in the lower crust are mainly resolved by P_mP reflections. The velocity-undulations correlate to some extent with the areas of higher velocity uncertainty ($\sim$0.2 km/s).

Concluding this analysis, a velocity-depth ambiguity is restricted to the lower part of the crust. The upper and middle crustal domains are well covered by refracted arrivals and therefore a possible velocity-depth ambiguity minor.

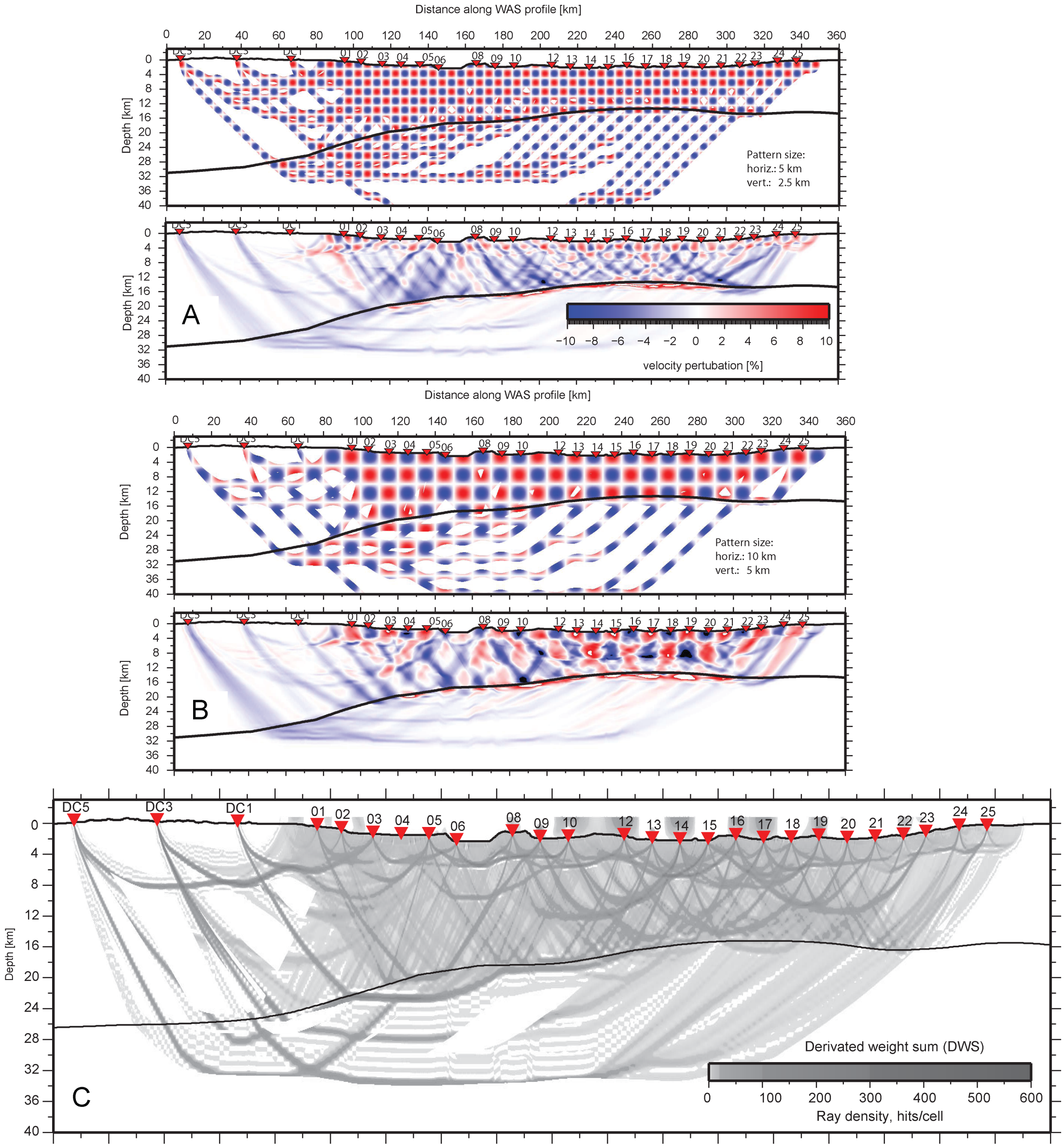

Figure 4.10.: (A) and (B): Checkerboard tests for two different patterns indicate the quality of structural resolution.(C) shows the derivative weight sum (DWS) which represents the ray density of the model.

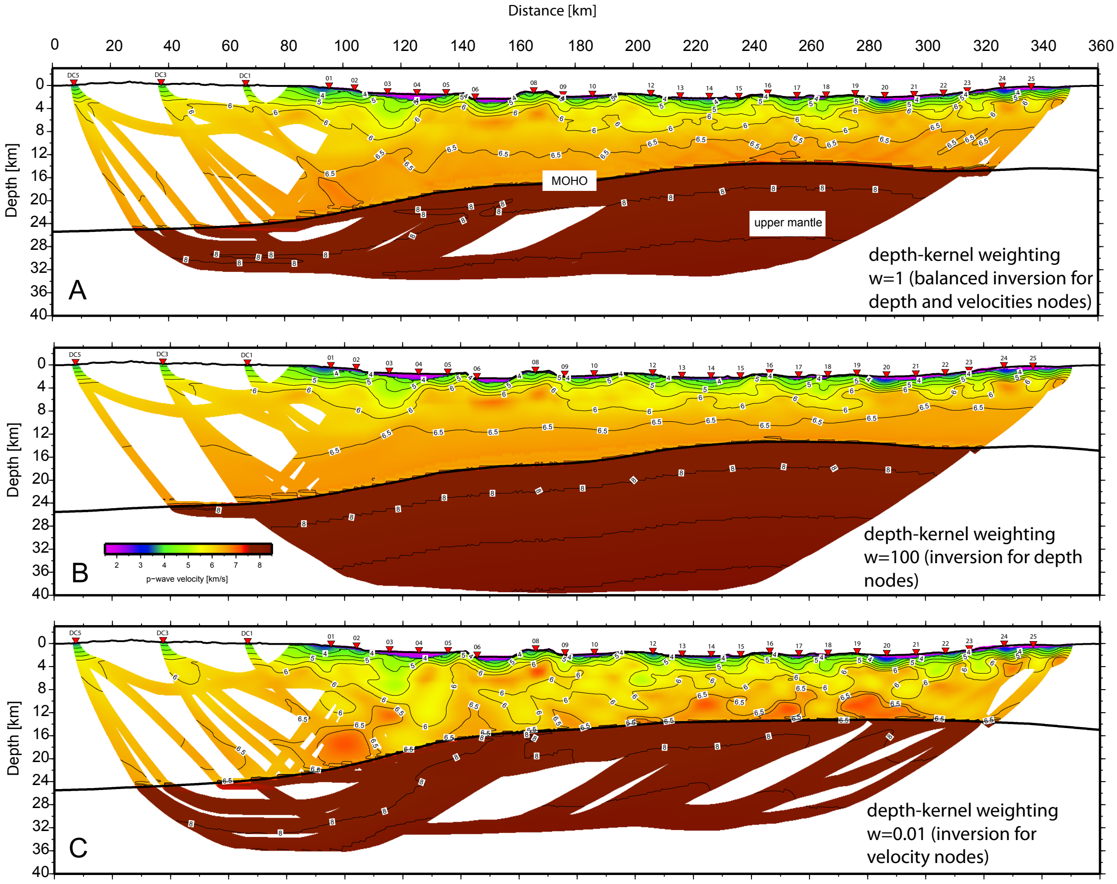

Figure 4.11.: (A) shows the final model with a balanced factor ($w = 1$) inverting for depth and velocity. Two end-member for a low and high depth kernel weighting factor are shown in (B) and (C). Note that the model with a high value for w represents a smoothed version of (A). In (C) noticeable velocity variations are restricted to the lower crust, which is just covered by P_mP wide-angle reflections.

5. Early-stage rifting of the northern Tyrrhenian Sea Basin

Manuscript 1: Early-stage rifting of the northern Tyrrhenian Sea Basin Results from a combined wide-angle and multichannel seismic study

Authors: Moeller, S.[1], Grevemeyer, I.[1], Ranero, C.R.[2], Berndt, C.[1], Klaeschen, D.[1], Sallares, V.[3], Zitellini, N.[4], de Franco, R.[5]

1. GEOMAR Helmholtz Centre for Ocean Research Kiel, Kiel
2. Barcelona Center for Subsurface Imaging, ICM, ICREA at CSIC, Barcelona
3. Barcelona Center for Subsurface Imaging, ICM, CSIC, Barcelona
4. Istituto Scienze Marine ISMAR-CNR, Bologna
5. Istituto per la Dinamica dei Processi Ambientali, CNR, Milan

This manuscript has been accepted for publication in *Geochemistry, Geophysics, Geosystems (G-Cubed).* It contains an own reference list.

Abstract

Extension of the continental lithosphere leads to the formation of rift basins and ultimately may create passive continental margins. The mechanisms that operate during the early-stage of crustal extension are still intensely debated. We present the results from coincident multichannel seismic and wide-angle seismic profiles that transect across the northern Tyrrhenian Sea basin. The profiles cross the Corsica Basin (France) to the Latium Margin (Italy) where the early-rift stage of the basin is well preserved. We found two domains, each with distinct tectonic style, heat-flow and crustal thickness. One domain is the Corsica Basin in the west that formed before the main rift-phase of the northern Tyrrhenian Sea opening (∼8-4 Ma). The second domain is rifted continental crust characterized by tilted blocks and half-graben structures in the central region and at the Latium Margin. These two domains are separated by a deep (∼10 km) sedimentary complex of the eastern portion of the Corsica Basin. Travel-time tomography of wide-angle seismic data reveals the crustal architecture and a sub-horizontal 15-17 ± 1 km deep Moho discontinuity under the basin. To estimate the amount of horizontal extension we have identified the pre-, syn-, and post-tectonic sedimentary units and calculated the relative displacement of faults. We found that major faults initiated at angles of 45°-50° and that the rifted domain is horizontally stretched by a factor of $\beta = 1.3$ (∼8-10 mm/a). The crust has been thinned from ∼24 to 17 km indicating a similar amount of extension (∼30%). The transect represents one of the best imaged early-rifts and implies that the formation of crustal-scale detachments, or long-lived low-angle normal faults, is not a general feature that controls the rift initiation of continental crust. Other young rift basins, like the Gulf of Corinth, the Suez-Rift or Lake Baikal, display features resembling the northern Tyrrhenian Basin, suggesting that half graben formations and distributed homogeneous crustal thinning are a common feature during rift initiation.

1. Introduction

The formation of rift basins and rifted margins by normal faulting and crustal thinning has many open questions. To contribute to the understanding of basin evolution, investigations of early-stage continental rift settings are important. Numerous studies have shown that the amount of fault displacement imaged on seismic cross-sections cannot easily explain the vertical crustal thinning estimated from wide-angle seismic studies. This phenomenon is known as the extension discrepancy (Artyushkov, 1990; White, 1990; Walsh et al., 1991; Reston, 2007). Another observation is that rifts seem to be asymmetric in extensional style. Symmetry is mostly absent, for instance at the young Gulf of Corinth (Bell, 2008), the North Sea rift (Lister et al., 1991) or at the conjugate margins of Newfoundland and Iberia (Shillington et al., 2006). It has been proposed that rifts become asymmetric by the role of low-angle normal faulting in the early stage (Bosworth, 1985), similar to the crustal-scale or lithospheric-scale simple-shear model (e.g. Wernicke, 1985). This model has been very popular to explain the structure of numerous conjugate rifted margins in an upper and a lower plate margin corresponding to the large-scale hanging wall and footwall blocks of the detachment. Slip on low-angle normal faults ($<30°$) or large detachments would generate a large amount of horizontal extension and might explain the extension discrepancy. However, the existence of such detachments is a matter of debate because these types of faults have not been observed in young rift settings with an initially normal thick crust. Allemand (1990) showed that the initial fault angle can be controlled by the thickness of the brittle layer and hence can be less than 60°. Buck (1993) suggested that low-angle faults initiated at steeper angles and subsequently rotated to shallower angles. Alternative explanations argue that extension is not well estimated because of the limited resolution of seismic data and hence smaller faults or a previous generation of faults contributing to the total amount of extension is unrecognized (Reston, 2007; Marrett & Allmendinger, 1992; Walsh et al. 1991). An alternative to these models is that much of the extension is not caused by large arrays of faults working simultaneously, but as extension progresses, strain localizes into a relatively narrow rift center via sequential faulting (Ranero and Pérez-Gussinye, 2010). The model proposes that individual successive faults cut crust that had been previously extended by earlier individual faults explaining the structure observed in West Iberia and Newfoundland conjugate margins. The model explains both the apparent horizontal extension and the formation of asymmetric conjugate margins by simple Andersonian faulting at 65°-55° and rotating to 45°-30° as observed in seismic images. Sequential fault activity has also been observed in some young rift settings e.g., the Suez-Rift (Gawthorpe et al., 2003).

In this study, we have prestack depth migrated and interpreted a 190 km long multichannel seismic reflection line (MCS) and modeled a coincident 240 km long wide-angle seismic (WAS) profile across the northern Tyrrhenian Sea Basin to investigate the relationship between faulting, crustal thinning and basin formation in an early-stage of continental extension. From the MCS images we determined the geometry of syn- and post-tectonic sediment and infer the evolution of rift structures.

2. Tectonic framework and bathymetric features

The Tyrrhenian Sea is the youngest extensional basin in the Western Mediterranean Sea (Kastens et al. 1988) bounded by Corsica and Sardinia in the west, the Italian peninsula to the east and north and by Sicily to the south. Subduction of the Tethys Mesozoic oceanic lithosphere underneath the European plate commenced during the late Cretaceous (Faccenna et al., 2001; Jolivet et al., 1999) and triggered the episodic opening of several back-arc basins in the Western Mediterranean Sea due to the rollback and subsequent bending of the trench axis (Faccenna et al., 2001). The formation of extensional basins began along southern France and Iberia with the separation of the Balearic block and of Sardinia and Corsica from continental Europe coupled with the opening of the Gulf of Lion and the Valencia Trough in the Oligocene ~30 Ma ago (Rosenbaum et al., 2002; Cherchi and Montadert, 1982). Post-Oligocene (21-16 Ma; Faccenna et al., 2001) rifting in the Gulf of Lion and in the Ligurian Sea continued and the Sardinia-Corsica block of European continental crust underwent a counter-clockwise rotation of 30°, subsequently colliding with the Adriatic foreland. From the Langhian to Tortonian, continental sediments started folding and thrusting and led to the formation of the N-S striking Apennine orogenic belt along the Italian peninsula. Moreover, volcanic rocks on Sardinia are believed to be a remnant volcanic arc of the subduction process east of Sardinia (Cherchi and Montadert, 1982). The eastward migration of the subduction zone led to the opening of the Tyrrhenian back-arc basin (Malinverno and Ryan, 1986; Rosenbaum et al., 2002). Rifting of the Northern Tyrrhenian basin segment started during upper Tortonian age (8-9 Ma) and ceased in Early-Pliocene (5 Ma) (Sartori, 1990; Rosenbaum et al., 2002). This is seen in the Tyrrhenian by the widespread presence of two major unconformities that mark the start and the end of rifting (Trincard and Zitellini, 1987).

To the southeast, rifting proceeded toward the Calabrian arc (Fig. 5.1A) with an increased gravity anomaly (Fig. 5.1 B). Here, a narrow but well-defined Wadati-Benioff seismic zone and volcanic edifices in the Aeolian region indicate the existence of a subducted slab (Faccenna et al., 2001; Malinverno and Ryan, 1986).

The northern portion of the Tyrrhenian basin between Corsica, the Latium Margin and south of Elba Island is the main focus of this study (Fig. 5.1). Based on the seafloor relief, the region is divided into two distinct areas: An area with relatively smooth topography that contains the Tuscany Archipelago and the flat Corsica Basin west of the islands and a second area to the south and east of the Corsica Basin that contains parallel N-S striking horst and graben structures across the center of the Tyrrhenian basin into the Latium Margin. The seafloor in the Corsica Basin is ~900 m deep whereas the bathymetry in the east ranges from 360 m on the ridges to 1700 m in the sediment filled grabens. The Corsica Basin is bounded to the east by the sedimentary Pianosa Ridge (A1 in Fig. 5.1). The island of Corsica consists of two parts: the Alpine part in the northeast and the Hercynian part in the southwest. These two parts are separated by the Solenzara-fault that bounds the Corsica Basin to the south (Fig. 5.1). The Pianosa

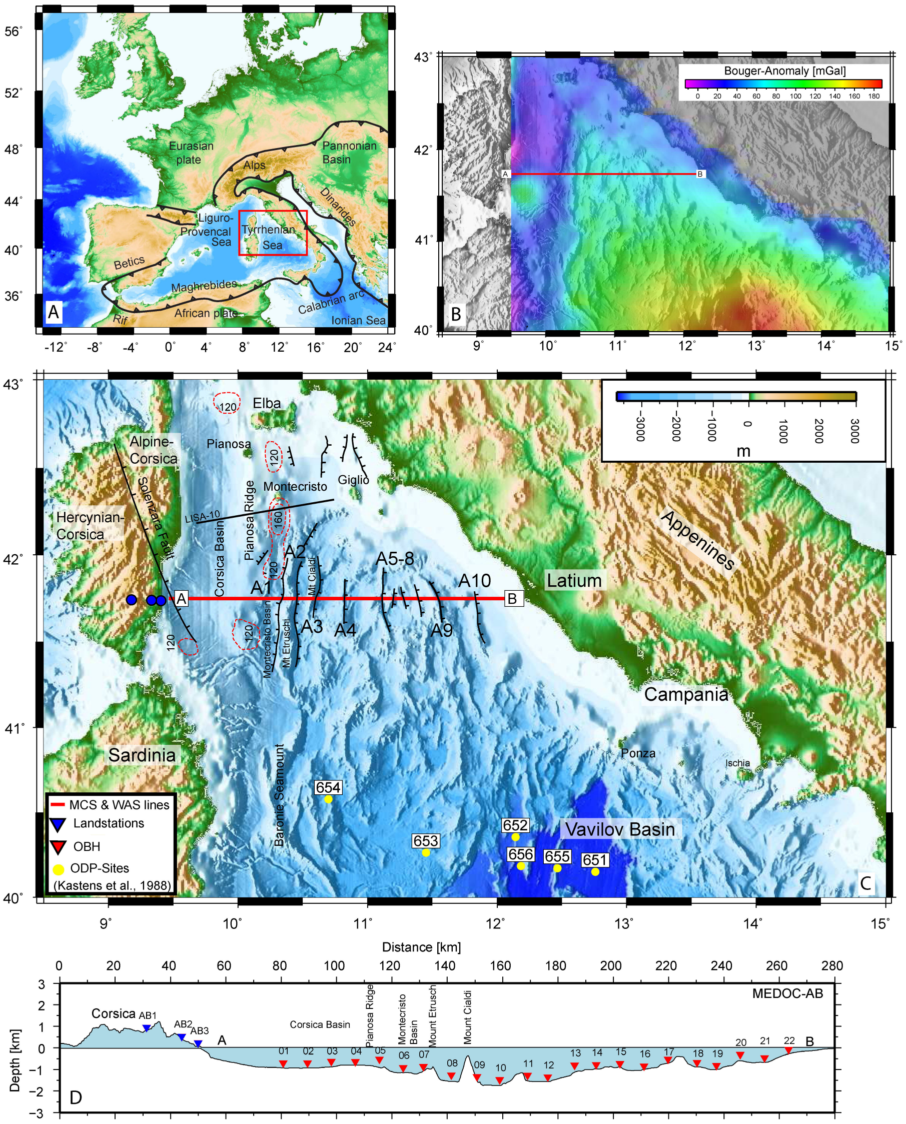

Figure 5.1.: A) The recent plate configuration of the Western Mediterranean region and central Europe (Schellart, 2010). The red box in the Tyrrhenian Sea defines the working area shown in B and C. B) The map shows the Bouger-Anomaly in the northern and central region of the Tyrrhenian Sea which is increasing towards the SE. C) The bathymetric map of the northern and central part of the Tyrrhenian Sea. The seismic transect (red line) crosses the main bathymetric rift features that are N-S orientated (Fig. 5.3 and 5.7). The ridges (blocks) are labeled from A1 to A10. Orientations of major normal faults along the seismic transect come from this study. Other fault orientations were taken from Mauffret et al. (1999). The black line (LISA-10) marks the location of a previous refraction experiment (Contrucci, 2009). Red dotted areas mark locations of high magnetic anomalies larger 120 nT (reduced to pole). Magnetic and gravity data is a courtesy of Getech UK. D) The cross-section shows the bathymetric features along the MEDOC-AB transect and the positions of the land- and OBH stations.

Ridge is associated with prominent magnetic anomalies probably related to magmatic intrusions (Mauffret et al., 1999), although the presence of an ophiolitic body may be another potential explanation (Fig. 5.1). More than 200 heat flow measurements have been carried out in the Tyrrhenian Sea out during the last decades (Della Vedova et al., 1984). The main feature in the Northern Tyrrhenian Sea is a regional trend from low heat flux values at the margin of Sardinia and Corsica ($50mW/m^2$), which is typical for old and cold continental crust (Della Vedova et al., 1984), to higher heat flow values of $100-150mW/m^2$ toward the margin of the Italian peninsula (Wang et al., 1989).

3. Seismic Data: Acquisition, Processing and Analysis

3.1 Acquisition

The new MCS and WAS data were acquired in the framework of the MEDOC project (El MEDiterráneo OCcidental) during a two-ship experiment in April and May 2010. 22 GEOMAR ocean-bottom-hydrophones (OBH) were deployed from the Italian vessel RV Urania for the wide-angle seismic experiment. The station spacing was 7-8 km. The Spanish vessel B/O Sarmiento de Gamboa provided additional ocean-bottom-seismometers (OBS) and fired shots every 90 s using an array consisting of 2 sub-arrays of 12 G.Gun II airguns with a total volume of $4600in^3$. In addition to the OBH stations, the profile was extended by using three land stations on Corsica (Fig. 5.1C). A coincident marine MCS line was acquired using a 3450 m, 276-channel streamer with a group interval of 12.5 m. The source was a $3040in^3$ G.Gun II array. The shot interval was 50 m, resulting in a common-mid-point (CMP) fold of 35.

3.2 Processing & Data Analysis

3.2.1 Refraction and wide-angle reflection seismic data

The wide-angle seismic data (WAS) recorded by the ocean-bottom-instruments were sampled at 4 and 5 ms in a continuous trace. Before and after recovery data loggers were synchronized with the GPS time signal to correct for internal clock drift. The data were cut into single receiver traces using the shot times and converted into SEG-Y format. The assumed position on the seafloor was corrected using the arrival times of the direct wave. To enhance the S/N ratio, a statistical deconvolution and a time- and offset-variant Butterworth filter were applied to the data. The deconvolution suppressed the reverberations of the airgun signal using a prediction lag of 0.23 s and an operator length of 1 s. The Butterworth-filter moves within four windows toward lower frequencies as time and offset increase. For the near offset traces the bandpass ranged from 4-35 Hz and at far offsets from 2.5-14 Hz.

Nearly all stations recorded data of good quality, except for OBH02 and OBH11 which failed to record any useful data. Record sections from OBH stations 03, 09 and 19 are presented in Figure 5.2. A sufficient S/N ratio allowed identification of first arrival crustal phases (Pg) between offsets of 30 and 120 km. First arrival branches in the near-offset, i.e. offsets less than 30 km, show Pg phases with rapidly increasing velocities correspoding to a high velocity gradient in the upper part of the crust. First arrivals with an offset larger than ∼30 km show that the velocity gradient at depth is smaller than in the upper part of the crust. A prominent secondary arrival between 40 and 80 km offset is interpreted as the wide-angle PmP reflection. The beginning of these high amplitude arrivals at 40 km offset is roughly the critical distance for reflections in the final tomographic model. Wide-angle PmP reflections are clearly observed on almost all OBH seismic records. Arrivals of refracted phases travelling through the upper mantle (Pn) at larger offsets cannot be identified. A late reflected arrival was recorded by stations OBH06 to OBH10 between 6-8 s and 60 to 80 km offset (see PimP at OBH09 in Fig. 5.2). These arrivals were first interpreted as PmP reflections, but during modeling it was clear that they do not fit well to reflections from the crust-mantle boundary. Rather, they appear to come from a deep and steep intra-mantle reflector.

Stations OBH01 to OBH05 are located in the western part of the profile at the Corsica Basin. Pg-phases travelling through the basin are relatively slow and indicate the presence of a thick sediment pile. Here, first arrivals can be observed up to offsets of 20-30 km. The seismogram of OBH05 (Fig. 5.2) is an example of a station at the Corsica Basin. It shows that the velocities in the near offset range to the east are slower than to the west. Seismic arrivals at the stations east of the Corsica Basin differ from those located at the basin. They recorded faster Pg phases and PmP reflections over offset-ranges up to 60 km. The influence of the lower velocities in the Corsica Basin at OBH09 is observed at ∼40 km offset to the west where the first arrival slope is steeper. The land stations on Corsica recorded arrivals just over a short offset range (40 - 60 km) and can only contribute to determining the sediment velocity structure in the Corsica Basin. The pick-uncertainties of the arrival times increase from 50 ms at near offsets to 100 ms at far offsets. These uncertainties also include phase changes and time-shifts related to filtering and predictive deconvolution. After phase identification and picking we used the forward modeling code Rayinvr (Zelt & Smith, 1992) to build a reference "best fit" p-wave velocity model that was subsequently refined by travel-time tomography. For this purpose we used the code tomo2D (Korenaga et al. 2000) that jointly inverts for travel-times of both refracted and reflected seismic phases. The seafloor and topography of Corsica was gridded at a spacing of 750 m. The velocity field was implemented as a sheared mesh grid with cells hanging below the seafloor topography. We chose a cell-size of 200 m in the horizontal and 100 m in the vertical direction increasing to 500 m at ∼30 km depth. To invert for PmP arrivals, the Moho is constrained as a floating reflector. The well determined geometry and velocities of the sedimentary sub-basins along the profile were adopted from the final depth-migrated MCS section and kept fixed during the forward modeling.

Our subsequent inversion strategy followed a downward stripping approach by first inverting for the upper crustal arrivals and then successively for all deeper crustal arrivals.

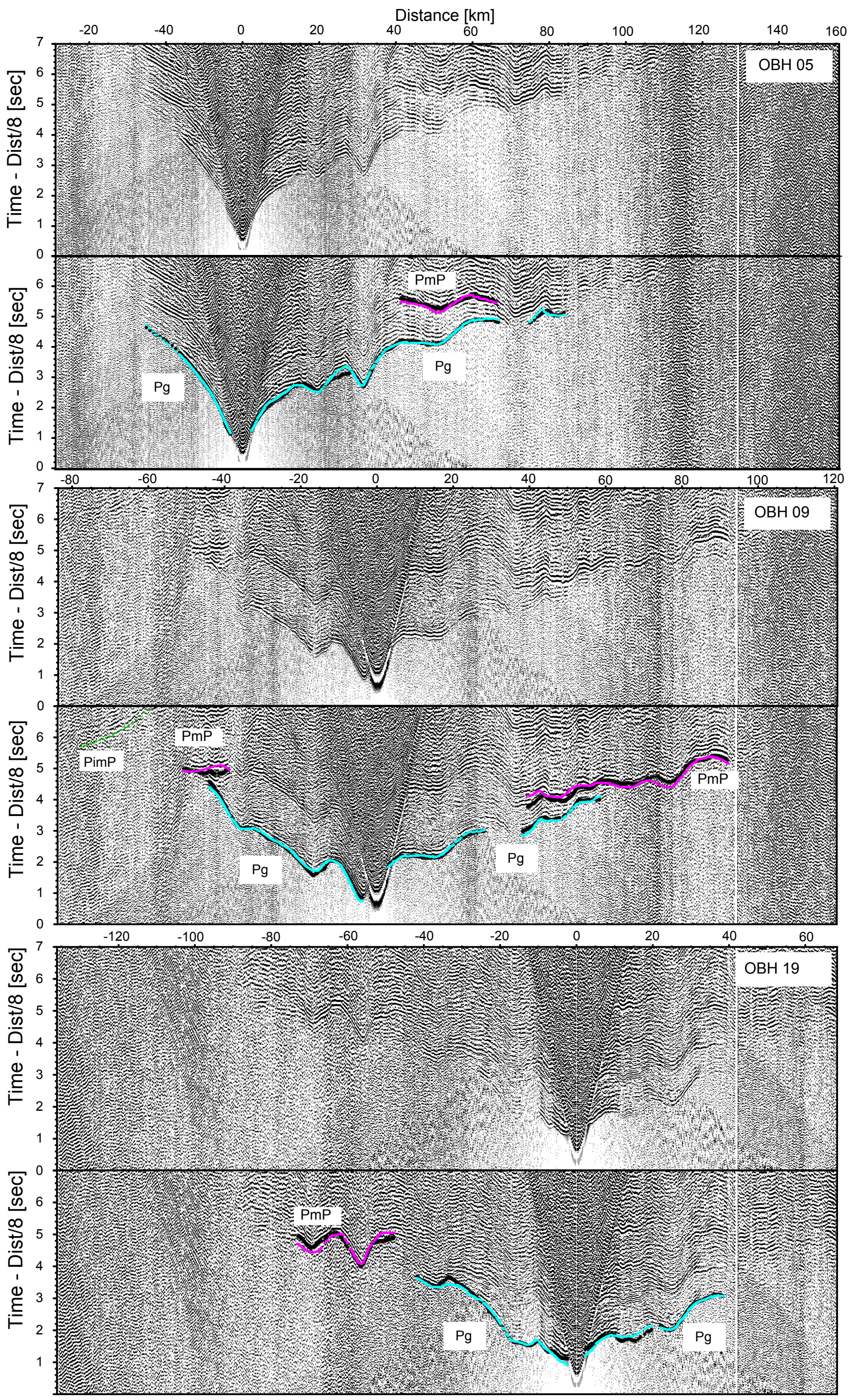

Figure 5.2.: Examples of record sections: A) OBH03 is located at the Corsica Basin (km 98). Slow arrivals of Pg phases indicate a thick sediment infill of the basin. B) OBH09 east of Corsica Basin (km 150). Velocities are faster in the east then in the west. PmP arrivals are observed over 40-60 km offset range. C) OBH19 at the eastern end of the profile (km 237). Black = picked arrivals ; purple, cyan and green = inverted arrivals

The effect of different smoothing and damping parameters as well as the interaction with the horizontal and vertical correlation lengths were tested for a broad set of parameters. The horizontal correlation lengths ranged from 1 km at the top of the model to 5 km at the bottom and vertical correlation lengths from ranged from 0.75 km to 2 km respectively. For velocities and depth, smoothing and damping weights were kept fixed for all phases with 170/20 and 30/20 respectively (Korenaga et al. 2000). A weighting factor of w=1 was used to invert for the depth and velocity nodes equally. In the last inversion step all Pg-phases were jointly inverted with the PmP-arrivals to determine the geometry of the Moho. Late reflections (PimP) observed on OBH06-10 were included in a later inversion step, because the code does not allow for inversion of multiple floating reflectors. We first inverted for all Pg and PmP phases, kept the final crustal model fixed and inverted for the deep arrivals afterwards. Figure 5.3 shows the crustal velocity model of the final inversion result.

3.2.2 Multichannel seismic data

The MCS data of profile A-B were processed using the software-package OMEGA2 (WesternGeco). Focusing-analysis, velocity model building and prestack depth migration was carried out with SIRIUS (GX-Technology). The processing steps were: setting geometry and the subsequent calculation of CMP locations on a crooked line, predictive deconvolution, prediction of multiples using the propagating wave-field followed by adaptive subtraction, sorting into CDP-gathers, initial velocity analysis using focusing-analysis and iterative prestack depth migration based on the Kirchhoff integral solution. Afterwards, primary events were overcorrected and an FK-filter and time-variant band-pass filter were applied. In the last step focusing-analysis was carried out again to achieve a final velocity field for the sedimentary and upper crustal structures. Velocities in the deeper part of the crust cannot be obtained from the MCS data itself and were therefore supplemented by the velocities from the wide-angle inversion result. The final result is the prestack depth migrated seismic section (PSDM) shown in Figure 5.7. For the prestack time section the velocity field in depth was transformed to two-way-traveltime (RMS) and then used for time migration.

4. Results

4.1 P-wave velocity model

Modeling of the WAS data resulted in the crustal velocity structure shown in Figure 5.3. The last inversion, including all phases, resulted in a misfit of 81 ms and $X^2 = 2.1$ after 8 iterations. Pg phases had a misfit of 54 ms and PmP phases of 123 ms. The inversion of additional deeper reflections (PimP) results in a larger misfit of 230 ms and is therefore only discussed qualitatively. The major feature in this profile is the 60 km wide and 6-7 km deep Corsica Basin. Here, Vp increases from 1.8 km/s at the seafloor to 2.5 km/s at a depth of 1.5 km, further to 3.5 km/s at a depth of 3 km (Fig. 5.4). The basement of the basin is located at a depth of 6-6.5 km with a Vp of 6 km/s. At the eastern rim, near the position of OBH05, the Corsica Basin is bounded to the

east by the Pianosa Ridge at km 115 in the model (Fig. 5.3). Here, a narrow area shows lower velocities of 3-3.5 km/s compared to the surrounding velocities of 4-4.5 km/s. In this zone, the seismic records (OBH03-OBH09) show that the amplitude of first arrivals diminishes and that the apparent p-wave velocities decrease. This can be seen for instance at -40 km offset on OBH09 (Fig. 5.2). The western rim of the basin, near the coast, is poorly constrained due to a gap of shots and receivers.
For the inversion of the late PimP phases, we attempted to invert for a steep dipping reflector underneath the Corsica Basin. We also tried to invert for a flat reflector within the mantle, but the inversion process shifted the reflector back to a steep and eastward dipping reflector. However, the actual geometry could not be resolved by the data. East of the Corsica Basin/Montecristo Basin, a series of horst and graben structures continues towards the Latium Margin. The sedimentary cover and the basin infill have velocities of 1.8-2.0 km/s in agreement with velocities obtained by focusing analysis of MCS data. The inversion result shows the block structures along the profile in horizontal and vertical extent. Velocities underneath the sedimentary cover increase rapidly from 3.5-4.0 km/s to 5.5 km/s at a depth of ∼2 km below basement (Fig. 5.3 and 5.4). In the middle part of the crust, velocities increase from 5.5 km/s to 6.0 km/s at a depth of 4-5 km below basement, but in two areas between km 160 and 180 and between km 210 to 260, they increase to 6 km/s at a depth of 3 km below basement. The lower part of the crust has velocities between 6.0 and 6.8 km/s. 1-D profiles extracted from 5 km wide portions of the model show that velocity in the middle crust (5-9 km below basement) is representative of typical continental crust (Fig. 5.4). Vp values in the lower crust of 6.8 km/s are 0.3 km/s faster than the average continental crust (Christensen & Mooney, 1995). The inversion of PmP phases reveals a crystalline-crustal thickness varying from ∼15 km beneath the sedimentary infill of the Corsica Basin to ∼17 km beneath the N-S trending ridge structures east of the Corsica Basin. Except for some minor undulations, the Moho shows no variation in depth.

4.1.1 Model Resolution and Uncertainties

To find model uncertainties and check the robustness of the final model we produced a range of starting models by modifying the velocity field by ± 5%, crustal thicknesses by ± 1, 2 and 3 km and combinations of all parameters. We found that nearly all perturbed starting models evolve towards the final preferred model (Fig. 5.5c). Hence, the model is robust. Statistical calculations (Korenaga et al., 2000) yield the standard deviation for velocities and the uncertainty-width for the Moho location (Fig. 5.5b).

The uncertainties in the upper crustal domain are about 0.1-0.15 km/s except for some outliers (Fig. 5.5b). Velocities in the Corsica Basin are well determined (<0.1 km/s) although the ray density is less than in the eastern upper crust. Just beneath OBH03 at 8 km depth, the uncertainty grows to 0.2 km/s due to less dense ray coverage. In the middle and lower crust, p-wave uncertainties are 0.1-0.2 km/s. Figure 5.5a shows the derivative weight sum (DWS), which is a measurement of ray density passing

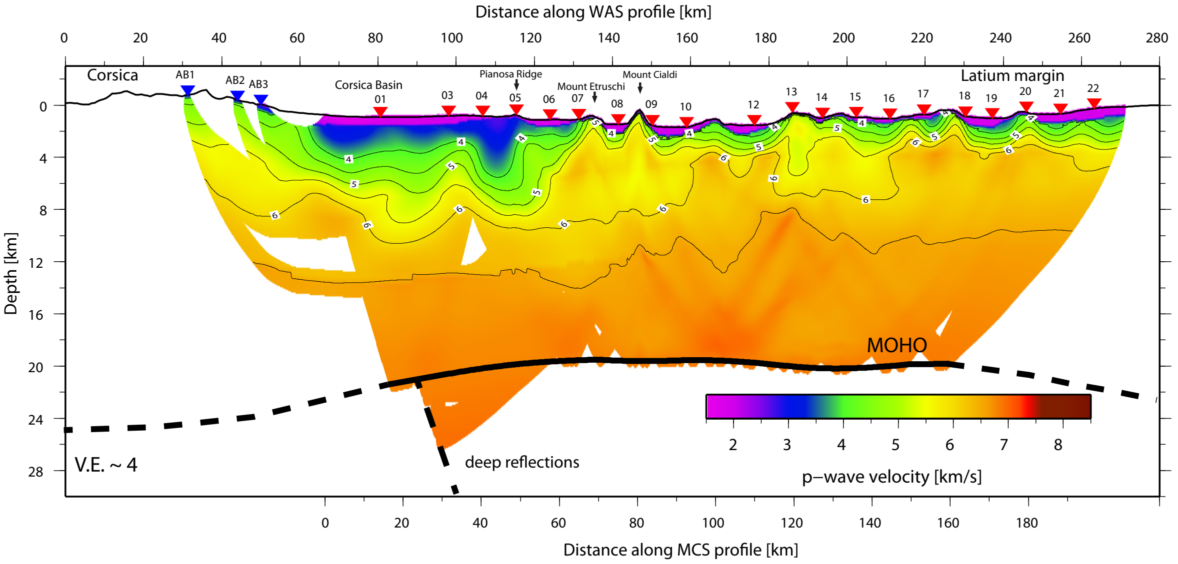

Figure 5.3.: The final result of the P-wave tomography along the MEDOC-AB line reveals the architecture of the crust and the crustal thickness. The section can be divided in two domains: 1) the Corsica Basin to the west bounded by the Pianosa Ridge to the East and a series of fault-bounded horsts- and grabens towards the Latium Margin.

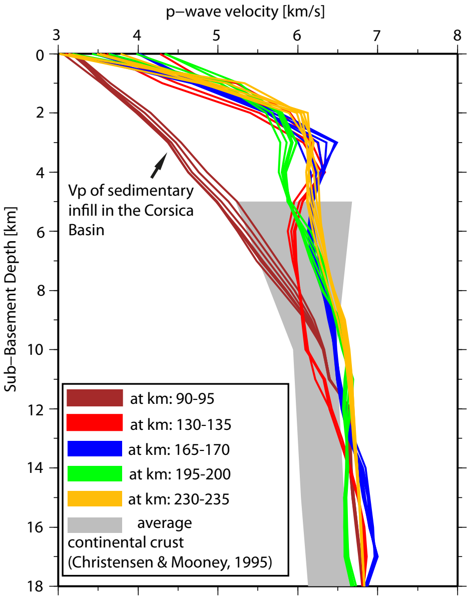

Figure 5.4.: 1D-velocity profiles extracted from the tomographic inversion result. Vp between km 130 and km 235 are compared with the average global velocities in continental crust published by Christensen & Mooney, 1995. Vp shown for the Corsica Basin (km 90-95) start at Top-Messinian (Y).

each cell. From the ray density we infer that the upper and middle crust between km 120 and 220 is well covered by rays. Furthermore, the DWS indicates that velocities in the middle and lower crust are mainly constrained by ray paths of PmP reflections and thus are not as dense as those covered by rays as in the upper crust. We carried out a resolution-test of our section by adding a checkerboard pattern with high and low velocity cells of 10 km width and 5 km height. The velocity perturbation was ± 10%. The checkerboard resolution test reveals that the upper crust and the Corsica Basin are well resolved. In the middle and lower crust, the resolution decreases (Fig. 5.6).

4.2 Tectonic structure and sediment deposits

The prestack depth-migrated image is shown in Figure 5.7 and overlain with the final tomographic wide-angle velocity model of Figure 5.3 to show the good correlation of the different features depicted by both data sets, including the sedimentary units and crystalline basement. The sedimentary units in the Tyrrhenian basin have been studied by many authors (e.g. Zitellini et al., 1986, Trincardi & Zitellini, 1987, and Sartori et al., 2004, among others).

The start and end of the rifting is associated with two regional unconformities: the "L" unconformity, which is late Tortonian in age and the "X" unconformity, which is Early-Pliocene in age (Trincardi & Zitellini, 1986). Between these two unconformities the "Y" unconformity marks the top of the Messinian sequences. In the Corsica Basin and northernmost part of the Tyrrhenian Sea sediment units are calibrated with two exploratory wells (Mauffret et al., 1999). In addition, scientific drilling was carried out in the 1980´s (ODP leg 107) on a NW-SE transect (Fig. 5.3). Although, the Site 654 of ODP leg 107 (Fig. 5.1) is located ∼100 km further south, it supports our age interpretation of the seismic units (Kastens et al., 1988).

4.2.1 The Corsica Basin

The PSDM image (Fig. 5.7) shows well-imaged sedimentary units of the Corsica Basin above the basement at 6.0 to 6.5 km depth (5 s TWT). The top basement depth is in good agreement with the tomographic model, where we observe velocities of ∼5.5 - 6.0 km/s (Fig. 5.3 and 5.7). Towards the east, the basin becomes thinner and is bounded by several westward dipping reflectors at the Pianosa Ridge. The youngest sedimentary unit (Early-Pliocene to Holocene) in the basin is ∼600 m thick and thins to ∼250 m towards the east. Sediments are sub-horizontal with velocities of 1.8-2.0 km/s. A high amplitude reflector below, is identified as the Y Messinian reflection (Fig. 5.8), indicating that the sediments above are Pliocene to Quaternary in age. However, the "X" reflector of Early-Pliocene age (Trincardi & Zitellini, 1987) is difficult to identify within the basin. The sequence is undisturbed and shows no evidence of major tectonic activity.

The end of the Messinian depositional sequence is marked by a prominent reflection beneath the transparent and younger basin infill and can be observed along the complete seismic profile (Y in Fig. 5.8). At places, the Top-Messinian in the Corsica Basin is an

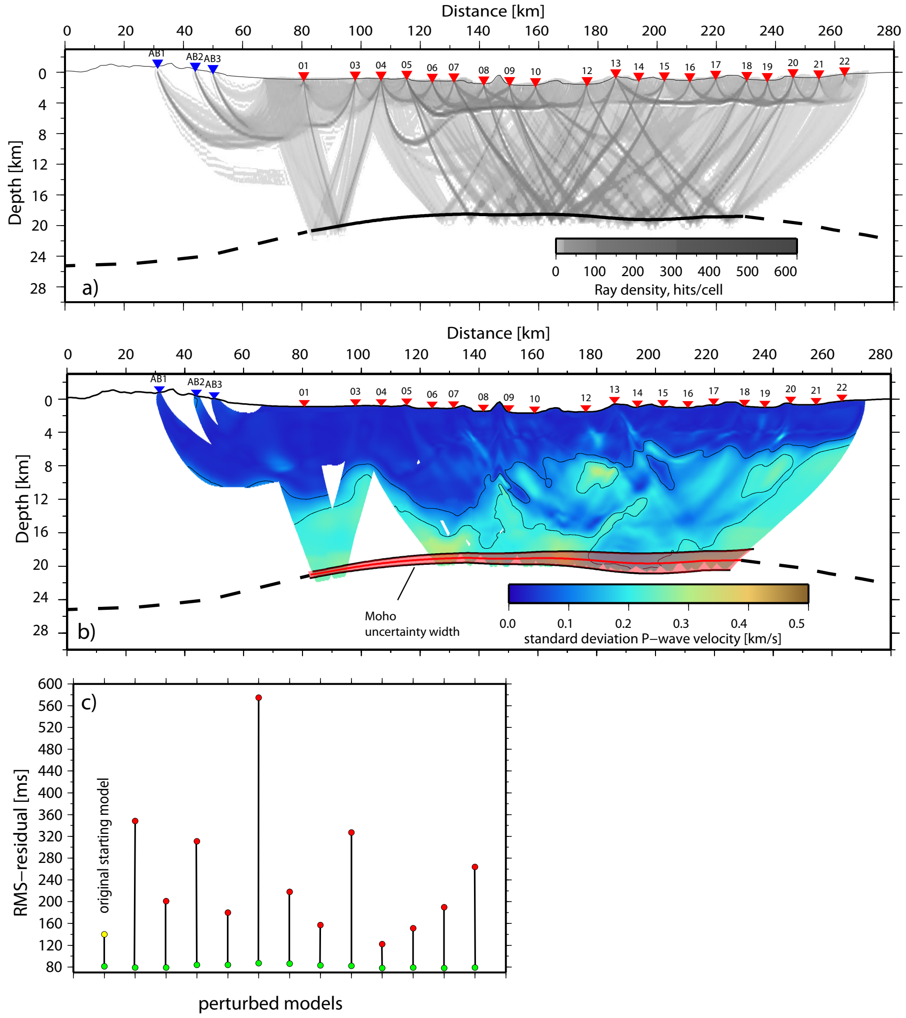

Figure 5.5.: a) Ray density (DWS), b) standard deviation for p-wave velocities derived by the inversion of perturbed starting models. c) RMS-residuals for perturbed starting models. Red dot indicates the residual at the start of inversion. Green dots mark the residual after the last iteration. All perturbed models evolve close to the final model of the original starting model (yellow dot).

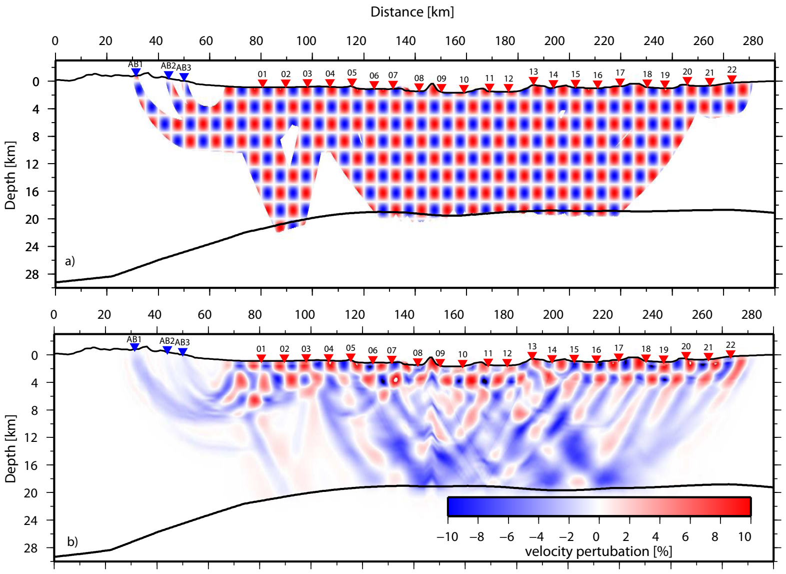

Figure 5.6.: a) Checkerboard test: Velocity perturbations of 10% with wave-length of 5x10 km were added to the data. b) The recovery shows that the upper crust and the deeper parts of the Corsica Basin are well recovered.

erosional unconformity that is intersected by drainage canyon structures (Mauffret et al., 1999, Zitellini et al., 1986). Furthermore, this reflector is tilted, dipping toward the west.

In the upper part of the 800 m thick Messinian unit (Fig. 5.8), the layering is more or less undisturbed. However, it is slightly deformed in the lower part of the unit, which is characterized by a succession of thin and discontinuous reflectors. Velocities in the Messinian unit increase with depth from 2.5 km/s to 3.5 km/s. Below the Messinian units another high-amplitude reflection marks the top of Langhian deposits (Mauffret et al, 1999) followed by a succession of several thick layers. The top Langhian horizon shallows from a depth of 2500 m in the west to 1000 m depth in the east. Velocities increase with depth from 3.5 to 5.5-6.0 km/s. At the Pianosa Ridge Langhian and pre-Langhian sediments terminate against the westward dipping unit (Fig. 5.7 and 5.8). This area is marked by a large and prominent Vp-anomaly of 2.5-3.5 km/s that is clearly observed in our WAS data at km 115 (Fig. 5.3 and 5.8).

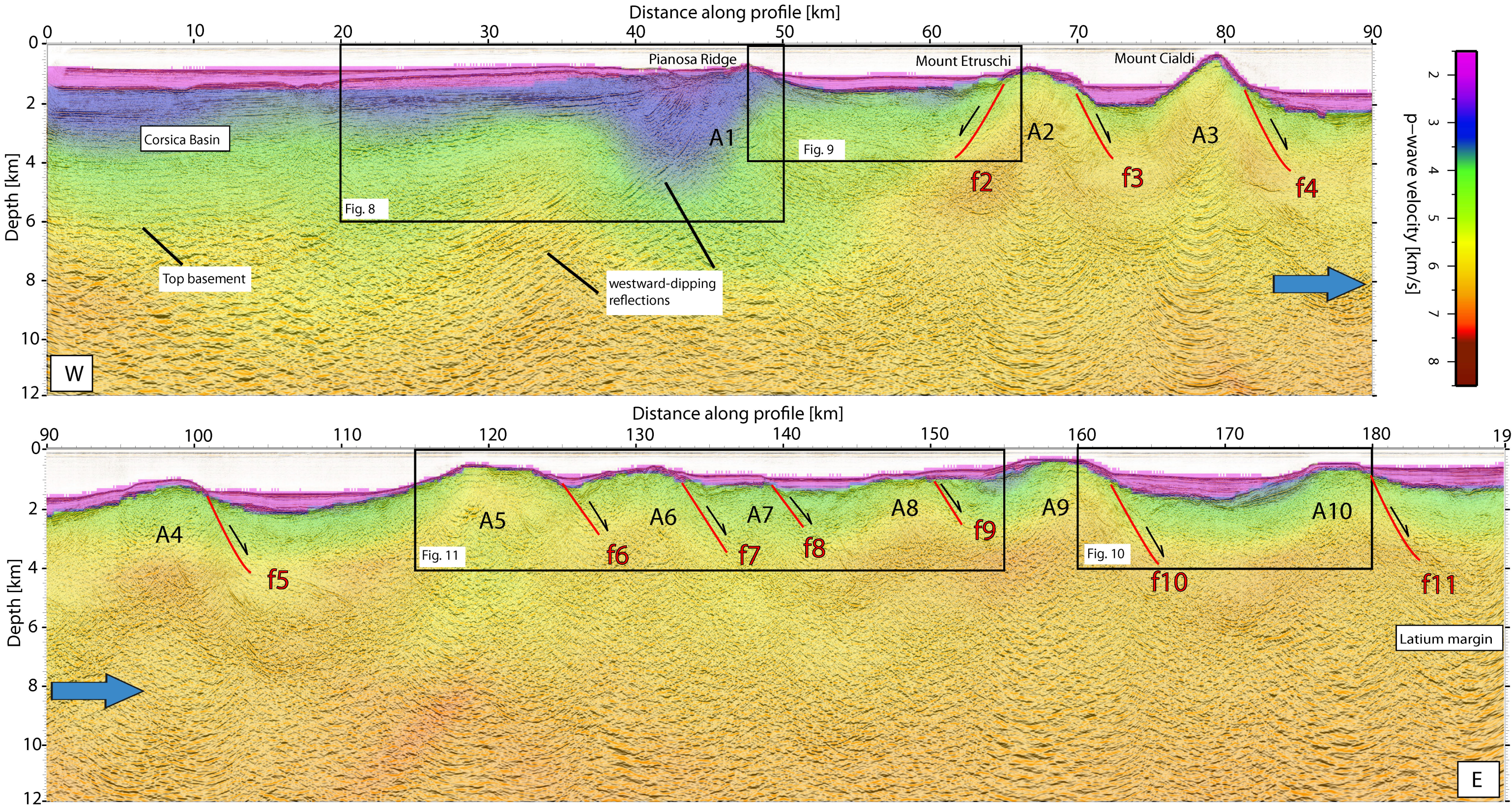

Figure 5.7.: Prestack depth migrated section overlain with the velocities obtained from the tomographic inversion of WAS data. The basement of the Corsica Basin is located at 6-6.5 km depth and bounded to the east by westward dipping reflections. East of the Corsica Basin the main faults f2 to f11 bound large rotated basement blocks (A1-A10) towards the Latium Margin

4.2.2 Fault-bounded blocks and sedimentary basins

East of the Corsica Basin a series of blocks (A1-A10 in Fig. 5.7) separated by sedimentary basins extends onto the Latium Margin. The structures are also seen in the bathymetry data where the sediment cover is thin. Major faults (f2-f11) are clear in the PSDM section to a depth of 3-4 km and are apparently not linked at depth. The general observation is that the blocks rotated on eastward dipping and major faults (synthetic faults). This led to the formation of half-grabens with syn-tectonic and pre-rift structures dipping westward. Fault dips vary between 25° and 50° (Table 1 and Fig. 5.11) and lower syn-tectonic deposits are tilted 10° to 25°. An exception is the block A2 (Mount Etruschi), which is bounded by the faults f2 and f3 (Fig. 5.7). The adjacent blocks A3-A10 are bounded by faults dipping 30°-40°. The size of the blocks decreases from A5 - A7 towards the east and Block A8 is fractured by a set of smaller synthetic and antithetic faults dipping 30° (Fig. 5.11). Blocks A9 and A10 are larger and separated by fault f10.

The sediment infill can be divided into three main units. 1) The horizontally deposited and undeformed sediment sequence of Early-Pliocene to Quaternary age with a thickness of 200 m to 600 m; 2) the end of Messinian to Early-Pliocene unit with amplitudes similar to the sequence above but cut by small faults; and 3) the Messinian and Tortonian successions that can be traced throughout the entire section, typically abutting block-bounding faults and internally cut by small normal faults. Below the stratified Messinian-Tortonian sequence, a domain with less stratified reflectivity can be interpreted as the basement. Reflections within the basement are weak and in many places absent.

The different sedimentary units are well imaged in the Montecristo Basin (Fig. 5.9) located between block A1 (Pianosa Ridge) and A2 (Mount Etruschi). Here, the Early-Pliocene to Quaternary unit marks the post-rift sedimentation. Like in the Corsica Basin, the top of the Messinian deposits is marked by a high-amplitude reflector. Across the basin, the Messinian unit is cut by normal faults forming small tilted blocks. Its internal structure is chaotic in the eastern segment, wavy or folded possibly by slumping (e.g., at the top of block A6 in Fig. 5.11). Tilted Messinian strata indicate that the main rift phase occurred during this age. The shape of the syn-tectonic sequence in the Montecristo Basin (Fig. 5.9) is fan-shaped but at other sites it has rather constant thickness and seems to be uplifted or onlapping on the footwall. At the Latium Margin between blocks A9 and A10 the Messinian deposits are fan-shaped near the footwall, but lying stratified on the hanging wall (Fig. 5.10). Extension, which is generated by the fault displacements that occurs along the profile, varies between a few hundred meters (e.g. f2) and several kilometers, for instance the pre-tectonic basement of block A9 and A10 (Fig. 5.10).

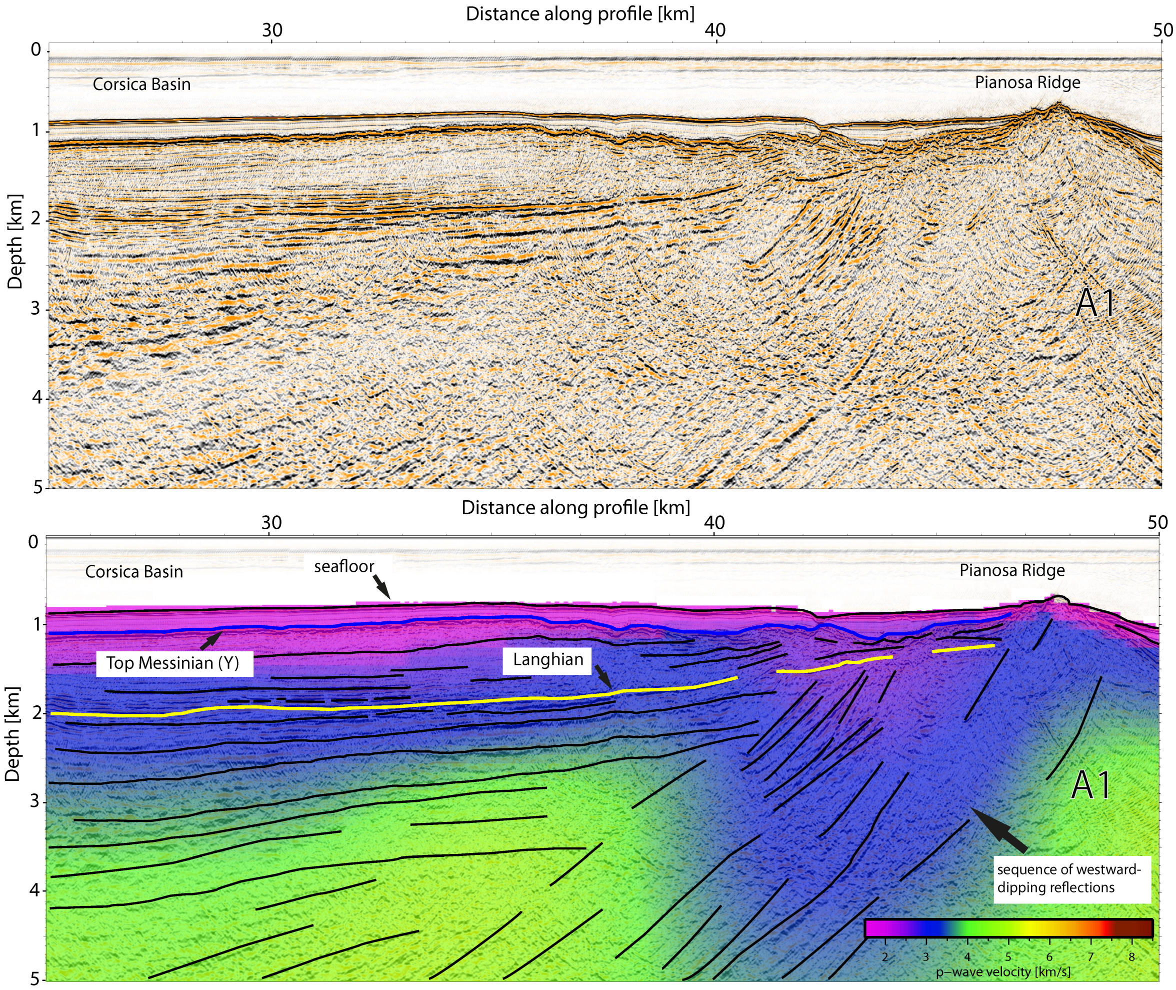

Figure 5.8.: The sedimentary structures in the Corsica Basin terminate against westward dipping reflectors which can be observed in the seismic data to a depth of at least 10 km depth. P-Wave velocities in the upper part of this complex are reduced to 2.5-3.5 km/s and indicate higher fracturing.

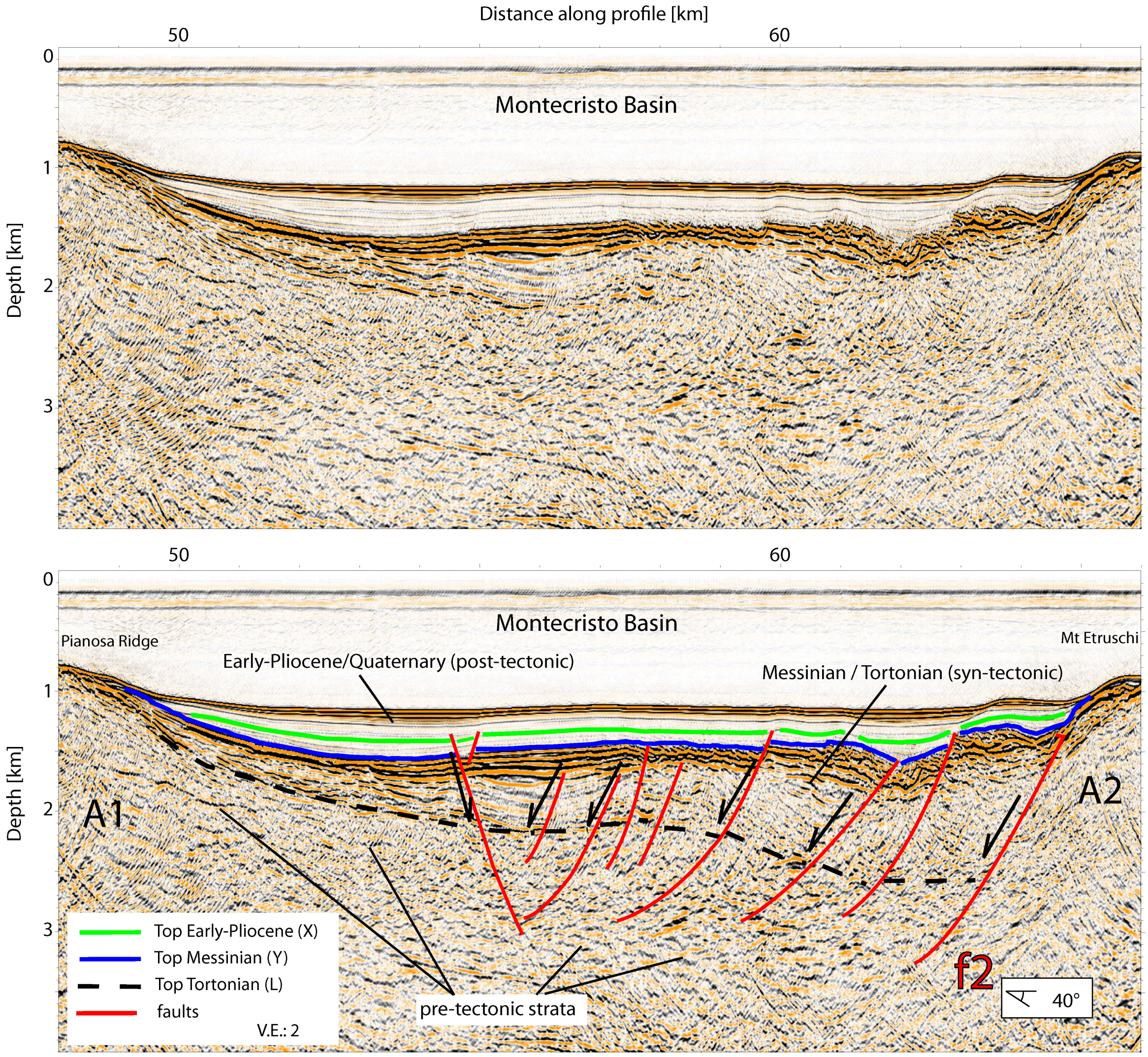

Figure 5.9.: The sedimentary infill of the Montecristo Basin shows that tectonic activity mainly took place during Early-Pliocene (X) to Tortonian age (L). This fan-shaped syn-tectonic sequence is cut by normal faults and overlain by undisturbed Early-Pliocene to Quaternary sediments. Weak reflections within the crust are interpreted as pre-tectonic strata.

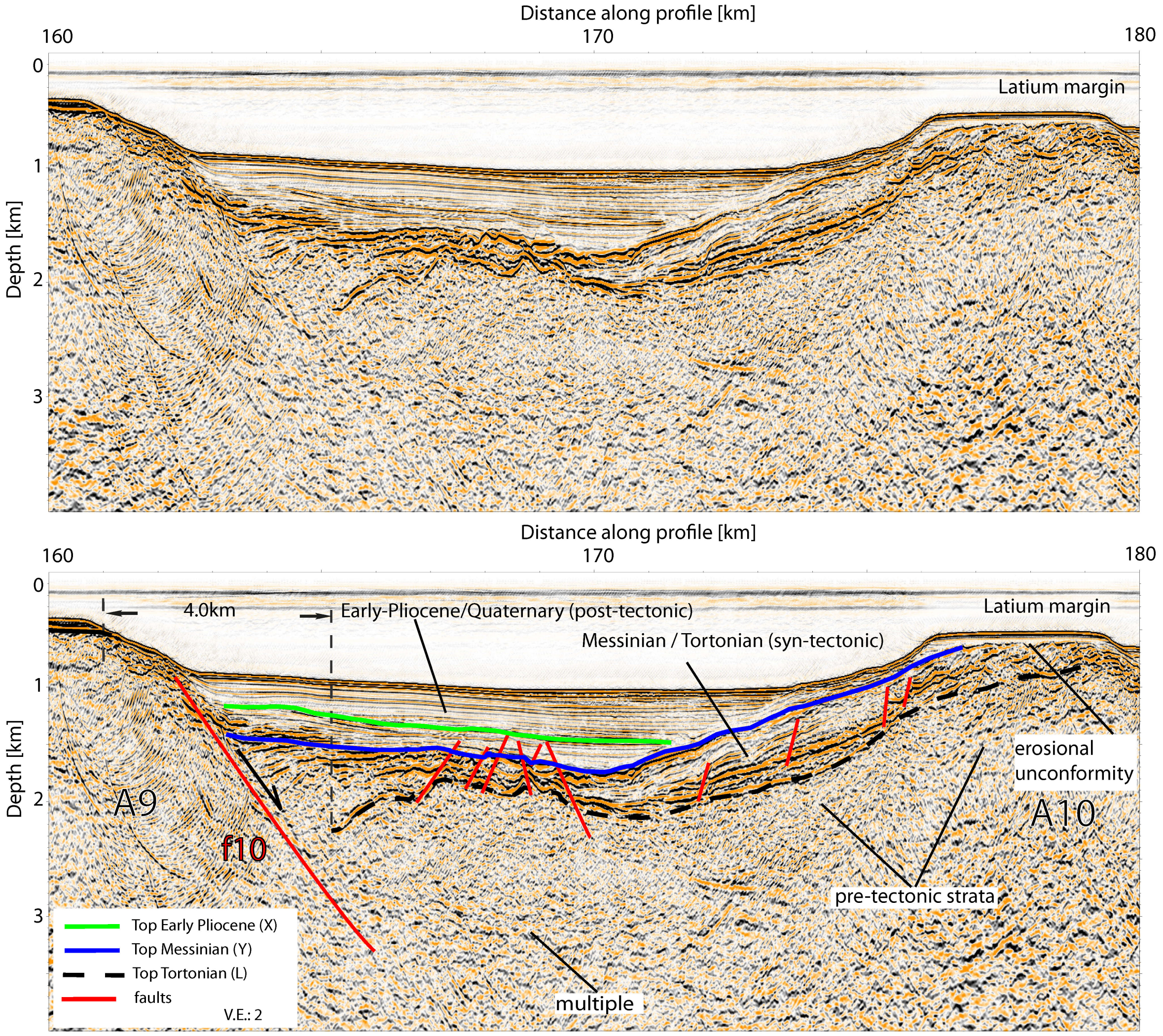

Figure 5.10.: The syn-tectonic sequence near the Latium Margin forms a fan-shaped geometry at the footwall of block A9 and is stratified deposited on top of the hanging wall of A10. The flat summits and the unconformity on top of block A10 indicate that during the active rift-phase the Latium Margin was above sea-level and subsided when rifting stopped.

5. Estimating horizontal extension

To determine the amount of extension we made several assumptions: a) the dip of the faults on the PSDM section is the true angle, because the seismic section is orientated perpendicular to the horst and graben structures. Hence, the fault angle and the length of the pre-tectonic crust in the seismic data will be accurate. b) We assumed that faults are planar and that the angle can therefore be measured directly. c) The top of the pre-tectonic crust of Tortonian age is the base of the continuous strata of the Messinian deposits assuming it marks an isochrone. Hence, horizontal extension is the difference of the current profile length to the pre-tectonic crustal length or, alternatively, the sum of fault offsets produced by all faults. d) For domino-like rotated blocks the relative extension β_f can also be calculated by the fault dip α and the rotation of the bed θ by the following expression (Wernicke & Burchfiel, 1982):

$$\beta_f = \frac{sin(\alpha + \theta)}{sin(\alpha)} \tag{5.1}$$

We applied two different methods to determine the amount of horizontal extension based on assumption c) and d). In the first approach we estimated the ratio of the length of the pre-rift basement to the actual profile length to obtain β_{pb} (Fig. 5.11). In a second method we used the dips of the major faults and tilted strata of the hanging wall to determine a relative extension factor β_f by using Equation 5.1. We excluded the Corsica Basin and westward dipping reflectors between km 0 to km 48. The Corsica Basin formed during an earlier rift stage that is coeval with the development of the Ligurian-Provencal basin during the Oligocene-Early Miocene (Mauffret et al., 1999). In addition, there is only minor evidence for tectonic activity in Messinian to Langhian (16 Ma) sediments within the Corsica Basin, showing that the basin was not affected by the main Tyrrhenian rift phase.

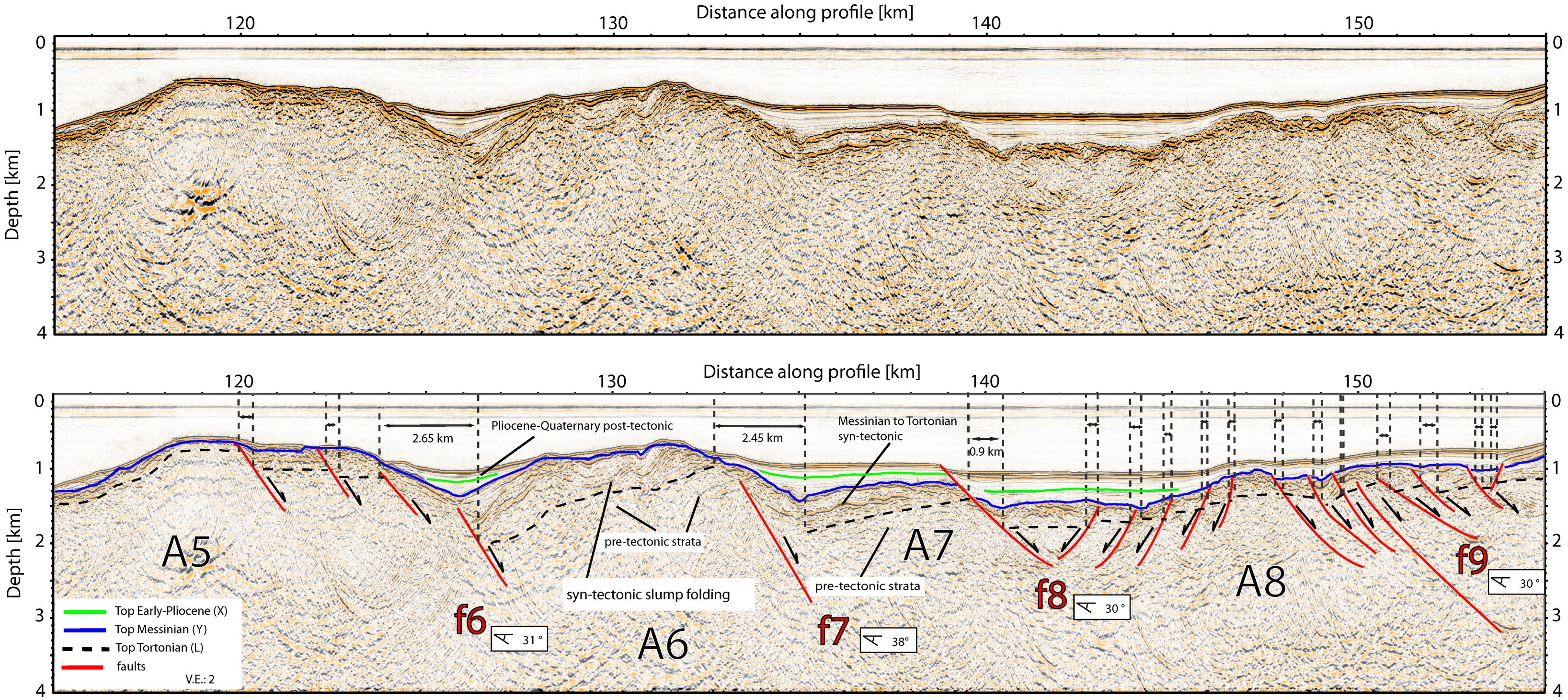

Figure 5.11.: Close-up of MCS section from Fig. 5.7. The vertical dashed lines show the horizontal component of space accommodated by the heave of normal faults. Thick dashed lines indicate the base of the stratified syn-tectonic sequences of Messinian age that is interpreted as the top of the basement.

Table 1 lists the measured fault dips (α) of the faults f2 to f11 bounding the largest blocks and the rotation angle of the top of basement (β) of the hanging blocks. Nearly all faults dip ~30° to 40° and the base of the syn-tectonic / pre-tectonic successions are tilted 10° to 15°. The error of the fault dip estimation is ± 5°. For the estimation of the rotated basement dip, we estimate an error of ± 2°. The maximum error with Equation 5.1 occurs for asymmetric uncertainty combinations (Table 1). The result for β_f is then 1.27 +0.09/ -0.10.

By quantifying the length of the crust in the hanging wall we included the displacements of all faults identified in the seismic section. As an example, the interpretation of the segment between km 115 and km 155 shows the Early-Pliocene-Quaternary post-tectonic deposits and the Messinian/Tortonian syn-tectonic sequence (Fig. 5.11). The black dashed line indicates the assumed and measured pre-tectonic basement. Towards the east the measurements stop at block A10 (km 180) because the next block is not fully imaged (Fig. 5.7). Thus, the profile length considered is 132 km. The length of the basement adds up to 101 km, resulting in an extension factor (β_{pb}) of 1.3 or 30%. This result is very close to the relative extension factor (β_f) of 1.27, or 27%, produced by the main faults. Hence, the opening rates of the basin in this area can be calculated to 7.8-10.3 mm/a assuming an active rift phase of 3-4 Ma.

major fault	fault dip $\alpha \pm 5°$	basement dip $\theta \pm 2°$	initial fault angle $(\alpha + \theta)$	$\beta_f / -(\alpha), +(\theta) / +(\alpha), -(\theta)$
f2	40	10	50	1.19 /1.27 /1.13
f3	50	25	75	1.26 /1.34 /1.19
f4	40	11	51	1.26 /1.29 /1.14
f5	40	10	50	1.19 /1.27 /1.13
f6	31	14	45	1.37 /1.52 /1.26
f7	38	11	49	1.28 /1.32 /1.16
f8	30	10	40	1.28 /1.42 /1.19
f9	30	12	42	1.33 /1.48 /1.23
f10	30	10	40	1.28 /1.42 /1.19
f11	38	10	48	1.26 /1.29 /1.14

Table 5.1.: Extension factor β_f calculated by the measured dips of the main faults (f2-f11) and rotated basements of the hanging walls. The sum of these angles is assumed to be the initial fault angle. Maximum uncertainties for β_f occur for negative and positive combinations of the estimated uncertainties for faults and basement dips.

6. Discussion

6.1 Crustal structure and thinning

The velocity structure and thickness of the crust is obtained by inversion of the WAS data (Fig. 5.3). The tomographic inversion yields a ∼15 ± 1 km thick crystalline crust under the Corsica Basin and a 6 km thick sedimentary infill. The Bouger-anomaly map shows values of +10 mGal in this area (Fig. 5.1B). Beneath the horst and graben structures a 17 ± 1 km thick crust has been revealed. The crustal thickness shows no significant variation in agreement with the gravity field of +70 mGal (Fig. 5.1B).

A SW-NE receiver function transect obtained from teleseismically-recorded earthquakes, found a 25 km thick crust under northern Corsica that thins to 20 ± 2 km towards the Tuscany margin and increases to 50 km under the northern Apennines (Mele & Sandvol, 2002). Contrucci et al. (2005) modelled marine shots recorded on land 50 km north of the profile (line LISA-10 in Fig. 5.1). They found a 15 km thick crust under the Corsica Basin and a 23-25 km thick crust between Pianosa Ridge and the Tuscany Margin. Along our transect, the crust is also 15 km thick under the Corsica Basin and is 17 ± 1 km thick east of Pianosa Ridge. This comparatively thinner crust (17 ±1 km) indicates a more intense period of stretching toward the south.

Assuming that the 17 ± 1 km crust originally had an initial thickness comparable to current Corsican crust (∼24 km) implies a thinning factor β_v of ∼0.70 (∼30%). The factor β_v is correct only if the crust has not modified by magmatic additions. The tomographic inversion (Fig. 5.3) shows, that the lower crust is fairly homogeneous eastward of km 115 without high-velocity anomalies that might indicate important magmatic intrusions. However, velocity-depth profiles from four different locations along the profile (Fig. 5.4) display typical continental crust values in the upper crust (upper 8 km of basement) but with slightly higher values in the lower crust of 6.6 to 6.8 km/s compared to average continental crust (Christensen & Mooney, 1995). These velocities probably indicate a higher-than-average percentage of mafic minerals but they are still not evidence for large-scale intrusive magmatism.

Nevertheless, the deep wide-angle reflections under Corsica Basin, recorded on OBH06-10, might indicate magmatic intrusions in the upper mantle. The Corsica Basin is bordered to the east by a curved band of high-amplitude magnetic anomalies of 120-160nT (Fig. 5.1C) that might be related to magmatic intrusions. This band extends from west of Elba Island to Pianosa Island and along the Pianosa and Montecristo Ridges to the southwest. The profile crosses Pianosa Ridge where the anomaly has decreased amplitude. Here, velocities range between 3.5-5 km/s at a depth of 10 km, which are possibly too slow for a magmatic intrusions related to rifting.

However, the source of magnetic anomalies might have a deeper origin, perhaps from the mantle where the PimP-reflection originates. Similar reflections occur at the same depth near Elba Island (Ponziani et al., 1995) in the area of high magnetic anomalies. This suggests that the late reflections might originate from an intrusive structure, even though they could have been recorded as side reflections from shallower structures. A positive gravity anomaly just south of the profile is coincident with a magnetic anomaly and might support the existence of an intrusive feature (Fig. 5.1B & C).

The west-dipping sediment unit at the eastern edge of the Corsica Basin might be related to thrusting formed during the collisional phase between Corsica-Sardinia and the Apulian continental block (Keller & Coward, 1995). Mauffret et al. (1999) propose that the basin formed over a collisional prism in a forearc position between Corsica and the Adriatic plate, and that the thrusts are Alpine. Our inversion of WAS data reveal that this area has reduced velocities of 2.5-3.5 km/s in the upper 5 km, which may indicate a highly fractured region (Fig. 5.8). Alpine thrusts might represent an inherited structure that mechanically decoupled the Corsica Basin from the crust in the east.

6.2 Style of extension

The rifted continental crust between the Pianosa Ridge and the eastern Latium Margin is characterized by continental half-graben fault blocks. PSDM images show that the blocks are bounded by normal faults that accommodate space in the upper crust.

The geometry of syn-tectonic strata reveals the sense of block rotation, dip-angle of bounding faults and helps to recognize the rotated top of the basement. We found that nearly all major faults dip at angles of 30-40° to the east. The respective dip of the pre-tectonic strata at the hanging walls (base of the syn-tectonic deposits) ranges from 10°-15°. The only exception is block A2 (Fig. 5.7). The faults bounding this block dip at angles of 40° (f2) to the west and 50° to east (f3). We therefore interpreted that Mount Cialdi (A3) rotated on f3 and the block A4 on the fault f4. This is supported by the thickening geometry of syn-tectonic deposits in the half-graben east of the block A3 (Fig. 5.7). Thus, it is reasonable to deduce that the western flank of A3 forms the top of the basement. The rotation direction of A2 (Mount Etruschi) is not clear in the images. Syn-tectonic deposits indicate that block A1 and the basement of Montecristo basin, tilted westward on the fault f2. This is inferred from fan-shaped eastward thickening of syn-tectonic strata (Fig. 5.9). The adjacent blocks A3-A5 are bounded by faults dipping 30°-40°. The Messinian deposits seem to be uplifted in the vicinity of the footwall of blocks A3 and A4 (Fig. 5.7) or lying stably on the flank of the hanging wall of block A10 (Fig. 5.10). A possible explanation for this sedimentary architecture is that the stress-field was not exactly orientated W-E during part of the rifting process and had a strike-slip component which led to oblique faulting. Furthermore, the syn-tectonic deposits are of similar thicknesses and ages, from which we infer that the faults were active and rotated mainly during the Messinian.

At km 120-140, the dip of the faults bounding blocks A6 and A7 is 31° and 38°, respectively. The top of basement dip of A6 is higher than of A7 (14° and 11°) and the syn-rift deposits thicker on top of A6. This might be an indication for eastward propagation of fault activity.

Block A8 is cut by a set of small synthetic and antithetic faults dipping 30° either west or east and contributing to the total extension with small displacements (Fig. 5.11). Block A9 and A10 are comparatively larger and separated by the fault f10 (Fig. 5.10).

The top of the blocks A9 and A10 may have been above sea-level during the Messinian salinity crisis and are relatively flat, probably cut by wave erosion. Wave base erosion is inferred from the erosional unconformity truncating syn-tectonic strata on the summit of block A10 (Fig. 5.10). The thicker syn-tectonic deposits between A9 and A10 may be the eroded material from the top of the blocks (Fig. 5.10). Block A9 is in fact a 20 km long NW-SE orientated extended plateau with a maximum width of 5 km (Fig. 5.1) that probably belong to a former shelf region.

We found that the space accommodated by the main faults (f2-f11) is on average 27% ($\beta_f = 1.27$). By estimating the pre-tectonic length using the top of the basement as a marker horizon and including all seismically-imaged faults, we found a stretch factor (β_{pb}) of 1.3 (30%). The minor difference of β_f and β_{pb} shows that the space accommodated in this rift is mainly localized by the heaves of large surface-breaking faults and implies that smaller faults within the hanging walls do not significantly contribute to the entire stretching.

6.3 Comparison with other rifts

6.3.1 Half-graben formation

The northern Tyrrhenian Basin opened due to the formation of ten major east-dipping offshore faults that generated crustal extension and led to the formation of half-graben structures (Fig. 5.7 and 5.12). Thus, the fault vergence of the major normal faults in this early rift stage appears to be different to the conceptual pure-shear model (e.g. McKenzie, 1978). Hence, the upper crustal tectonic structure in the rift appears asymmetric, sharing similarities with observations from other young continental rifts.

Asymmetric fault block structure has been described at the western Gulf of Corinth (Bell, 2008), the Galicia interior Basin (Perez-Gussinye et al., 2003), the intra-continental Baikal rift (Hutchinson et al., 1992) and the Upper Rhine Graben (Derer, et al., 2005). Detailed field work has characterized asymmetric half-graben structures at the Hammam-Faraun block of the Suez-rift. From this rift, it has been shown that the active block-bounding major faults formed after the onset of rifting, and that smaller intra-block faults are older but abandoned with time (Gawthorpe et al., 2003). Subsequent fault displacement was localized during the development of the major fault systems. Localization is similar to the observations on the image presented of the northern Tyrrhenian Sea.

The study on the Hammam-Faraun fault block further shows, that the major faults formed sequentially in time. From the PSDM image, we have no evidence of the relative age of smaller faults within fault blocks and the major fault system bounding them. Thus, it remains uncertain whether the smaller faults are older or are coeval to block deformation. In a model that explains rift structures of the West Iberia and Newfoundland conjugate margins it is proposed that individual successive faults cut crust that had been previously extended by earlier individual faults (Ranero and Perez-Gussinye, 2010). We point out that the series of tilted blocks A5-A7 may have undergone a similar

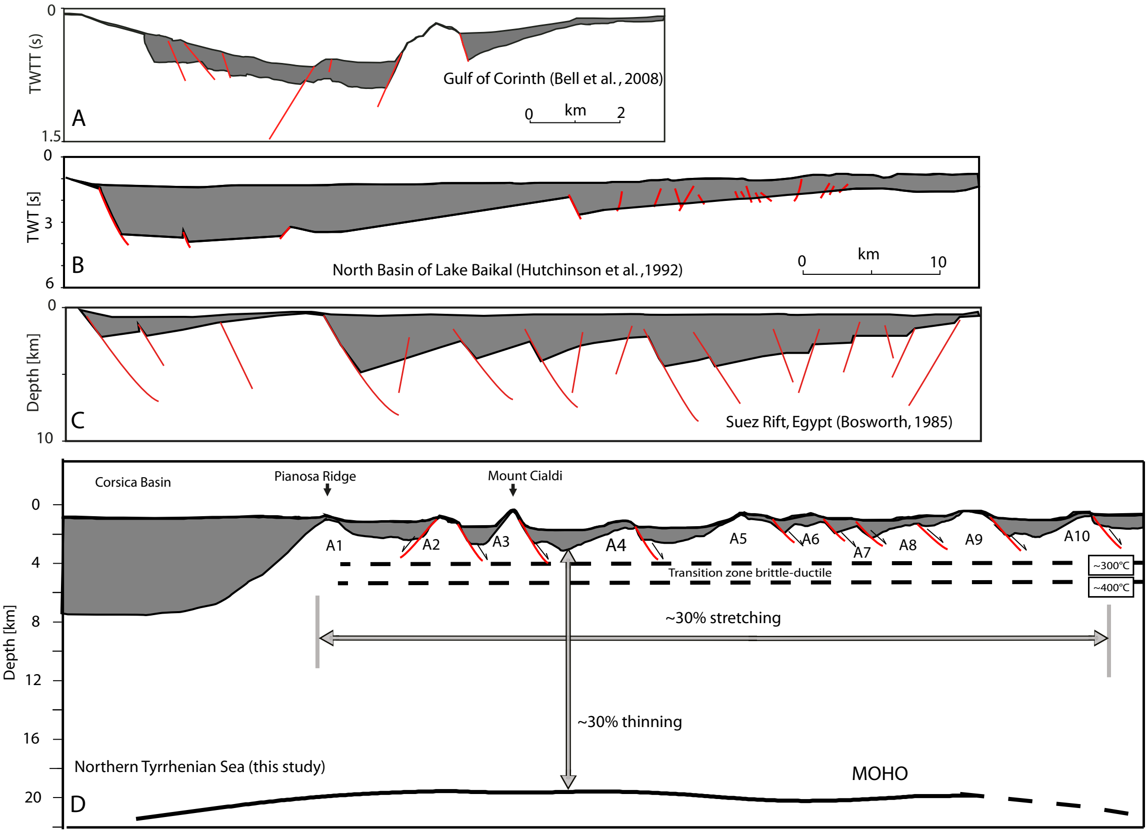

Figure 5.12.: Structural comparison of seismic cross sections from other young rift settings (A-C) with the seismic cross-section presented here (D). Grey colored areas indicate sedimentary deposits. Half graben formation and asymmetry seem to be a general feature of rifts. D) East of the Corsica Basin the crust is stretched by 30% which is equal to the amount of crustal thinning. Heat flow data and thermal gradients from Della Vedova et al., 1984.

development because the dimensions of the half-grabens and block size diminish toward the east (Fig. 5.11).

6.3.2 Fault initiation and thermal state

The major faults imaged on the PSDM dip 30-40° and the hanging wall is rotated 12° (Table 1). This suggests that the initial fault angles were approximately 45°-50°. This angle is smaller than for an optimally orientated high-angle normal fault that initially dips at 65° with coefficients of friction of 0.6-0.85 (Abers, 2009). Early rift faults, like at the Suez-Rift (Gawthorpe et al., 2003), exhibit major faults dipping 60°-80° in their shallower segments. However, earthquakes at extensional settings, for instance in the Gulf of Corinth rift, show that the majority of large events nucleate on normal faults that dip 40°-50 ° (Jackson, 1983). This observation supports the notion that major faults in the northern Tyrrhenian may have initiated at this angle. However, this estimation contains considerable uncertainty. This is because the scarcity of well-imaged pre-rift strata that may have been deposited horizontally precludes an accurate estimate.

The initiation angle of the faults is dependent upon the rheological state of the crust. If the crust is weak faults might initiate at shallower angles. Possible weak regions in the Tyrrhenian Sea might be inherited pre-existing tectonic features that can be reactivated. Field work on Elba Island shows that extensional features related to the opening of the Northern Tyrrhenian Sea overprint former compressional features (Keller & Coward, 1996). Thus, the initial angle of the major normal faults may have been controlled by the reactivation of relatively high-angle thrust faults.

The higher heat flow in the northeastern Tyrrhenian is in agreement with a lithospheric thickness of just 30 km in the Tuscany region just north of our study area (Contrucci et al., 2005). The thermal state of this area suggests that the crust might have been thermally weakened, because the present heat-flow in this area locally exceeds values of $\sim 100mW/m^2$. Allemand (1990) showed from field data and experimental modelling, that if faults are generated at angles $<$50°, the brittle-ductile transition is located in the crust and a ductile lower crust therefore exists. Hence, it is possible that increased heat-flow might have been present prior to active rifting, thereby explaining the initial fault angles of 45°-50°. Higher thermal gradients would influence the depth at which rocks behave brittly ($<$ 300°-400°C) or ductily ($>$ 400°C) (Odedra et al., 2001). This means that at a depth of 3-4 km underneath the seafloor, rocks start to behave ductily and thus deeper brittle faulting should be constrained to above these depths.

6.3.2 Detachments and low-angle normal faults

Asymmetry of the tectonic structure of rift systems is often associated with the existence of large-scale long-lived detachment faults that cut the entire crust or perhaps even the whole lithosphere (e.g. Bosworth, 1985; Wernicke, 1985). Most studies have interpreted rifted structures after break-up, but in the northern Tyrrhenian Sea our profile provides an image of the structure during the early period of asymmetric development.

The existence of crustal-scale low-angle normal faults or long-lived detachments in the northern Tyrrhenian basin seems implausible for of two reasons. First, there is no evidence in the seismic images for shallow dipping intra-crustal features giving rise to top of basement faults, similar to those observed in oceanic core complexes (e.g. Ranero and Reston 1999). In general, detachment faults are active in the brittle domain and thus, their presence in the northern Tyrrhenian segment should be relatively shallow and they should be easily detectable with seismic methods. Second, an estimation of the total fault displacement (β_f and β_{pb}) does not require additional slip on large-scale low-angle faults, since the estimated extension matches the amount of entire crustal thinning (β_v). Although a low-angle fault exists onshore Elba (Zuccale fault), its formation is assumed to be related to the presence of foliated mineral phases that makes the fault weak (Collettini, 2009). While such structures may exist, our data indicate that they do not play an important role accommodating space during the early rifting phase. At other regions in an early-rifting stage, it has been shown that low-angle faults are not necessary to explain extension, e.g. in the Gulf of Corinth (Bell, 2008). Seismic images from the Porcupine Basin and the Deep Galicia Margin reveal structures that have been interpreted as low-angle detachment faults that may have been active at high stretching factors (larger than 3). However, those features have not been observed in the parts of the Porcupine Basins where the extension is considerably less (Reston et al., 2004).

6.4 Implications for early-stage continental rifting

Comparison of these results with previous studies of other young rift basins such as the Gulf of Corinth, the Suez-Rift or Lake Baikal (Fig. 5.12) reveals that the formation of half graben structures by strain localization mechanisms on major normal faults is commonplace for the early phases of stretching. The rift initiation is not controlled by the formation of long-lived detachment faults and it can be considered to be the normal style of rifting for continental crust with small extension factors(β <1.3). Crustal stretching and thinning is distributed homogeneously across the northern segment of the Tyrrhenian Sea and suggests that additional slip on shallow dipping detachments that link fault-bounded blocks such as offshore Iberia (Ranero & Pérez-Gussinye, 2010) or like those in the northern Porcupine Basin, develop only with larger stretching factors (Reston, 2004).

The pre-rift temperature-gradient controls the thickness of the brittle and ductile layers and might have controlled the initiation angle of faults in the Tyrrhenian basin at shallower dip angles than standard rheology predicts. In the lower part of the crust where the temperature exceeds 350°-400°, rocks undergo ductile deformation by an amount of stretching that is roughly similar to that obtained by shallower brittle faulting (Fig. 5.12 D).

7 Conclusions

The study of the northern Tyrrhenian Basin, contributes to the basic understanding of the processes of early continental extension. We analyzed new wide-angle seismic data as well as a pre-stack depth-migrated image of multichannel seismic data between Corsica and Italy. We found two domains each with a distinct tectonic style and crustal thickness. The 6 km deep Corsica Basin in the west developed mainly during an older rift-phase in the Oligocene. The basin is filled with post-tectonic Early-Pliocene to Quaternary sedimentary deposits. Beneath, the Messinian to Langhian and older sediments together form a fan-shaped syn-tectonic sequence. Tomographic inversion show that the crystalline crust has thinned to ∼15 ± 1 km. Velocities at the top of the crystalline crust increase from 6 km/s to 6.7 km/s at the base of the crust. The depth-migrated image shows that the Corsica Basin is bounded by a ∼10 km deep westward dipping sedimentary complex near the Pianosa Ridge. Velocities in the upper part of this feature at Pianosa Ridge are reduced and imply high fracturing. East of the Corsica Basin, a second domain exhibit rifted crust at the center of the northern Tyrrhenian segment and the Latium Margin. Two unconformities mark the active rift phase confining syn-tectonic deposits of late Tortonian, Messinian and Early-Pliocene age. The area subsided and developed prominent tilted blocks and asymmetric half-graben structures by rotation on ten major faults. We found that the crust has been stretched by a factor β_f of ∼1.30 and that the majority of extension was localized by the displacements on surface-breaking major faults. Furthermore, we found that major faults dip 30-40° to the east and rotated beds in the hanging wall dip ∼12° to the west. This suggests an initial fault angle of ∼45-50°, perhaps related to the reactivation of pre-existing crustal features or a possible weakening of the crust due to a higher pre-rift heat-flow. Tomographic inversion reveals a ∼17 ± 1 km thick crust and a sub-horizontal Moho which is well constrained by PmP-reflections. Upper crustal velocities below the thin sedimentary cover represent typical values for continental crust (3.5-6.0 km/s). Velocities in the lower crust are slightly higher (6.6-6.8 km/s), presumably related to a higher proportion of mafic minerals. Assuming an initial crustal thickness of 24 km, as is currently observed under Corsica, the crustal thickness of the basin obtained by inversion of wide angle data indicates a crustal thinning of ∼30%. This result matches the horizontal stretching estimated from fault displacements. Thus, there is no extension discrepancy. Moreover, crustal-scale detachment faults should be imaged in the seismic data but are not. Assuming that the duration of the main rift activity lasted 3-4 Ma and taking into account the total horizontal displacement, the opening rate of this basin can be calculated to be between 7.8-10.3 mm/a.

We propose that the young northern Tyrrhenian Basin evolved homogeneously by stretching and block rotation in the brittle upper crust and ductile deformation in the lower crust. Other young rift basins, like the Gulf of Corinth, the Suez-Rift, or Lake Baikal resemble the northern Tyrrhenian Basin to a large extent. This may suggest that half graben formation and distributed, homogeneous crustal thinning is a common feature during rift initiation. Furthermore, our seismic images reveal no evidence for low-angle detachment faulting in the main part of the basin. Again, this is similar to other young rift basins elsewhere and may imply that detachment faults do not develop until higher stretching factors are reached.

Acknowledgments
Funding for data acquisition was provided by Spain (projects CTM2007-66179-C02-01/MAR and CTM2009-07772-E/MAR) and Italy which we gratefully acknowledge. We thank J.R. Hopper and an anonymous reviewer for their helpful comments on a previous version of this manuscript. Thank you to Grant George Buffett for copy editing. We thank the ships' officers and the crews of B/O Sarmiento de Gamboa and R/V Urania who helped to conduct the data acquisition for the MEDOC project successfully. A great thank goes also to all in the MEDOC-Team. This work was funded by the Deutsche Forschungsgemeinschaft (DFG) under grant GR 1964 /14-1.

References

Abers, G. A., 2009: Slip on shallow-dipping normal faults. Geology, 37 (8), 767-768, doi:10.1130/focus082009.1.

Allemand, P. and J.-P. Brun, 1991: Width of continental rifts and rheological layering of the lithosphere. Tectonophysics, 188, 63-69,

Bell, R. E., L. C. McNeill, J. M. Bull, and T. J. Henstock, January: Evolution of the offshore western gulf of corinth. Geological Society of America Bulletin, 120 (1-2), 156-178.

Bosworth, W., 1985: Geometry of propagating continental rifts. Nature, 316 (6029), 625-627.

Buck, R. W., (1993), Effect of lithospheric thickness on the formation of high- and low-angle normal faults Geology, v. 21, p. 933-936,

Cherchi, A. and Montadert, L., (1982), Oligo-Miocene rift of Sardinia and the early history of the Western Mediterranean Basin. Nature, 298, 736-739, doi:10.1038/298736a0.

Collettini, C., A. Niemeijer, C. Viti, and C. Marone, 2009: Fault zone fabric and fault weakness. Nature, 462 (7275), 907-910.

Contrucci, I., Mauffret, A., Brunet, C., Nercessian, A., Béthoux, N., Ferrandini, J., (2005), Deep structure of the North Tyrrhenian Sea from multi-channel seismic profiles and on land wide angle reflection/refraction seismic recording (LISA cruise): Geodynamical implications, Tectonophysics, 406, 3-4, 141-163, doi:10.1016/j.tecto.2005.05.015.

Della Vedova, B., Pellis, G., Foucher, J.P., Rehault, J.-P., (1984), Geothermal structure of the Tyrrhenian Sea, Marine Geology , 55, 271-289.

Derer, C. E., M. E. Schumacher, and A. Schaefer, 2005: The northern upper rhine graben: basin geometry and early syn-rift tectono-sedimentary evolution. International Journal of Earth Sciences, 94, 640-656, doi:10.1007/s00531-005-0515-y

Faccenna, C., Becker, T. W., Lucente, F. P., Jolivet, L. and Rossetti, F., (2001), History of subduction and back-arc extension in the Central Mediterranean. Geophysical Journal International, 145: 809-820. doi: 10.1046/j.0956-540x.2001.01435.x.

Gawthorpe, R. L., C. A.-L. Jackson, M. J. Young, I. R. Sharp, A. R. Moustafa, and C. W. Leppard, (2003): Normal fault growth, displacement localisation and the evolution of normal fault populations: the hammam faraun fault block, suez rift, egypt. Journal of Structural Geology, 25 (6), 883-895,

Jackson, J. A., 1987: Active normal faulting and crustal extension. Geological Society, London, Special Publications, 28 (1), 3-17,

Jolivet, L., Frizon de Lamotte, D., Mascle, A., Seranne, M., (1999), The Mediterranean Basins: Tertiary Extension within the Alpine Orogen - an introduction. Geological Society, London, Special Publications, 156, 1-14, doi:10.1144/GSL.SP.1999.156.01.02

Kastens, K.A., Mascle, J., Others, (1988), ODP Leg 107 in the Tyrrhenian Sea: Insights into passive margin and back-arc basin evolution, Geological Society of American Bulletin, 100. 1140-1156, doi: 10.1130/0016-7606(1988)100<1140:OLITTS>2.3.CO;2.

Keller, J.V.A., and Coward, M.P., (1996), The structure and evolution of the Northern Tyrrhenian Sea, Geol. Mag., Cambridge University Press, 133, 1-16,
doi:10.1017/S0016756800007214

Korenaga, J., W. S. Holbrook, G. M. Kent, P. B. Kelemen, R. S. Detrick, H.-C. Larsen, J. R. Hopper, and T. Dahl-Jensen (2000), Crustal structure of the southeast Greenland margin from joint refraction and reflection seismic tomography, J. Geophys. Res., 105(B9), 21, 591-21, 614,doi:10.1029/2000JB900188.

Lister, G.S., Etheridge, M.A., Symonds, P.A., 1991, Detachment models for the formation of passive continental margins, Tectonics, Vol. 10, No. 5, 1038-1064

Malinverno, A. and Ryan, W.B.F., (1986), Extension in the Tyrrhenian Sea and shortening in the Apennines as result of arc migration driven by sinking of the lithosphere. Tectonics, 5, 2, 227-245, doi:10.1029/TC005i002p00227

Marett, R., and Allmendinger, R.W., (1992), Amount of extenison on "small" faults: An example from the Viking graben, Geology, 20, 47-50, doi; 10.1130/0091.

Mauffret, A., Contrucci, C., Brunet, C., (1999), Structural evolution of the Northern Tyrrhenian Sea from new seismic data. Marine and Petroleum Geology, 16, 5, 381-407, ISSN 0264-8172, 10.1016/S0264-8172(99)00004-5.

Mauffret, A., and Contruccci, I., (1999), Crustal structure of the North Tyrrhenian Sea: first results of the multichannel seismic LISA cruise. In: Durand, B., Jolivet, L., Horvath, F. & Seranne, M. (eds) The Mediterranean Basins: Tertiary Extension within the Alpine Orogen. Geological Society London, Special Publications, 156, 169-193.

McKenzie, D., (1978), Some remarks on the development of sedimentary basins, Earth and Planetary Science Letters, 40, 25-32.

Mele, G., Sandvol, E., (2003), Deep crustal roots beneath the northern Apennines inferred from teleseismic receiver functions, Earth and Planetary Science Letters, 211, 1-2, 69-78, doi:10.1016/S0012-821X(03)00185-7.

Odedra, A., Ohnaka, M., Mochizuki, H., Sammonds, P., (2001), Temperature and pore pressure effects on the shear of strength of granite in the Brittle-Plastic Transition Regime, Geophysical Research Letters, 28, 15, 3011-3014, doi:10.1029/2001GL013321.

Pérez-Gussinyé, M., Ranero, C. R., Reston, T. J., Sawyer, D. (2003) Structure and mechanisms of extension at the Galicia Interior Basin off West Iberia. Journal of Geophysical Research 108, doi10.1029/2001JB000901.

Ponziani, F., De Franco, R., Minelli, G., Biella, G., Federico, C., Pialli, G., Crustal shortening and duplication of the Moho in the Northern Apennines: a view from seismic refraction data (1995), Tectonophysics, 252, 1-4,391-418, doi:10.1016/0040-1951(95)00093-3.

Ranero, C. R., Reston, T. J. Detachment faulting at Inside Corners. Geology, vol 27, 983-986 (1999).

Ranero, C.R. & Pérez-Gussinye, M., (2010), Sequential faulting explains the asymmetry and extension discrepancy of conjugate margins, Natur, 468, 294-300,
doi:10.1038/nature09520.

Reston, T., Extension discrepany at North Atlantic nonvolcanic rifted margins:
Depth-dependent stretching or unrecognized faulting? (2007), Geology, 35, 367-370, doi; 10.1130/G23213A.1.

Reston, T.J., Gaw, V., Klaeschen, D., Stubenrauch, A., Walker, I., (2004), Extreme crustal thinning in the south Porcupine Basin and the nature of the Porcupine Median High: implications for the formation of non-volcanic rifted margins, Journal of the Geological Society, London, Vol. 161, pp. 783-798, doi:10.1144/0016-764903-036

Rosenbaum, G., Lister, G. S., and Duboz, C., (2002), Reconstruction of the tectonic evolution of the western Mediterranean since the Oligocene. Journal of the Virtual Explorer, 8: 107-130. doi:10.3809/jvirtex.2002.00053.

Sartori, R., Torelli, L., Zitellini, N., Carrara, G., Matteo, M., Mussoni, P., Crustal features along a W-E Tyrrhenian transect from Sardinia to Campania margins (Central Mediterranean) (2004), Tectonophysics, 383, 3-4, 171-192,
ISSN 0040-1951, 10.1016/j.tecto.2004.02.008.

Sartori,R., (1990), The main results of ODP Leg 107 in the frame of neogene to recent geology of perityrrhenian areas, Proceedings of the Ocean Drilling Program, Scientific Results, Vol. 107 Schellart, W.P., (2010) Mount-Etna-Iblean volcanism caused by rollback-induced upper mantle upwelling around the Ionian slab edge: An alternative to the plume model, Geology, v. 38 no. 8, p. 691-694

Shillington, D. J., W. S. Holbrook, H. J. A. Van Avendonk, B. E. Tucholke, J. R. Hopper, K. E. Louden, H. C. Larsen, and G. T. Nunes (2006), Evidence for asymmetric nonvolcanic rifting and slow incipient oceanic accretion from seismic reflection data on the Newfoundland margin, J. Geophys. Res., 111, B09402, doi:10.1029/2005JB003981.

Trincardi, F. and Zitellini, N., (1987), The rifting of the Tyrrhenian Basin, Geo-Marine Letters, 7, 1-6, doi: 10.1007/BF02310459.

Wang, C.Y., Hwang, W.T., Shi, Y., Thermal evolution of a Rift Basin: The Tyrrhenian Sea (1989), Journal of Geophysical Research, Vol. 94, No. B4, pages 3991-4006.

Walsh, J., Watterson, J., Yielding, G., (1991), The importance of small-scale faulting in regional extensions, Nature, 351, 391-393; 10.1038/351391a0.

Wernicke, B., (1985), Uniform-sense normal simple shear of the continental lithosphere, Can. J. Earth Sci., 22, 108-125

Wernicke, B., Burchfiel, C. B., (1982), Modes of extensional tectonics, Journal of Structural Geology, 4, 2, 105-115, doi:10.1016/0191-8141(82)90021-9.

White, N., 1990, Does the uniform stretching model work in the North Sea? in Blundell, D.J., and Gibbs, A.D., eds., Tectonic evolution of the North Sea rifts: International Lithosphere Program Publication 181, p. 217-239.

Zelt, C. A. and Smith, R. B., (1992), Seismic traveltime inversion for 2-D crustal velocity structure, Geophysical Journal International, 108: 16-34, doi: 10.1111/j.1365-246X.1992.tb00836.x.

Zitellini N., Trincardi F., Marani, M., Fabbri, A., (1986), Neogene tectonics of the northern Tyrrhenian Sea, Giorn. Geol, 48, 1, 2

6. Crustal thinning in the northern Tyrrhenian Rift Basin

Manuscript 2: Crustal thinning in the northern Tyrrhenian Rift Basin. Insights from multichannel and wide-angle seismic data

Authors: Moeller, S.[1], Grevemeyer, I.[1], Ranero, C.R.[2], Berndt, C.[1], Klaeschen, D.[1], Sallares, V.[3], Zitellini, N.[4], de Franco, R.[5]

1. GEOMAR Helmholtz Centre for Ocean Research Kiel, Kiel
2. Barcelona Center for Subsurface Imaging, ICM, ICREA at CSIC, Barcelona
3. Barcelona Center for Subsurface Imaging, ICM, CSIC, Barcelona
4. Istituto Scienze Marine ISMAR-CNR, Bologna
5. Istituto per la Dinamica dei Processi Ambientali, CNR, Milan

This manuscript has been submitted to *Journal of Geophysical Research, Solid Earth.* It contains an own reference list.

Abstract

Extension of the continental lithosphere leads to rift basins or passive continental margins after break up. Seismic investigations have shown that margins are often asymmetric in tectonic structure and amount of extension. Here, we present two coincident seismic wide-angle and multichannel seismic profiles across the northern Tyrrhenian rift system sampling the crust at southward increasing stages of extension. Tomographic inversion reveals that the crust has thinned uniformly to ∼17 km between the Corsica Basin and the Latium Margin with a β-factor of 1.3. On the southern transect (80 km apart) the crust thinned eastwards from ∼24 km beneath Sardinia to a maximum of ∼11 km in the eastern region near the Campania Margin (β-factor of 2.2). This thinning is accompanied by a zone of reduced velocities in the upper crust that spread progressively towards the south-east. We suggest that the velocity reduction could be related to rock fracturing caused by a higher degree of brittle faulting as observed on MCS images. Moreover, basalt flows are imaged within this zone and heatflow values locally exceed 100 mW/m^2. However, velocities within the entire crust of 4.5-6.7 km/s are typical for continental rocks and significant magmatic under-plating is not observed. The characteristics of the pre-, syn-, and post-tectonic sedimentary units allow us to infer the timing of active rifting. In the western part of the southern transect thick post-rift sediments were deposited in half-grabens that are bounded by large blocks. In the east, fault spacing and block size diminish and recent tectonic activity is expressed by faults cutting the seafloor near the mainland of Italy. The evolution from the less extended rift in the north to distinct asymmetric margins further south is consistent with W-E rift propagation and southward increasing extension rates.

1. Introduction

Extension of the lithosphere controls the evolution of rift basins or passive conjugate margins. Conjugate rifted margins are reported by many workers as asymmetric structures including the magma-poor margins in the North Atlantic (Pérez-Gussinyé et al. 2003, Shillington et al., 2006, Ranero & Pérez-Guissyné, 2010), or the transition from active continental extension to seafloor-spreading e.g., in the Woodlark-Basin (Taylor et al., 1995, Speckbacher et al., 2011), or in back-arc basins, such as the East Scotia Sea (Barker & Hill, 1980), or the triangular shaped Lau-Basin (Dunn & Martinez, 2011). Conjugate margins often differ in crustal thickness or the amount of faulting. Moreover, in several cases the upper crustal extension in seismic cross-sections apparently does not match the extension of the lower crust (Reston et al. 2005). A conceptual hypothesis that explains asymmetric rift structures is the simple-shear model (e.g. Wernicke 1985). It proposes that the crust is separated into an upper and lower part by a crustal-scale or even lithospheric-scale detachment fault. Although shear zones within the mantle are observed on seismic images (e.g., Reston 1993) they remain controversial. Potential shallow dipping detachment faults have been detected at the Iberia rifted margin or in the Porcupine Basin (P- and S-reflector) (e.g. Reston 2004). However, such features may just be present at large stretching factors of > 3.5 when the entire crust has become brittle (Pérez-Guissyné and Reston, 2001). The impedance contrast of the detachment might be related to the transition of the brittle-ductile deformation zone or to the top of partly serpentinized peridotite. In little extended rifts, e.g., the northern Porcupine Basin, it is reported that the style of rifting changed from symmetric to asymmetric extension with the development of detachment faults cutting under the entire basin (Reston et al., 2001). Alternative models, e.g. for the conjugate margins of Newfoundland and Iberia propose that faulting in a rift basin may change from coeval to sequential. This leads to a change from symmetrical to asymmetric structures by planar Andersonian faulting. No low-angle detachment fault is needed (Ranero & Pérez-Gussinyé, 2010). Sequential faulting has also been reported from field campaigns in the young Suez-Rift (Gawthorpe, 2003). In most of these models little is known about the initial conditions prior to rifting, for instance the crustal thickness or inherited zones of weakness and structures. Similarly, few examples exist documenting the transition from little extended symmetric structures to asymmetric conjugate margin structures. From analogue experiments, Corti & Manetti (2006) showed that the pre-rift Moho topography might have a great control on the rift process. Asymmetric Moho conditions may lead to asymmetries in the amount of extension accommodated by faults.

We present the results of two coincident wide-angle seismic (WAS) and prestack time migrated seismic profiles (PSTM) transecting the northern Tyrrhenian Sea Basin (Fig. 6.1). The modelling and the interpretation of the line AB has been presented by Moeller et al. (2013). In this contribution we present the crustal-scale velocity models and prestack time migrated seismic images of the line CD as well as a joint geological interpretation of both seismic transects.

The triangular shaped and structurally asymmetric Tyrrhenian Basin is located in the Western Mediterranean Sea. It is confined by the islands of Corsica, Sardinia, Sicily and mainland Italy (Fig. 6.1 A). The aim of our study is to reveal the sedimentary and crustal architecture by combining both datasets. Further, we will investigate the development of structures that are typically observed at the early-stage of passive margin evolution. The Tyrrhenian Basin underwent little stretching in the northern sector, with increasing amount of stretching towards the south, where full continental break-up occurred and basalt-floors basins and serpentinized mantle peridotite have been drilled (Kastens et al., 1988). Thus, the basin is an interesting area to study the processes of rifted continental margins as a function of changes in the amount of extension. In this contribution we examine the rifting stage in which the deformation is changing from the early-rift phase (30% stretching on line AB, Moeller et al. (2013)) to higher extension factors (line CD) and display distinct asymmetric crustal features.

2. Geological Setting

The extension creating the basins of the Western Mediterranean Sea is the result of trench migration due to rollback of the Tethys Mesozoic oceanic lithosphere which subducted underneath the European plate from Cretaceous time (Faccenna et al., 2001; Jolivet et al., 1999). Tensile stress behind the trench triggered the episodic opening of several back-arc basins in the Western Mediterranean Sea. This development began along southern France and Iberia with the drift of the Balearic block, Sardinia and Corsica away from continental Europe and led to the opening of the Gulf of Lion and Valencia Trough during Oligocene time ∼30 Ma ago (Rosenbaum et al., 2002; Cherchi & Montadert, 1982). Extension continued in the Gulf of Lion and Ligurian Sea during post-Oligocene time (21-16 Ma; Faccenna et al., 2001) and the Sardinia-Corsica block of European continental crust underwent counter-clockwise rotation of 30° to finally collide with the Adriatic foreland.

This event led in the Miocene to the formation of the NW-SE striking Apennine orogenic fold- and thrust belt, rotating counterclockwise in the Adriatic area (D'Agostino et al., 2008). Ongoing trench migration finally triggered the opening of the Tyrrhenian back-arc basin (Malinverno & Ryan, 1986; Rosenbaum et al., 2002) from Tortonian age (9-10Ma) to late Pliocene (5 Ma) in the northern part of the basin. Rifting proceeded towards the south-east where the existence of a subducted slab is indicated by a narrow, NW-SE-directed Wadati-Benioff zone beneath the Calabrian Arc and the active volcanic archipelago of the Aeolian region (Faccenna et al., 2001; Malinverno & Ryan, 1986). The rift propagation is also reflected by the age of volcanic rocks. Volcanic rocks have ages of ∼30-15 Ma years onshore Sardinia and Corsica. Further east, samples from Elba, Montecristo and Mt. Vercelli have ages of 8-6 Ma, 5-2 Ma on Giglio Island or even recent on mainland Italy (Fig. 6.1, Savelli, 2002).

The rifting phase is marked by the presence of prominent unconformities that are interpreted to indicate the duration of the active rift phase (Trincardi & Zitellini, 1987; Zitellini, 1986).

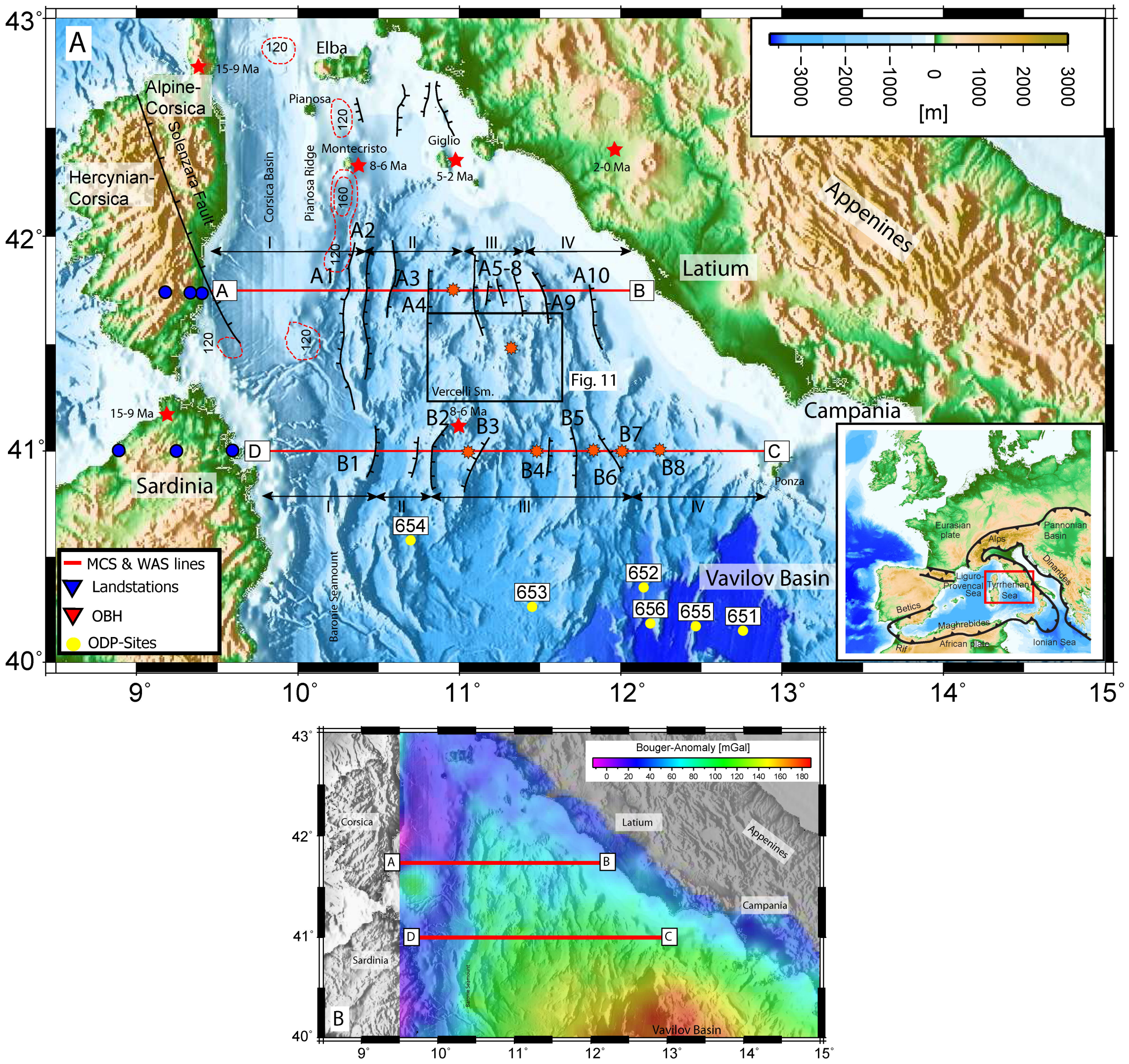

Figure 6.1.: (A) Bathymetry map of the northern Tyrrhenian Sea. The inset (lower right corner) shows the location of the working area in the Western Mediterranean and the recent large-scale plate boundary situation. Plate boundaries are taken from Schellart (2010) and Jolivet et al., (1999). N-S striking block structures visible in map view are labeled with "A" along the seismic transect AB and with "B" along the transect CD. Furthermore, lines are sub-divided in zones with respect to bathymetric characteristics and velocity distribution on crustal-scale wide-angle models (see Fig. 6.3). Red stars mark locations and ages of selected magmatic samples adopted from Savelli (2002). Orange asterisks mark locations where volcanic features are recognized on seismic sections presented in this study, or on the bathymetry map. An enlargement of the black frame is shown in Fig. 6.11. Drill sites of the ODP-Leg 107 are marked with yellow dots (Kastens et al., 1988).(B) Gravity-anomaly map shows increasing values towards the central Tyrrhenian Basin (courtesy of Getech, UK).

The focus of this work lies on the northern portion of the Tyrrhenian Basin (Fig. 6.1) between Corsica and the Latium Margin (Transect 1, line AB) and between Sardinia and the Campania Margin (Transect 2, line CD). Seafloor relief is smooth near Corsica (Corsica Basin) and around the Tuscany Archipelago south of Elba Island. Water depth is $<$ 1000 m. To the south, the seafloor is generally deeper (2000 m) and appears more rugged. It is characterized by N-S striking continental blocks, separated by sediment filled half-grabens. Most of these ridges end north of ~40.5° N where the regional water depth abruptly increases to $>$ 3000 m (Fig. 6.1). This is the so-called Vavilov Basin with basement locally formed by basalts and serpentinized mantle rocks (Kastens et al., 1988).

2.1 Sedimentary units and unconformities

The main seismo-stratigraphic units of the Tyrrhenian Basin were established in the seventies as the result of numerous MCS campaigns. The data were calibrated by several samples of the sea bottom (Colantoni et al., 1981) and by an ODP drilling campaign (Leg 107, Kastens, Mascle et al., 1988). The sedimentary package can be subdivided, from top to bottom, in three major depositional sequences: the post-rift, the syn-rift and the pre-rift sequence. They are separated by two regional unconformities: The "X" unconformity between the post-rift and the syn-tectonic sediments and the "L" unconformity between the syn-tectonic and the pre-tectonic deposits (Trincardi & Zitellini, 1987). Following the nomenclature adopted by previous workers, the syn-rift deposits are termed "A" and are mainly Early-Pliocene to Quaternary in age. The sequence below is termed Unit B and ranges from upper Tortonian to Early-Pliocene (ODP 654). The sequence is bounded at its base by the "L" unconformity. It is further subdivided in B1, B2 and B3 with respect to post-evaporitic, evaporitic and pre-evaporitic sequences (Hsü et al., 1977, Curzi, et al., 1980). B1, B2 and B3 represent the syn-tectonic sequences. However sub-units of B3 are also identified as pre-rift sediments of Tortonian to Serravallian age and have been cored, e.g. at a flank of a tilted block on the Sardinia Margin (Sartori et al., 2001). Within Unit B, the high amplitude reflector "Y" marks the top of Messinian main evaporites of Unit B2. It is well recognizable over most of the Tyrrhenian Basin due to a strong impedance contrast. The sedimentary package is limited downward by the "Z" unconformity which tops a weak reflective seismo-stratigraphic unit named Unit C. It comprises crystalline-metamorphic rocks. However, "Z" is often not noticeable, because pre-rift reflections appear to be weak. In our data we observe an intra-crustal discontinuous reflection which can be identified mainly on the line CD within the acoustic basement. The nature of the reflector is unclear. It could represent a pre-tectonic structure or an intra-crustal lithological interface like a thin volcanic layer with high velocities. We will label it "Z" throughout this paper.

3. Data acquisition and analysis

3.1 Acquisition

MCS and WAS data were acquired in April and May 2010 onboard Spanish research vessel R/V Sarmiento de Gamboa and Italian R/V Urania during the MEDOC seismic campaign. Along lines AB and CD 22 and 25 ocean-bottom hydrophones (OBH) were deployed with R/V Urania at a spacing of 8-10 km. Furthermore, the profiles were extended to the west with three land stations onshore Corsica and Sardinia (Fig. 6.1). Shooting for the wide-angle experiment was carried out by R/V Sarmiento de Gamboa using an array with 2 sub-arrays of 12 G-II airguns with a total volume of 4600 in^3. Subsequently, the R/V Sarmiento de Gamboa acquired coincident MCS lines using a 3450 m long solid-state digital streamer with 276 channels with a 12.5 m channel interval, and a 3040 in^3 source a shot every 50 m. This yields a common-mid-point (CMP) fold of 35.

3.2 Data-analysis and processing

3.2.1 Refraction and wide-angle reflection seismic data

WAS data were recorded offshore on 25 ocean-bottom-hydrophones (OBH). The OBH data loggers were synchronized with GPS time before and after deployment to correct for internal clock drift. The sampling rate of the loggers was 200 and 250 Hz, depending on the type of recording unit. Data were recorded in a continuous trace. Subsequently, the data were cut into single receiver traces and converted into SEG-Y format. In a first step the arrival of the water-wave has been used to relocate the OBH position on the seafloor. Afterwards, a statistical deconvolution and a time- and offset-variant Butterworth filter were applied to improve the signal-to-noise ratio. For the deconvolution we used a prediction lag of 0.23 s and an operator length of 1 s to suppress reverberations related to the oscillating signal of the airgun. On line CD three stations (OBH04, 07 and 11) failed to record useful data. The remaining 22 OBH stations have good data quality and excellent quality on the land stations onshore Sardinia. Examples of land station (CD3, vertical component) and OBH stations (OBH05 and OBH12) are presented in Figure 6.2. All land stations recorded Pg-phases between offsets of 40-120 km and excellent Pn-arrivals travelling through the upper mantle up to the maximum offset of 300 km. A wide-angle arrival at 3 s and 40-80 km offset was first assumed to be the Moho reflection underneath Sardinia but during modelling it became clear that it was difficult to model this arrival as a PmP. It arrived too early for a reflection coming from the crust-mantle boundary and it might rather be related to an intra-crustal reflection or to a side-echo reflection. A later, weaker reflected arrival between 60 and 80 km offset at 4-4.5 s fits better as PmP reflection. The records of OBH05, located in the Sardinia Basin, show first arrivals of Pg-phases that are clearly identifiable to a maximum offset of 40-50 km. Reflections at 4.5-5 s and 30-60 km offsets could be identified as PmP-reflections. At offsets larger than 60 km the identification of the first-arrival onset is more difficult. A clear correlation is not possible. Also at station OBH12 (centre of the profile), Pg-arrivals are clearly identified to 50 km offset and PmP reflections up to 70 km offset. Larger offsets were not used due to a decrease of the S/N ratio. Pn-phases were not reliably identified on OBH records. After phase identification and travel-time picking the data was first modeled with the forward modelling code Rayinvr (Zelt & Smith, 1992). This forward approach was aimed to achieve a reasonable initial velocity field. The land and seafloor topography for the model input was gridded at a spacing of 750 m. The data came from a global topography grid (Smith & Sandwell, 1997) and from multibeam echo sounder data collected during the survey. Furthermore, the results of the MCS data were used to define the geometry and interval velocities of the sediment-filled grabens along the profile. This is well constrained from focusing-analysis and iterative prestack-depth migration. The forward velocity model was used as an initial model for tomographic travel-time inversion. We used the code tomo2D (Korenaga et al. 2000) that jointly inverts for arrival times of both refracted and reflected phases. Cell-size of the velocity field was 200 m in horizontal direction and 100 m in the vertical direction, increasing to a cell-size of ~500 m at a depth of 30 km scaled by a square-root function. We first inverted for Pg-arrivals recorded at the near offset range (0-15 km) showing an apparent higher velocity gradient in the upper part of the crust and subsequently for all Pg-phases up to 50 km offset (Tab. 1). Afterwards, Pg-phases were jointly inverted with the PmP-reflections. After 8 iterations the RMS misfit for the crustal model converged to a misfit of 87 ms. In a last step we included the travel-times of the Pn-phase and over-damped the velocity variations above the crust-mantle boundary by a value of 200 (Korenaga et al., 2000). The final velocity model including the Pn-phase has a misfit of 94 ms (Fig. 6.3).

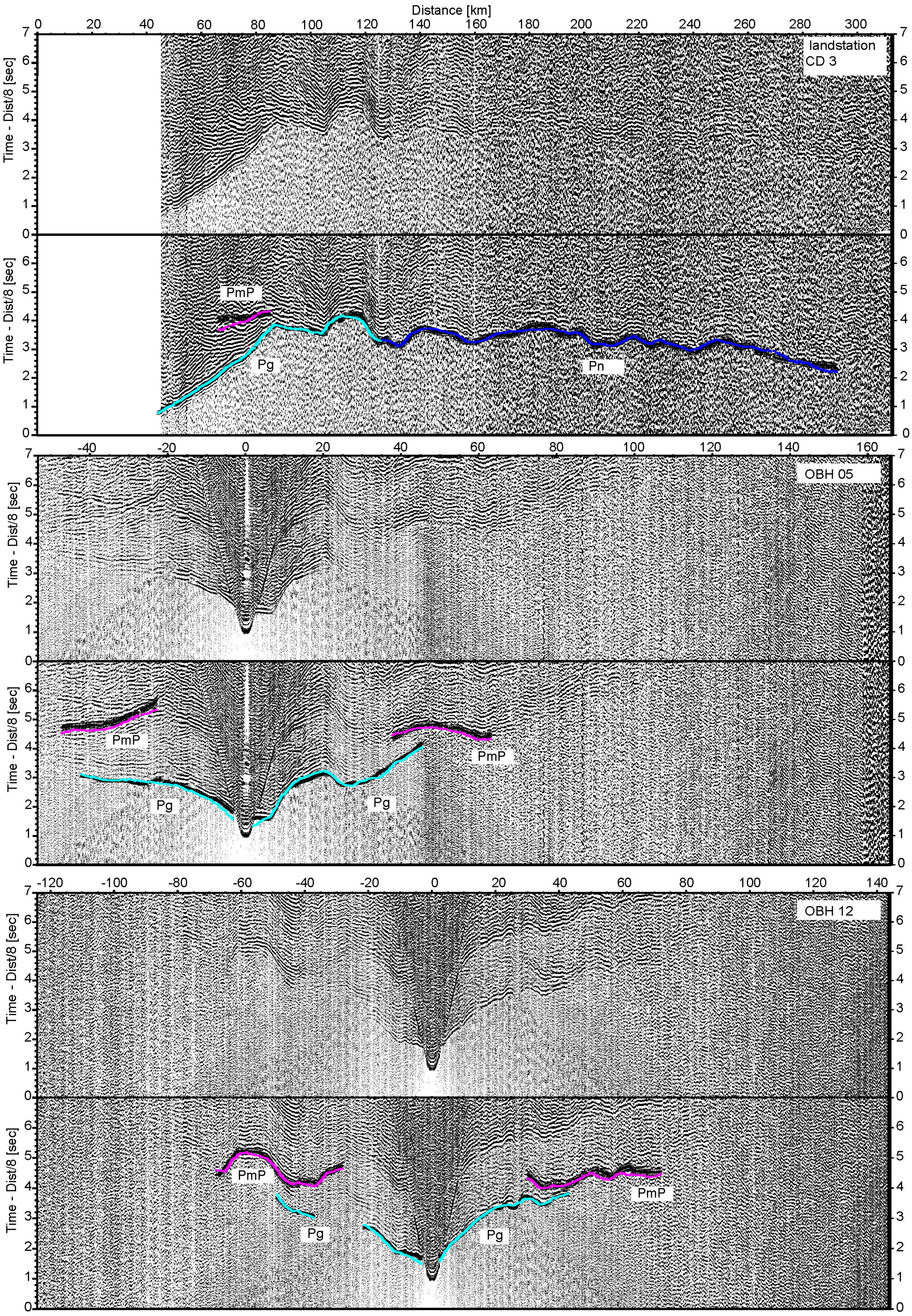

Figure 6.2.: Three examples of record sections of line CD. Travel-time picks including pick-uncertainties are used for forward modelling and subsequently for tomographic inversion. Travel-times obtained from the inverted model are light blue (P_g), blue (P_n) and pink (P_mP)

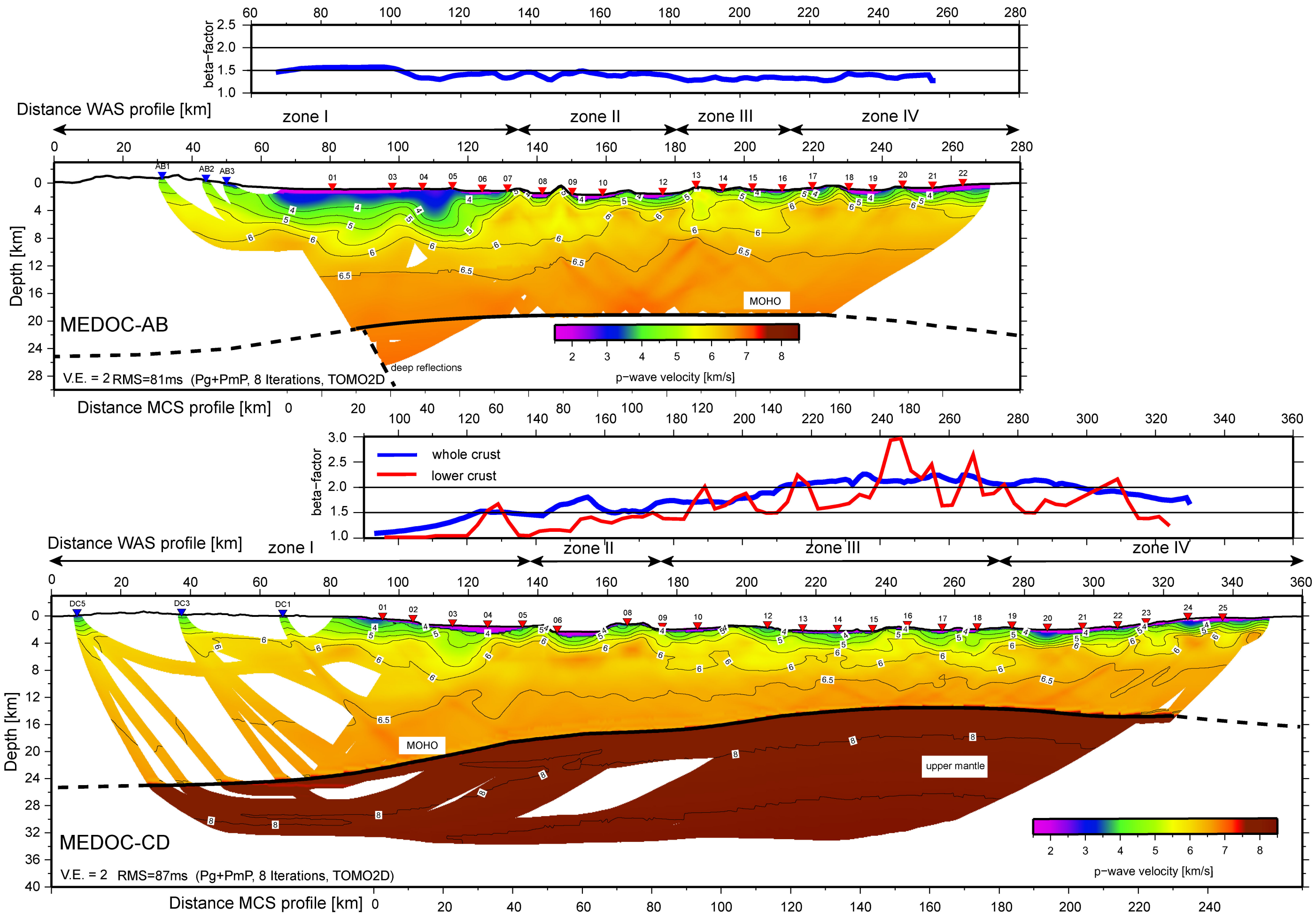

Figure 6.3.: Results of the travel-time inversion using the code TOMO2D (Korenaga et al., 2000). The two transects are divided into four zones (I-IV). The β-factor is calculated for both profiles (blue line). An initial crustal thickness of 24-25 km is assumed. For the line CD we calculated also the stretching-factor of the lower crust between the 6.5 km/s isoline and the Moho.

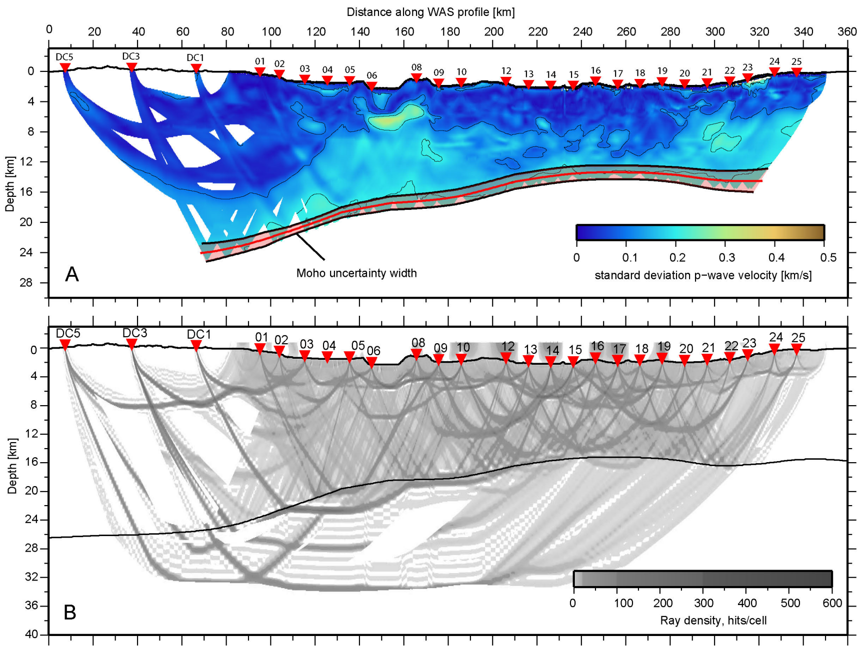

Figure 6.4.: Uncertainties of p-wave velocities along line CD. The uncertainties are estimated by calculating the standard-deviation of perturbed starting models. Moho uncertainties are in the range of ± 2 km beneath Sardinia and the Campania Margin and ± 1 km in the center of the profile.

3.2.2 Model uncertainties

To check the robustness and uncertainties of the final model we generated a set of modified starting models. The modifications were: 1) Increasing or decreasing the crustal velocities by 5%, except for the velocities in the upper sedimentary cover which are well defined by the MCS data. 2) Variations of crustal thickness by ± 1, 2 and 3 km and 3) a combination of the ± 3 km change of thickness with the ± 5% velocity perturbation. Additionally, we included some previous models that were developed during the stage of parameter testing. With this set of 18 models we calculated an average velocity field and the standard deviation (Korenaga et al., 2000) that yields the uncertainty of the model (Fig. 6.4A). The results show, that in the upper part of the model velocities are well determined (<0.1 km/s). Here, the ray density is high as indicated by the derivate-weight-sum (Fig. 6.4 B). Between km 180 and km 280, velocity uncertainties are also small in the entire upper part and down to the Moho. This area is well constrained by Pg-phases travelling 12-16 km deep into the model. Generally, velocities in the middle and lower parts have uncertainties of ∼0.2 km/s. The high uncertainty of 0.3 km/s at km 160 can be explained by the failure of OBH07 and the absence of crossing rays constraining this area. At the eastern part of the profile stations recorded fewer arrivals that travelled through the middle crust. Therefore the velocities in the lower crust are mainly determined by PmP reflections and uncertainties are higher (∼0.2 km/s), re-

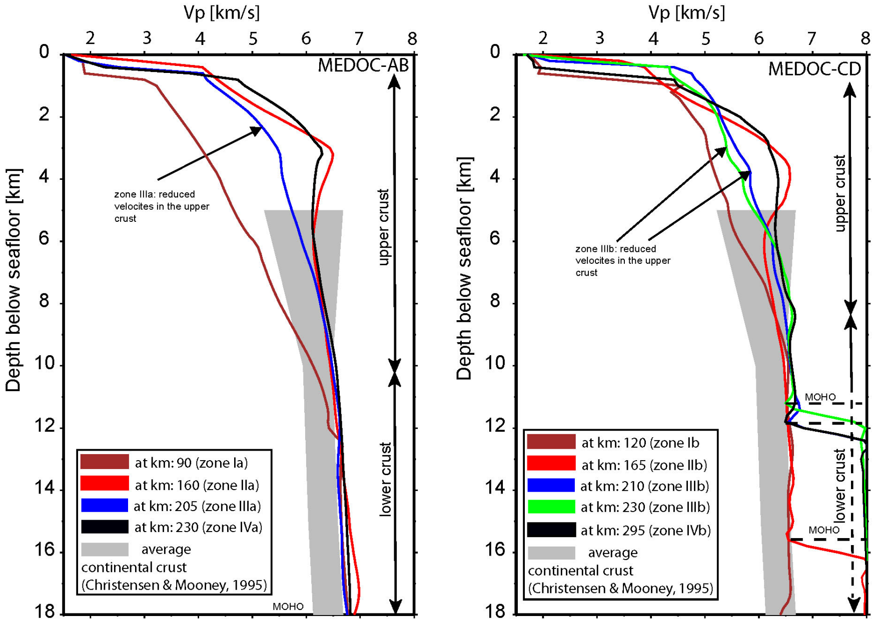

Figure 6.5.: 1D velocity-depth profiles extracted from the line AB and CD. Note that within zone III the velocities in the upper crust are lower than in the surrounding areas. Velocities at depth of 5-12 km match the global average velocities in continental crust (Christensen & Mooney, 1995) and are insignificantly higher in the lower crust.

flecting the velocity-depth tradeoff that is inherent to reflection inversion. Surprisingly velocities in the upper crustal domain underneath Sardinia/Sardinia Margin show just uncertainties of 0.1-0.15 km/s. This occurs although no reversal shoots cross the onshore domain. However, Pg- phases observed at OBH01-06 cross the upward-travelling Pg-phases of the land stations and may mitigate the uncertainties below Sardinia.
The depth of the Moho varies in a range of ± 2 km underneath Sardinia and the Sardinia Margin as well as at the Campania Margin. Between km 180 and km 280 the depth of the Moho varies just by ± 1 km. In this area the depth of the Moho and velocities are well determined and the ray-density is high. No identifiable arrivals of Pn-phases at the OBH stations exist. Hence, no rays travel through the uppermost mantle and cross the Pn-rays recorded by the land stations. Thus, velocity uncertainties in the uppermost mantle cannot be determined statistically. However, as we damped the upper crust during the last inversion step including the Pn-phases, we forced that modifications of the velocity field are mainly limited to the upper mantle.

3.2.2 Multichannel seismic data

The software packages OMEGA2 (WesternGeco) and SIRIUS (GX-Technology) were used for MCS seismic data processing and PSTM. In a first step we set geometry, applied a bandpass-filter to the data and suppressed the reverberations of the airgun signal by applying a statistical deconvolution to the shot-gathers within a window below the seafloor reflection. Multiples were attenuated by the prediction of the propagating wave-field followed by adaptive subtraction. Afterwards, the data were sorted into CMP-gathers and focusing analysis and iterative prestack depth migration were carried in order to build a first velocity field for the reflective sedimentary and upper crustal parts. After that, the velocity was calculated in a way that primary reflections at multiple reflection time dip upward and multiples downward. Subsequently, f-k-filtering was applied to remove the energy that belongs to the multiple. At near offsets where the dip of reflection events is small an inside-mute was additionally applied to remove multiples. At far offsets an outside-mute removed refracted arrivals. Focusing analysis with SIRIUS was carried out for a second time to build a final velocity model. In the weak/non-reflective crystalline crust velocities were adopted from inversion result of WAS data. The final velocity field was transformed into two-way-traveltime and used for partial stacking (stack width of 200 m) and subsequent prestack time migration. The final results of both sections are presented in Figure 6.5. We also transformed the velocity field obtained by the WAS data into TWT and illuminated the time-migrated sections.

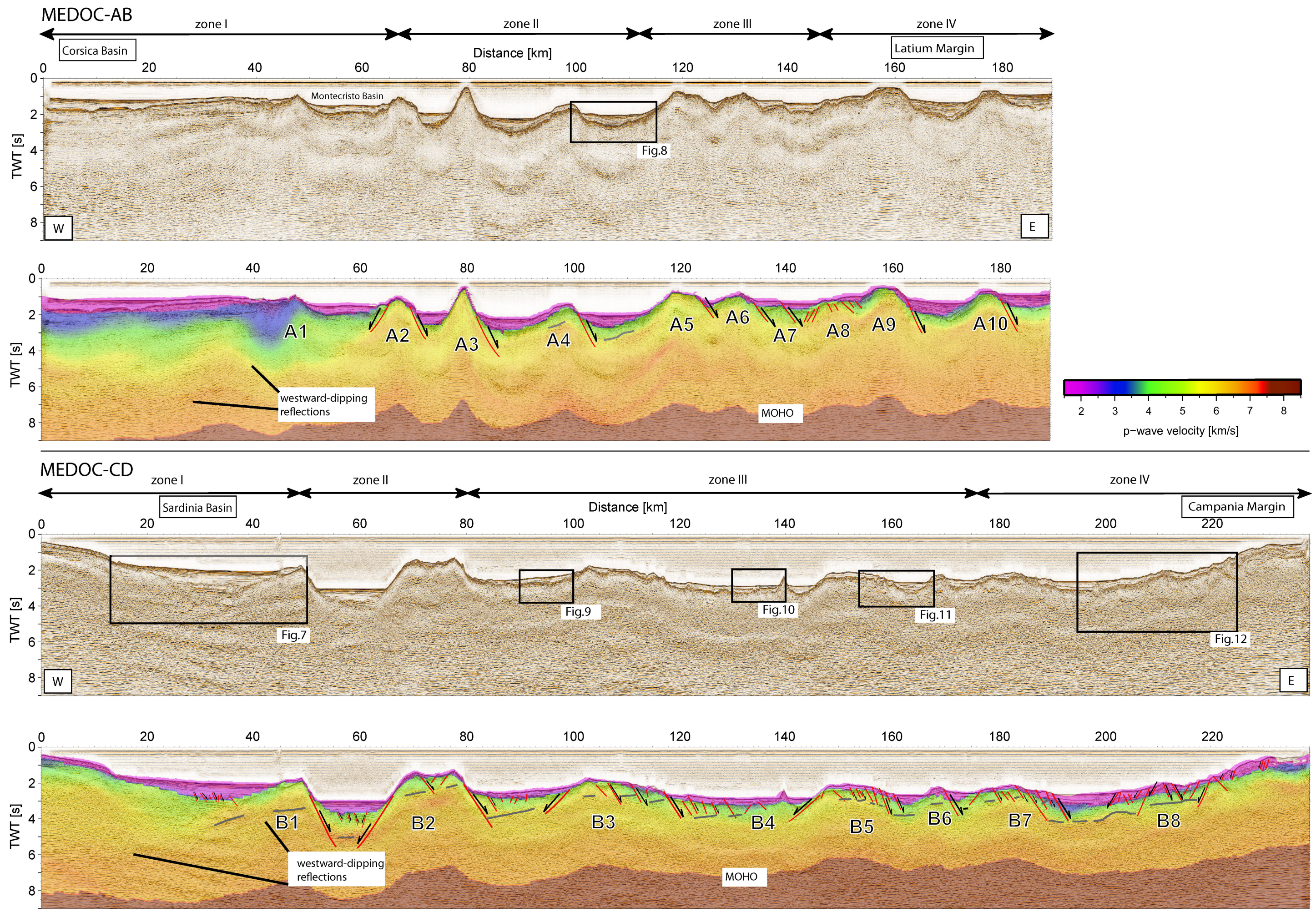

Figure 6.6.: Results of the prestack time-migrated sections with and without overlay of the velocities obtained from the wide-angle data. The grey line mark an almost continuous intra-crustal reflector (Z) which is offset by fault-bounded blocks.

4 Results

Tomographic inversion of WAS data and PSTM images provided complementary information for geological interpretation. Based on the prominent bathymetric features Mt. Baronie (B1) and Mt. Etruschi (A2) in Figure 6.1 and along strike variations in the wide-angle velocity models (Fig. 6.3) we divided both seismic lines from west to east into four zones (I-IV) (Fig. 6.3). Each zone carries specific characteristics. Zone I comprise the islands of Corsica and Sardinia and the Corsica and Sardinia Basin in the western part of the profile which are bounded by the blocks mentioned before. Zone II consists of large rotated block structures with a higher velocity gradient than in the adjacent Zone III, where a significant lower velocity gradient is observed. This can be seen on the 1-D profiles extracted at different locations (Fig. 6.5) as well as in the velocity models (Fig. 6.3). Zone IV includes the tectonic structures of the Latium and Campania Margin approaching the mainland of Italy. Here, the velocity gradient increases again. We also differentiate an upper crust (UC) characterized by Vp $< \sim$6.0-6.3 km/s, typical of upper crustal rocks (Christensen & Mooney, 1995), and a lower crust (LC) with Vp $>$ 6.5 km/s. We use these definitions to calculate stretching factors for the whole crust and for the lower crust (Fig. 6.3). For the initial crustal thickness we assumed a pre-rift crust of the thickness of Corsica and Sardinia Islands of 24-25 km (Contrucci et al., 2005, Mele & Sandvol, 2003). For the LC we assumed an initial thickness of 7 km as mapped beneath Sardinia and the Sardinia Margin. Stretching factors were only calculated where MCS data are available (Fig. 6.3). The description of line AB is briefly presented. A detailed description of the prestack depth migrated section is presented elsewhere (Moeller et al., 2013).

Zone I: The Corsica and Sardinia Margin

This zone contains the 50 km wide Corsica Basin and the Montecristo Basin in a water depth of ∼1000 m as imaged on line AB and the 30 km wide Sardinia Basin imaged on line CD. The Sardinia Basin is located in a water depth of 1550 m. It is bounded by the ridge like Baronie Seamount (B1) to the east (Fig. 6.1). The Corsica Basin hosts a thick pile of sediment as imaged in the PSTM section at 4.5 s TWT (Fig. 6.6). The acoustic basement of the Corsica Basin is in good agreement with velocities changing from ∼5 km/s to ∼6 km/s as obtained from the WAS model at a depth of ∼6 km (Fig. 6.3 and 6.6). Unit A is a post-tectonic sequence, well stratified and horizontally deposited (Fig. 6.6). Detailed seismic images are provided in Moeller et al. (2013). A clear boundary to unit B1 consisting of post evaporite Messinian deposits is not observed (Zitellini et al., 1986). B1 thins from 0.6 s to 0.15 s from west to east. The "Y" unconformity at the top of Unit B2 can be traced through the entire Corsica Basin and appears as an erosional unconformity intersected by canyon structures. Underneath the Messinian deposits, the Miocene infill is fan-shaped. This feature can be interpreted as a syn-tectonic sequence, deposited during the formation of the Corsica Basin that probably started 30 Ma ago in the Oligocene (Mauffret et al., 1999). The sedimentary sequences terminate against a

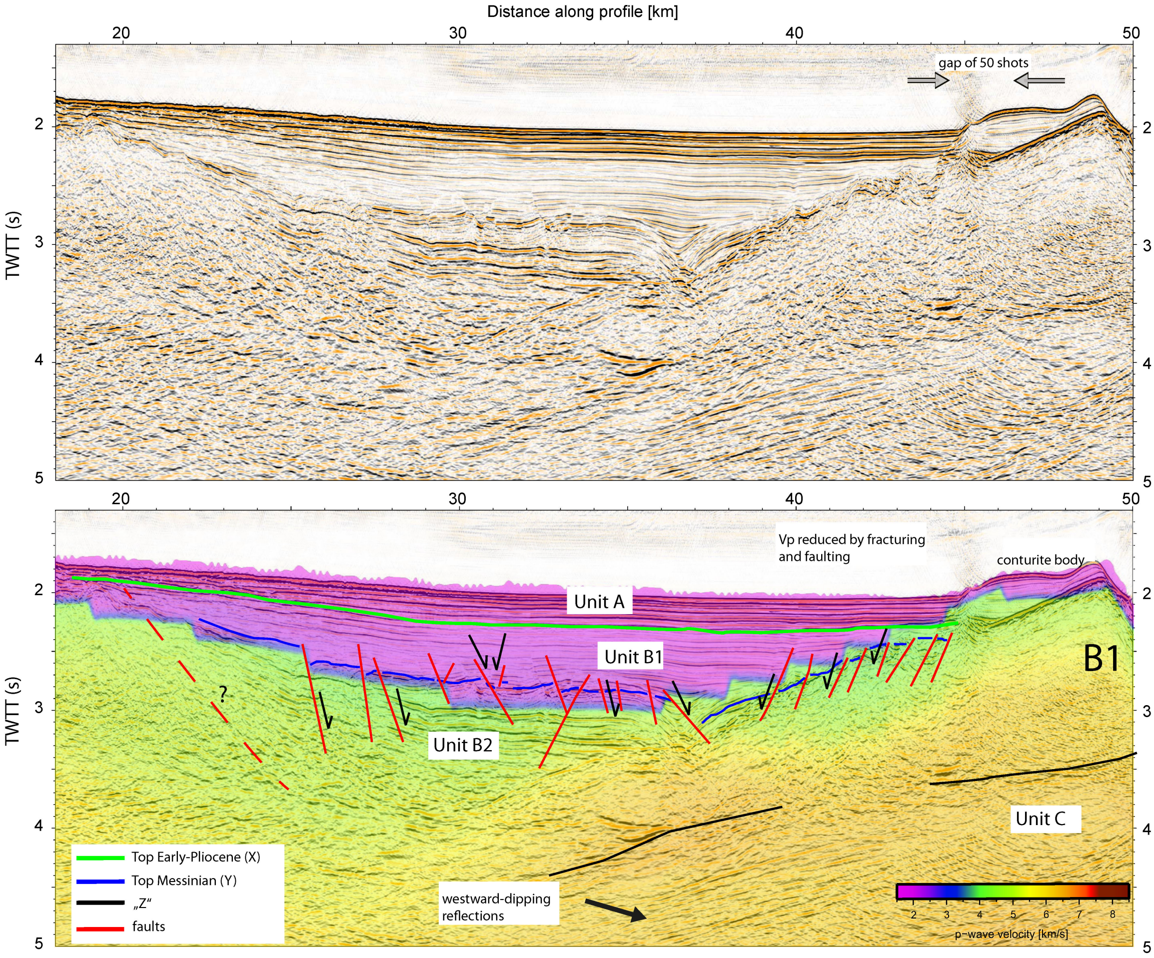

Figure 6.7.: Enlargement of the Sardinia Basin. The basin contains a 0.3 s thick layer of post-tectonic deposits (Unit A). Beneath this unit, post-evaporitic and evaporitic Messinian reflectors (Y) are identified. The upper part of the evaporites consists of thin and fine layers (B1), whereas the thick reflectors might belong to voluminous salt deposits (B2). Syn- and post-tectonic reflections are onlapping on the tilted block B1. Internal reflections within this block indicate the rotation direction. See Fig. 6.6 for location.

series of westward dipping reflectors near the Pianosa Ridge. Near the surface, reduced p-wave velocities are observed from the wide-angle data. We interpret this feature as a tilted continental block that rotated on the fault that bounds the Corsica Basin to the west and is fractured in the upper 2-3 km. The feature might also be related to thrusts of a former collisional prism (Mauffret et al., 1999). In the adjacent Montecristo-Basin a sequence of post-, syn-, and pre-rift strata is observed. The syn-rift strata are of Messinian age and indicate that this sub-basin developed after the formation of the Corsica Basin (Moeller et al., 2013). From Moho reflections (PmP) underneath the Corsica Basin, our tomography shows that the crystalline crust is 15 km thick similar to a seismic model further north (Contrucci et al., 2005). Thus the crust has thinned by a β-factor of $\sim$1.5 (Fig. 6.3).

Further south, the infill of the Sardinia Basin consists of a 0.3 s TWT thick Unit A which is thinner than in the Corsica Basin ($\sim$0.5 s TWT). The unit seems to be undisturbed and underwent little tectonic activity (Fig. 6.7). The interval velocity is $\sim$2.0 km/s. Below Unit A the "X" unconformity marks the top of Unit B which is $\sim$1.6 s thick. This sequence of Early-Pliocene to Messinian age can be clearly divided into an upper and a lower sequence (Curzi et al., 1980) which is cut by normal faults. The upper part is almost transparent and has also interval velocities of 2 km/s. It is bounded at depths by the high amplitude "Y"-reflector which is related to evaporites of Messinian age. Salt layers in this sub-basin have been mapped by Fabbri & Curzi (1979). At this unconformity Vp changes from 2.0 km/s to $\sim$3.5-4.0 km/s. This is related to the high velocities of evaporitic sequences. The upper evaporitic sequence (B1) is 0.2 s thick and fine laminated whereas the lower sequence (B2) shows deposits of greater thickness. Due to the deposition during active rifting the entire sequence is fan-shaped and tilted. Where the Messinian sequence terminates against the tilted block B1 the velocities increase suddenly to 5.5 km/s in the lower part and to 4.5 km/s in the upper part of the block. The reduced velocities coincide with faults and fractures (Fig. 6.8), indicating a relationship between both observations. This demonstrates a good structural correlation of the two data sets. The PSTM shows further, that reflections of internal block structures dip towards the west. They can be identified to $\sim$7s TWT (Fig. 6.6 and 6.8). We refer the bright top of dipping reflections to "Z" which is seen on many other rotated blocks farther east (Fig. 6.6). The dip direction is similar to those reflections that bound the Corsica Basin to the east (A1) and support that those reflections are rather related to tilted pre-rift strata. The wide-angle model reveals that Vp in the UC (Fig. 6.5) mimics velocities typical for continental crust (Christensen & Mooney, 1995). In the lower crust, however, Vp of 6.5-6.7 km/s is slightly higher than for average continental crust. The crust underneath Sardinia is 24-25 km $\pm$ 2 km thick and has been thinned at least by a factor of $\sim$1.3 - 1.5 to 16-19 km at the Sardinia Margin (Fig. 6.3). This is slightly thicker than the crystalline crust underneath the Corsica Basin.

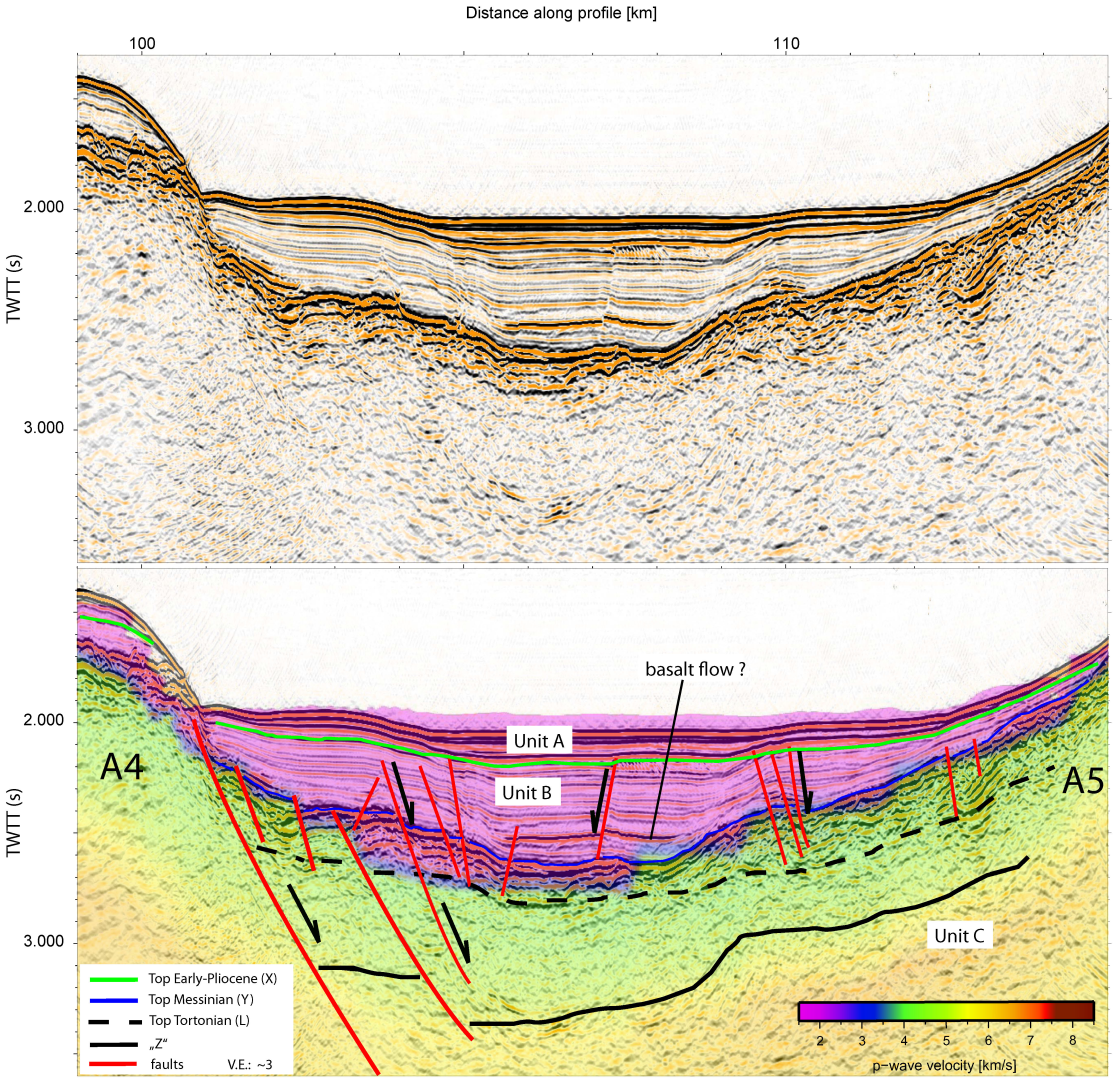

Figure 6.8.: : Example of the stratigraphic units in the northern Line AB (zone II). Horizontally layered deposits (Unit A) mark the post-tectonic sequence. The Early-Pliocene and Messinian deposits (syn-tectonic Unit B) and the basement (Unit C) are cut by normal faults. The weak reflector "Z" might represent an internal (maybe folded) layer within the crystalline basement. It coincides with a change in velocity from 4.5-5.5 km/s. For location see Fig. 6.6

Zone II: Deep sub-basins

East of the Corsica and Sardinia Basin the area is characterized by a series of horst- and graben structures. Zone II contains the deepest part of both profiles. The deepest basins are bounded by the rotated blocks A2 and A5 and B1 and B2 (Fig. 6.6). In the sub-basin bounded by block A4 and A5 Unit A appears ~0.2 s thick and is horizontally stratified. In Unit B, normal faults indicate tectonic activity during Pliocene and Messinian age (Fig. 6.8). The Top Messinian is marked by the high amplitude reflector "Y" and shows internal structures which are partly chaotic. Here, Vp increase rapidly from 2 km/s to 3.5-4 km/s. Below the Messinian sequence weak reflections, perhaps pre-rift strata, are visible and bounded by a discontinuous reflection. The reflection might represent the top of a pre-tectonic intra-basement layer ("Z"). It coincides with increasing velocities from 4.5-5.5 km/s. A high amplitude reflection within Unit B might be related to a volcanic feature and is discussed together with similar features that occur along line CD.

In this zone the geometry of the Moho is flat-lying with a crustal thickness of 17 km indicating a stretching factor of ~1.3 (Fig. 6.3). The sub-basin east of the Sardinia Basin is bounded by the large blocks B1 and B2. It is the deepest locus along the line CD. Here, the topography on the western flank deepens from 1000 m to 2300 m water depth (Fig. 6.6). The infill of the graben shows a sedimentary sequence similar to the infill of the Sardinia Basin (Fig. 6.8). Some small chaotic features are likely to be related to debris flow deposits from the steep flanks. Faults that cut the lower Messinian evaporites are clearly imaged and a fan-shaped geometry is more distinct. Reflections within the block B2 dip also towards the west and mimic the velocity isoline distribution revealed by the wide-angle data (Fig. 6.6). From the wide-angle model it is derived, that the velocities increase from 4 km/s at the top of the block to 6 km/s at a depth of ~3 km and to 6.5 km/s at a depth of 12 km (Fig. 6.5). Beneath, the lower crust has velocities of 6.5-6.7 km/s and is ~5 km thick. The crust in this deep zone has locally thinned by a β-factor of 1.7 and is 3-4 km thinner than the crustal thickness on line AB.

Zone III: Highly fractured and thinned crust

The inversion of WAS data of line AB reveal a 40 km wide zone (Fig. 6.3) where the velocity gradient to a depth of 4-5 km is lower (~0.5 s^{-1}) than in the surrounding zones II and IV (~1 s^{-1}) (Fig. 6.5). In this area the block size (A5-A8) decreases while the number of faults increases, e.g. the fractured block A8. However, there are no substantial variations of the crustal thickness on the line AB (~17 km) compared to a significant decrease on the line CD (~11 km). The zone III on line CD is characterized by a sudden decrease of velocities in the upper crust, similar to zone III on line AB. The 1-D velocity-depth-profiles in Figure 6.5 show, that the gradient of the upper crust is reduced (~0.3 s^{-1}) to a depth of 5-6 km below seafloor, compared to the velocities at km 165 and further east at km 295 where the upper crust has a gradient of ~1 s^{-1}. This velocity reduction is in the order of ~12%. The PSTM section shows further, that block sizes in this region diminish (Fig. 6.6) and the number of faults increases accord-

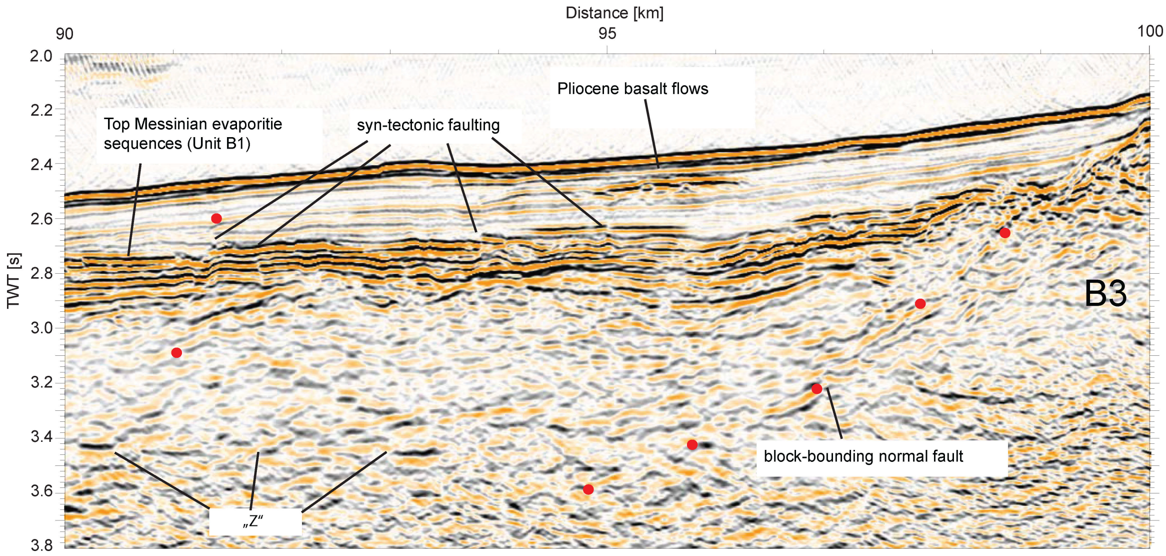

Figure 6.9.: Close up of the PSTM section from Zone III. Below the post-tectonic sequence fine laminated, party discontinuous, reflections might represent layers of gypsum of Messinian age (see Site 654 ODP-Leg 107, Kastens et al., 1988). Faults cut through this layer indicating higher fracturing. For location see inset in Figure 6.6

ingly. However, faults in zone III do not generate wide horizontal displacements like the blocks B1 and B2 in zone I and II (Fig. 6.9, 6.10 and 6.11). The minimum penetration of faults is indicated by the intra-basement reflector "Z" where it is apparently offset by faults (Fig. 6.11). Where "Z" is absent or weak, faults are just recognized within sedimentary deposits. However, it seems reasonable to suggest that velocities to 5-6 km depth and ∼6 km/s represent fractured and/or altered upper crustal rocks on the wide-angle model (Fig. 6.3). Below this depth, Vp increases rapidly from ∼6 km/s to 6.5 km/s within 2-3 km at mid-crustal levels. The lower crustal part is 3-4 km thick with Vp of 6.5-6.6 km/s. Zone III is also a region where the entire crust has thinned to a minimum of ∼11 km (Fig. 6.3). This corresponds to a stretching-factor of ∼2.2. The thinning is similar to the long wave-length thinning trend of the lower crustal parts by a factor of 2.

Moho reflections on the MCS data are not well imaged, because remains of the multiple occur at the same TWT. Therefore, differences between primary and multiples are not discernible.

The sedimentary Unit A has a constant thickness of 0.2-0.3 s TWT and locally 0.4 s in some deeper basins. On top of the main blocks, Unit A is disturbed by high-angle faults reaching the seafloor (Fig. 6.11) but are undisturbed deposited in some sub-basins. The Messinian evaporitic unit is partly fine stratified (Fig. 6.9) but in places chaotic and fractured, or even unnoticeable (Fig. 6.10). The "Z" reflector within the basement as

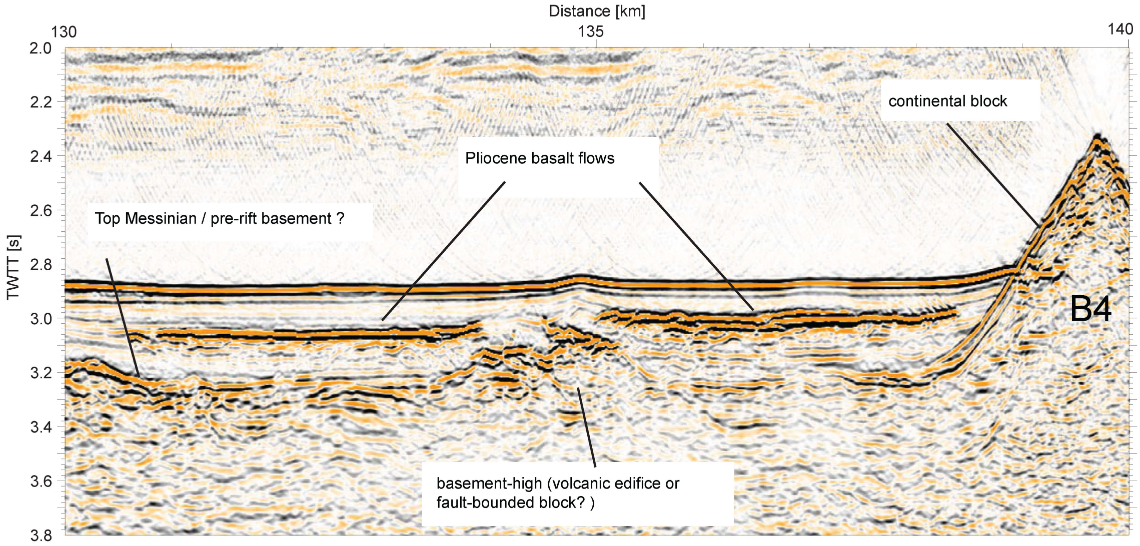

Figure 6.10.: High amplitude reflections in Zone III located within the post-tectonic sediments (Pliocene) are likely to be basalt flows (e.g. drilled at Site 654, ODP-Leg 107). The basement-high may correspond to a volcanic edifice. The reflector below the basalt flows might represent either Messinian deposits, pre-rift layers or older volcanic flows. For location see inset in Figure 6.6

well as similar reflectivity patterns below, are almost everywhere evident in this zone. They are characterized by a change of Vp from 4.5-5.5 km/s. Within the foot- and hanging wall "Z" is tilted and offset by faults.

In the PSDM section high amplitude features within the Plio-Pleistocene sediments are observed (Fig. 6.9, 6.10 and 6.11). These patterns are similar to a reflection pattern on line AB (Fig. 6.8). They have the polarity of the seafloor reflection and thus are not low-velocity, e.g. caused by the presence of free gas. These reflections can be interpreted as magmatic sills or flows, probably similar to the basaltic layer of 2 m thickness drilled during the ODP Leg 107 at Site 654 (Fig. 6.1) at a depth of 80 m below seafloor (Kastens et al, 1988). Due to the rapid cooling history it was assumed that this basaltic layer was an extrusive lava flow and not a sill. The widths of the magmatic layers range between 1-3 km on the seismic images. In the flat area between the block B3 and B4 (Fig. 6.10) apparently two basalt layers of ~3 km extent come close to a basement-high. This might be a small continental block or a volcanic edifice. In Figure 6.11 the basaltic extrusions between block B6 and B5 occur at three depth-levels within the Pliocene deposits. The lowermost basaltic layer is clearly fractured, similar to the basalt flow in Fig. 6.8.

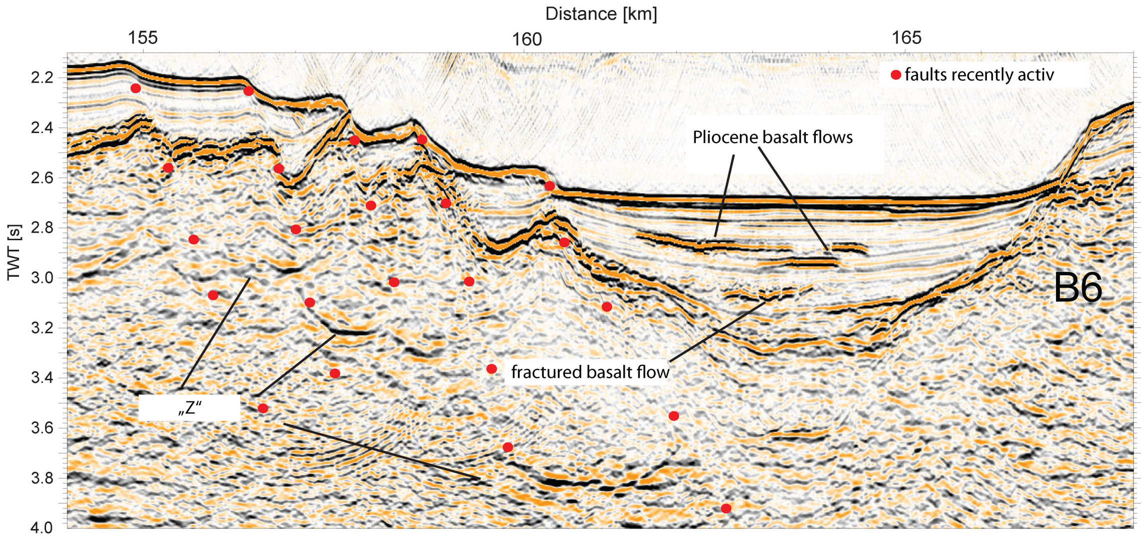

Figure 6.11.: At least three volcanic eruptions are recorded within this sub-basin. Faults cutting through block B5, crop out at the seafloor indicating recent tectonic activity. The basement layer "Z" is dissected by these faults. Its nature is rather a lithological interface than a detachment. For location see inset in Figure 6.6

Zone IV: The Latium and Campania Margin

Towards the Latium Margin (line AB) the block size increases again and the blocks A9 and A10 are just bounded by main faults dipping to the east. A dense small-scale fault population like in zone III is not observed in the PSTM section and can explain the increase in p-wave velocities. The flat summits of blocks A9 and A10 and an angular unconformity indicate wave erosion, suggesting that this area was above sea-level at the onset of rifting (Fig. 6.6). At the Campania Margin (line CD) the water depth shallows to 400 m. Here, the crust has a thickness of 13 km implying a β-factor of $\sim$1.8. The sedimentary Unit A is cut by high-angle normal faults reaching the seafloor. The underlying Messinian Unit B is much thinner, predominantly discontinuous or even absent. Faults intersect this unit and cut also through the underlying basement (Fig. 6.12). At km 199 a cone-like body buried by post-tectonic sediments can be seen. It is underlain by some short and discontinuous reflections of higher amplitude with similar reflectivity characteristic to "Z". The area of these reflective patterns coincides with a velocity anomaly between km 270 and km 300 km (Fig. 6.3) reaching 6 km/s just 2 km below the seafloor (Fig. 6.3). An undulating and east-dipping continuous reflector of low-frequency and high amplitude occurs within the basement between km 190 and km 220 at 3.5-4 s TWT and may represent "Z" (Fig. 6.12).

5 Discussion

Results from PSTM and WAS data provide new clues to better understand the evolution of extension in the northern Tyrrhenian Sea Basin. The PSTM sections display the sedimentary and tectonic structures. Crustal thickness and velocity distribution obtained by tomographic inversion provide constraints on basin formation and rift evolution. Our main observations are:
1) The crust has thinned homogeneously by block rotation and crustal thinning along the line AB with a stretching factor of 1.3 (Moeller et al., 2013). Extension concentrated from upper Tortonian to Early-Pliocene. 2) Along the line CD, 80 km farther south, the crust thinned with a stretching factor varying from 1.3-1.5 on the western Sardinia Margin to a maximum of 2.2 towards the Campania Margin. 3) On both lines we observe a decrease of the velocity gradient in zone III near the center of the basin. This feature coincides with a decrease of fault spacing and an increase of the amount of smaller faults bounding smaller blocks. On line CD the PSTM section reveal an intra-crustal reflection "Z" that is offset by normal faults and is perhaps related to a thin volcanic sheet. Moreover, magmatic activity is observed and recognized by high amplitude reflectors within the post- and syn-tectonic sedimentary deposits. This feature is confirmed by drilling results of ODP Site 654 (Kastens et al., 1988).

5.1 Temporal and spatial distribution of deformation

The timing of the main rift phase can be confirmed by the depositional characteristics of the sedimentary infill of the sub-basins. The absence of faults and the uniform stratification of the Late-Pliocene to Holocene sediments (Unit A) covering the line AB east of the Corsica Basin indicates that tectonism were not active during this time. High-angle normal faults cut the sedimentary architecture up to Early-Pliocene age and let infer the onset of rift cessation. Below, tilted and fan-shaped, partly highly fractured sequences show that the main rift phase occurred between upper Tortonian to Messinian age. From the amount of rotation of the hangingwall and footwall blocks (A5-A7) it can be locally inferred that rifting along the line tended to move sequentially eastwards (Moeller et al., 2013). Based on geological and older seismic datasets it was inferred that the opening of the basin did not occur before Late Miocene or upper Tortonian age (e.g., Rosenbaum et al. (2004), Sartori (1990)). It has been noted, e.g. by the ages of volcanic rock samples (Savelli, 2002), that the rift moved eastward probably related to subduction rollback (Jolivet et al., 1998, Faccenna et al., 2001). However, from the age of the syn-tectonic sequences the propagation is barely noticeable on the seismic image AB (zones II-IV). This excludes the evolution of the Corsica Basin because its development is related to an earlier extensional stage that started in the Oligocene (Mauffret, 1999). On the line CD we observe an unequivocal change in the stage of deformation and also in the thickness of the syn- and post-sedimentary deposits from west to east. At the Sardinia Margin (zone I and II) thick Late-Pliocene to Holocene sedimentary structures are undisturbed (post-tectonic) but the underlying Early-Pliocene to

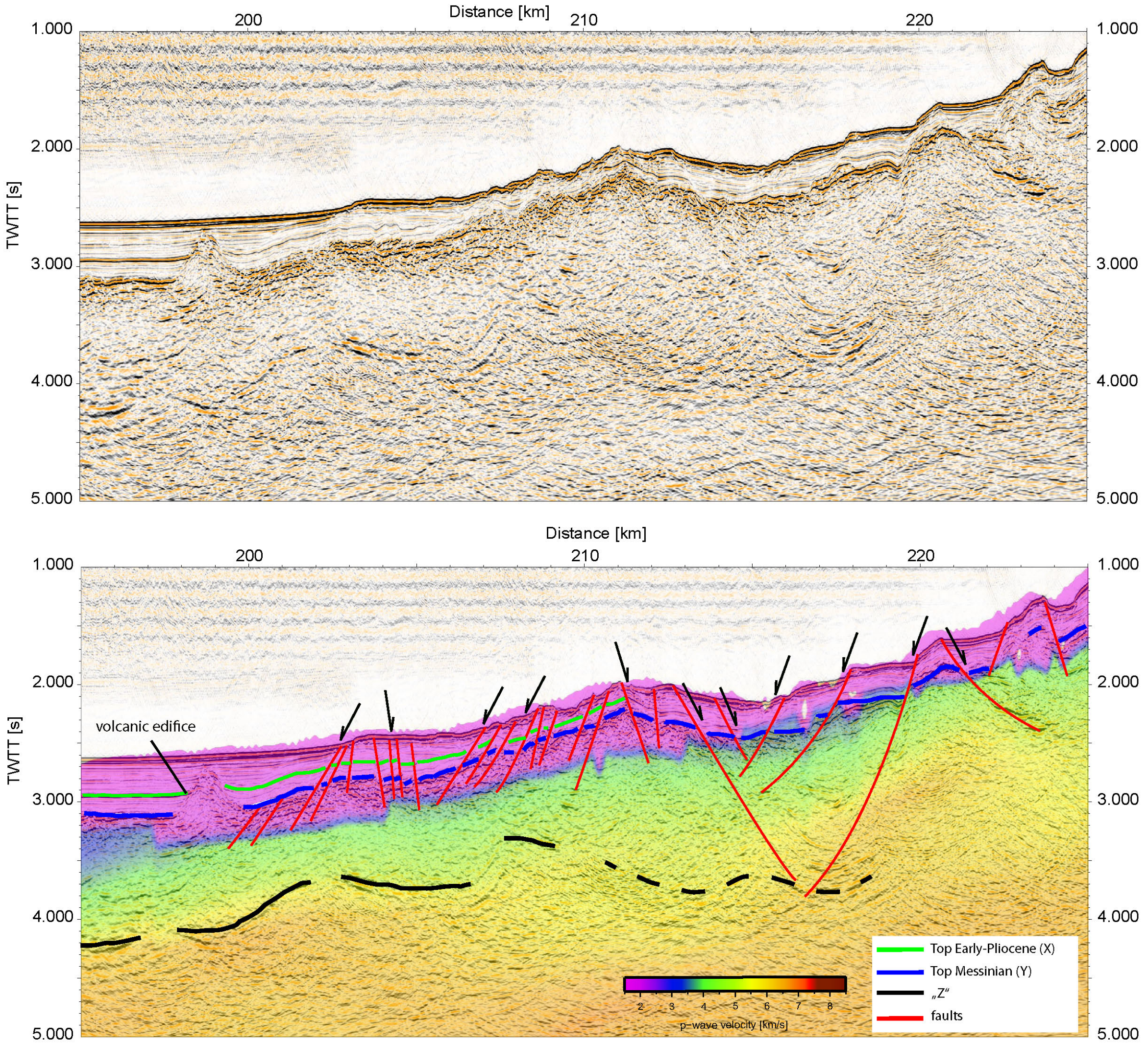

Figure 6.12.: The eastern margin of the line CD. Faults cut through the seafloor indicating that tectonic activity has not fully ceased. A cone-like structure might represent a volcanic feature. The internal basement reflector "Z" coincides with the velocity change from ∼4.5-5.5 km/s.

Messinian upper and lower main salt deposits (Hsü et al., 1977, Curzi et al., 1980) are offset by normal faults. They indicate syn-depositional tectonic activity (Fig. 6.7). This feature is similar to the Messinian sequences imaged on the line AB and implies that this area and the Sardinia Margin evolved approximately at the same time.

Within zone III of line CD the thickness of the Messinian evaporites is remarkably decreased but still unambiguously present, for instance shown in Figure 6.9. A conceivable explanation might be that the water depth was shallower and subsided later. Hence, the region underwent fewer cycles of flooding and desiccation during the Messinian salinity crisis. Drilling at Site 654 on the top of a tilted block (located ∼50 km south) revealed at least five intervals of finely laminated gypsum, inter-bedded with calcareous clay but no thick salt deposits (Kastens et al., 1988). This suggests that the densely spaced high-amplitude reflectors imaged in Figure 6.9 perhaps are also gypsum of the upper Messinian age. Their location is close to the N-NE projection of Site 654 onto the line CD and in similar water depth.

Moreover, the thickness of the Pliocene to Holocene cover in zone III is thinner than at the Sardinia Margin. This can be related to the greater distance to the land masses or to the high elevation of block B2. The block might act as a topographic barrier for further sediment transport from subaerial structures that leads to a reduced sedimentation rate in zone III.

Further east, from km 150 on towards the Campania Margin normal faults offset the intra-basement reflector "Z" and cut also through the young sedimentary cover up to the seafloor (Fig. 6.10). From those faults it can be deduced that to some extent tectonism is recently still present in the central and eastern region near the mainland of Italy.

All observation confirm either that extensional tectonism was first active in the northern and western region (Rosenbaum et al., 2004) and propagated E-SE, or that extension commenced contemporaneously in the entire northern Tyrrhenian area but is still active in the east while it ceased at the western margin. We believe that the locus of most active extension moved from west to east with time because the deep western sub-basins have apparently subsided more and began to cool earlier. The heat flow of 50 mW/m^2 is typical for a passive continental margin compared to the warmer eastern region with a present heatflow of ∼100 mW/m^2 (Della Vedova et al., 1984). A rift propagation to the SE is also confirmed by the drilling results of ODP-Leg 107 in the central Tyrrhenian Basin (Kastens et al., 1988, Sites 654 and 652 in Fig. 6.1), because continental blocks tilted during Tortonian to Messinian age at the upper Sardinia Margin (Site 654) and during Messinian to Pliocene age at the lower Sardinia Margin which is located further to the east (Site 652).

5.2 Asymmetric crustal thinning

The timing of rift activity and the amount of crustal thinning allows us to discuss the crustal evolution in the Northern Tyrrhenian Sea. The velocity model and rotated fault-bounded blocks of the line AB show no significant variations in extension and appear to be homogeneously stretched on a crustal scale.

At the line CD we infer from the data, that rifting at the Sardinia Margin commenced from late-Tortonian to Early-Pliocene age and propagated eastwards. With a delayed onset of rifting the central and eastern zones have been stretched to a maximum of 2.2. This factor is a minimum because the contribution of crust by magmatic intrusions and underplating is not known (Reston et al., 2004). Tectonism in zone III and zone IV is younger, suggesting that the crust has been affected by a shorter period of extension. Nevertheless, that the thinnest crust occurs in this area might imply two possible explanations in relation with the extension rate: 1) Extension rate increases while the most active rift zone moves eastwards. 2) The extension rate was constant but the pre-rift crustal thickness had lateral variations and might have controlled the necking of the crust (Corti & Manetti, 1995).

We favour the first scenario because it is known from GPS measurements that the Adriatic plate rotates counterclockwise around a pole of rotation situated north of the basin in the Po-Valley/French Alps (D'Agostino et al., 2008). Thus, extension rates are forced to increase with increasing distance from the pole.

From tectonic structures on the line CD we conclude that the degree of faulting and fracturing is highest in zone III (Fig. 6.6). This is constrained by the reduction of velocities (~12%) in this area as shown in Figure 6.5. Reduced upper crustal velocities due to altering and fracturing were also recognized in the Galicia interior Basin (offshore Iberia) in conjunction with the decrease of fault spacing and block size as extension increases at the locus of the thinnest crust (Pérez-Gussinyé et al., 2003). Decreasing proportions of structures and fault spacing with increasing extension-factors are also shown from analogue modelling (Ackermann et al., 2001). From Site 651 it is known, that the 3000 m deep Vavilov Basin to the south-east contains basalts and serpentinized peridotites (Kastens et al., 1988) indicating that mantle rocks are almost at the seafloor. This supports continental breakup and require even higher stretching rates. It has been reported that the Marsili Basin in the south-eastern Tyrrhenian Sea developed even at rates of 190 mm/y (Nicolosi, 2006).

The increase of stretching and crustal thinning from north to south shows similarities to the V-shaped Porcupine Basin west of Ireland. Here, the crust is only moderately stretched in the North while the crust in the South is stretched by a factor > 6, possibly in conjunction with the development a serpentinite diapir (Reston et al., 2004). Our observations in the northern Tyrrhenian Sea imply that the change from an apparently homogenously stretched basin to an asymmetric margin configuration is the result of N-S increasing extension rates superimposed with a W-E propagation of the locus of most active rifting. This may lead to the necking of the crust on a NW-SE orientation towards the abyssal areas of the central Tyrrhenian Sea. This characteristic is also indicated by the increasing positive gravity-anomaly to the centre of the basin (Fig. 6.1D).

5.2.1 Brittle and ductile extension

A common feature of rift basins and passive margins on seismic sections is, that the amount of brittle extension is often less than the lower crustal thinning. Some workers explained this discrepancy by different amounts of stretching in the brittle and ductile crustal domains (e.g., Davis & Kusznir, 2004) or by slip on detachments or low-angle normal faults generating wide horizontal extension (Forsyth, 1992, Colletini, 2009). In contrast, the amount of brittle extension could be underestimated in seismic data (e.g., Marrett & Allmendinger, 1992, Reston, 2005). We estimated the amount of brittle extension and whole crustal thinning on the little extended line AB by analyzing a prestack depth migrated section and wide-angle velocity model (Moeller et al., 2013). This estimation shows that the amount of fault heaves in the upper crust and ductile deformation in the lower crust is similar. Thus, non-uniform stretching is not necessary to explain little extended and rift basins. Moreover, long-lived detachment faults are not recognized on both seismic lines and seem not to be a feature of the rift basin at such extension factors. Testing if the brittle extension on the line CD matches the whole crustal thinning is not possible directly. Syn-tectonic sedimentary structures in zone III appear to be chaotic and highly fractured. This makes an estimation of the entire fault displacement difficult. Another approach would be comparing the amount of whole crustal thinning with that of the lower crust. Overall stretching factors for the lower crust match the long wave-length thinning trend of the whole crust of 2.0 and 2.2 (Fig. 6.3). This implies that the upper crust must have been extended by approximately the same amount by means of brittle failure. Large displacements on low-angle normal faults, like the Zuccale fault on Elba (Keller & Coward, 1996) are not detectable. However, if such a feature exists, it should be imaged on the seismic sections. We are aware of that the lower part of the crust we used for our estimations is not a geological unit that is constrained by any reflectivity. However, we can assume that the varying thickness between the 6.5 km/s isoline and the Moho is proportional to an entire lower crust.

The result let infer that the crust along the line CD has been stretched homogeneously by the increasing amount of brittle extension in the upper crust and ductile deformation in the lower crust. From the Galicia Interior Basin, it has also been shown that parts of the lower crust may enter into the brittle zone (Pérez-Gussinyé et al., 2001). Though, this would not change the interpretation.

5.2.3 Magmatism

From geochronological data Savelli (1987 and 2002) reported, that between Oligocene and recent time five episodes of magmatic activity affected the entire Tyrrhenian region. The oldest activity of Oligocene age took place onshore Sardinia and is getting younger towards the east (Fig. 6.1). This matches also the propagation of fault activity and crustal thinning to the east as it is recognized on line CD. The PSTM section shows also that in zone III magmatic activity is evident in smaller sub-basins (Fig. 6.9-11). At Site 654 a basalt layer was drilled and due to its cooling history it was interpreted as an extrusive flow (Kastens et al., 1988). Based on the stratigrapy we are able to date the eruptions along line CD at the same time of sedimentation. This is Pliocene age (Fig. 6.9-11) or even younger like the possible eruption close to the seafloor in Figure 6.9. The basement high in Figure 6.10 may have been part of the eruptive system because flows are located west and east of this feature. The sub-basin in Figure 6.11 shows at least three different phases of volcanic activity during Pleistocene age and maybe Late Messinian age. In the vicinity of line CD volcanic features are not detectable in the bathymetry data (500m resolution), but in the eastern zone between the profiles, cone-shaped topographic highs may indicate a cluster of volcanoes (Fig. 6.13D). At this location several heat flow measurements as high as 200 mW/m^2 have been conducted (Della Vedova et al., 1984). However, the distance to the volcanoes of 30-40 km is too far away to be the origin of the lava-flows imaged on line CD. Although, their presence may suggest that more magmatic features are present in the eastern part of the northern Tyrrhenian Basin. A magmatic feature may be the cone-shaped body buried by post-rift sediments visible in Figure 6.10. High amplitude reflections beneath this feature could also be related to volcanic layers or intrusives.

The NE-SW alignment of volcanoes on the bathymetry map and related features on both PSTM sections appears to be concomitant with the progressive crustal thinning to the SW in zone III (Fig. 6.3). This is also in agreement with heat flow and gravity data (Fig. 6.1B). It supports that the generation of magmatism might be a direct result of the crustal thinning and decompression process within the mantle. On the other hand, the eastward decreasing age of volcanic rocks might be related to the migration of a volcanic arc. Volcanic rocks (Oligocene age) onshore Sardinia are thought to be related to arc magmatism (Cherchi & Montadert, 1982). Therefore, the nature and origin of the magma cannot be answered finally here. Despite the occurrence of magmatism, there is no evidence for significant magmatic underplating as represented by the velocities in the lower parts of the crust. At active intra-oceanic arcs or at volcanic passive margins Vp exceed 7 km/s (Contreras-Reyes et al., 2011, Franke 2013) whereas 6.7-6.8 rather represents continental crust with a tendency to be slightly higher than in the average continental crust (Christensen & Mooney, 1995). This might be related to a higher degree of mafic minerals. The basin resembles rather the magma-poor margins of the North Atlantic where syn-rift magmatism is minor (Bown & White, 1995, Chian et al., 1995) instead of a margin where voluminous volcanic rocks are present.

5.3 Tectonic implications

The evolution of a homogeneously thinned crust to the formation of a crustal-scale asymmetry is observed in the northern Tyrrhenian Basin. It is mainly controlled by the W-E rift propagation with increasing extension rates to the south, most likely triggered by subduction rollback of the Ionian plate. This progression is characterized by a highly fractured zone III that has widened to the SW. It is further accompanied by crustal thinning, evidences for basaltic layers and a cluster of potential volcanoes (Fig.13D). Although, we do not have seismic constraints on the crustal thickness between the transects, it is reasonable that the crust thins progressively on a NW-SE trend. This is mirrored for instance by the long-wave length gravity anomaly field changing constantly from +70 mGal in the area of line AB and on the Sardinia Margin to +180 mGal in the region of the Vavilov Basin (Fig. 6.1B). The geometrical evolution of the basin shows similarities to the symmetric opening of the little extended part of the Porcupine Basin in the North-Atlantic west of Ireland. Farther south, the basin shows asymmetric structures at increasing extension-factors (Reston et al., 2004). However, in the Porcupine Basin it is observed that a detachment fault (P detachment) occurred on one side of the margin which might arise from the onset of serpentinization at the base of the brittle crust. Such a shallow dipping detachment is not observed in our data and obviously not necessary to control the formation of a rift basin with stretching factors $<$ 3-3.5 (Reston et al., 2004). The only candidate of a detachment is the undulating intra-crustal reflector in Figure 6.12. However, we rather think that this feature is the same reflector ("Z") that is identifiable on the entire line CD (Fig. 6.6). This reflector does not represent a detachment fault. Figure 6.7 (large blocks B1 and B2) and Figure 6.11 presumably show the same reflector appearing to be offset by normal faults. Because of the high elevation differences we exclude that this feature can be a continuous feature even considering the distortion effect on time sections (Hoffmann and Reston, 1992). Thus we assume that this reflection is in nature a lithological layer. This implies that this interface developed not during active rifting. It can also be interpreted as an Alpine nappe or an Hercynican basement like the 'K-reflector' in the Tuscany region (Contrucci et al., 2005 and references therein).

5.3.1 General implications

The early-phases of continental extension, accompanied by fault displacements, half-graben formation and homogeneous crustal thinning in the Tyrrhenian back-arc basin might be representative for the general early stages of rifted margins. On the basis of W-E rift propagation and a pole of rotation located at the northern tip of a tensional plate configuration, like that of the Adriatic plate, a possible schematic model is shown in Figure 6.13. Rifting commenced at a N-S orientated locus along the entire western margin generating large half-graben structures at relatively low stretching rates (Fig. 6.13 A). When the locus of active rifting shifts through time, new faults are generated and sedimentary deposits in some formerly generated half-grabens are older than syn-rift deposits in young half-grabens. The western area subsided earlier and thick post-rift sediments deposited in the oldest and deepest region of the propagating rift (like the Sardinia Margin). The location of the pole of rotation enforces, that the extension rates increase towards the south during ongoing eastward rift propagation. Then the crust should be enforced to stretch higher on a NW-SE axis to follow the drag of the stress field. This is accompanied by extensive faulting leading to smaller block sizes (Fig. 6.13 B and C). Due to the decompression of the upwelling upper mantle and asthenosphere, melting processes are partially generated and volcanic activity commenced. Ongoing extension leads to a distinct asymmetric margin configuration with large and inactive

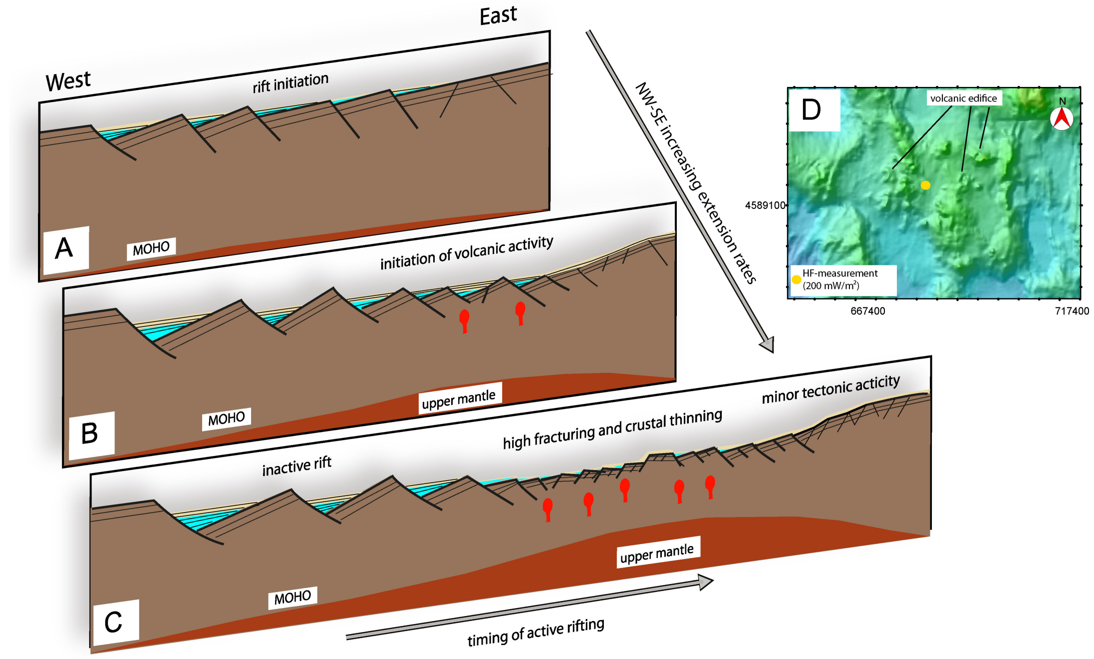

Figure 6.13.: Schematic model for basin evolution derived from seismic observations in the northern Tyrrhenian Sea. A) At the start of rifting, extension affected the crust just in a narrow region by few active faults. The crust was thinned homogeneously by brittle extension and lower crustal flow. B) Extension rates increase towards the south as the zone of active rifting propagates eastwards. This led to a higher stretched zone on a NW-SE orientation. It explains the occurrence of volcanic activity and younger faults in the east. C) Rift propagation goes on while the western margin becomes inactive and covered by post-rift sediments. A highly fractured zone developed as the result of increasing extension rates. This coincides with higher crustal thinning and volcanic activity. Young faults generate at the eastern margin and are to some extent still active. D) Ring-like structures and pins in the bathymetry data are perhaps related to volcanic edifices. These and volcanic-related features on both PSTM sections are aligned on a NW-SE axis. This is coincident with the axis of increasing stretching factors (see Fig. 6.1 A)

half-grabens on one margin of the rift and active faults on the other margin (Fig. 6.13 C). This model derived from the margin structures of the northern Tyrrhenian rift system may perhaps contribute to the general understanding of wide rifted and conjugate asymmetric margin configuration, for instance the asymmetric Atlantic-Type rifted margin structures.

6 Conclusions

The study of the northern Tyrrhenian Basin, which is tectonically the youngest basin in the Western Mediterranean Sea, contributes to the basic understanding of extension processes that lead to asymmetric rift basins and passive margin configuration. We analyzed two coincident wide-angle and prestack time-migrated multichannel seismic lines. This work provides new insights on the crustal architecture and sedimentary units in the northern Tyrrhenian Sea Basin that underwent different amounts of crustal stretching and thinning. The northern part of the basin opened between upper Tortonian to Early-Pliocene. However, we observe that tectonic activity is still to some extent active because high angle normal faults cut the seafloor near the mainland of Italy. In the western part of the basin, thick Messinian syn-tectonic and presumably evaporitic layers are covered by thick post-rift sedimentary deposits. This displays the W-E rift propagation as it has been observed by ages of volcanic rocks or drilling results. With the help of crustal-scale velocity models, derived from wide-angle seismic data, we found that the rift reveals little extended and homogeneously thinned crust between the Corsica Basin and the Latium Margin with a flat-lying Moho topography (β-factor=1.3). The system changes to a distinct asymmetric basin configuration between the Sardinia Margin and the Campania Margin. The asymmetry between the Sardinia Margin and the Campania Margin is characterized by a relatively cold ($\sim$50 mW/m^2) and thick crust comprising large rotated blocks at the Sardinia Margin in contrast to the higher fractured and warm (100 mW/m^2) thinned crust towards the mainland of Italy. The initial crust underneath Sardinia has been estimated to be 24-25 km ± 2 km thick. Hence, the 16-19 km thick crust in the west is just moderately thinned by a stretching factor of 1.3-1.5, whereas towards the Campania Margin the crust has a minimum thickness of 11 km and is stretched by a β-factor of 2.2. This is just north of the Vavilov Basin, where drilling-results of ODP Leg 107 report serpentinized mantle peridotite which let suggest full-continental break-up.

Tomographic inversion of wide-angle data shows that the upper crystalline crust has velocities of $\sim$4.0 km/s to 6.3 km/s with a velocity gradient of $\sim$1 s^{-1}. However, a zone in the center of the line AB that widens on the line CD, display reduced velocities ($\sim$12%) where the gradient is less ($\sim$0.5 s^{-1}). On both seismic transects this occurrence coincides with an increased number of continental block structures dissected by high-angle normal faults. On the line AB, the crustal thickness is not changing, though on the line CD the highly fractured zone coincides with the minimum crustal thickness of 11 km. Thus, the reduced velocities reflect the higher degree of faulting due to increased strain rates.

Velocities in the lower crust range from 6.5 km/s to 6.7 km/s and show a similar along strike trend of thinning. This supports that the amount of brittle extension should be also similar. Large-scale and shallow dipping detachment features are not imaged on PSTM sections.

This zone of increased fracturing is also a site, where volcanic activity is manifested as basaltic layers within post- and syn-rift sedimentary layers. Volcanic edifices are observed on the seismic images and on the bathymetry map. The alignment is approximately orientated on the NW-SE area with maximal crustal thinning. Melts could have been generated due to decompression and uplift of the asthenosphere.

We suggest that this development is related to W-E orientated rift propagation and the N-S increasing extension-rates controlled by increasing distance from the pole of rotation. This leads to a progressive NW-SE crustal thinning. The propagating rift-system and variability of extension rates in the Tyrrhenian Sea Basin could contribute to the understanding of the observed asymmetry on other rift basins and wide rifted margins, e.g. the conjugate and asymmetric margins in the North Atlantic.

Acknowledgments

Funding for data acquisition was provided by Spain (projects CTM2007-66179-C02-01/MAR and CTM2009-07772-E/MAR) and Italy which we gratefully acknowledge. Thank you to Grant George Buffett for copy editing. We thank the ships' officers and the crews of B/O Sarmiento de Gamboa and R/V Urania who helped to conduct the data acquisition for the MEDOC project successfully. A great thank goes also to all in the MEDOC-Team. This work was funded by the Deutsche Forschungsgemeinschaft (DFG) under grant GR 1964 /14-1.

References

Ackermann, R. V., Schlische, R. W. and Withjack, M. O., (2001), The geometric and statistical evolution of normal fault systems: an experimental study of the effects of mechanical layer thickness on scaling laws. J. Struct. Geol. 23, 1803-1819, doi: 10.1016/S0191-8141(01)00028-1.

Barker, P. F. and Hill, I.A., (1980), Asymmetric spreading in back-arc basins, Nature 285, 651-654, doi:10.1038/285652a0

Bown, J. W. and R. S. White (1995), Effect of finite extension rate on melt generation at rifted continental margins, J. Geophys. Res., 100(B9), 18011-18029, doi:10.1029/94JB01478.

Cella, F., Fedi, M., Florio, G., Paoletti, V., and Rapolla, A. (2008). A review of the gravity and magnetic studies in the Tyrrhenian Basin and its volcanic districts. Annals Of Geophysics, 51(1). doi:10.4401/ag-3035

Cherchi, A. and Montadert, L., (1982), Oligo-Miocene rift of Sardinia and the early history of the Western Mediterranean Basin. Nature, 298, 736-739, doi:10.1038/298736a0

Chian, D., Keen, C., Reid, I., and Louden, K. E., (1995), Evolution of nonvolcanic rifted margins: New results from the conjugate margins of the Labrador Sea. Geology, v. 23; no. 7; p. 589-592;

Christensen, N. I. and W. D. Mooney (1995), Seismic velocity structure and composition of the continental crust: A global view, J. Geophys. Res., 100(B6), 9761-9788, doi:10.1029/95JB00259.

Colantoni, P., Fabbri, A., Gallignani, P., Sartori, R., Rehault, J.P., (1981). Carta Litologica e Stratigrafica dei Mari Italiani. Litografia Artistica Cartografica, Firenze.

Collettini, C., A. Niemeijer, C. Viti, and C. Marone, 2009: Fault zone fabric and fault weakness. Nature, 462 (7275), 907-910.

Contreras-Reyes, E., I. Grevemeyer, A. B. Watts, E. R. Flueh, C. Peirce, S. Moeller, and C. Papenberg (2011), Deep seismic structure of the Tonga subduction zone: Implications for mantle hydration, tectonic erosion, and arc magmatism, J. Geophys. Res., 116, B10103, doi:10.1029/2011JB008434.

Contrucci, I., Mauffret, A., Brunet, C., Nercessian, A., Béthoux, N., and Ferrandini, J., (2005), Deep structure of the North Tyrrhenian Sea from multi-channel seismic profiles and on land wide angle reflection/refraction seismic recording (LISA cruise): Geodynamical implications, Tectonophysics, 406, 3-4, 141-163, doi:10.1016/j.tecto.2005.05.015.

Corti, G. and Manetti, P., Asymmetric rifts due to asymmetric Mohos: An experimental approach, Earth and Planetary Science Letters, Volume 245, Issues 1-2, 15 May 2006, Pages 315-329, ISSN 0012-821X, 10.1016/j.epsl.2006.02.004.

Curzi, P., Fabbri, A., and Nanni, A.,(1980 The Messinian evaporitic event in the Sardinia Basin area (Tyrrhenian Sea), Marine Geology, Volume 34, Issues 3-4, Pages 157-170, ISSN 0025-3227, 10.1016/0025-3227(80)90070-5.

D'Agostino, N., A. Avallone, D. Cheloni, E. D'Anastasio, S. Mantenuto, and G. Selvaggi (2008), Active tectonics of the Adriatic region from GPS and earthquake slip vectors, J. Geophys. Res., 113, B12413, doi:10.1029/2008JB005860.

Davis, M. and Kusznir, N. J. in Proc. NSF Rifted Margins Theor. Inst. (ed. Karner, G. D.) 92-136 (Columbia Univ. Press, 2004).

Della Vedova, B., Pellis, G., Foucher, J.P. and Rehault, J.-P., (1984), Geothermal structure of the Tyrrhenian Sea, Marine Geology, 55, 271-289.

Fabbri, A., Curzi, P., (1979) distribution of the Messinian deposits in the Tyrrhenian Sea, Giornale di Geologica, Vol. 43, Pl. 29

Faccenna, C., Becker, T. W., Lucente, F. P., Jolivet, L. and Rossetti, F., (2001), History of subduction and back-arc extension in the Central Mediterranean. Geophysical Journal International, 145: 809-820. doi: 10.1046/j.0956-540x.2001.01435.x.

Forsyth, D. W., (1992), Finite extension and low-angle normal faulting, Geology, v. 20, p. 27-30, doi:10.1130/0091-7613(1992)020<0027:FEALAN>2.3.CO;2

Franke, D., (2013), Rifting, lithosphere breakup and volcanism: Comparison of magma-poor and volcanic rifted margins. Marine and Petroleum Geology, 43 (0), 63-87.

Gawthorpe, R. L., C. A.-L. Jackson, M. J. Young, I. R. Sharp, A. R. Moustafa, and C. W. Leppard, (2003): Normal fault growth, displacement localisation and the evolution of normal fault populations: the hammam faraun fault block, suez rift, egypt. Journal of Structural Geology, 25 (6), 883-895,

Hoffmann, H. J. and Reston, T. J., (1992) Nature of the S reflector beneath the Galicia Banks rifted margin: Preliminary results from prestack depth migration Geology, v. 20, p. 1091-1094, doi:10.1130/0091-7613(1992)020<1091:NOTSRB>2.3.CO;2

Hsü, K.J., Montadert, L., Bernoulli, D., Cita, M. B., Erickson, A., Garrison, R.E., Kidd, R. B., Melieres, F., Müller, C. and Wright, R., (1977), History of the Mediterranean salinity crisis, Nature 267, 399-403 doi:10.1038/267399a0

Jolivet, L., Frizon de Lamotte, D., Mascle, A., and Seranne, M., (1999), The Mediterranean Basins: Tertiary Extension within the Alpine Orogen - an introduction. Geological Society, London, Special Publications, 156, 1-14, doi:10.1144/GSL.SP.1999.156.01.02

Kastens, K.A., Mascle, J., and others, (1988), ODP Leg 107 in the Tyrrhenian Sea: Insights into passive margin and back-arc basin evolution, Geological Society of American Bulletin, 100. 1140-1156, doi: 10.1130/0016-7606(1988)100<1140:OLITTS>2.3.CO;2.

Keller, J.V.A., Coward, M.P., (1996). The structure and evolution of the Northern Tyrrhenian Sea. Geological Magazine 133, 1 - 16.

Korenaga, J., W. S. Holbrook, G. M. Kent, P. B. Kelemen, R. S. Detrick, H.-C. Larsen, J. R. Hopper, and T. Dahl-Jensen (2000), Crustal structure of the southeast Greenland margin from joint refraction and reflection seismic tomography, J. Geophys. Res., 105(B9), 21, 591-21, 614, doi:10.1029/2000JB900188.

Malinverno, A. and Ryan, W.B.F., (1986) Extension in the Tyrrhenian Sea and shortening in the Apennines as result of arc migration driven by sinking of the lithosphere. Tectonics, 5, 2, 227-245, doi:10.1029/TC005i002p00227

Mauffret, A., Contrucci, C., and Brunet, C. (1999) Structural evolution of the Northern Tyrrhenian Sea from new seismic data. Marine and Petroleum Geology, 16, 5, 381-407, ISSN 0264-8172, 10.1016/S0264-8172(99)00004-5.

Mauffret, A., and Contruccci, I. (1999) Crustal structure of the North Tyrrhenian Sea: first results of the multichannel seismic LISA cruise. In: Durand, B., Jolivet, L., Horvath, F. and Seranne, M. (eds) The Mediterranean Basins: Tertiary Extension within the Alpine Orogen. Geological Society London, Special Publications, 156, 169-193.

McKenzie, D. (1978) Some remarks on the development of sedimentary basins, Earth and Planetary Science Letters, 40, 25-32.

Mele, G., and Sandvol, E., (2003), Deep crustal roots beneath the northern Apennines inferred from teleseismic receiver functions, Earth and Planetary Science Letters, 211, 1-2, 69-78, doi:10.1016/S0012-821X(03)00185-7.

Moeller, S., Grevemeyer, I., Ranero, C.R., Berndt, C., Klaeschen, D., Sallares, V., Zitellini, N., and de Franco, R., (2013, in press)., Early-stage rifting of the northern Tyrrhenian Sea Basin Results from a combined wide-angle and multichannel seismic study, G-Cubed

Nicolosi, I., F. Speranza, and M. Chiappini, 2006: Ultrafast oceanic spreading of the Marsili basin, southern Tyrrhenian Sea: Evidence from magnetic anomaly analysis. Geology, 34 (9), 717-720, doi:10.1130/G22555.1

Pérez-Gussinyé, M., Ranero, C.R., Reston, T. J., and Sawyer ,D., (2003), Mechanisms of extension at nonvolcanic margins: Evidence from the Galicia interior basin, west of Iberia, J. Geophys. Res., 108, 2245, doi:10.1029/2001JB000901, B5.

Pérez-Gussinyé, M., and T. J. Reston (2001), Rheological evolution during extension at nonvolcanic rifted margins: Onset of serpentinization and development of detachments leading to continental breakup, J. Geophys. Res., 106(B3), 3961-3975, doi:10.1029/2000JB900325.

Ranero, C.R. and Pérez-Gussinye, M., (2010), Sequential faulting explains the asymmetry and extension discrepancy of conjugate margins, Natur, 468, 294-300, doi:10.1038/nature09520.

Reston, T. J. (1993), Evidence for extensional shear zones in the mantle, offshore Britain, and their implications for the extension of the continental lithosphere, Tectonics, 12(2), 492-506, doi:10.1029/92TC01564.

Reston, T. J., Pennell, J., Stubenrauch, I., Walker, I., Perez-Gussinye, M., (2001), Detachment faulting, mantle serpentinization, and serpentinite- mud volcanism beneath the Porcupine Basin, southwest of Ireland, Geology; v. 29; no. 7; p.587-590

Reston, T.J., Gaw, V., Klaeschen, D., Stubenrauch, A., Walker, I., (2004), Extreme crustal thinning in the south Porcupine Basin and the nature of the Porcupine Median High: implications for the formation of non-volcanic rifted margins, Journal of the Geological Society, London, Vol. 161, pp. 783-798, doi:10.1144/0016-764903-036

Reston, T.J., (2005) Polyphase faulting during the development of the west Galicia rifted margin, Earth and Planetary Science Letters, Volume 237, Issues 3-4, 15 September 2005, Pages 561-576, ISSN 0012-821X, 10.1016/j.epsl.2005.06.019

Reston, T., (2007) Extension discrepany at North Atlantic nonvolcanic rifted margins: Depth-dependent stretching or unrecognized faulting?, Geology, 35, 367-370, doi; 10.1130/G23213A.1.

Rosenbaum, G., Lister, G. S., and Duboz, C., (2002), Reconstruction of the tectonic evolution of the western Mediterranean since the Oligocene. Journal of the Virtual Explorer, 8: 107-130. doi:10.3809/jvirtex.2002.00053.

Sartori, R., 1990: The main results of ODP leg 107 in the frame of Neogene to recent geology of perityrrhernian areas. in: Kastens, K. A., Mascle, J., et al., 1990. Proc. ODP, Sci. Results, 107: College Station, TX (Ocean Drilling Program).

Sartori, R., Torelli, L., Zitellini, N., Carrara, G., Matteo, M., and Mussoni, P., (2004) Crustal features along a W-E Tyrrhenian transect from Sardinia to Campania margins (Central Mediterranean), Tectonophysics, 383, 3-4, 171-192, ISSN 0040-1951, 10.1016/j.tecto.2004.02.008.

Sartori, R., Carrara, G. , Torelli, L., and Zitellini, N., 2001: Neogene evolution of the southwestern Tyrrhenian Sea (Sardinia basin and western Bathyal plain). Marine Geology, 175, 47 -66, doi:10.1016/S0025-3227(01)00116-5.

Savelli, C., (2002) Time-space distribution of magmatic activity in the western mediterranean and peripheral orogens during the past 30 ma (a stimulus to geodynamic considerations). Journal of Geodynamics, 34 (1), 99 - 126, doi:10.1016/S0264-3707(02)00026-1.

Schellart, W.P., (2010) Mount-Etna-Iblean volcanism caused by rollback-induced upper mantle upwelling around the Ionian slab edge: An alternative to the plume model, Geology, v. 38 no. 8, p. 691-694

Shillington, D. J., W. S. Holbrook, H. J. A. Van Avendonk, B. E. Tucholke, J. R. Hopper, K. E. Louden, H. C. Larsen, and G. T. Nunes (2006), Evidence for asymmetric nonvolcanic rifting and slow incipient oceanic accretion from seismic reflection data on the Newfoundland margin, J. Geophys. Res., 111, B09402, doi:10.1029/2005JB003981.

Speckbacher, R., Behrmann, J. H., Nagel, T. J., Stipp, M., and Devey, C. W., (2011) Splitting a continent: Insights from submarine high-resolution mapping of the Moresby Seamount detachment, offshore Papua New Guinea Geology, v. 39, p. 651-654, doi:10.1130/G31931.1

Smith, W. H. F., and D. T. Sandwell, (1997), Global seafloor topography from satellite altimetry and ship depth soundings, Science, v. 277, p. 1957-1962 Taylor, B., Goodliffe, A., Martinez, F., and Hey, R., 1995, Continental rifting and initial sea floor spreading in the Woodlark Basin: Nature, v. 374, p. 534-537, doi:10.1038/374534a0.

Trincardi, F. and Zitellini, N., (1987), The rifting of the Tyrrhenian Basin, Geo-Marine Letters, 7, 1-6, doi: 10.1007/BF02310459.

Wernicke, B., (1985), Uniform-sense normal simple shear of the continental lithosphere, Can. J. Earth Sci., 22, 108-125

Zelt, C. A. and Smith, R. B., (1992), Seismic traveltime inversion for 2-D crustal velocity structure, Geophysical Journal International, 108: 16-34, doi: 10.1111/j.1365-246X.1992.tb00836.x.

Zitellini N., Trincardi F., Marani, M., Fabbri, A., (1986) Neogene tectonics of the northern Tyrrhenian Sea, Giorn. Geol, 4-8, 1, 2.

7. Conclusions and Outlook

The aim of this thesis was to investigate the formation of rifted continental crust in the northern Tyrrhenian Sea Basin and to contribute to the general understanding of rifts and rifted margins. This basin is located in the Western Mediterranean and represents the youngest basin in this region. It is a triangular shaped back-arc basin at the rear of the Apenninic subduction zone, formed due to the tensional stress field of the retreating subducted plate (Jolivet et al., 1999). For this thesis, multichannel and wide-angle seismic data of two transects from the 2010 MEDOC project (240 and 350 km long), that sample different stretched sectors, were analyzed, processed and interpreted. Results and discussion are presented within two manuscript (Chapter 5 and 6). The transects are orientated perpendicular to the main strike direction of horst and graben structures to image the true geometries of rift-related features like faults, potential detachments and syn-sedimentary sequences. To achieve a true ground model, focusing-analysis and iterative prestack depth migration are carried out using state-of-the-art software packages. The thicknesses and velocities of post- and syn-tectonic sedimentary sequences are well determined with small depth errors of <10-20 m and <50 m. The coincident refraction and wide-angle seismic experiment, recorded on OBHs and land station, provide data to obtain the p-wave velocity structure of the crust and upper mantle. Final velocity models are derived by applying forward modelling and joint refraction- and reflection tomography of P_g, P_mP and P_n phases. On both sections, velocites are determined in the error-range of ± 0.1 km/s in the upper crust and ± 0.2 km/s in the lower crust. Uncertainties for the depth of the Moho range between ± 1-2 km depending on the ray-coverage. Both data sets complement each other at different depth domains where they are most powerful.

The main results of this thesis can be summarized as follows:

Line AB

- The northern line crossing the rift-system between Corsica and the Latium Margin reveal two different domains; the sedimentary Corsica Basin and a series of horst and half-graben structures extending towards the Latium Margin. The Corsica Basin is reported as a basin that formed during Oligocene age (Mauffret et al., 1999). Sediments older than Langhian age appear as a wedge-like infill, representing this extensional phase. Younger sediments of Messinian to Holocene age are well stratified indicating that this part of the northern Tyrrhenian Sea was not affected during the latest rift-phase. The PSDM section reveals that the crystalline basement of the basin is located at a depth of 6 km. The two domains are separated by a westward tilted structure that can be recognized up to a depth of 10-12 km. In the upper part it is characterized by a Vp reduction which is interpreted as a result of a higher degree of fracturing. The feature itself might represent an Alpine thrusts decoupling the Corsica Basin from the young rift domain.

- In the half-graben domain, correlation of the seismic images with drilling results reveal that the syn-tectonic deposits in the sub-basins are upper Tortonian to Early-Pliocene age. These units are dissected by high-angle normal faults and confined by the major fault systems bounding large footwall blocks and the rotated basement of the hanging wall.
- The wide-angle velocity model reveals a Vp-distribution in the upper crust that is typical for continental crust (3.5 km/s -6.3 km/s) with a high velocity gradient of $\sim$1 s^{-1}. Vp in the lower crust of 6.7-6.8 km/s at the Moho is slightly faster than in average continental crust. Voluminous magmatic underplating can be excluded, because if present, Vp is expected to be much higher ($\sim$7.0-7.2 km/s). The crustal thickness, measured from the top of the basement is $\sim$15 km beneath the Corsica Basin and $\sim$ 17 km at the half-graben domain. An initial crustal thickness of $\sim$ 24 km, implies similar stretching and thinning factors for the brittle and ductile domain. This excludes the extension discrepancy and depth-dependent stretching at this rift stage. Average opening rates for the basin along this transect could be estimated to 7.8-10.3 mm/a.
- The style of extension along the transect is characterized by asymmetric half-graben structures with synthetic major fault systems dipping mainly to the east (30°-40°). In a limited area of smaller blocks and less fault spacing, antithetic faults are present. This zone is accompanied by a decrease of p-wave velocities.
- Estimations of upper crustal stretching is carried out by two different methods: 1) The relative fault displacement for each major fault is estimated by measuring fault dip and rotated basement. Subsequently, displacements are averaged. 2) A line balancing of the length of the unconformity that marks the start of rifting yields the pre-tectonic crustal length. The results of both methods reveal that the difference is just minor (β=1.27 and 1.3). This indicates, that strain localization on the major fault systems generated almost the entire horizontal extension and the contribution of smaller faults is minor at this stage of extension. An important finding is, that major faults appear not to be connected at depths (brittle-ductile transition zone). Hence, long-lived and large-scale detachments are no element of the early rift-phase in this tectonic setting. The northern Tyrrhenian Basin shares the asymmetric half-graben characteristic with other young rift settings like the Gulf of Corinth Rift (Bell et al., 2008) or the Baikal-Rift (Hutchinson et al., 1992).

- Most of the major faults dip 30°-40° and rotated beds dip ∼12°. This let assume that initial fault angles were 45°-50° which is less than typical initial fault angles of 60°-65° (Abers, 2009). Related to the former compressional phase that led to the formation of the Apennines, pre-tectonic weak structures like thrusts could have been present and reactivated. Moreover, an abnormal heatflow prior to rifting might have weakened the crust.

Line CD and comparison with AB

- The vicinity of the Sardinia Margin is characterized by large rotated blocks and deep sub-basins. The syn-tectonic infill is of similar age than that of the half-graben domain on line AB. This implies that the Sardinia Basin is younger than the Corsica Basin. However, similar internal block structures like the westward dipping sequence might represent the same lithological layering. An internal basement reflector (Z) is observed along the entire section and coincides with a velocity of 6 km/s, perhaps related to a volcanic sheet. However, this layer has not been drilled, sampled or reported elsewhere. Thick syn-rift layers (max. 1500 m) at the Sardinia Margin are marked by high amplitude reflections. They are presumably related to evaporitic sequences. This indicates, that this area before and during the Messinian salinity crisis was already a deep water trough. The regions further east should have been located at shallower water depths since the thickness of evaporites decrease or is partly absent. Indications, for the sub-aerial emplacement at the onset of rifting come from wave eroded blocks on line AB.

- The MCS images of line CD reveal that fault ages, indicating tectonic activity, become younger from west to east. Sediments of Early-Pliocene to recent (300-500 m thick) are undisturbed near the Sardinia Margin and represent the post-rift successions. They are locally cut by normal faults in the central part of line CD and especially near the Campania Margin, where high-angle normal faults dissect young sediments. This depicts the apparent shift of active rifting from west to east following the stress field of the trench roll-back. On line AB, the rift propagation cannot be clearly inferred from the age of syn-sedimentary sequences. Indirect indications come from sequential fault patterns dipping eastwards and the eroded summits located lately above sea-level. Blocks in the west do not show this characteristic.

- The joint interpretation of the MCS images and crustal-scale velocity models reveal, that the basin changes from north to south to a distinct W-E asymmetric basin configuration. This is characterized by changes in block size and fault spacing, heatflow and crustal thickness. Beneath Sardinia and Sardinia Margin the crustal thickness is ∼24-25 km with Vp of ∼4.0 km/s to ∼6.3 km/s in the upper crystalline crust increasing by a gradient of ∼1 s^-1. The lower crust, similar to line AB, has Vp of 6.5 km/s to 6.7 km/s. The heatflow in this region is ~50 mW/m^2. The crust in the east thins to 13 km thickness near the Campania Margin and has velocity distribution similar to the Sardinia Margin. However, the heatflow is ~100 mW/m^2. The thinnest crust of 11 km (β=2.2) is found just close to this margin, located within a 100 km broad zone. This zone is characterized by a reduced velocity gradient Vp (~0.5 s-1) that is directly related to extensive faulting on the MCS images. Here, the fault spacing is less and continental blocks are much smaller. This broad zone shares characteristics with a narrow zone (40 km width) on the line AB, 80 km apart. The alignment of both zones is orientated on a NW-SE axis. On this axis, the necking of the crust and upwelling of the lithospheric mantle is supported by the increase of the gravity anomaly from +70 to +120 mGal.

- Within the zone of crustal necking, magmatic features are observed on the MCS images. These features could be related to rising melts, either generated due to decompression of the overburden or is related to the subduction process. If such features are extrusive basalt layers, they erupted between upper Messinian to Pliocene/Pleistocene age (6-2 Ma). Moreover, cone-like features on the bathymetry map might indicate volcanic edifices.

- The eastward opening of the northern Tyrrhenian Basin around a pole of rotation located at the northern tip of the basin could explain the observed asymmetric tectonic setting. The incipient W-E rift propagation and N-S increasing extension rates might explain most observations with a crustal necking on a NW-SE axis. It explains further the recent tectonic activity in the vicinity of the Campania Margin and the decrease of block sizes from west to east due to higher strain-rates.

Outlook

The study proposes a progressive crustal thinning from the Tuscany Archipelago towards the Vavilov Basin where the crust has fully separated and serpentinized peridotities and basalts have been drilled (Kastens et al., 1988). This thinning trend is approximately orientated parallel to the mainland of Italy and parallel to the subducted oceanic lithosphere dipping westwards beneath the basin. This large-scale feature has been imaged by tomographic inversion technique using teleseismic arrival times (Lucente et al., 1999). A detailed seismic refraction and wide-angle profile along this transect would give insights about the transition from less extended to higher stretched continental crust leading over to exhumed mantle as a function of NW-SE increasing stretching rates. Such a profile would contribute to the three-dimensional understanding of the rift. The proposed line would cross the site of potential volcanoes, which are located between the two seismic transects and might contribute to the understanding of rift-related back-arc magmatism.

Bibliography

Abers, G. A., 2009: Slip on shallow-dipping normal faults. *Geology*, **37 (8)**, 767–768, doi:10.1130/focus082009.1.

Al-Yahya, K., 1989: Velocity analysis by iterative profile migration. *GEOPHYSICS*, **54 (6)**, 718–729, doi:10.1190/1.1442699.

Axen, G. J., 2007: Research focus: Significance of large-displacement, low-angle normal faults. *Geology*, **35 (3)**, 287–288, doi:10.1130/0091-7613(2007)35[287:RFSOLL]2.0.CO;2.

Bell, R. E., L. C. McNeill, J. M. Bull, and T. J. Henstock, 2008: Evolution of the offshore western gulf of corinth. *Geological Society of America Bulletin*, **120 (1-2)**, 156–178.

Berryhill, J. R. and Y. C. Kim, 1986: Deep-water peg legs and multiples; emulation and suppression. *Geophysics*, **51 (12)**, 2177–2184.

Bickel, S., 1990: Velocity-depth ambiguity of reflection traveltimes. *GEOPHYSICS*, **55 (3)**, 266–276, doi:10.1190/1.1442834.

Bosworth, W., 1985: Geometry of propagating continental rifts. *Nature*, **316 (6029)**, 625–627.

Buck, W. R., 1993: Effect of lithospheric thickness on the formation of high- and low-angle normal faults. *Geology*, **21 (10)**, 933–936.

Byerlee, J., 1978: Friction of rocks. *Pure and Applied Geophysics PAGEOPH*, **116**, 615–626.

Cerveny, V., 2001: Seismic ray theory. *Cambridge University Press.*

Cherchi, A. and L. Montadert, 1982: Oligo-miocene rift of sardinia and the early history of the western mediterranean basin. *Nature*, **298 (5876)**, 736–739.

Chian, D., C. Keen, I. Reid, and K. E. Louden, 1995: Evolution of nonvolcanic rifted margins: New results from the conjugate margins of the labrador sea. *Geology*, **23 (7)**, 589–592.

Condie, K. C., 2005: Earth as an evolving planetary system. *Elsevier Academic Press*, 447.

Contrucci, I., A. Mauffret, C. Brunet, A. Nercessian, N. Bethoux, and J. Ferrandini, 2005: Deep structure of the north tyrrhenian sea from multi-channel seismic profiles and on land wide angle reflection/refraction seismic recording (lisa cruise): Geodynamical implications. *Tectonophysics*, **406**, 141 – 163, doi:10.1016/j.tecto.2005.05.015.

Curzi, P., A. Fabbri, and T. Nanni, 1980: The messinian evaporitic event in the sardinia basin area (tyrrhenian sea). *Marine Geology*, **34**, 157 – 170, doi:10.1016/0025-3227(80)90070-5.

Davis, N., M. andKusznir, 2004: Depth-dependent lithosphere stretching at rifted continental margins, in karner, g.d., ed., proceeding of nsf rifted margins theoretical institute:. *New York, Columbia University Press*, 92–136.

Della Vedova, B., G. Pellis, J. Foucher, and J.-P. Rehault, 1984: Geothermal structure of the tyrrhenian sea. *Marine Geology*, **55**, 271 – 289, doi:10.1016/0025-3227(84)90072-0.

Driscoll, N. W. and G. D. Karner, 1998: Lower crustal extension across the northern carnarvon basin, australia: Evidence for an eastward dipping detachment. *Journal of Geophysical Research: Solid Earth*, **103 (B3)**, 4975–4991, doi:10.1029/97JB03295.

Duschenes, J., M. C. Sinha, and K. E. Louden, 1986: A seismic refraction experiment in the tyrrhenian sea. *Geophysical Journal of the Royal Astronomical Society*, **85 (1)**, 139–160, doi:10.1111/j.1365-246X.1986.tb05175.x.

Franke, D., 2013: Rifting, lithosphere breakup and volcanism: Comparison of magma-poor and volcanic rifted margins. *Marine and Petroleum Geology*, **43 (0)**, 63–87.

Gawthorpe, R. L., C. A.-L. Jackson, M. J. Young, I. R. Sharp, A. R. Moustafa, and C. W. Leppard, 2003: Normal fault growth, displacement localisation and the evolution of normal fault populations: the hammam faraun fault block, suez rift, egypt. *Journal of Structural Geology*, **25 (6)**, 883–895.

Hoffmann, H. J. and T. J. Reston, 1992: Nature of the s reflector beneath the galicia banks rifted margin: Preliminary results from prestack depth migration. *Geology*, **20 (12)**, 1091–1094.

Hsu, K. J., et al., 1977: History of the mediterranean salinity crisis. *Nature*, **267 (5610)**, 399–403.

Hutchinson, D. R., A. J. Golmshtok, L. P. Zonenshain, T. C. Moore, C. A. Scholz, and K. D. Klitgord, 1992: Depositional and tectonic framework of the rift basins of lake baikal from multichannel seismic data. *Geology*, **20 (7)**, 589–592.

Jolivet, L., D. Frizon de Lamotte, A. Mascle, and M. SÃ©ranne, 1999: The mediterranean basins: Tertiary extension within the alpine orogen â€” an introduction. *Geological Society, London, Special Publications*, **156 (1)**, 1–14.

Jones, I. F., R. L. Bloor, B. L. Bionid, and J. T. Etgen, 2008: Prestack depth migration and velocity model building. *Society of Exploration Geophysicists*, **Geophysics reprint series No. 25**, doi:10.1190/1.9781560801917.

Julien, P. and J. Raoult, 1989: Adaptive subtraction of emulated multiples. *SEG Technical Program Expanded Abstracts*, 1118–1120, doi:10.1190/1.1889859.

Kastens, K., et al., 1988: Odp leg 107 in the tyrrhenian sea: Insights into passive margin and back-arc basin evolution. *Geological Society of America Bulletin*, **100 (7)**, 1140–1156.

Korenaga, J., 2003: tomo2d: a c++ package for 2-d joint refraction and reflection travel-time tomography (user guide). *earth.yale.edu.*

Korenaga, J., 2011: Velocity-depth ambiguity and the seismic structure of large igneous provinces: a case study from the ontong java plateau. *Geophysical Journal International*, **185 (2)**, 1022–1036, doi:10.1111/j.1365-246X.2011.04999.x.

Korenaga, J., W. S. Holbrook, G. M. Kent, P. B. Kelemen, R. S. Detrick, H.-C. Larsen, J. R. Hopper, and T. Dahl-Jensen, 2000: Crustal structure of the southeast greenland margin from joint refraction and reflection seismic tomography. *Journal of Geophysical Research: Solid Earth*, **105 (B9)**, 21 591–21 614, doi:10.1029/2000JB900188.

Levin, F., 1983: The effects of streamer feathering on stacking. *GEOPHYSICS*, **48 (9)**, 1165–1171, doi:10.1190/1.1441539.

Lister, G. S., M. A. Etheridge, and P. A. Symonds, 1991: Detachment models for the formation of passive continental margins. *Tectonics*, **10 (5)**, 1038–1064, doi:10.1029/90TC01007.

Liu, Z., 1995: Migration velocity analysis. *Center for Wave Phenomena, Colorado School of Mines*, **(Doctoral Thesis)**.

Lucente, F. P., C. Chiarabba, G. B. Cimini, and D. Giardini, 1999: Tomographic constraints on the geodynamic evolution of the italian region. *Journal of Geophysical Research: Solid Earth*, **104 (B9)**, 20 307–20 327, doi:10.1029/1999JB900147.

MacKay, S. and R. Abma, 1992: Imaging and velocity estimation with depth-focusing analysis. *GEOPHYSICS*, **57 (12)**, 1608–1622, doi:10.1190/1.1443228.

Malinverno, A. and W. B. F. Ryan, 1986: Extension in the tyrrhenian sea and shortening in the apennines as result of arc migration driven by sinking of the lithosphere. *Tectonics*, **5 (2)**, 227–245, doi:10.1029/TC005i002p00227.

Marrett, R. and R. W. Allmendinger, 1992: Amount of extension on "small" faults: An example from the viking graben. *Geology*, **20 (1)**, 47–50.

Mascle, J. and J.-P. Rehault, 1990: A revised seismic stratigraphy of the tyrrhenian sea: implications for the basin evolution. *In Kastens, K.A., Mascle, J., et al., Proc. ODP, Sci. Results, 107: College Station, TX (Ocean Drilling Program)*, 617â€“636, doi:doi:10.2973/odp.proc.sr.107.119.1990.

Mauffret, A., I. Contrucci, and C. Brunet, 1999: Structural evolution of the northern tyrrhenian sea from new seismic data. *Marine and Petroleum Geology*, **16 (5)**, 381 – 407, doi:10.1016/S0264-8172(99)00004-5.

McKenzie, D., 1978: Some remarks on the development of sedimentary basins. *Earth and Planetary Science Letters*, **40 (1)**, 25 – 32, doi:10.1016/0012-821X(78)90071-7.

Meissner, R. and W. Mooney, 1998: Weakness of the lower continental crust: a condition for delamination, uplift, and escape. *Tectonophysics*, **296 (1)**, 47–60, doi:doi:10.1016/S0040-1951(98)00136-X.

Mele, G. and E. Sandvol, 2003: Deep crustal roots beneath the northern apennines inferred from teleseismic receiver functions. *Earth and Planetary Science Letters*, **211**, 69 – 78, doi:10.1016/S0012-821X(03)00185-7.

Moser, T. J., G. Nolet, and R. Snieder, 1992: Ray bending revisited. *Bulletin of the Seismological Society of America*, **82(1)**, 259â€“288.

Paige, C. C. and M. A. Saunders, 1982: Lsqr: An algorithm for sparse linear equations and sparse least squares. *ACM Trans. Math. Software*, **8**.

Peacock, K. and S. Treitel, 1969: Predictive deconvolution: Theory and practice. *GEOPHYSICS*, **34 (2)**, 155–169, doi:10.1190/1.1440003.

Perez-Gussinye, M., C. R. Ranero, T. J. Reston, and D. Sawyer, 2003: Mechanisms of extension at nonvolcanic margins: Evidence from the galicia interior basin, west of iberia. *Journal of Geophysical Research: Solid Earth*, **108 (B5)**, n/a–n/a, doi:10.1029/2001JB000901.

Ranero, C. R. and M. Perez-Gussinye, 2010: Sequential faulting explains the asymmetry and extension discrepancy of conjugate margins. *Nature*, **468 (7321)**, 294–299.

Reston, T., 2005: Polyphase faulting during the development of the west galicia rifted margin. *Earth and Planetary Science Letters*, **237**, 561 – 576, doi:10.1016/j.epsl.2005.06.019.

Reston, T., 2007: Extension discrepancy at north atlantic nonvolcanic rifted margins: Depth-dependent stretching or unrecognized faulting? *Geology*, **35 (4)**, 367–370.

Reston, T., 2009: The structure, evolution and symmetry of the magma-poor rifted margins of the north and central atlantic: A synthesis. *Tectonophysics*, **468**, 6 – 27, doi:10.1016/j.tecto.2008.09.002, <ce:title>Role of magmatism in continental lithosphere extension continental lithosphere extension</ce:title>.

Reston, T., V. Gaw, J. Pennell, D. Klaeschen, A. Stubenrauch, and I. Walker, 2004: Extreme crustal thinning in the south porcupine basin and the nature of the porcupine median high: implications for the formation of non-volcanic rifted margins. *Journal of the Geological Society*, **161**, 783–798.

Rosenbaum, T., G. Lister, and C. Dunoz, 2002: Reconstruction of the tectonic evolution of the western medterranean since the oligocene. *Journal of the Virtual Explorer, 8:*, 107–130.

Ruppel, C., 1995: Extensional processes in continental lithosphere. *Journal of Geophysical Research: Solid Earth*, **100 (B12)**, 24 187–24 215, doi:10.1029/95JB02955.

Sartori, R., 1990: The main results of odp leg 107 in the frame of neogene to recent geology of perityrrhernian areas. *in: Kastens, K. A., Mascle, J., et al., 1990. Proc. ODP, Sci. Results, 107: College Station, TX (Ocean Drilling Program).*

Sartori, R., L. Torelli, N. Zitellini, G. Carrara, M. Magaldi, and P. Mussoni, 2004: Crustal features along a w-e tyrrhenian transect from sardinia to campania margins (central mediterranean). *Tectonophysics*, **383**, 171 – 192, doi:10.1016/j.tecto.2004.02.008.

Savelli, C., 2002: Time-space distribution of magmatic activity in the western mediterranean and peripheral orogens during the past 30 ma (a stimulus to geodynamic considerations). *Journal of Geodynamics*, **34 (1)**, 99 – 126, doi:10.1016/S0264-3707(02)00026-1.

Sheriff, R., 1980: Nomogram for fresnel zone calculation. *GEOPHYSICS*, **45 (5)**, 968–972, doi:10.1190/1.1441101.

Shillington, D. J., W. S. Holbrook, H. J. A. Van Avendonk, B. E. Tucholke, J. R. Hopper, K. E. Louden, H. C. Larsen, and G. T. Nunes, 2006: Evidence for asymmetric nonvolcanic rifting and slow incipient oceanic accretion from seismic reflection data on the newfoundland margin. *Journal of Geophysical Research: Solid Earth*, **111 (B9)**, n/a–n/a, doi:10.1029/2005JB003981.

Smith, W. H. F. and D. T. Sandwell, 1997: Global sea floor topography from satellite altimetry and ship depth soundings. *Science*, **277 (5334)**, 1956–1962.

Steinmetz, L., F. Ferrucci, A. Hirn, C. Morelli, and R. Nicolich, 1983: A 550 km long moho traverse in the tyrrhenian sea from o.b.s. recorded pn waves. *Geophysical Research Letters*, **10 (6)**, 428–431, doi:10.1029/GL010i006p00428.

Trincardi, F. and N. Zitellini, 1987: The rifting of the tyrrhenian basin. *Geo-Marine Letters*, **7**, 1–6, doi:10.1007/BF02310459.

Verschuur, D., P. Hermann, N. Kinneging, C. Wapenaar, and A. Berkhout, 1988: Elimnation of surface-related multiply reflected and converted waves. *SEG Technical Program Expanded Abstracts*, pp. 1017–1020.

Walsh, J., J. Watterson, and G. Yielding, 1991: The importance of small-scale faulting in regional extension. *Nature*, **351 (6325)**, 391–393.

Wernicke, B., 1985: Uniform-sense normal simple shear of the continental lithosphere. *Canadian Journal of Earth Sciences*, **22**, 108–125.

White, R. and D. McKenzie, 1989: Magmatism at rift zones: The generation of volcanic continental margins and flood basalts. *Journal of Geophysical Research: Solid Earth*, **94 (B6)**, 7685–7729, doi:10.1029/JB094iB06p07685.

White, R. S., L. K. Smith, A. W. Roberts, P. A. F. Christie, and N. J. Kusznir, 2008: Lower-crustal intrusion on the north atlantic continental margin. *Nature*, **452 (7186)**, 460–464, doi:dx.doi.org/10.1038/nature06687.

Whitmarsh, R. B., G. Manatschal, and T. A. Minshull, 2001: Evolution of magma-poor continental margins from rifting to seafloor spreading. *Nature*, **413 (6852)**, 150–154.

Wiggins, J. W., 1988: Attenuation of complex water-bottom multiples by wave-equation-based prediction and subtraction. *Geophysics*, **53 (12)**, 1527–1539.

Yilmaz, 2001: *Seismic Data Analysis: Processing, Inversion and Interpretation of Seismic Data*. Society of Exploration Geophysicists (SEG).

Zelt, C. A. and R. B. Smith, 1992: Seismic traveltime inversion for 2-d crustal velocity structure. *Geophysical Journal International*, **108 (1)**, 16–34.

Zitellini, N., F. Trincardi, M. Marani, and A. Fabbri, 1986: Neogene tectonics of the northern tyrrhenian sea, giorn.geol, 48, 1, 2.

List of Figures

List of Tables

A. Appendix

A.1. PSDM image (Line CD)

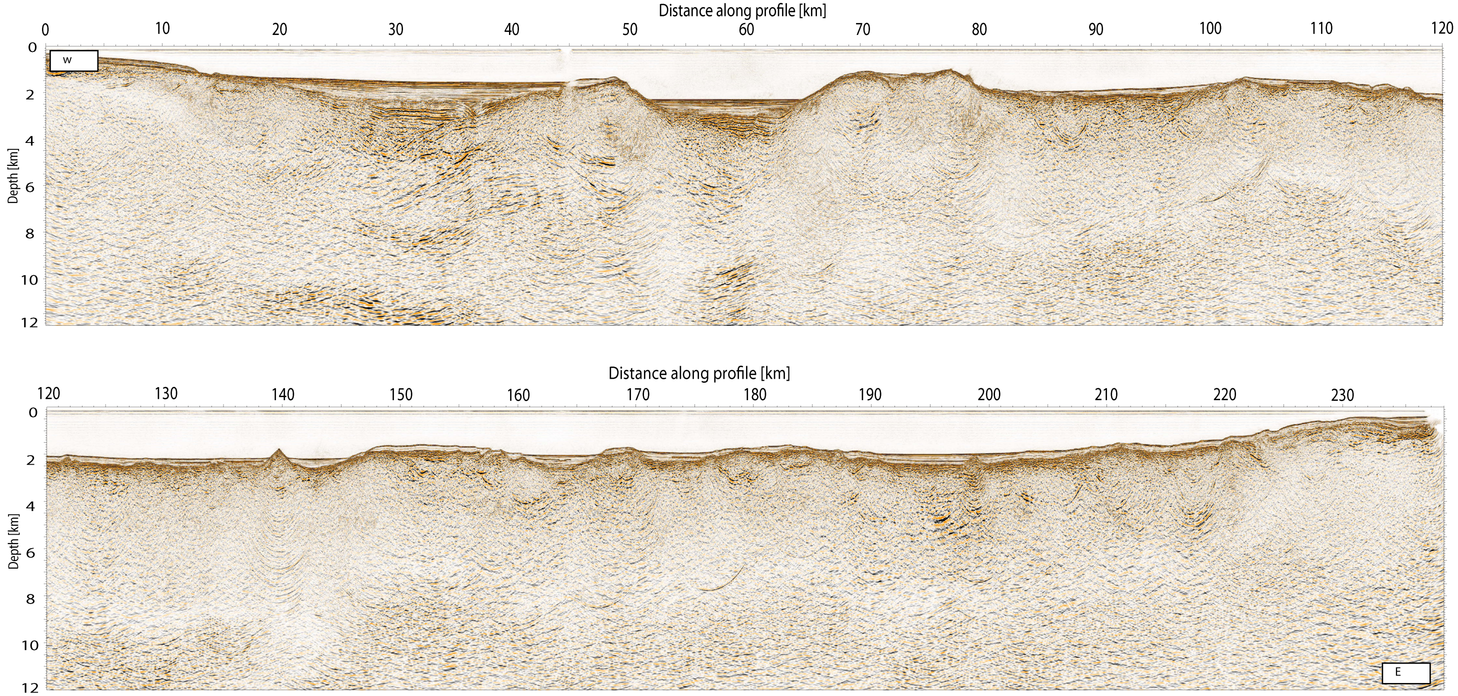

Figure A.1.: Prestack-depth image of Line CD (V.E.=2)

A.2. Velocity model PSDM/PSTM

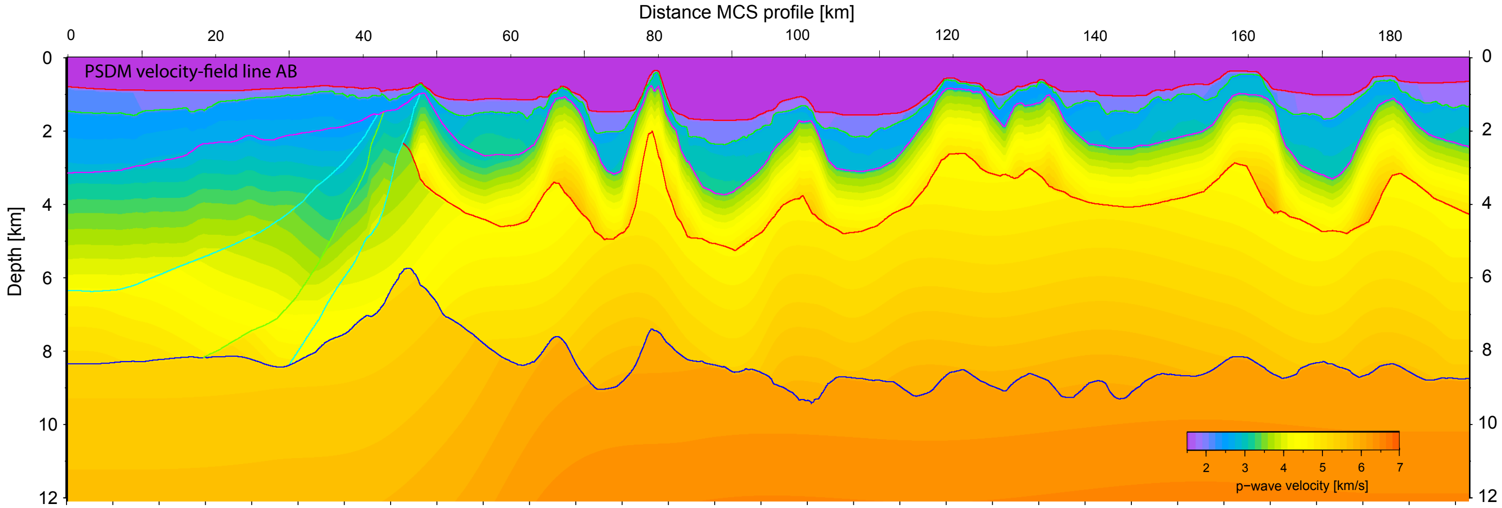

Figure A.2.: Velocity model for prestack-depth migration of line AB.

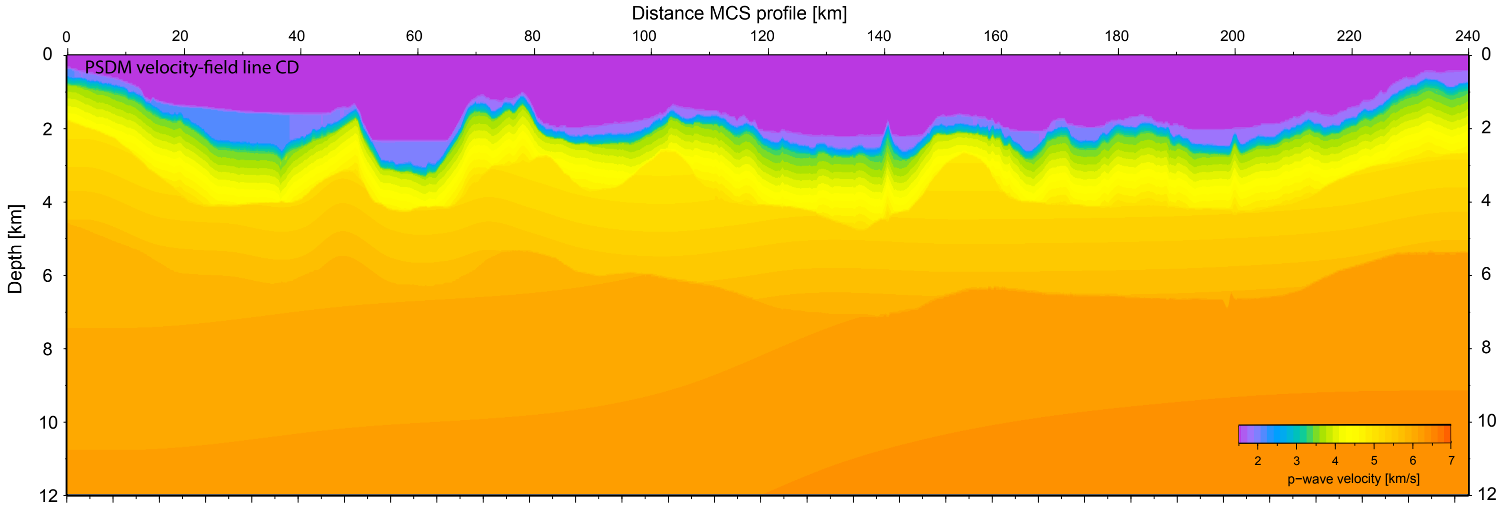

Figure A.3.: Velocity model for prestack-depth migration of line CD.

A.3. Record sections of land and OBH stations

A.3.1. Line AB

Station	Latitude	Longitude	water depth [m]
OBH22	41° 45,009	11° 58,551’	227
OBH21	41° 45,002’	11° 52,256’	662
OBH20	41° 45,001’	11° 45,956’	510
OBH19	41° 45,007’	11° 39,661’	1020
OBH18	41° 44,989’	11° 34,648’	875
OBH17	41° 45,026’	11° 27,062’	721
OBH16	41° 45,021’	11° 20,776’	1039
OBH15	41° 45,020’	11° 14,524’	928
OBH14	41°44,981’	11° 08,274’	975
OBH13	41° 44,614’	11° 02,675’	532
OBH12	41° 44,986’	10° 55,653’	1549
OBH11	41° 44,959’	10° 50,255’	1478
OBH10	41° 44,007’	10° 43,056’	1682
OBH09	41° 45,032’	10° 36,736’	1540
OBH08	41° 45,021’	10° 30,484’	1465
OBH07	41° 44,832’	10° 23,165’	1062
OBH06	41° 44,980’	10° 17,984’	1112
OBH05	41° 45,022’	10° 11,628’	725
OBH04	41° 45,007’	10° 05,341’	834
OBH03	41° 45,008’	09° 59,028’	826
OBH02	41° 45,007’	09° 52,771’	904
OBH01	41° 44,998’	09° 46,455’	900
AB1	41° 44,737’	9° 24.198’	-19
AB2	41° 44,340’	9° 19,866’	-332
AB3	41° 44,514’	9° 10.680’	-744

Table A.1.: Deployment coordinates of OBH and land stations.

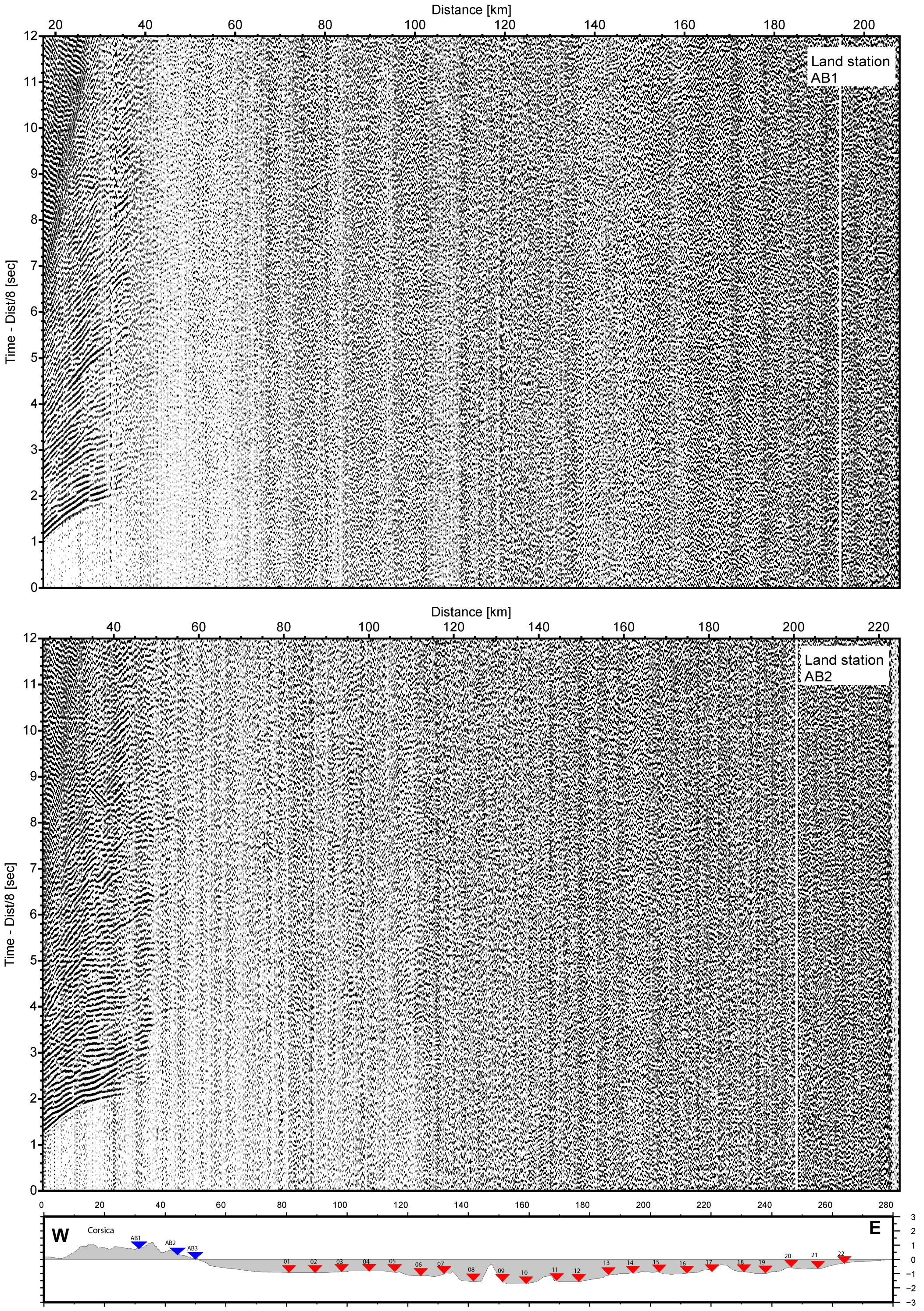

Figure A.4.: Record sections of land station AB1 and AB2.

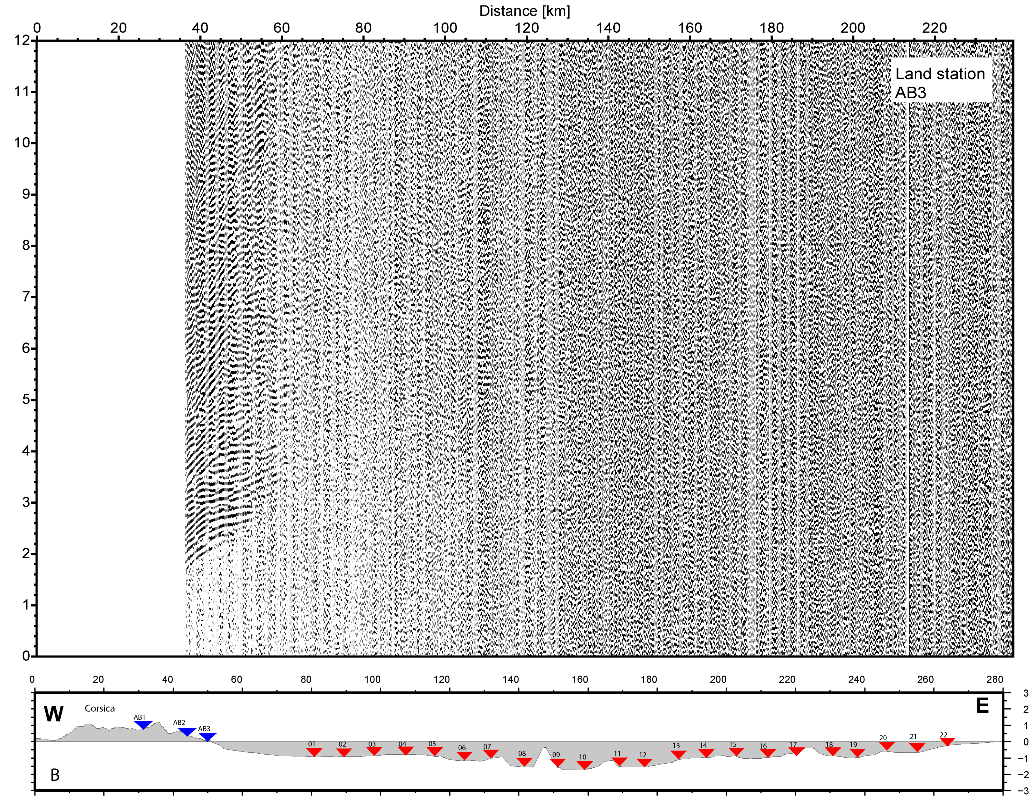

Figure A.5.: Record section of land station AB3.

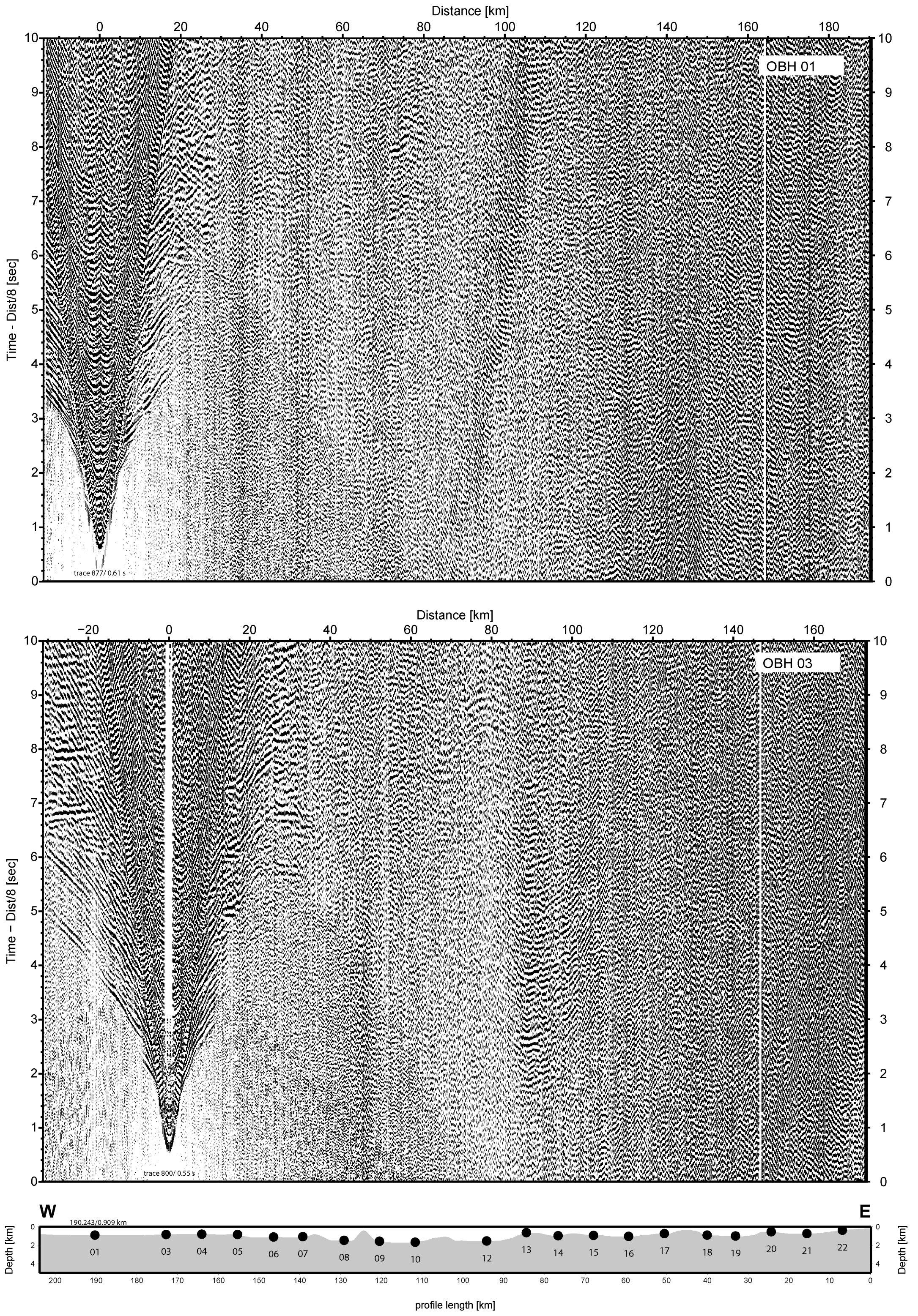

Figure A.6.: Record sections of OBH01 and OBH03.

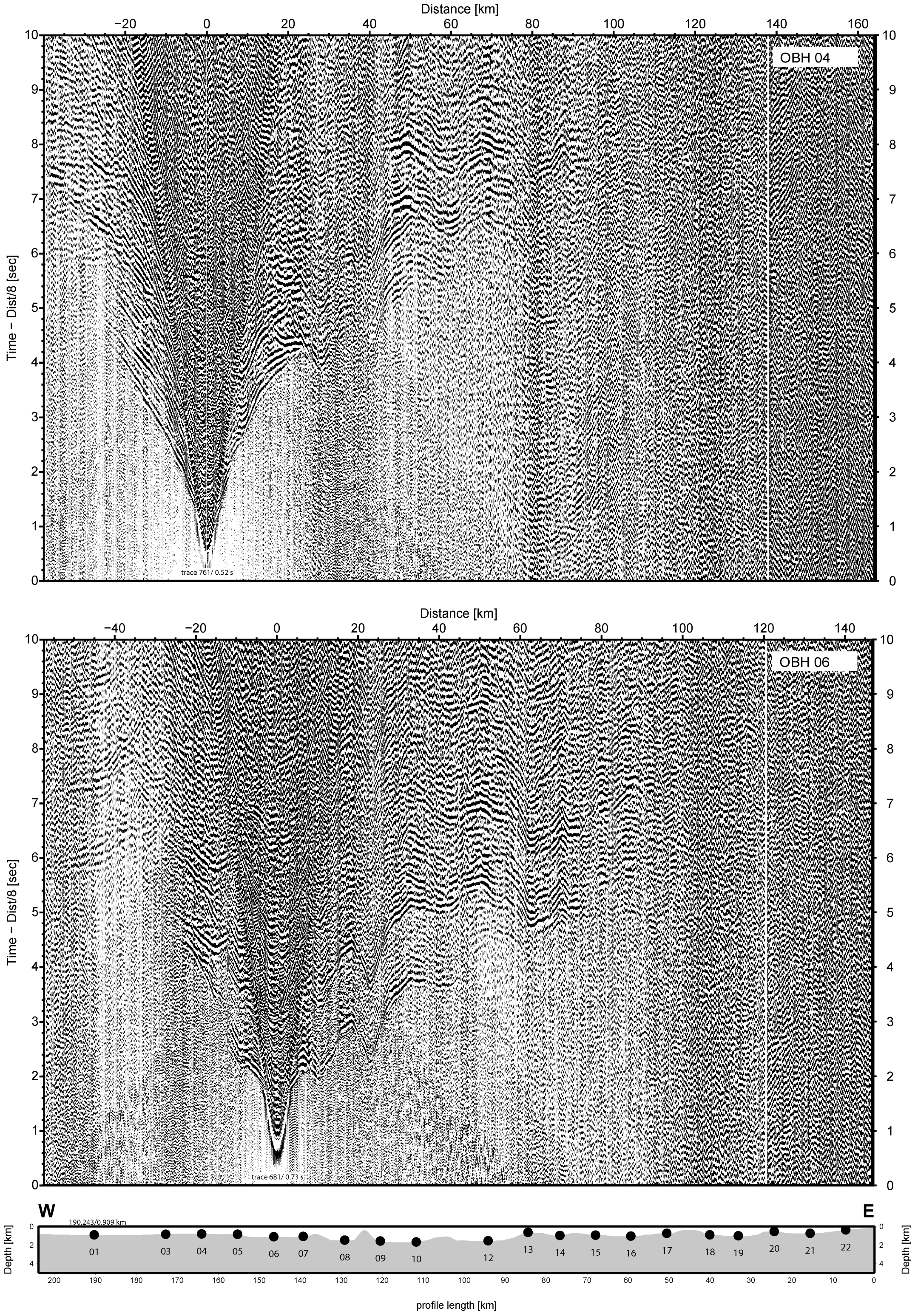

Figure A.7.: Record sections of OBH04 and OBH06.

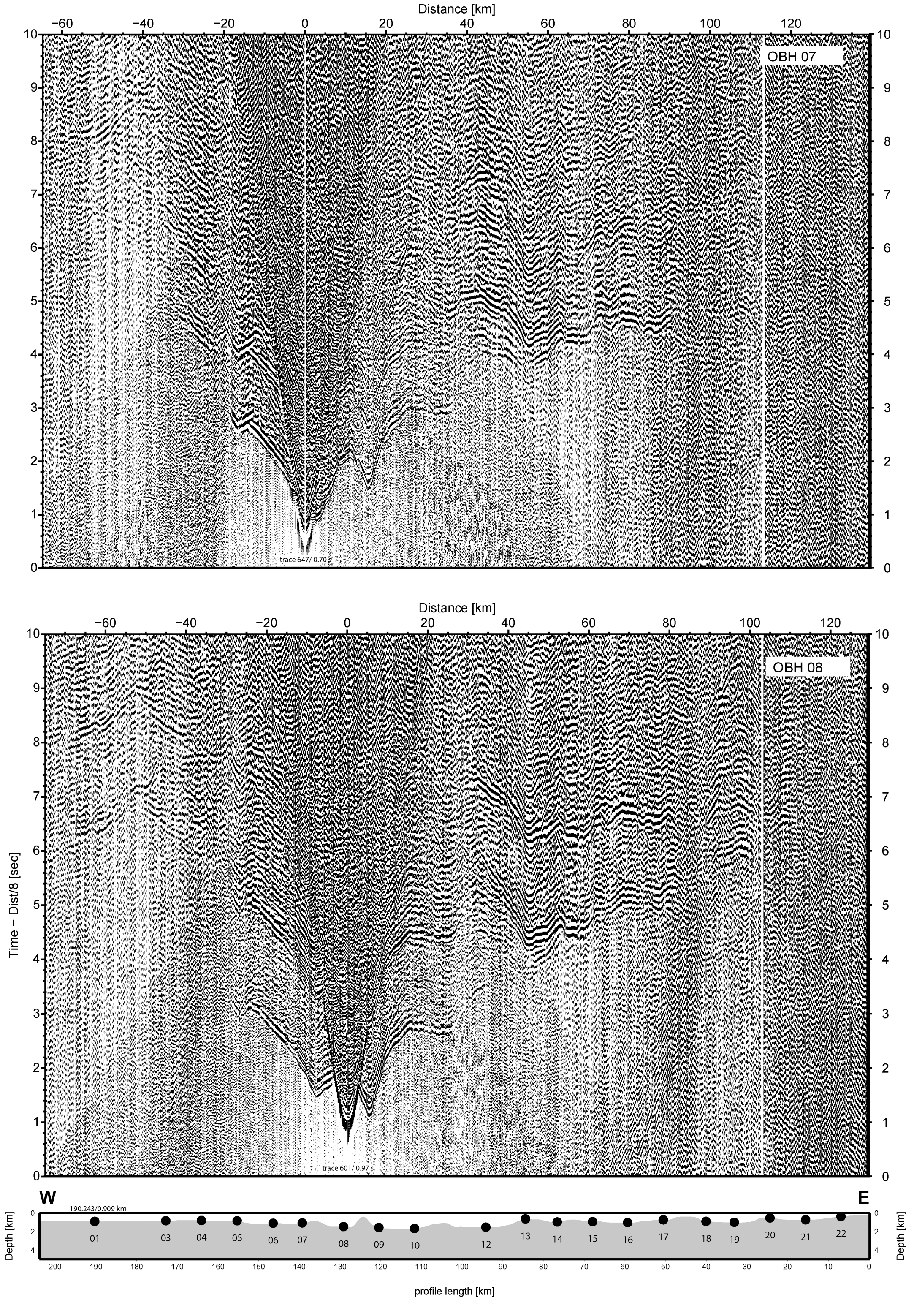

Figure A.8.: Record sections OBH07 and OBH08.

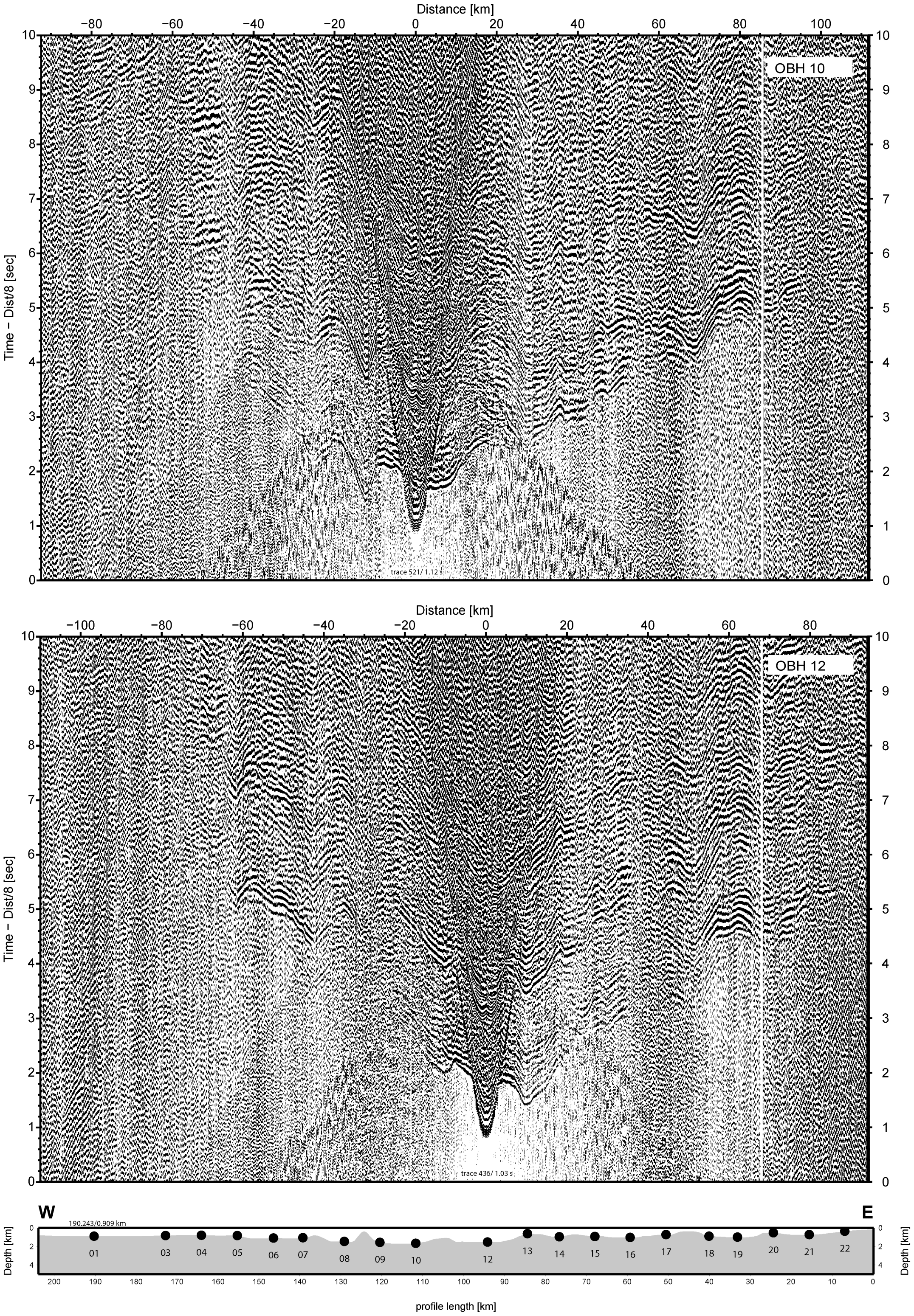

Figure A.9.: Record sections of OBH10 and OBH12.

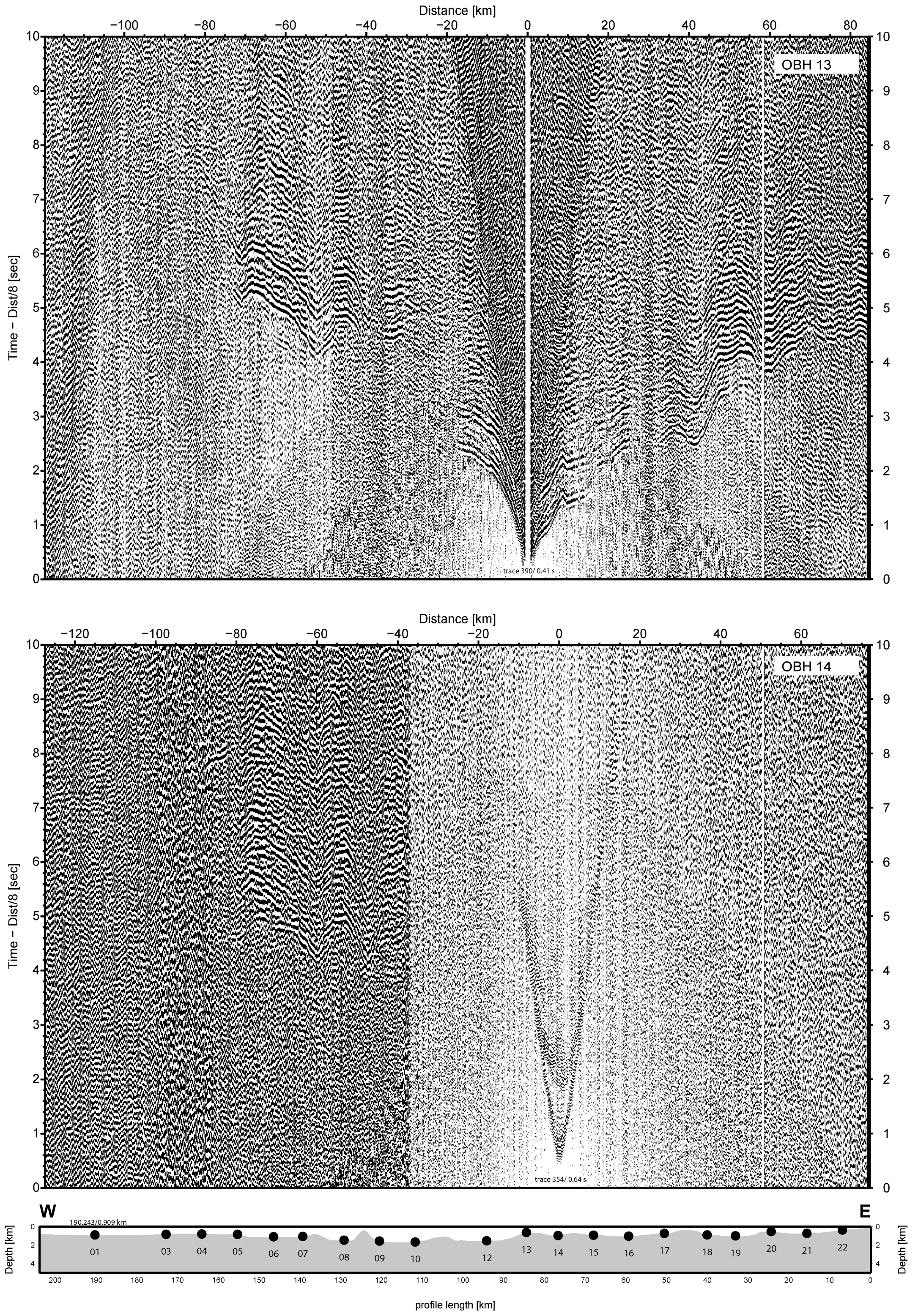

Figure A.10.: Record sections of OBH13 and OBH14.

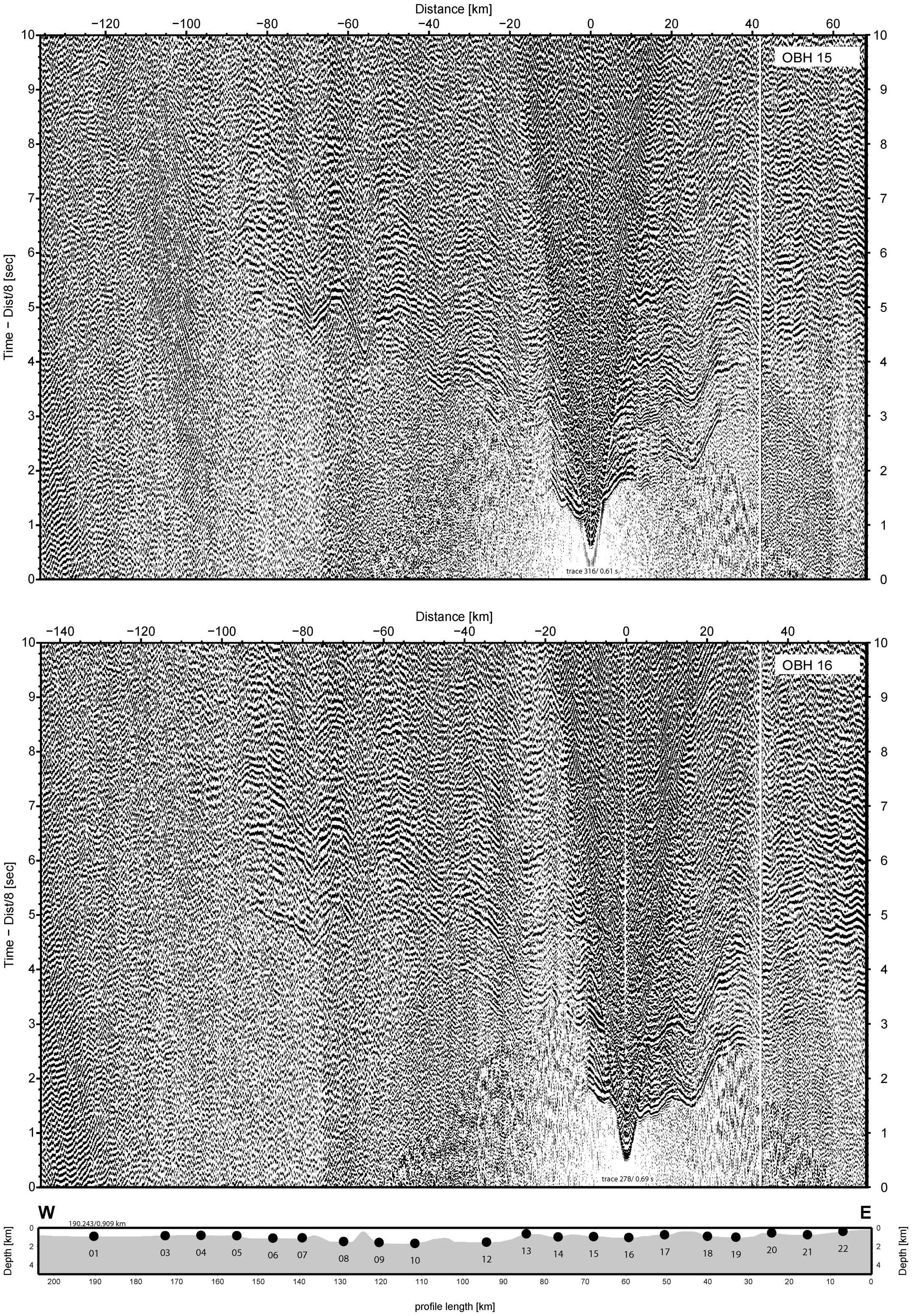

Figure A.11.: Record sections of OBH15 and OBH16.

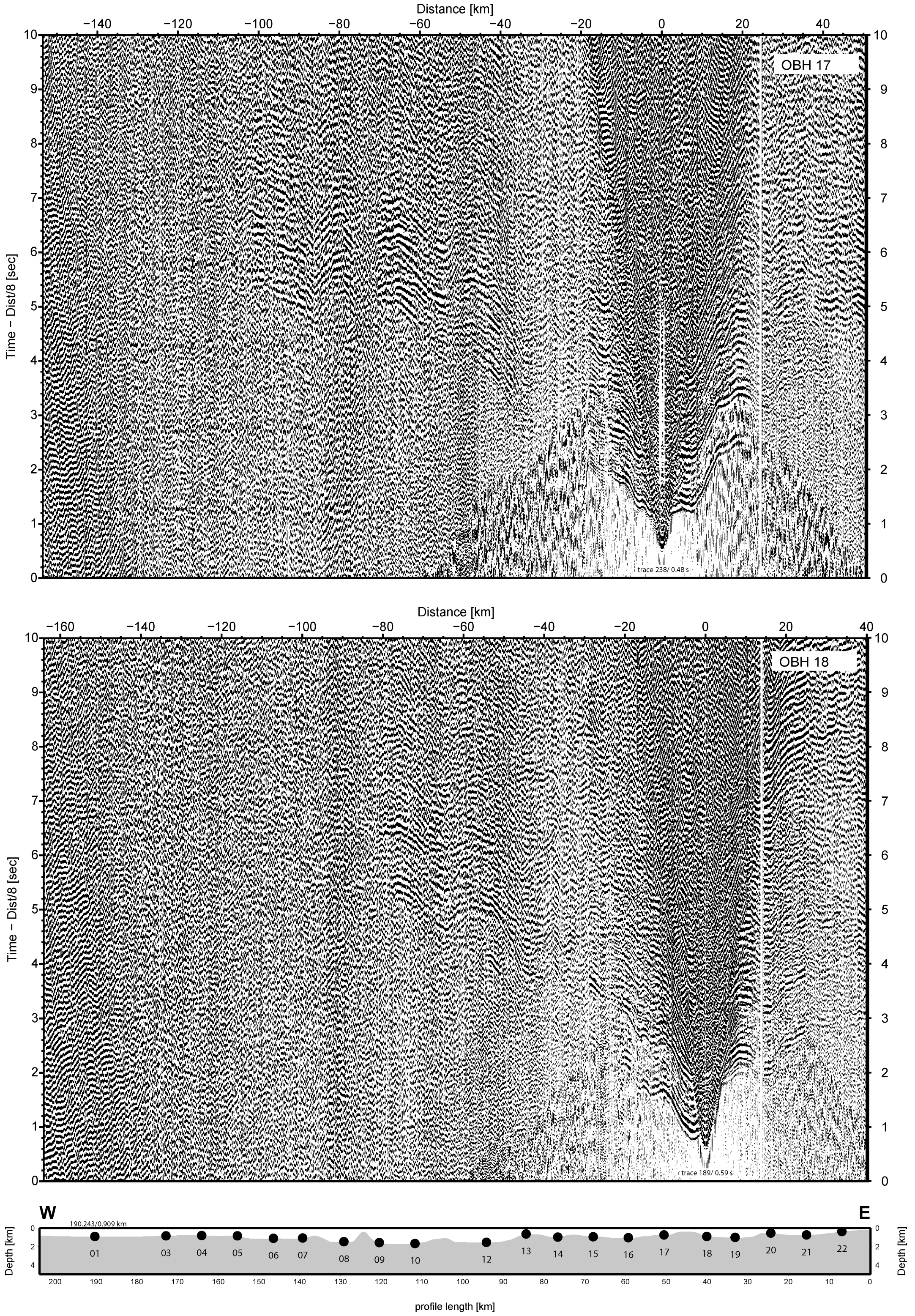

Figure A.12.: Record sections of OBH17 and OBH18.

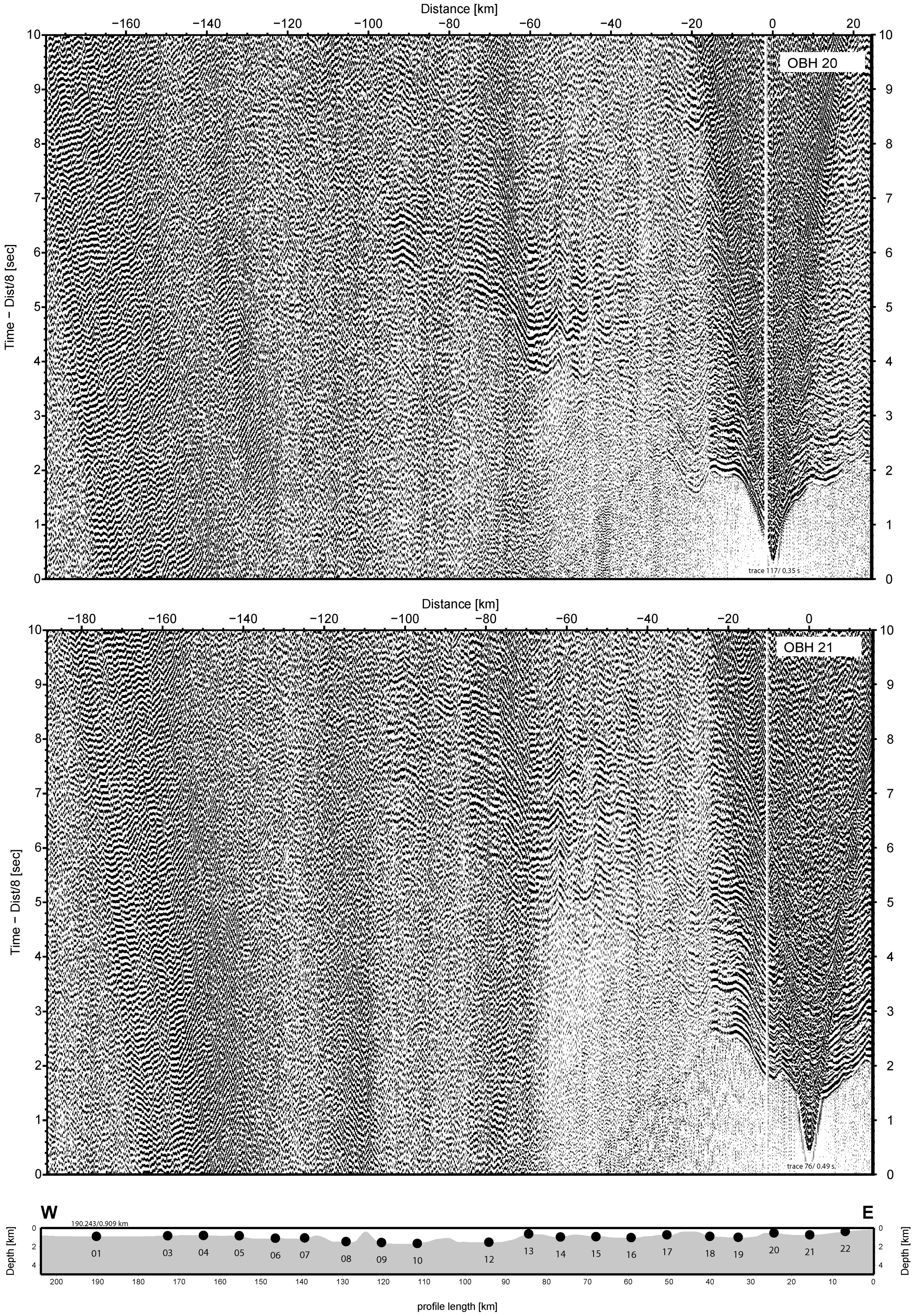

Figure A.13.: Record sections of OBH20 and OBH21.

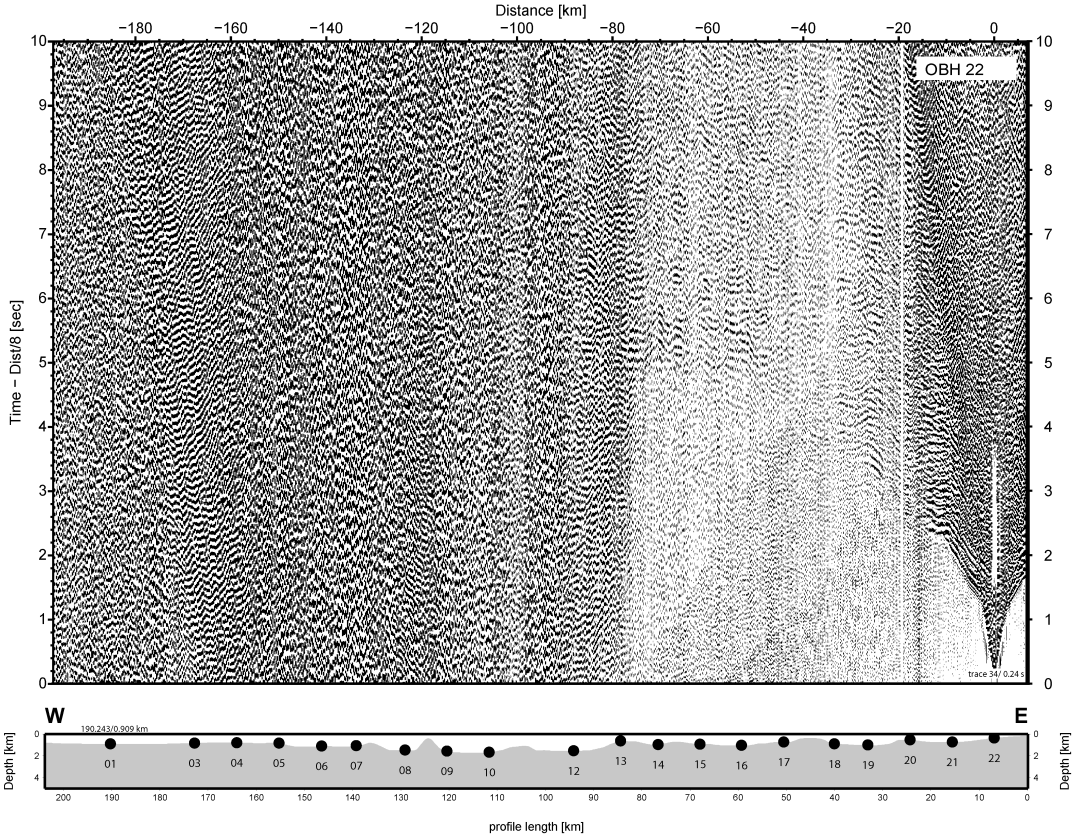

Figure A.14.: Record section of OBH22.

A.3.2. Line CD

OBH Station	Latitude	Longitude	water depth [m]
OBH25	40° 59,998’	12° 48,905’	480
OBH24	40° 59,985’	12° 41,722’	429
OBH23	40° 59,311’	12° 33,104’	1212
OBH22	40° 59,991’	12°27,312’	1632
OBH21	41° 00,001’	12° 20,090’	1862
OBH20	40° 59,002’	12° 12,877’	2011
OBH19	41° 00,034’	12° 05,613’	1703
OBH18	40° 59,986’	11° 58,427’	1955
OBH17	40° 59,995’	11° 51,261’	2047
OBH16	41° 00,014’	11° 44,071’	1639
OBH15	41° 00,029’	11° 36,852’	2190
OBH14	41° 00,023’	11° 29,656’	2194
OBH13	40° 59,998’	11° 22,457’	2092
OBH12	41° 00,011’	11° 15,252’	1662
OBH11	41° 00,002’	11° 08,035’	1334
OBH10	41° 00,003’	11° 00,857’	1824
OBH09	41° 00,005’	10° 53,638’	1926
OBH08	41° 00,003’	10° 46,422’	1205
OBH07	41° 00,010’	10° 39,212’	2309
OBH06	41° 00,007’	10° 32,013’	2306
OBH05	41° 00,014’	10° 24,828’	1564
OBH04	41° 00,004’	10° 17,630’	1540
OBH03	40° 59,988’	10° 10,433’	1391
OBH02	41° 00,663	10° 02,269	738
OBH01	40° 59,986	09° 56,010	405
CD1	41° 0,233’	9° 35,616’	-46
CD3	40° 59,966’	9° 14,796’	-204
CD5	41° 0,150’	8° 53,280’	-132

Table A.2.: Deployment coordinates of OBH and land stations.

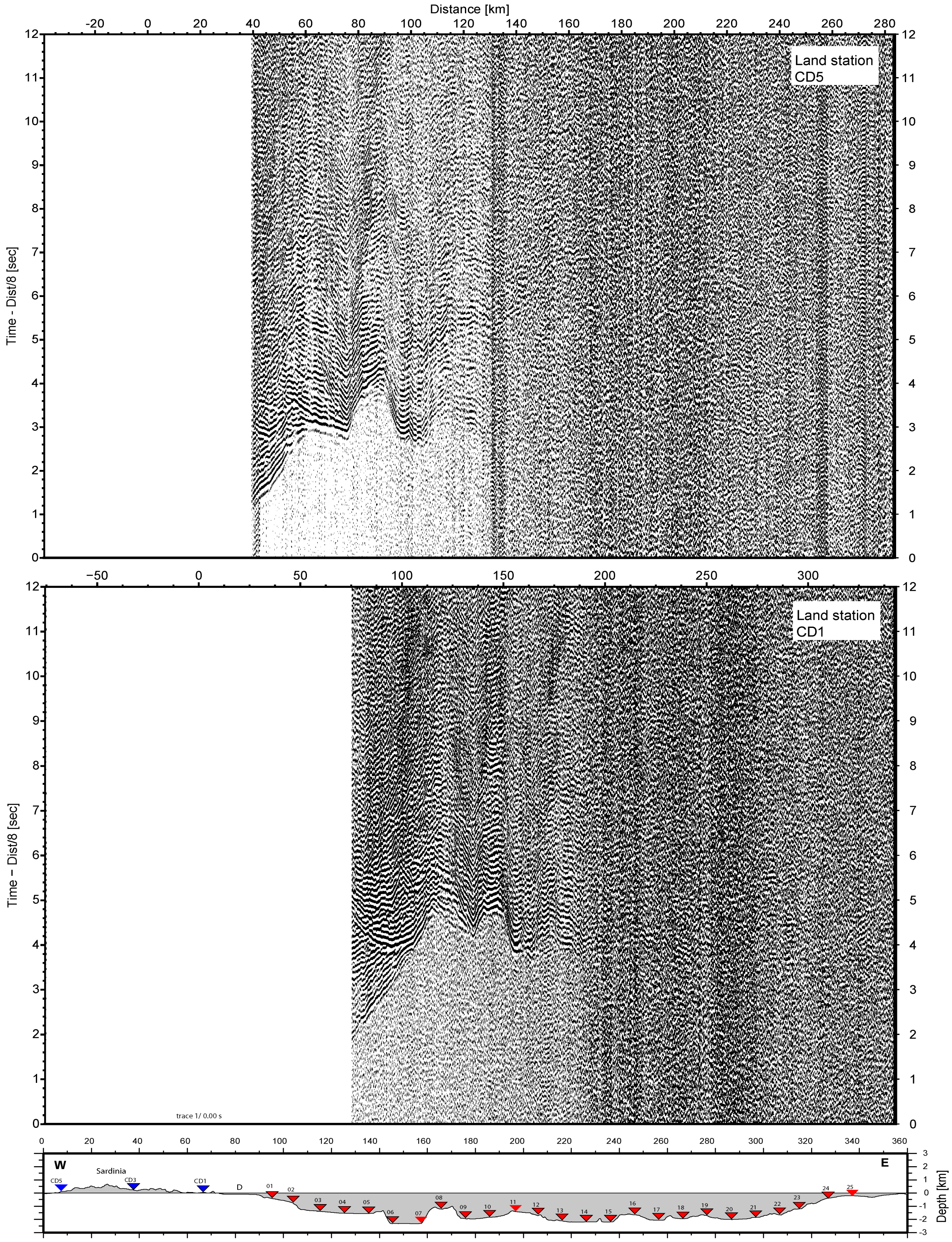

Figure A.15.: Record sections of land station CD1 and CD2.

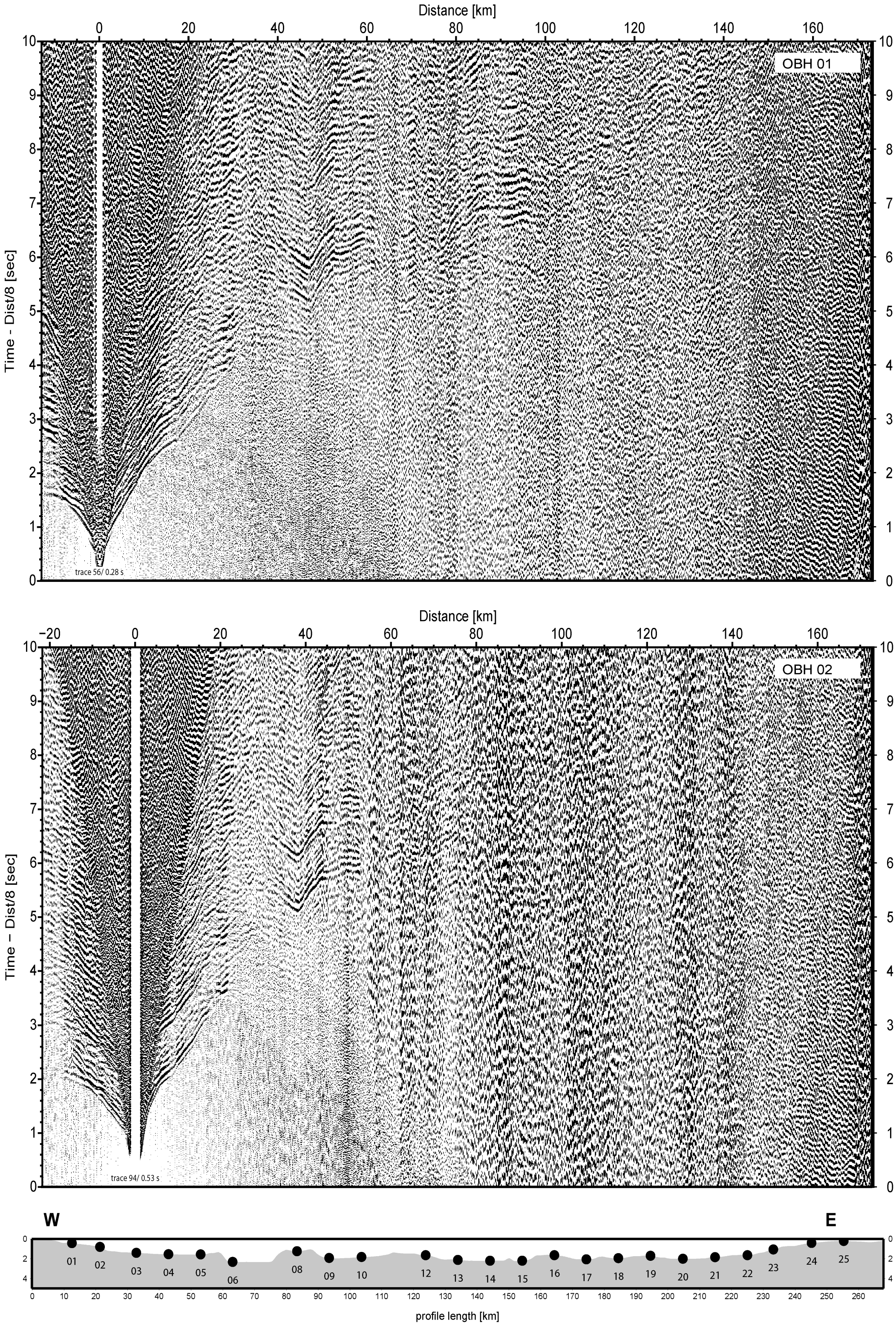

Figure A.16.: Record sections of OBH01 and OBH02.

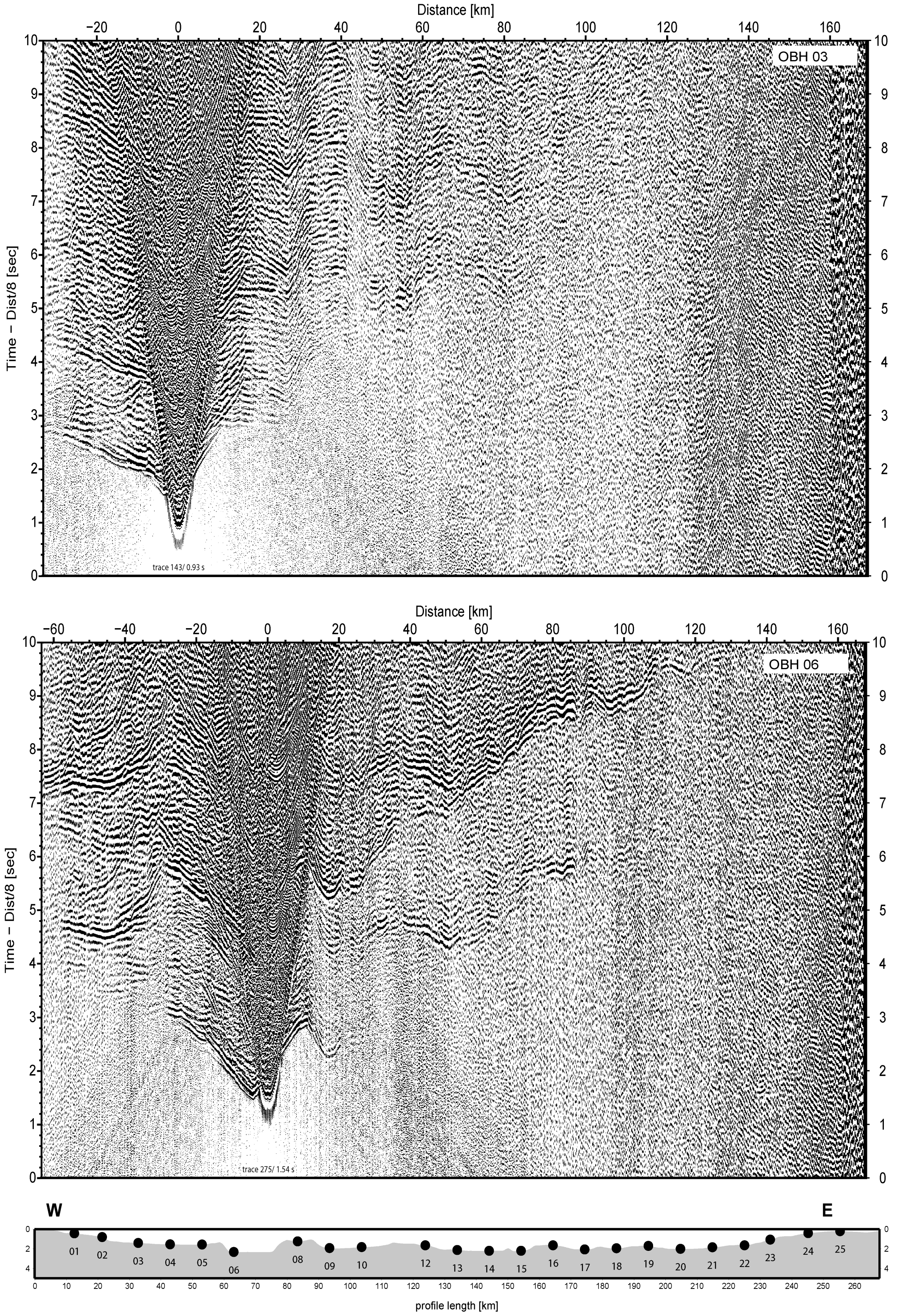

Figure A.17.: Record sections of OBH03 and OBH06.

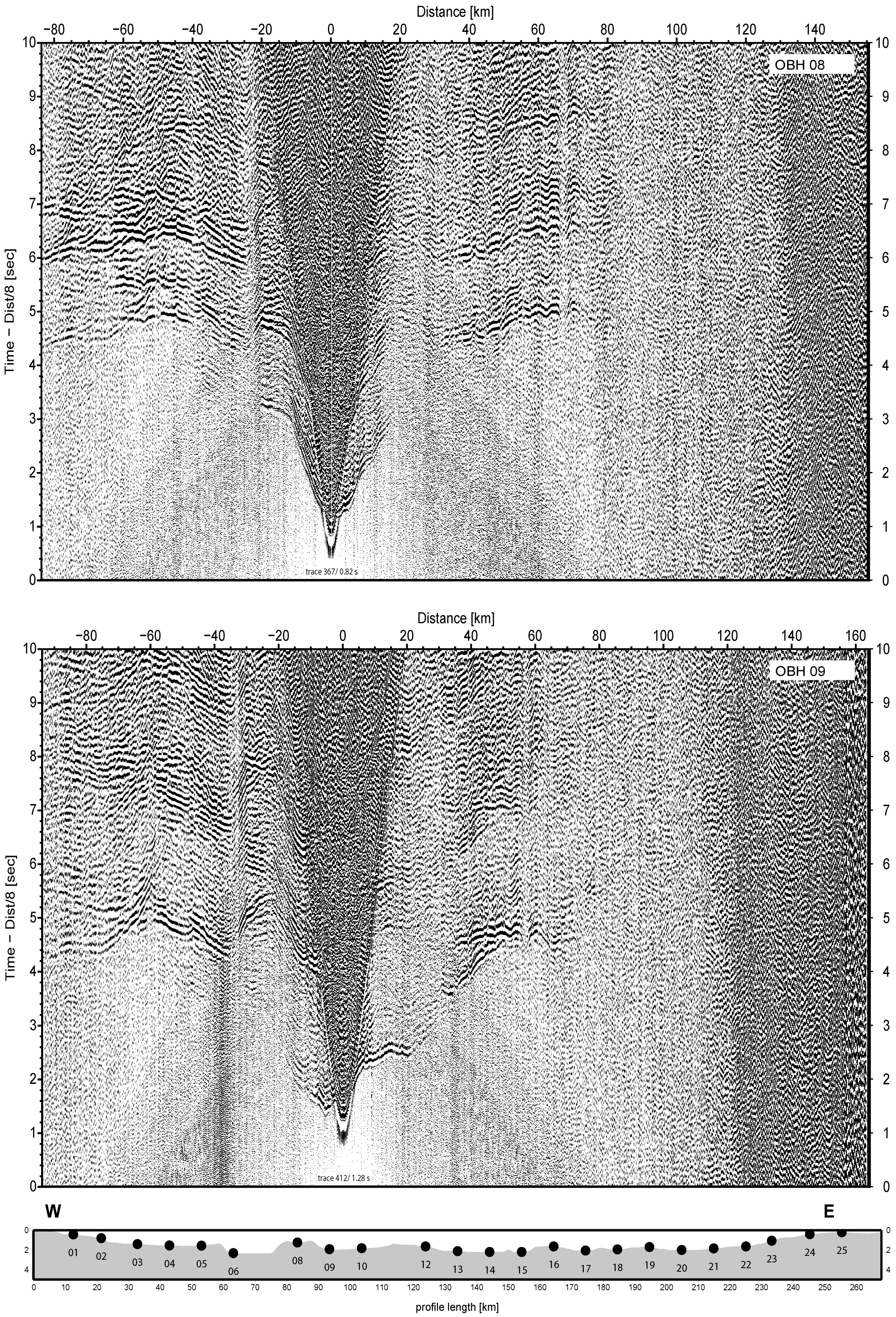

Figure A.18.: Record sections of OBH08 and OBH09.

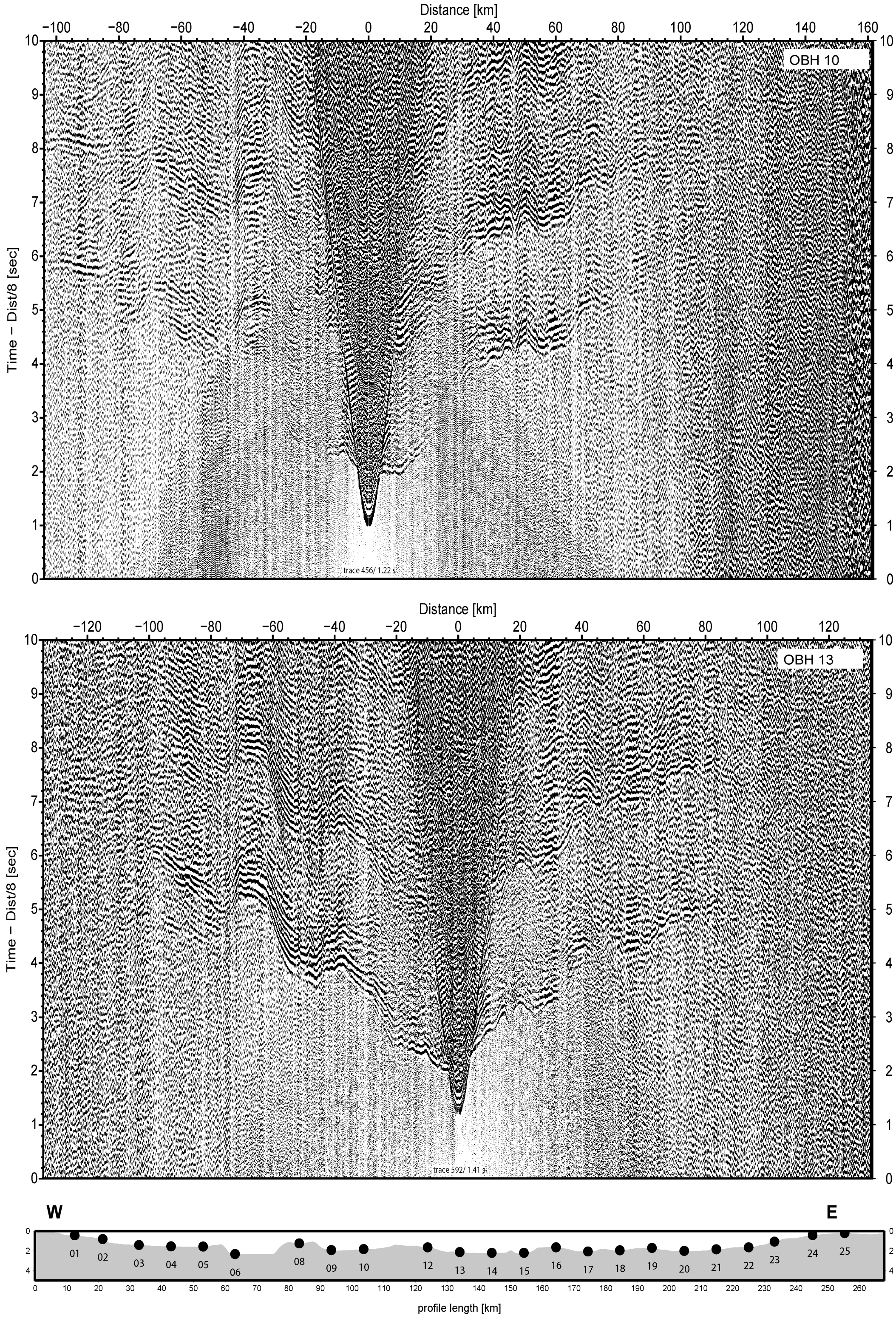

Figure A.19.: Record sections of OBH10 and OBH13.

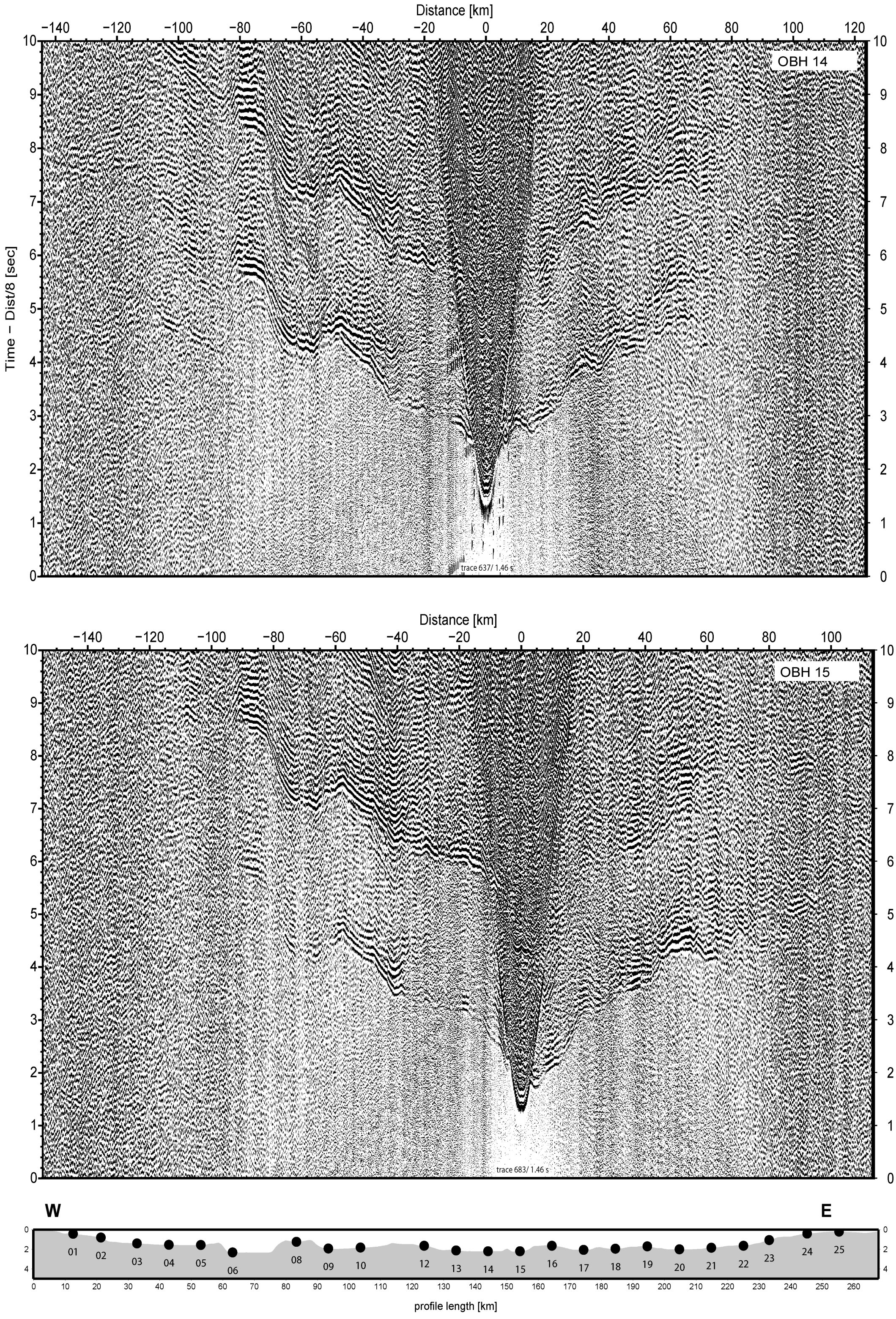

Figure A.20.: Record sections of OBH14 and OBH15.

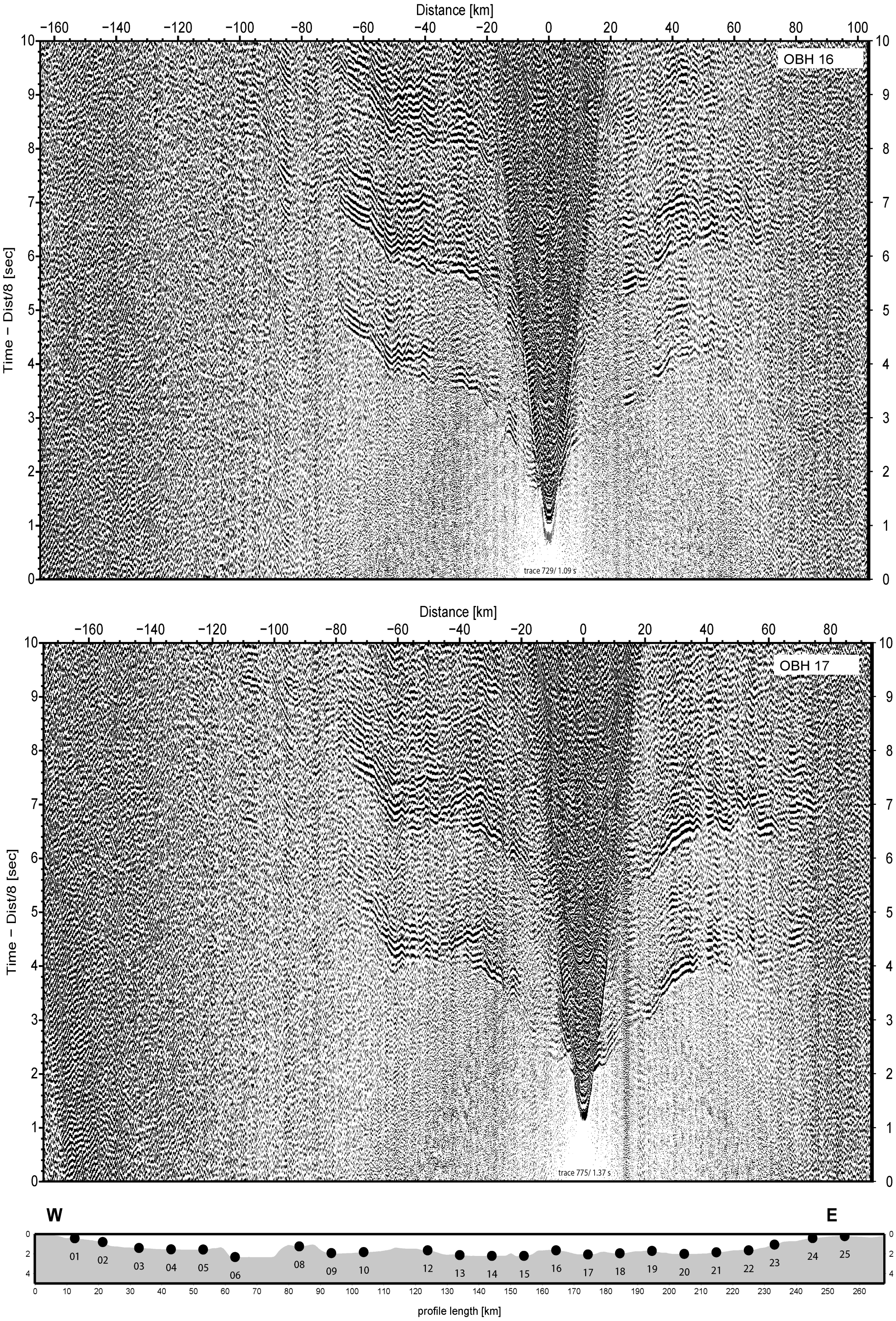

Figure A.21.: Record sections of OBH16 and OBH17.

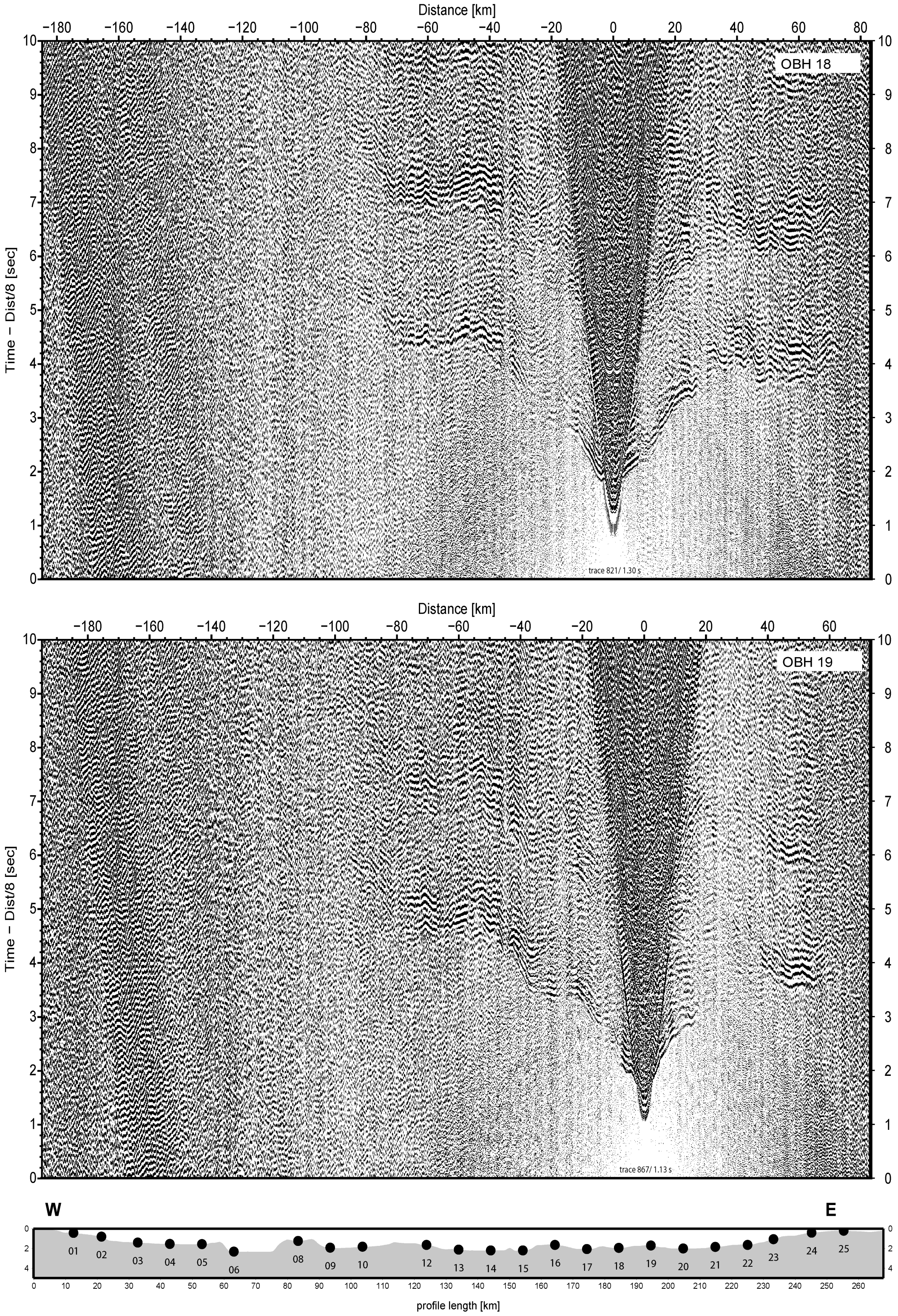

Figure A.22.: Record sections of OBH18 and OBH19.

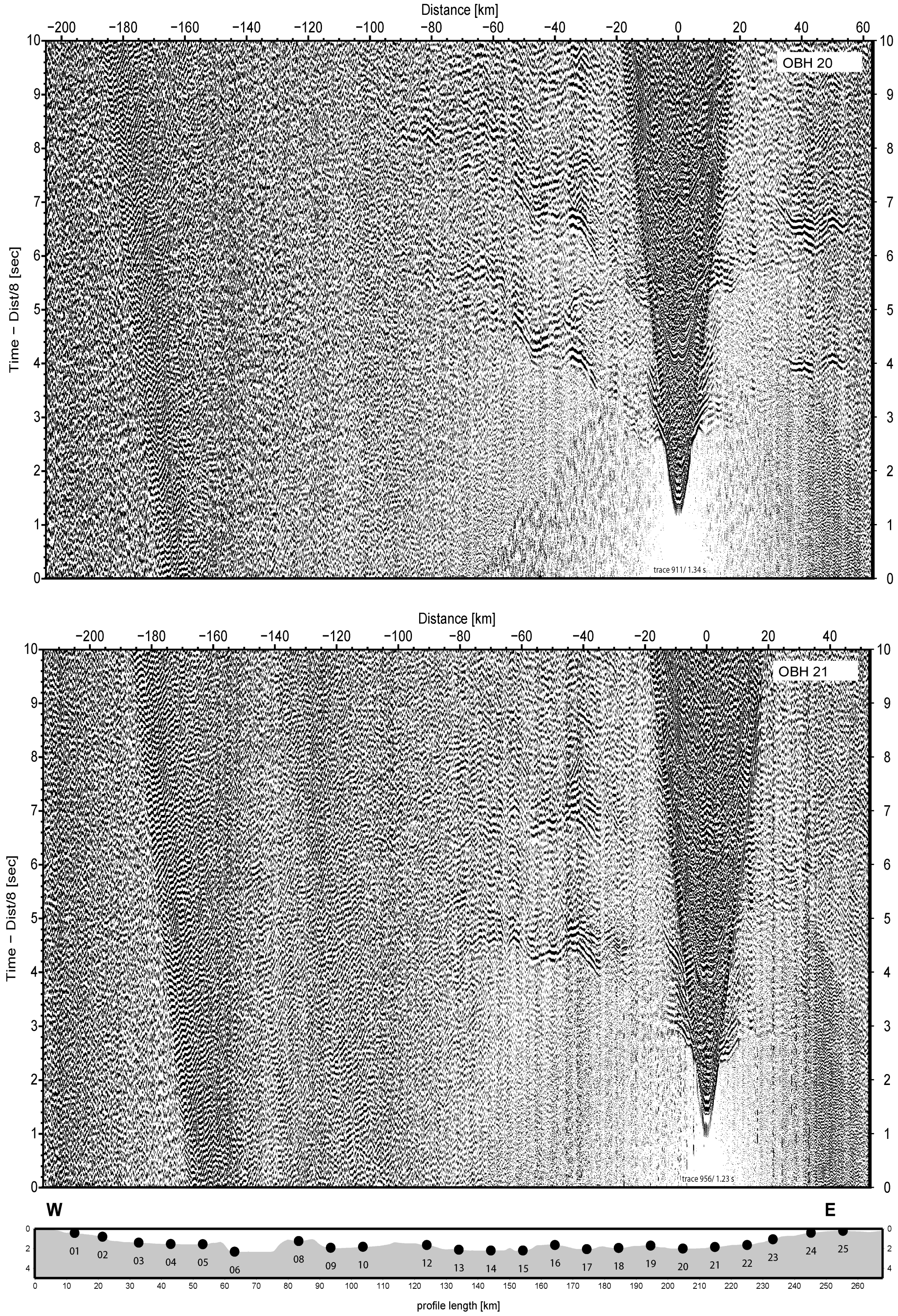

Figure A.23.: Record sections of OBH20 and OBH21.

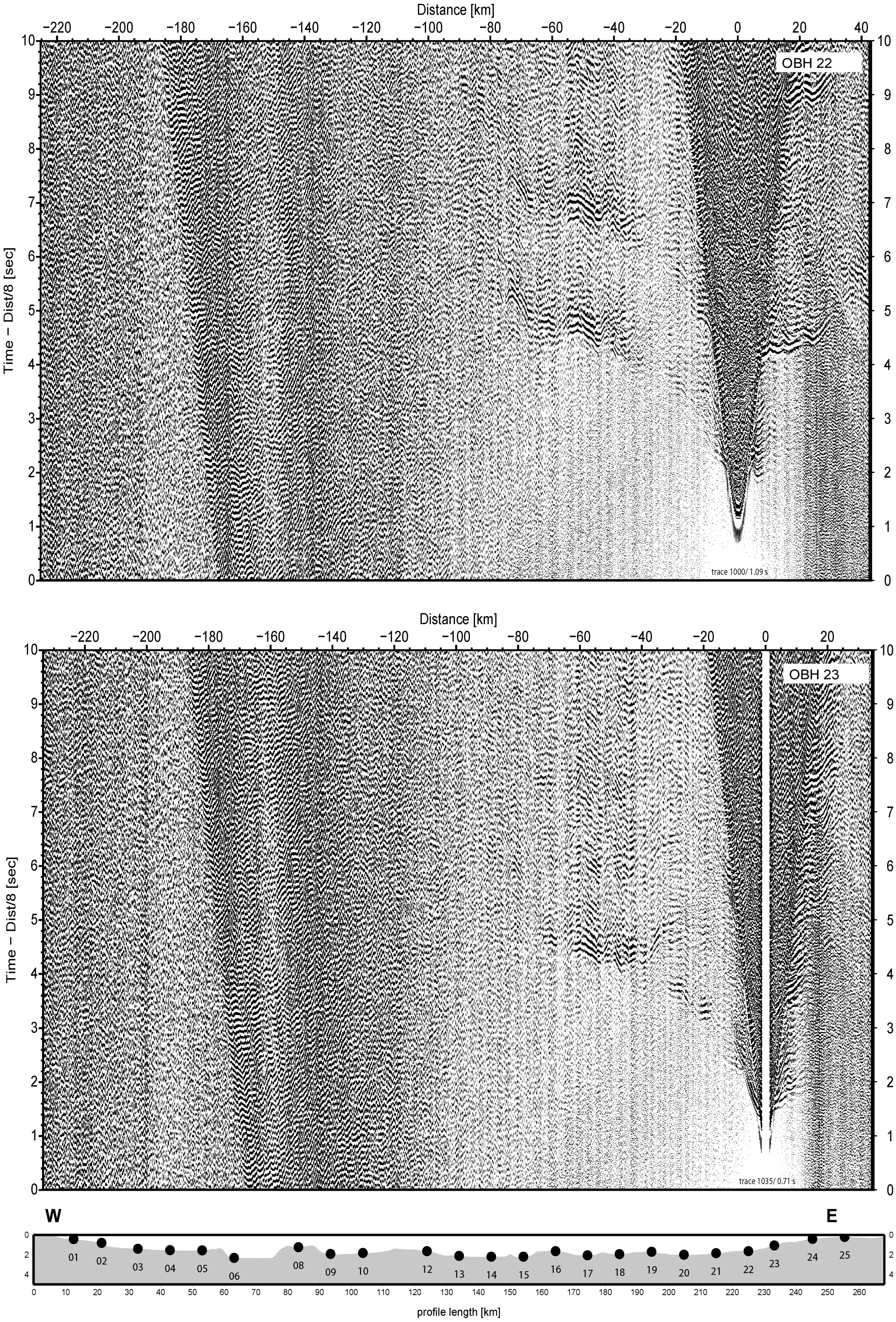

Figure A.24.: Record sections of OBH22 and OBH23.

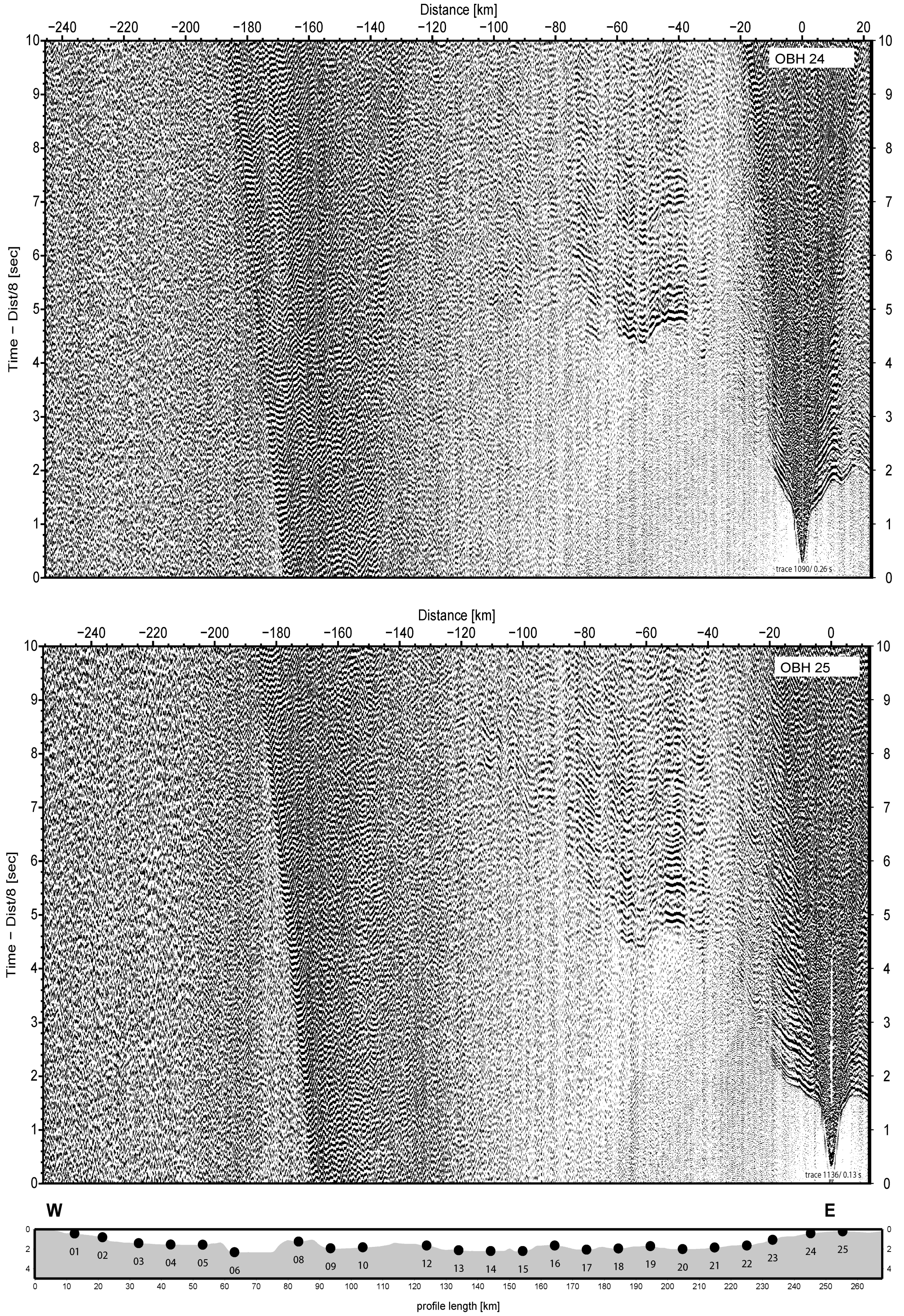

Figure A.25.: Record sections of OBH24 and OBH25.

Acknowledgments

First of all I want to thank Ingo Grevemeyer and Christian Berndt. They have permanently supervised my work during the last years, gave me always new impulses and a perfect scientific guidance. I am very grateful to them for organizing the financial support of this project and for giving me the opportunity to attend in international scientific conferences and several sea-going expeditions. Thanks for all these great experiences.

Many thanks go to César Ranero who initiated the MEDOC-project. I am very grateful to him for all the fruitful discussions and advices.

I thank Dirk Kläschen for his support with the seismic data processing. I have learned a lot from him and without his guidance the data wouldn´t be as they are. Many thanks go to Cord Papenberg for his help with writing scripts and data processing.

Thanks to all members of the MEDOC-Team who helped to conduct this project. Although there are much more involved, my special thanks go to Nevio Zitellini, Valenti Sallares, Manel Prada Dacasa and Roberto de Franco.

Many thanks to Ernst Flüh for financial support at the beginning of the PhD study.

I wish to thank everybody of the Geodynamics Department for the assistance and the nice time I had here. Thanks go to Anne Krabbenhöft, Anke Dannowski, Romed Speckbacher, Jens Karstens, Gareth Crutchley, Wiebke Brunn and Grant George Buffet. Special thanks go to my colleagues in the "B-Block". They make it much more comfortable to work in this lonely building. Thank you to Kathrin Lieser and Thorge Möller for Latex-Support. I thank Kai Schumann, Romed Speckbacher and Björn Kluß for proof-reading the thesis.

Finally, I would like to thank all my friends and my whole family for their support during this time. Most important I thank Heike for her great encouragement during the final stages of this work and all the things beyond work.

Eidesstattliche Erklärung

Hiermit bestätige ich, dass die vorliegende Abhandlung, abgesehen von der Beratung durch die Betreuer, nach Inhalt und Form die eigene Arbeit ist. Ich bestätige weiterhin, dass diese Arbeit unter Einhaltung der Regeln guter wissenschaftlicher Praxis der Deutschen Forschungsgemeinschaft entstanden ist. Es wurden keine anderen als die angegebenen Quellen und Hilfsmittel verwendet. Ich versichere, dass diese Arbeit noch nicht im Rahmen eines Prüfungsverfahrens an anderer Stelle vorgelegen hat.

Kiel, den

(Stefan Möller)

Curriculum Vitae

Name:	Stefan Möller
Place of residence:	Kiel, Germany
Date and place of birth:	05.11.1981 in Flensburg
Citizenship:	German
2003:	Technical college (GBS Flensburg), University Entrance qualification
2004-2009:	Study of Geophysics at the Christian-Albrechts University of Kiel, Diploma (MSc) in Geophysics
since 2009:	PhD student at GEOMAR, Kiel